PHD

Solid state X-ray structural studies

Sparkes, Hazel Anne

Award date:
2005

Awarding institution:
University of Bath

Solid State X-Ray Structural Studies

Hazel Anne Sparkes

A thesis submitted for the degree of Doctor of Philosophy
University of Bath
Department of Chemistry
October 2005

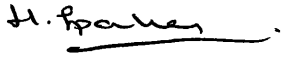

ProQuest LLC
789 East Eisenhower Parkway
P.O. Box 1346
Ann Arbor, MI 48106-1346

For My Grandparents:

Geoffrey and Mary Sparkes

Acknowledgments

I am extremely grateful to each of my supervisors, whose contribution has been invaluable during the time that I have known them, and without whom this thesis would not be in its current form. Paul Raithby for both patience and a wacky sense of humour (even at 3am on a Daresbury experiment!); Mary Mahon for immeasurable support and encouragement over the years; Gregory Shields for a wealth of knowledge on the workings of the CSD and ability to solve my computational problems and Frank Allen for the provision of insightful ideas and discussions.

I would also like to thank the members of the Raithby group, both past and present, for creating a pleasant working atmosphere and making the three years enormously enjoyable.

Clearly, it would not have been possible for me to carry out the studies detailed within this thesis without funding, for which, I would like to express my gratitude to the EPSRC and the CCDC.

Finally, I would like to acknowledge my friends for their constant support and my family for encouraging me to strive to reach my potential.

Abstract

Single crystal and powder X-ray diffraction studies were employed throughout this thesis to investigate solid state phenomena. The investigations detailed within, demonstrate how the applications of X-ray diffraction have expanded with advances in both instrumentation and software.

Chapter 1 introduces the procedures for structure solution and refinement from both single crystal and powder X-ray diffraction data, prior to reviewing the wide range of solid state reactions reported to proceed within single crystals. Within this, the application of Schmidt's topochemical principals to solid state [2+2] cycloaddition reactions is examined.

The application of the Bürgi-Dunitz structure-structure correlation hypothesis to gain insights into the mechanism of a solid state [2+2] cycloaddition reaction is explored in Chapter 2. 'Reactant' and 'product' datasets identified from the Cambridge Structural Database (CSD) have been analysed using principal component analysis to detect significant symmetry deformation coordinates.

Experimental photo induced solid state [2+2] cycloaddition reactions have been detailed in Chapter 3. The reactivity upon irradiation of five compounds has been studied and correlated with their respective single crystal structures, prior to employing powder X-ray diffraction to interrogate reaction mechanisms.

Chapter 4 investigates the existence of carbonyl-carbonyl interactions in carbonyl containing first row transition metal compounds identified from the CSD. The geometry and occurrence of the potential interaction motifs have been determined and subsequently compared with analogous motifs previously observed in organic compounds.

Single crystal X-ray diffraction has been used to probe the structures of two light induced metastable sulphur dioxide linkage isomers in $[Ru(NH_3)_4(H_2O)(SO_2)](CH_3C_6H_4SO_3)_2$ in Chapter 5. The effect of irradiation time on the achievable excitation levels has been examined prior to carrying out a *pseudo* steady state measurement.

Chapter 6 details the methods employed to achieve structure solutions and refinements from datasets demonstrating reticular, merohedral, *pseudo* merohedral or non-merohedral twinning, along with experimental examples for the latter three cases.

Abbreviations

Abbreviation	Definition
α	Alpha
Å	Angstrom
f_i	Atomic Scattering Factor
β	Beta
PDB	Brookhaven Protein Databank
CSD	Cambridge Structural Database
cm	Centimetre
CCD	Charge-Coupled Detector
χ	Chi
°	Degrees
°C	Degrees Celcius
DFT	Density Functional Theory
$CDCl_3$	Deuterated Chloroform
DCM	Di-chloromethane
η	Eta
e.g.	For Example
esd	Estimated Standard Deviation
γ	Gamma
g	Grammes
HOMO	Highest Occupied Molecular Orbital
IR	Infra-red
ICSD	Inorganic Crystal Structure Database
I_{hkl}	Intensity of Reflection *hkl*
IR	Irreducible Representation
K	Kelvin
τ	Lifetime
LUMO	Lowest Unoccupied Molecular Orbital
MDF	Metals Data File
mm	Millimetre
MS1	Metastable State 1
MS2	Metastable State 2
μs	Micro-second

Abbreviation	Definition
hkl	Miller Indices (*hkl*)
ml	Milli-litre
mg	Milli-grammes
ms	Milli-second
MO	Molecular Orbital
MM2	Method of Applying Molecular Mechanics
nm	Nanometre
ns	Nano-second
NMR	Nuclear Magnetic Resonance
%	Percentage
Ph	Phenyl
KBr	Potassium Bromide
R_1	*R*-factor
s	Second
F_{hkl}	Structure Factor for Reflection *hkl*
SDC	Symmetry Deformation Coordinate
i.e.	That Is
θ	Theta
V	Volume
W	Watt
λ	Wavelength
R_{wp}	Weighted Profile *R*-factor
w*R*2	Weighted *R*-factor

List of Tables and Figures

Chapter 3

Chapter 4

Chapter 5

Contents

Chapter 1

X-Ray Crystallography and its Applications

1.1 Aims of Thesis

This thesis sets out to illustrate the wide range of situations in which X-ray diffraction techniques can be applied, by demonstrating how advances in both instrumentation and software have allowed the uses of X-ray diffraction to exceed simple structure solution or compound identification. X-ray diffraction will be applied to obtain information in the following studies:

1. *Solid state reactions within crystals* - A variety of solid state reactions have been reported within crystalline materials. As would be expected, the movement of atoms or molecules contained within a solid is restricted by the close proximity of other atoms or molecules. Therefore, both the mechanisms by which solid state reactions occur and the factors that govern them are likely to be different to those that apply to gas or solution phase reactions. The investigations detailed within, aim to provide further insight into the mechanism of photochemically induced [2+2] cycloaddition reactions from both a theoretical and experimental perspective. This in turn may lead to an enhanced understanding of the crystalline properties permissible in the structures of compounds that may potentially undergo solid state [2+2] cycloaddition reactions.

2. *Intermolecular interactions* - The effect of intermolecular interactions on material properties can be significant, and extending the understanding of such interactions would be beneficial in many areas of chemistry. It is intended that a database study will provide a greater appreciation of one particular type of dipole-dipole interaction, carbonyl-carbonyl interactions, in transition metal compounds. The examination will focus on the impact of the interaction both in terms of its occurrence and geometric requirements.

3. *Solid state excitation within crystals* - Excitation of atoms or molecules within crystals can result in non permanent changes to their crystal structures, which can be examined using X-ray diffraction techniques. It is hoped that a series of single crystal X-ray diffraction experiments will provide conclusive structural evidence for the geometry of previously identified metastable sulphur dioxide linkage isomers of $[Ru(NH_3)_4(H_2O)(SO_2)](CH_3C_6H_4SO_3)_2$.

4. *Structure solution from crystals that contain more than one domain (twinned crystals)* - Datasets from crystals containing more than one domain used to be routinely discarded, as it was very difficult and time consuming to correctly process the data. While it is always preferable to obtain a single crystal with one domain, this may not be possible for some compounds that are prone to twinning, or alternatively twinning may not have been identified prior to the structure solution stage. In such situations it is now practicable to undertake structure solution and refinement from twinned datasets. The final chapter of this thesis affords successful structure solution and refinement from datasets that show different types of twinning.

In view of the fact that the investigations detailed within this thesis rely almost exclusively on data acquired during X-ray diffraction experiments, it is worth examining the development of X-ray diffraction techniques, which are used to study crystalline materials, beginning with a review of the internal structure of crystalline solids.

1.2 Introduction

1.2.1 Historical

In the 17th Century, Kepler began research which, at its conclusion in the 19th Century, had shown that the average distance between atoms in a simple ionic salt crystal would be 1-2 Å, a theory deduced from studies of crystal geometries, densities, atomic weights and knowledge of Avogadro's number. This suggested that crystals would act as three dimensional diffraction gratings provided that the radiation employed had a similar wavelength to the interatomic distances within the crystal. In 1895, Wilhelm Röntgen discovered X-rays, which were subsequently shown to have wavelike characteristics by von Laue in 1912. On the basis of their wavelength he suggested that these waves might be diffracted by crystals. Within the year, this hypothesis had been confirmed by Friedrich and Knipping with the production of the first diffraction photographs [1.1][1.2].

1.2.2 Bragg's Law [1.1][1.2][1.3]

In 1913, W.L. Bragg solved the first crystal structures of NaCl and KCl, by treating the diffraction spots as if they had arisen through the reflection of the X-ray beam from sets of parallel planes in the crystal, each set characterised by Miller indices (*hkl*) and an interplane separation distance (*d*). He went on to derive an equation, now known as Bragg's Law, which allows simple visualization of the conditions that must be fulfilled in order to achieve constructive interference of the X-rays and thus observe diffraction spots, see Figure 1.1 [1.1][1.4][1.5]. It is important to register two points at this stage: firstly Bragg's Law does

not tell us anything about the intensity of the 'reflected' beam and secondly reflection as a concept in incorrect, in practice the X-rays are diffracted by the electron clouds that surround the atomic nuclei in the crystal.

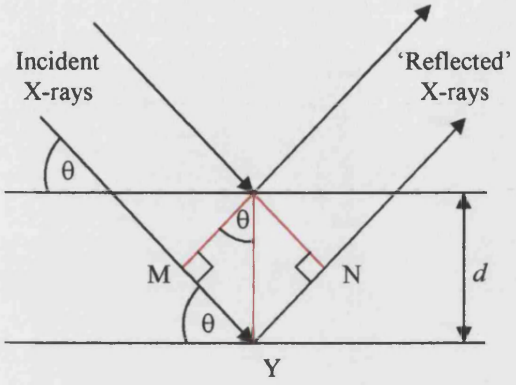

For constructive interference to be observed
Path Difference = MY +NY = nλ
Sin θ = MY/d
So MY = *d* Sin θ
Path Difference = 2*d* Sin θ = nλ
Bragg's Law 2*d* Sin θ = nλ

Figure 1.1 - *Derivation of Bragg's Law in 2-dimensions [1.1][1.4].*

The ability of an atom to scatter X-rays is given by the atomic scattering factor (f_i). At low Bragg angle, this is proportional to the number of electrons around the nucleus, but this function tails off as the Bragg angle increases due to incoherent scattering, producing a concomitant decrease in diffracted intensity [1.2].

1.2.3 Crystal Lattices, Unit Cells and Bravais Lattices [1.1][1.6][1.7]

Crystals can be viewed as three-dimensional periodic arrangements of matter, in other words their internal structure consists of a regular repeating pattern of atoms, molecules or ions, known as the crystal lattice. This can be represented by a network of points, which are located at positions of identical environment by translation to form a space lattice. While this does not account for the precise arrangement of the objects it does provide a complete description of how the repeat occurs, in terms of one of the four basic lattice types: *P* (primitive), *C* (centred), *I* (body centred) and *F* (face centred), see Figure 1.2.

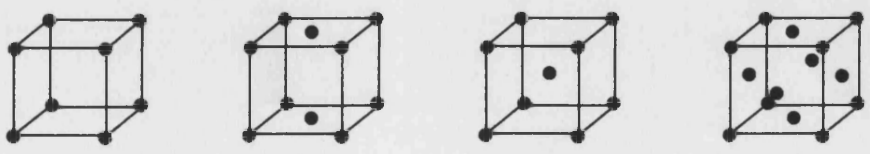

Primitive *(P)* Centred *(C)* Body Centred *(I)* Face Centred *(F)*

Figure 1.2 - *Illustration of the four basic lattice types, where ● represents a lattice point.*

The unit cell is defined as the smallest unit within the crystal lattice which when replicated by translation alone shows the full symmetry of the crystal structure (see Figure 1.3). The different unit cell shapes are known as the seven crystal systems - cubic, trigonal (or rhombohedral), hexagonal, tetragonal, orthorhombic, monoclinic and triclinic - these are uniquely characterised by the three cell axes *a*, *b* and *c* and the angles between them α (between *b* and *c*), β (between *a* and *c*) and γ (between *a* and *b*).

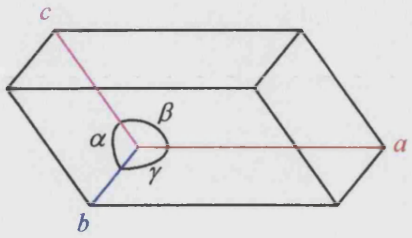

Figure 1.3 - *The unit cell.*

The arrangement of lattice points in terms of one of the seven crystal system and one of the four basic lattice types gives rise to fourteen unique Bravais lattices (see Table 1.1), which when stacked together in three dimensions will fill all space.

Table 1.1 - Table showing how the 14 Bravais Lattices are distributed across the 7 Crystal Systems [1.1].

Crystal System	Lattice types	Parameters
Cubic	*P, I, F*	$a = b = c$, $\alpha = \beta = \gamma = 90°$
Trigonal (or Rhombohedral)	*P*	$a = b = c$, $\alpha = \beta = \gamma \neq 90°$
Hexagonal	*P*	$a = b \neq c$, $\alpha = \beta = 90°$, $\gamma = 120°$
Tetragonal	*P, I*	$a = b \neq c$, $\alpha = \beta = \gamma = 90°$
Orthorhombic	*P, C, I, F*	$a \neq b \neq c$, $\alpha = \beta = \gamma = 90°$
Monoclinic	*P, C*	$a \neq b \neq c$, $\alpha = \gamma = 90°$, $\beta \neq 90°$
Triclinic	*P*	$a \neq b \neq c$, $\alpha \neq \beta \neq \gamma$

1.2.4 Symmetry Elements within Crystals [1.4][1.7]

Unlike molecules where a range of symmetry operations can relate one part to another, only six symmetry elements are possible within crystals to describe how molecules or parts of them relate to each other within the unit cell and these are illustrated in Figure 1.4.

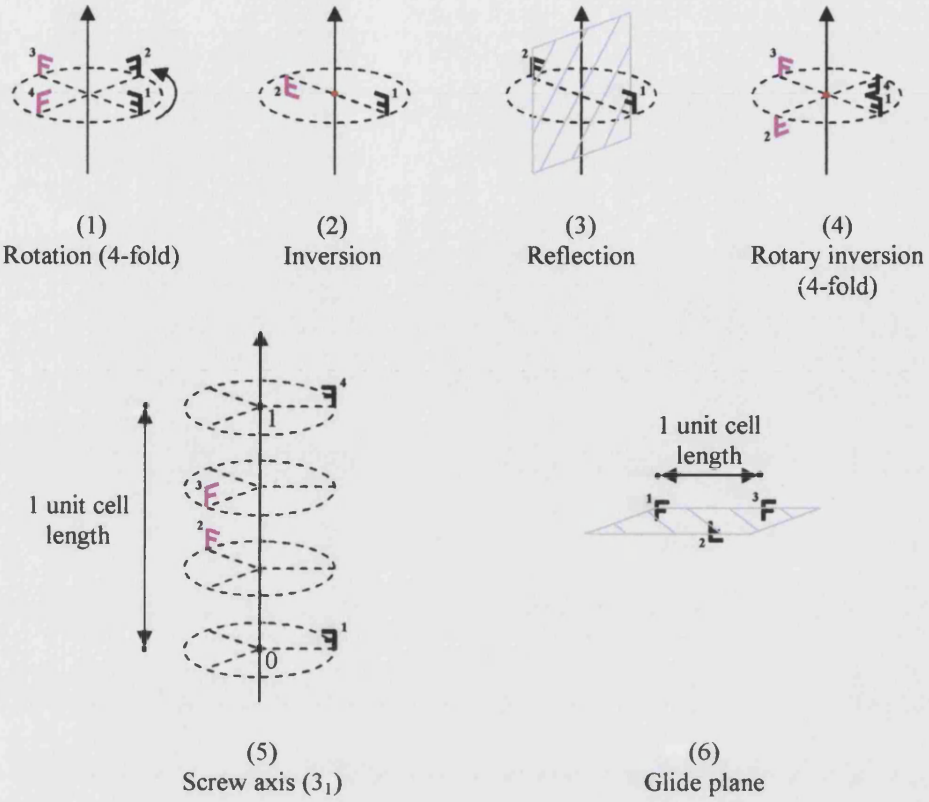

Figure 1.4 - *Illustration of the the six symmetry elements possible within crystals, where F represents an asymmetric object [1.4]. Crystallographic rotations are always anticlockwise and can only be 1-, 2-, 3-, 4- or 6-fold.*

The first three symmetry elements are familiar from group theory and the fourth is fairly self explanatory being a rotation followed by an inversion, however, the final two are slightly less obvious. A screw axis involves a rotation followed by a translation up the unit cell, so for example, a 3_1 screw axis along *a* is a rotation of 120° (360°/3) followed by a translation of a 1/3 up the *a*-axis. A glide plane involves a translation of 1/2 a unit cell followed by a reflection, so a *c*-glide perpendicular to *b* means a translation by *c*/2 followed by reflection in a mirror plane perpendicular to the *b*-axis. Crystallographic rotations are always anticlockwise and can only be 1-, 2-, 3-, 4- or 6-fold, whether they are straight rotations or part of a rotary inversion or screw axis.

The six symmetry elements can be divided in two categories: the first four (rotations, inversions, reflections and rotary inversions) are non-translational and do not cause systematic absences in the diffraction data, while the final two (screw axes and glide planes) are translational and result in absences.

1.2.5 Absences and Intensity Distributions

Absences in crystallographic data arise when the intensity of a reflection is systematically zero as opposed to accidentally zero. This arises either as a result of lattice

centering (general absences) or the presence of translational symmetry elements (systematic absences). General absences affect the whole dataset while systematic absences only affect subsets of reflections. For example, *C* centering affects all reflections where $h + k$ is odd whereas a 2_1 screw axis along *a* only affects reflections with odd *h* values if *k* and *l* are zero.

Although non-translational symmetry elements do not cause absences, their presence does affect the intensity distribution within a diffraction pattern and this can be analysed by statistical tests on the normalized intensities. At best, the results provide a probability of a particular symmetry element being present, as the analyses are frequently unreliable, particularly for rotation axes and mirror planes where only small subsets of the data can be used in the analysis. As a result, the only non-translational symmetry element routinely tested for in this manner is an inversion centre, since the whole data set can be employed. When no crystallographic inversion is present the data are acentric, with the normalized intensities not varying significantly from their mean, however, when an inversion centre is present the data become centric and show more overall variation, see Figure 1.5 [1.8].

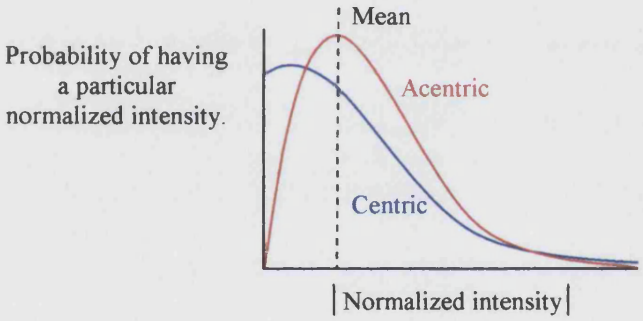

Figure 1.5 - *Illustration of the normalized intensity distribution for an acentric and centric dataset [1.8].*

1.2.6 Space groups [1.4][1.7]

All possible combinations of solid state symmetry elements give rise to 230 unique three dimensional space groups which are distributed across the seven crystal systems. These space groups represent the position of the symmetry elements. The smallest part of the unit cell from which the complete crystal structure can be obtained through a combination of the symmetry elements is known as the asymmetric unit [1.2]. Equivalent position diagrams describe the locations of the asymmetric unit (shown as equivalent positions) while space group diagrams provide the position of all of the symmetry elements within the unit cell. All space groups are illustrated in the *International Tables for X-ray Crystallography, Volume A* [1.9].

The space group for a given crystal can be determined on the basis of the systematic absences present, once the unit cell parameters and Bravais lattice have been established. Although many of the common space groups can be uniquely identified, this is not always the case and as a result structure solution may have to be attempted in several space groups to identify the correct one.

It is worth noting that enantiomerically pure chiral molecules cannot crystallize in space groups containing an inversion centre or mirror plane as these symmetry elements automatically generate the other enantiomer. As a result their crystal structures never contain inversion centres, mirror planes, rotary inversion axes or glide planes.

1.3 X-ray Diffraction Experiments

Although the information recorded in single crystal and powder X-ray diffraction experiments is essentially the same, the former is by far the preferred technique for obtaining accurate structural data [1.10]. This is due to the fact that the data can be recorded in three dimensions from a single crystal, whereas from a powder they are compressed on to one angular dimension as the sample contains multiple randomly orientated crystallites, see Figure 1.6 [1.3]. This compression of data results in peak overlap making X-ray powder diffraction a more complex and a less accurate procedure for obtaining a crystal structure. The continued use and development of powder diffraction as a structural method is due to the fact that it provides the possibility of obtaining data from reasonably crystalline samples unsuited to single crystal techniques where, for example, crystals are too small, of insufficient quality, or twinned.

Figure 1.6 - *Illustration of the relationship between single crystal and powder diffraction data, (left) single crystal frame, (middle) equivalent to data from several single crystals, (right) powder data arises from multiple crystallites in random orientations [1.3].*

1.3.1 Single Crystal X-ray Diffraction

1.3.1.1 Background

Single crystal X-ray diffraction experiments used to be time consuming with one structure taking months to complete, however, the advent of the area detector has decreased standard data collection times from week(s), required by a point detector, to a matter of hours. In conjunction with this, computational advances have allowed the data, from even the most complex structures, to be processed and modelled in greatly reduced periods of time. Hence, single crystal diffraction has become a routinely used analytical technique to determine or confirm the structure of a material. Thus, only a brief outline of the procedure is provided below.

1.3.1.2 Experimental Set-Up for Single Crystal X-ray Diffraction Experiments [1.3]

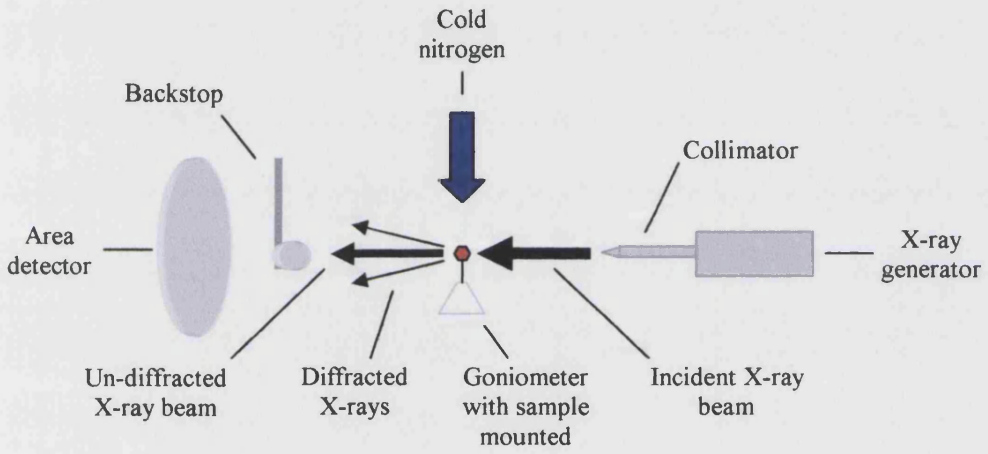

Figure 1.7 - *Schematic of an X-ray diffractometer with an area detector.*

Figure 1.7 shows a schematic of the standard set-up for a single crystal X-ray diffraction experiment. The X-rays are generated by firing electrons at a metal target, typically molybdenum, they are then monochromated and collimated so that only a parallel beam of K_α radiation reaches the sample. As the majority of the X-rays are not diffracted by the crystal, the backstop is present to remove them, so that only the diffraction itself is recorded by the area detector. The crystal is rotated through 0.5° to 2° during the collection of every frame of data to optimize the number of diffraction spots a frame contains, each 'spot' corresponds to diffraction from one set of Miller planes for which Bragg's Law has been satisfied. Subsequent rotation of the crystal allows the conditions for constructive interference from other sets of Miller planes to be attained, and their diffraction intensities measured. In order to reduce the thermal motion of the atoms during data collection liquid nitrogen is normally used to cool the sample to around 150 K.

1.3.1.3 Single Crystal X-Ray Crystallographic Collection Procedure

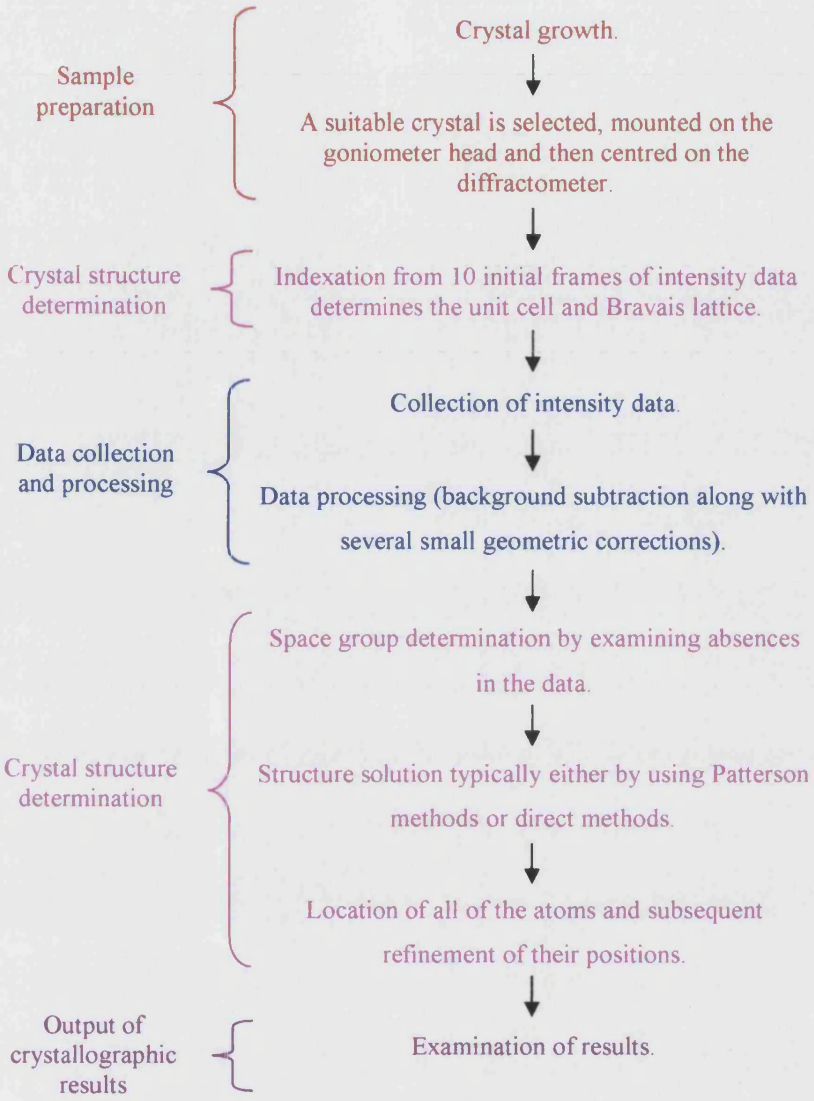

Figure 1.8 - *Schematic of the stages involved in a single crystal X-ray diffraction experiment to determine a crystal structure [1.4].*

The schematic in Figure 1.8 highlights the main stages in a standard single-crystal X-ray diffraction experiment using a diffractometer fitted with an area detector [1.4]. The procedure for crystal structure determination is discussed below:

1.3.1.4 Indexing

The unit cell and Bravais lattice of the crystal can be identified from the symmetry of the diffraction pattern and general absences relating to lattice centering using only a small set of frames in software such as DENZO [1.11] or DIRAX [1.12].

1.3.1.5 Space Group Determination

Once the complete data set has been collected, attempts can be made to determine the space group from the systematic absences which arise if translational symmetry elements are present, however, as discussed above unique identification is not always possible. In such circumstances, information from statistical tests about the centricity of the data can be employed, to indicate whether the crystal structure is likely to be centrosymmetric or non-centrosymmetric *i.e.* with or without an inversion centre. Even so, it is not an uncommon necessity to attempt a structure solution in several space groups in order to identify the correct one. A variety of computer programs are available to analyse the intensity of reflections across the complete dataset and identify absences, such as WINGX [1.13] or XPREP which is part of the SHELXTL suite [1.14].

1.3.1.6 Structure Solution [1.4]

X-ray diffraction experiments measure the intensity (I_{hkl}) of the diffracted beam from each set of Miller planes (*hkl*) and this is proportional to the square of the structure factor (F_{hkl}) from those planes. Although, the absolute value of the structure factor can be determined from the experimental data using the relationship given in Equation 1.1, its phase cannot.

$$(I_{hkl}) = K(F_{hkl})^2(Lp)(Abs)$$

Equation 1.1 - *Relationship between the intensity of a reflection (I_{hkl}) and its structure factor (F_{hkl}) for the Miller plane (hkl), K is a scale factor, Lp represents the geometric Lorentz and polarization corrections and Abs is the absorption factor [1.2].*

In order to produce an electron density map during the structure solution stage, however, both the structure factor and its phase are required, see Equation 1.2, this is known as the crystallographic phase problem.

$$\rho(xyz) = 1/V \times \Sigma_{all(h)} \Sigma_{all(k)} \Sigma_{all(l)} (F_{hkl})\cos[2\pi(hx + ky + lz) - \alpha]$$

Equation 1.2 - *The relationship between the electron density ($\rho(xyz)$) at the point xyz in the unit cell and the structure factor (F_{hkl}) for a particular set of Miller indices (hkl). V is the volume of the unit cell and α is the phase angle [1.7].*

The first stage in structure solution is therefore to identify an appropriate method to overcome the phase problem. There are two standard approaches depending on the type of compound [1.2][1.7].

1. *Patterson methods* - This strategy is used for samples containing heavy atoms, by producing an initial Fourier series based on $(F_{hkl})^2$ from which the peaks relating to the heavy atom(s) can be easily identified and their positions calculated. Heavy atom programs include DIRDIF [1.15] and SHELXS (Patterson) [1.16].

2. *Direct methods* - This approach is used for samples where there is no dominant scatterer, and it relies on assigning phases to some of the strongest reflections in the dataset on the basis of mathematical inequalities in the data. This, in turn, has implications for the phases of other strong reflections present. These phases are then used to calculate structure factors and subsequently, an electron density map from which a structural fragment can normally be identified. Structure solution programs employing this methodology include SHELXS-97 [1.16] and SIR-97 [1.17].

1.3.1.7 Fourier Difference Maps and Refinement [1.3][1.4]

The final stage in crystal structure determination is refinement, which aims firstly to identify and locate any atoms unaccounted for in the structure solution stage from difference electron density maps, and secondly to improve the fit between the calculated and observed structure factors. The refinement is usually carried out either on the amplitudes of (F_{hkl}) or more generally using $(F_{hkl})^2$ as the phases of the observed structure factors are unknown.

At the end of the refinement the fit of a solution to the experimental data is normally assessed using either an *R*-factor (R_1) based on (F_{hkl}) or a weighted *R*-factor (w*R*2) based on $(F_{hkl})^2$, see Equations 1.3 and 1.4. Typically, the aim is to achieve an *R*-factor between 2% and 7% with no significant residual electron density, the weighted *R*-factor is always greater. Errors in atomic positions, displacement parameters, and in bond parameters are checked to confirm that they are acceptable, and that the overall model makes chemical sense. Refinements are often carried out using SHELXL [1.18].

$$R_1 = \frac{\Sigma||F_{calc}| - |F_{obs}||}{\Sigma|F_{obs}|}$$

Equation 1.3

$$wR2 = \left[\frac{\Sigma[w(F_{obs}^2 - F_{calc}^2)^2]}{\Sigma[w(F_{obs}^2)^2} \right]^{1/2}$$

Equation 1.4

Equations 1.3 and 1.4 - *Definition of the R-factor and wR2 factor which are used to assess crystallographic refinements, where F_{obs} is the observed structure factor, F_{calc} is the calculated structure factor and w is a weighting factor [1.19].*

1.3.2 X-Ray Powder Diffraction

1.3.2.1 Background

X-ray powder diffraction is a bulk sampling technique and as result has a wide range of applications. In addition to identification of materials it can be used for both qualitative and quantitative sample analysis, for example, to check its purity, to confirm its identity against a reference sample or to determine the relative amounts of a polymorph that it contains [1.20]. It also provides a convenient method for examining materials that are produced as microcrystalline powders e.g. in the pharmaceutical industry, where these powders are subsequently compacted into tablets.

However, the procedure for obtaining a structure determination from powder diffraction data is more complicated that those from single crystal data. Nonetheless automation of the technique in the late 1970s has allowed significant advances to be made in *ab initio* structure determination, while development of computer analysis techniques has increased the complexity of structures that can be solved. However, where available, it is still common to exploit prior structural knowledge in setting up the geometrical restraints used during structure solution and refinement from powder data [1.21]. Consequently, care has to be taken to ensure that the restrictions are appropriate and do not reduce the possibility of obtaining a structure solution [1.22].

1.3.2.2 Experimental Set-Up for X-ray Powder Diffraction Experimental

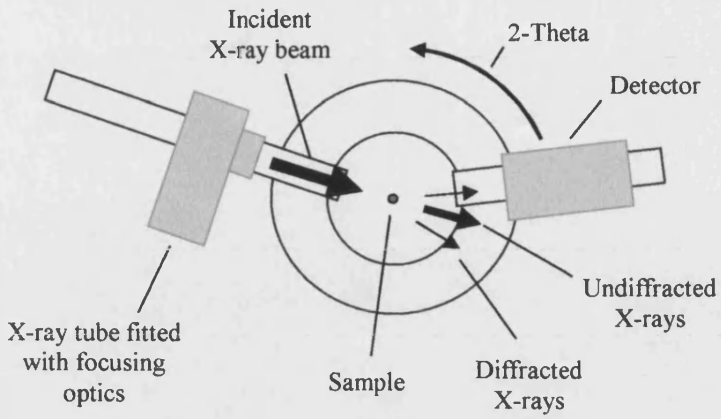

Figure 1.9 - *Schematic of a powder diffractometer set up for capillary sample collection.*

X-ray powder diffraction experiments tend to employ copper radiation (λ = 1.5461 Å), which has a longer wavelength than that of molybdenum (λ = 0.7107 Å) normally used for single crystal work. As a result the diffraction pattern is expanded and peak overlap is reduced. Once generated, the X-rays are generally monochromated using graphite so that only K_α radiation reaches the sample, which is either contained in a capillary or mounted on a flat plate. The powder pattern is usually recorded with a scintillation counter and displayed as a trace of intensity versus 2-theta position. A typical powder diffractometer set-up is illustrated in Figure 1.9.

1.3.2.3 Powder Diffraction X-Ray Crystallographic Collection Procedure

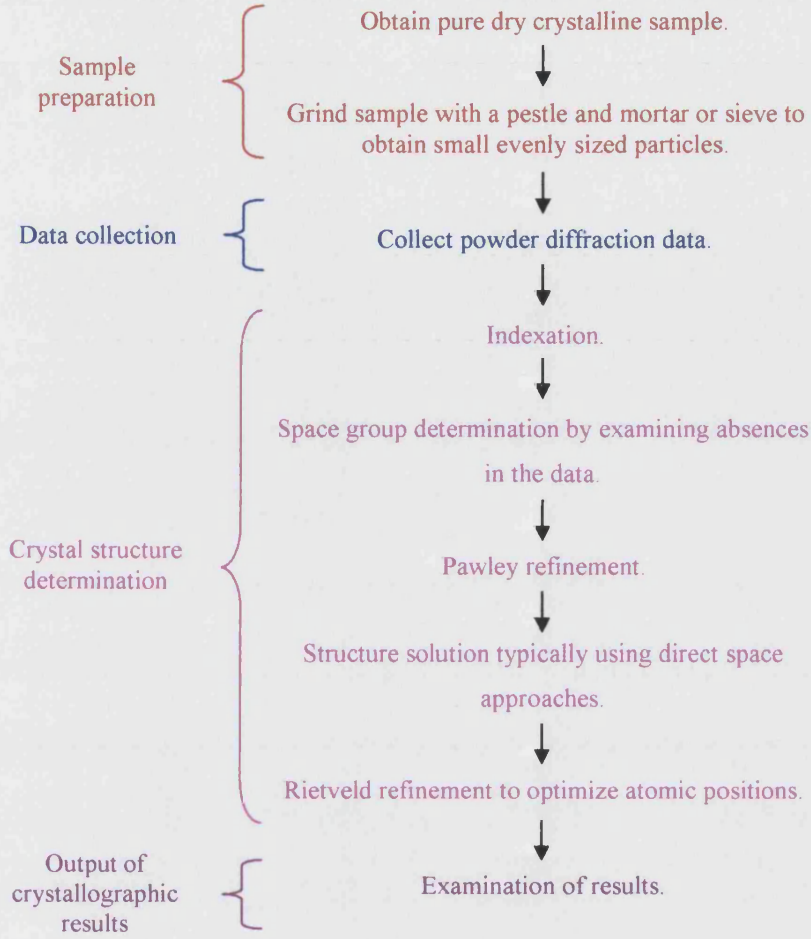

Figure 1.10 - *Schematic of the stages involved in an X--ray powder diffraction experiment to determine a crystal structure.*

Figure 1.10 illustrates the main stages in a powder diffraction experiment and the key steps involved in crystal structure determination are described below:

1.3.2.4 Indexation

The ability to achieve a structure solution is highly dependent upon obtaining the correct indexation. It is necessary to identify around 20-30 of the initial low Bragg angle peak positions for an indexation as this is where most of the structural information lies. Although there are a variety of peak-picking programs available, it is often better to manually select the peaks to ensure that shoulders are not missed or 'peaks' from the noise included, as the success of an indexation is affected by extraneous or missing peaks.

Prior to the data collection automation, powder diffraction patterns were indexed manually, however, this is only really practicable for high symmetry cells where peak

overlap is minimal and there is a simple relationship between the diffraction angle and lattice parameters, Equation 1.5.

$$\frac{4\sin^2\theta}{\lambda^2} = \frac{h^2}{a^2} + \frac{k^2}{b^2} + \frac{l^2}{c^2}$$

Equation 1.5 - *Relationship between diffraction angle and lattice parameters for an orthogonal system i.e.* $\alpha = \beta = \gamma = 90°$.

Nowadays, there are a variety of powerful computational programs capable of dealing with low symmetry cells, where the relationship between diffraction angle and lattice parameters is far more complicated. These indexation programs operate using different algorithms, for example DICVOL [1.23] and ITO [1.24] employ a reduction procedure based upon the relationships between theta and the cell parameters, while TREOR [1.25] uses a trial and error method. The programs perform well in different circumstances: DICVOL is very good at indexing a pattern provided the sample does not contain impurities, whereas ITO is capable of eliminating spurious reflections, although it is a less effective indexation program. Alternatively, TREOR is often more successful than ITO at solving one or two parameter problems [1.24]. As a result it is generally advisable to use more than one indexation program, which is easily achievable in the CRYSFIRE [1.26] suite which contains links to seven indexation programs: LZONv6.23b [1.27], KOHLv7.01b [1.28], TAUPv3.3a [1.29], DICVOL91, ITO12, TREOR90 and FJZNv6.22a [1.30].

As discussed earlier peak overlap and the presence of multiple randomly orientated crystallites means that powder diffraction patterns contain less information than single crystal diffraction patterns. Therefore, it is necessary to narrow the cell parameter limits within which the programs search for a solution:

- *Cell volume* - This is normally limited by taking the average volume of a non-hydrogen atom to be around 18 to 20 $Å^3$ and that of a hydrogen to be 2 $Å^3$, a possible volume range is then calculated using the primary assumption that there is a maximum of 4 asymmetric units each containing one molecule in the unit cell. Although, this is not valid in all cases, for example orthorhombic or higher symmetry cells, it allows an initial limit to be placed on the cell volume.

- *Cell axes and cell angles* - These are more difficult to limit, some restrictions may be possible from a study of the structures of similar compounds. However, if none are available, restrictions may be able to be placed by examining the cell volume and contents, if both are probably small it is unlikely that there are long cell axes and vice-versa.

- *Crystal system* - It is normal to specify an initial search in all crystal systems except triclinic, which takes longer to search as it is very low symmetry. The search is only extended if no reasonable solutions are found in the higher symmetry crystal systems.

The outputs from indexation programs usually consist of several possible sets of lattice parameters, these are ranked on the basis of figures of merit, which give an indication as to how well the measured peak positions coincide with the solution. It is normally a good indicator if multiple programs identify the same cell parameters with high figures of merit, however, as indexation is basically a trial and error process Pawley refinement and structure solution may have to be attempted using several different possibilities in order to find the correct lattice parameters. In this instance it is usual to begin with the highest symmetry crystal system identified [1.31].

1.3.2.5 Space Group Determination

As with single crystal X-ray diffraction experiments the space group is determined on the basis of absences, however, the complex nature of powder patterns means that this is not a trivial process. There are essentially two options: manual comparison of the predicted and observed peak positions for each space group to determine the best match or use of a program such as EXTINCTION SYMBOL [1.32] which identifies the most probable space group on the basis of the peak positions and their intensities after a Pawley fit has been carried out. It is important to understand that it is not always possible to uniquely identify the space group at this stage and it may be necessary to carry out a structure solution in several different space groups in order to identify the correct one [1.31].

1.3.2.6 Pawley Refinement [1.33]

Once the cell parameters and space group have been identified, the aim of Pawley refinement is to take into account the influence of the diffractometer and sample on the powder profile by fitting the observed pattern in the absence of a structural model. Around 8-10 peaks that appear to be single are selected from across the pattern and subjected to a Pawley refinement using a combination of the following parameters:

- Background.
- Unit cell.
- Zeropoint.
- Sigma (size).
- Sigma (strain).
- Gamma (size).
- Gamma (strain).

The first two parameters are self-explanatory, the third parameter is related to the zeropoint of the machine, and the final four all related to the machine dependence of the peak shape.

The Pawley χ^2 gives an indication of how well the observed and calculated patterns fit, and in general the value should be between 1 and 5, see Equation 1.6. If χ^2 has a value less than one, this usually indicates that the esds have been overestimated. Although obtaining a good Pawley fit is required before a structure solution is attempted, a good figure of merit does not signify that an indexation is definitely correct. However, inability to achieve a reasonable Pawley refinement may suggest a problem with the indexation, space group or instrument parameters.

$$\chi^2 = \frac{\Sigma_i[w_i(y_i - y_{ci})^2]}{(N-P+C)}$$

Equation 1.6 - *Definition of the profile χ^2, y_i is the intensity of the i^{th} observed point, y_{ci} is the intensity of the corresponding point in the calculated pattern, w_i is the weighting factor of the i^{th} point, N is the number of observations, P the number of parameters and C the number of constraints [1.34].*

1.3.2.7 Structure Solution

The methods used to try and achieve a structure solution can essentially be divided into two categories: traditional and direct space.

1.3.2.7.1 Traditional Approaches

Traditional approaches to structure solution from powder diffraction data rely upon the extraction of the intensities of the individual reflections, as they are based upon the single crystal methods *i.e.* Patterson [1.35] and direct methods [1.2][1.31]. The success of these methods has been somewhat limited [1.36][1.37][1.38] as peak overlap often makes it difficult to unambiguously identify peak intensity, particularly when dealing with organic molecules in a low symmetry crystal system [1.39]. The development of direct space

approaches has largely led to redundancy of 'traditional methods' in structure solutions from powder diffraction data, hence no further discussion is included on them.

1.3.2.7.2 Direct Space Approaches

The main advantage of direct space approaches over traditional methods is that they avoid the need to extract individual reflection intensities, thus allowing more complex structure solutions to be achieved even when there is significant Bragg peak overlap [1.40]. These strategies operate in direct as opposed to reciprocal or Patterson space, requiring the user to generate a trial structural model for which a powder diffraction pattern can be simulated and compared with the experimental pattern on the basis of a figure of merit or weighted *R*-factor (R_{wp}). Refinement is attained by adjusting the atomic positions of the trial structure, calculating the resultant powder diffraction pattern and comparing it to the observed data. An improved fit is automatically accepted, however, the two closely related direct space approaches that are usually employed in structure solution, namely, Monte Carlo [1.41] and simulated annealing [1.42], have different acceptance criteria for worse matches. It is noteworthy that direct space approaches are time consuming as all of the moves are random and the programs do not 'remember' the space that they have already sampled.

1.3.2.7.3 Monte Carlo Methods [1.41]

The Monte Carlo method for *ab initio* structure solution from powder diffraction data is based upon the Metropolis importance sampling algorithm [1.43], normally used to lower the energy of a system. However, in this case the crystallographic agreement factor R_{wp}, defined in Equation 1.7, is incorporated to give a measure of the match between the experimental and calculated patterns [1.41].

$$R_{wp} = 100 \times \sqrt{\frac{\sum w_i(y_i - y_{ci})^2}{\sum w_i y_i^2}}$$

Equation 1.7 - *Definition of R_{wp}, y_i is the intensity of the ith observed point, y_{ci} is the intensity of the corresponding point in the calculated pattern (generated using the forward Fourier transform equation) and w_i is the weighting factor of the ith point [1.21].*

The Monte Carlo method employs random numbers to generate a Markov sequence of configurations (X_i: i = 1...N, where N is a user specified number of trials) [1.44]. The initial structure in the sequence, X_1, is obtained through the random positioning of the trial structural fragment within the unit cell. Each successive step in the chain, known as a Monte Carlo move, involves the generation of subsequent structures (X_{i+1}) from the previous

configuration in a Markovian fashion rather than from scratch. The procedure is set out in Figure 1.11.

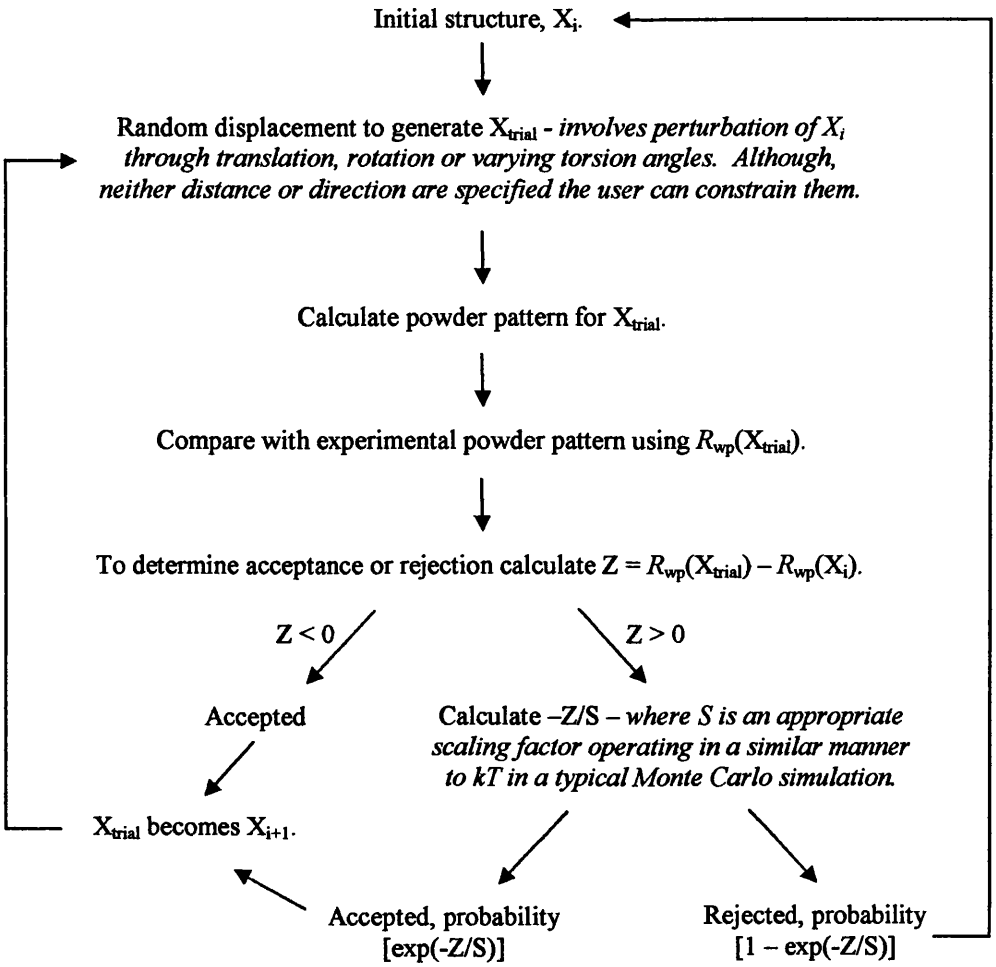

Figure 1.11 - *Flow diagram to illustrate the Markovian generation of structures in a Monte Carlo structure solution from powder diffraction data [1.31][1.41].*

The most efficient use of the Monte Carlo algorithm has been determined to involve acceptance of approximately 40% of the trial structures in the Markov chain, which can be achieved by adjusting the maximum displacement and the S value. It is important to understand that the method is not designed to minimize R_{wp}, which would tend to locate local minima as opposed to the global minimum (*i.e.* where the correct structure lies). It actually aims to explore trial space in a manner that favours areas associated with low R_{wp} values [1.31]. Termination of a run usually occurs at some user defined point such as a specific R_{wp} value or after a certain number of moves.

The main advantage of the Monte Carlo approach to structure solution is that it allows many configurations to be studied in a relatively short time. This is particularly useful for powder diffraction data as it contains significantly less independent information

than a single crystal dataset. Of course the method has limitations, the principal one being the number of degrees of structural freedom that can be varied during the calculation. Hence, non-rigid structures require a considerable amount of computational time, rendering the technique most feasible for fairly rigid structures [1.31][1.40][1.45].

1.3.2.7.4 Simulated Annealing [1.31][1.42][1.46][1.47]

Simulated annealing is essentially a more advanced form of the Monte Carlo method described above. Although, it follows essentially the same procedure as outlined in Figure 1.11, the crucial difference arises in the manner in which the S parameter is used to control acceptance or rejection for structures where $Z > 0$. In a Monte Carlo run S is fixed or manually varied so that the optimum proportion of trial structures is accepted. However, in a simulated annealing process, S is systematically decreased according to an annealing schedule or temperature reduction process, which is automatically altered if there are large fluctuations in the 'profile χ^2' value, used to give an indication of the match between the observed and calculated patterns (Equation 1.6). This means that the number of trial structures with $Z > 0$ that are accepted decreases as the run proceeds when hopefully the global minimum will have been located.

There are three main reasons why simulated annealing is preferable to the Monte Carlo approach: firstly, there is a greater chance of locating the global minimum as opposed to a local minima, due to the manner in which the S parameter is employed. Secondly, it can cope with flexible molecules and, finally, the resultant structures are more likely to be chemically plausible as each atomic position is described in terms of bond lengths, bond angles and torsion angles as opposed to fractional coordinates [1.22][1.45][1.46].

In addition, the simulated annealing procedure has been shown to have several clear advantages over other methods of structure solution [1.48]:

1. Rapid data collections are possible as the technique works even if the spatial resolution of the data is low.

2. Input models are read in terms of internal coordinates and can often be created in standard chemical drawing programs using standard bond lengths and angles.

3. The method is structure factor (F_h) driven, thereby removing the need for time consuming intra- or inter-molecular distance or energy checks.

4. Structures can be rapidly accepted or rejected, as the agreement factor is quick to calculate, particularly in the structure solution of small molecules where rates exceeding 1000 structure evaluations per second have been reported.

Structure solution within DASH [1.49] is based on a simulated annealing approach, where a good solution generally has a profile χ^2 that does not exceed five times the Pawley χ^2.

1.3.2.8 Refinement

As with single crystal structure solution refinements, the aim is to increase the accuracy of the fit between the calculated and experimental powder patterns by optimizing the atomic positions. Towards this end, there are two main methods that are employed in the refinement stage - difference Fourier synthesis [1.31] and more commonly, Rietveld refinement [1.50].

1.3.2.8.1 Difference Fourier Methods [1.31]

Like traditional approaches to structure solution this refinement method is constrained by the problem of extracting accurate intensities from a pattern, particularly where peak overlap is significant. Difference peaks are output indicating the presence of unaccounted electron density, either as a result of a missing atom or an incorrect atom assignment. Difference Fourier methods have potential for completing structures where the model is incomplete. However, for structures that do not contain a dominant scatterer, at least 50% of the electron density needs to have been correctly assigned to successfully locate the remaining atoms.

1.3.2.8.2 Rietveld Refinement [1.31]

The intensity of the corresponding points in the experimental and calculated powder patterns are compared, using a variety of crystallographic *R*-factors, typically R_{wp} and R_p, see Equations 1.8 and 1.9. The main advantage of Rietveld refinement over difference Fourier methods is that it avoids the need to extract the individual intensities thus side-stepping problems associated with peak overlap. However, the initial structural model has to be very close to the correct structure or the refinement will fail and it is therefore common to include restraints in the model.

1.4 Structural Databases

Advances in X-ray diffraction techniques have resulted in the rapid generation of substantial amounts of structural data. Much of this information is recorded in the four main crystallographic databases:

1. *The Cambridge Structural Database (CSD)* [1.51] - The CSD contains crystallographic data for organic and metal organic species.

2. *The Inorganic Crystal Structure Database (ICSD)* [1.52] -The ICSD is a database of structural data for inorganic and mineral structures.

3. *The Brookhaven Protein Databank (PDB)* [1.53] -The PDB gathers together crystallographic data relating to macromolecules and proteins.

4. *The Metals Data File (MDF)* [1.54] - The MDF contains structural data relating to metals and alloys.

The structural information in each of the databases is easily accessible through the use of software interfaces that allow the user to create searches to identify specific species or groups of species. These searches can be constructed using text, numerical or structural queries, either individually or in combination, depending upon the database. As a result, the databases have a wide range of applications from basic checks to determine whether structures have been previously reported or to confirm the geometry of a fragment, to more advanced systematic studies identifying potential interaction motifs [1.55] or gaining information on reaction mechanisms [1.56]. However it is important to register that the more complex investigations require carefully constructed searches to ensure that the results are meaningful and not distorted by data relating to inappropriate fragments.

1.5 Solid State Reactions within Crystals

As outlined in Section 1.1, one of the aims of this thesis is to look at processes that can occur in crystals, when the crystal is subjected to some external agency. In this context, it is timely to begin with a review of the literature relating to solid state reactions focusing on those occurring in single crystals.

1.5.1 Single Crystal to Single Crystal Transformations

Despite the fact that crystals are rigid in the solid state, molecules or parts of molecules contained therein often have sufficient degrees of freedom to undergo surprising

amounts of movement, thus allowing a wide range of solid state transformations to occur upon thermal or photochemical initiation [1.57][1.58][1.59]. In a small number of cases these transformations occur in a single crystal to single crystal fashion with the integrity of a single crystal being maintained during the conversion. Such reactions were first documented at the beginning of the 19th century [1.60], but a lack of understanding about packing effects within crystals or reaction pathways prevented this field becoming a large research area. In recent years, however, solid state reactions have become an active area of research, as the techniques available to study solid state materials have become more powerful, thereby allowing chemists to gain a greater understanding of crystalline materials in terms of sterics, electronics and intermolecular interactions. A selection from the wide variety of single crystal to single crystal transformations that have been reported in the literature are discussed below:

i) Polymerisation

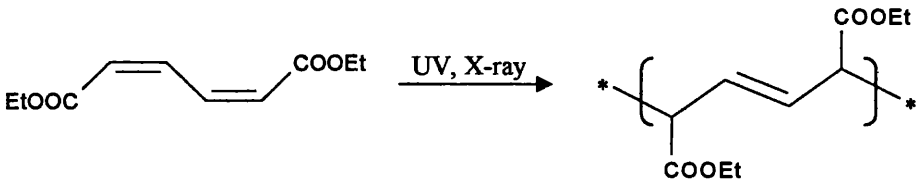

Figure 1.12 - *The polymerisation reaction of diethyl cis, cis-muconate (EMU) [1.59].*

Polymerisation reactions that proceed in a single crystal to single crystal fashion allow the formation of highly controlled polymer structures that can be difficult to obtain by other methods [1.61]. This can clearly be seen by examining the polymerisation that occurs when crystals of diethyl *cis, cis*-muconate are irradiated, see Figure 1.12 [1.59][1.62]. During the transformation the monoclinic $P2_1/c$ symmetry of the reactant lattice was maintained and the closest separation between potentially reacting carbons reduced from 3.79 Å in the monomer to 1.60 Å in the polymer. This synthesis was reported as being both topochemical and topotactic, in other words it proceeded under the structural restraints imposed by the monomer crystal lattice (topochemical), and with a 3-dimensional relationship between the orientation of the monomer and polymer crystal (topotactic), as illustrated in Figure 1.13.

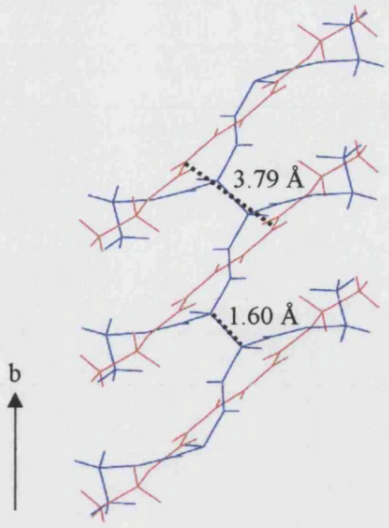

Figure 1.13 - *Overlay of the structures of the monomer diethyl cis, cis-muconate (red) and its polymer polyethyl cis, cis-muconate (blue) [1.59].*

ii) [2+2] Cycloaddition

The literature reveals a significant number of solid state photochemical [2+2] cycloaddition reactions, most of which occur in a topochemical fashion with small changes in the cell parameters [1.57][1.63][1.64][1.65]. The photo-induced conversion of *trans*-4-methylcinnamamide to 2,4-*bis*(4-methylphenyl)cyclobutane-1,3-dicarboxamide (Figure 1.14) provides a typical example of this transformation type [1.66]. Upon irradiation, the C---C distance, C_1-C_2, increases from a double bond length of 1.33 Å to a single bond length of 1.54 Å, while the separation between C_1---C_{2a} and C_2---C_{1a} decreases from 3.67 Å in the monomer to 1.60 Å in the dimer. The resultant cyclobutane ring is planar reflecting the fact that the alkene double bonds (C_1-C_2 and C_{1a}-C_{2a}) were parallel to each other in the reactant, and the monoclinic *C*2/*c* symmetry of the reactant was maintained in the dimer with small changes in the lattice parameters.

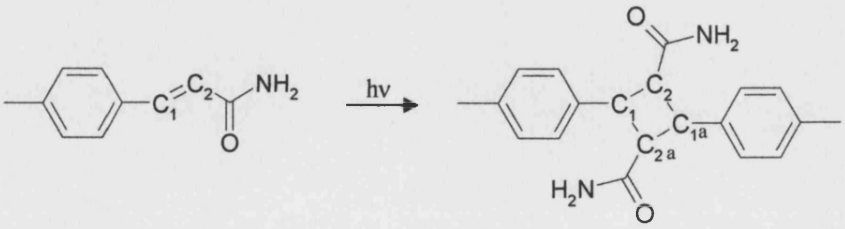

Figure 1.14 - *Photochemical [2+2] cycloaddition reaction of trans-4-methylcinnamamide (left) to form 2,4-bis(4-methylphenyl)cyclobutane-1,3-dicarboxamide (right) [1.66].*

It is also noteworthy that the photoproduct obtained from a compound in the solid state is not always the same as that obtained in solution. For example, when *trans*-cinnamic acid is irradiated in the solid state it produces the photodimer truxillic acid, whereas in solution *cis*-cinnamic acid is formed through a *trans-cis* isomerisation, see Figure 1.15 [1.60][1.63][1.67].

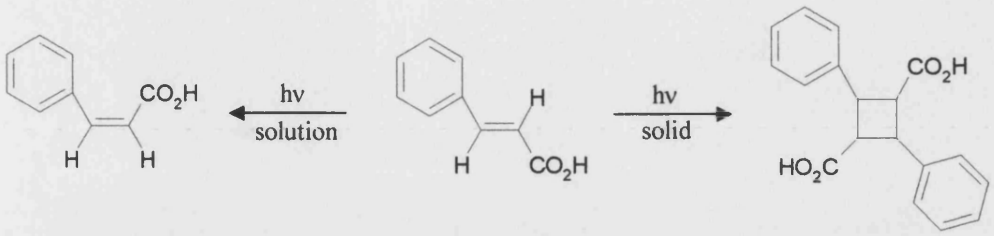

cis-cinnamic acid | *trans*-cinnamic acid | truxillic acid

Figure 1.15 - The *different reactions of trans-cinnamic acid upon irradiation in the solid or solution state [1.60][1.63].*

iii) Cyclisation

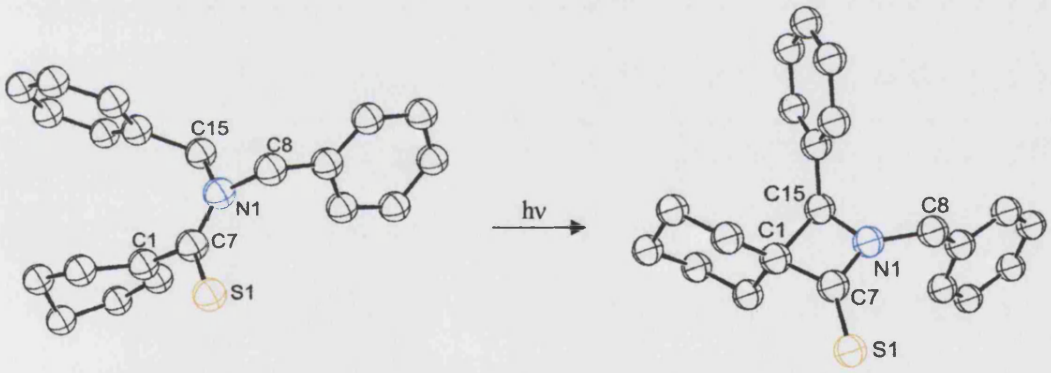

Figure 1.16 - *Cyclisation reaction of thioamide to form β-thiolactam [1.68].*

Several examples of solid state cyclisation reactions have been reported [1.58][1.69][1.70][1.71], one of which is the intramolecular cyclisation of thioamide to form *β*-thiolactam, see Figure 1.16 [1.68]. During the transformation the C_1-C_{15} distance decreases from a non-bonding 2.86 Å to a single bond length of 1.60 Å, while the lattice symmetry increases from monoclinic ($P2_1$) to tetragonal ($P4_1$). The change in symmetry reflects by an approximate doubling of one cell axis from 8.760 Å to 17.133 Å and a decrease in the β angle from 100.15° to 90°, while the other cell parameters do not alter significantly. It was noted that the reaction produced a 100% conversion without phase separation, implying that the cyclisation occured with a minimum amount of molecular movement. As a result, the authors proposed that the reaction mechanism involved hydrogen

abstraction to form a diradical followed by cyclisation, which is consistent with the stereochemical relationship between the reactant and the product, see Figure 1.17.

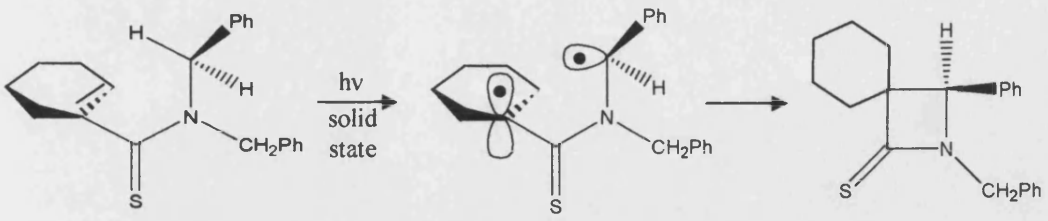

chiral crystal (+)-1 diradical (*R*)-(+)-2

Figure 1.17 - *The proposed reaction scheme for the cyclisation of thioamide with a minimum amount of molecular movement [1.68].*

iv) Asymmetric synthesis [1.57][1.72]

Asymmetric synthetic routes are highly desirable particularly in the pharmaceutical industry, due to the relative biological potency of different diastereoisomers. As discussed in Section 1.2.6, enantiomerically pure chiral compounds can only crystallise in space groups that do not possess mirror planes or inversion centres, *i.e.* 65 of the 230 space groups. Since many single crystal to single crystal transformations maintain the crystallographic symmetry of the reactant lattice, attempts have been made to achieve solid state asymmetric synthesis using reactants which crystallise in chiral space groups [1.60], and interest has grown around trying to engineer chiral crystals suitable for solid state photoreactions [1.73].

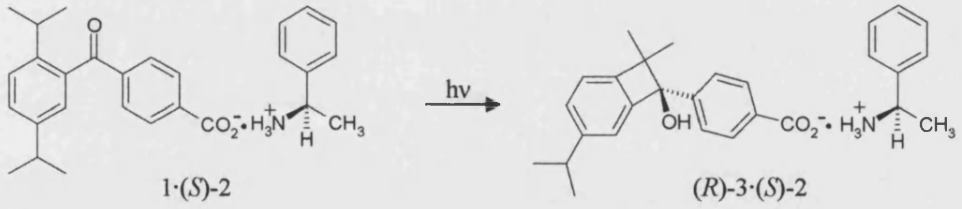

1·(*S*)-2 (*R*)-3·(*S*)-2

Figure 1.18 - *Reaction scheme for the asymmetric synthesis of the (S)-phenylethylamine salt of (R)-(+)-cyclobutenol from the corresponding salt of 2,5-diisopropyl-4'-carboxybenzophenone [1.58].*

A series of successful asymmetric synthesis reactions have been carried out as single crystal to single crystal transformations [1.57][1.72][1.74][1.75] including the enantiospecific formation of (*R*)-(+)-cyclobutenol within salt crystals of (*S*)-phenylethylamine and 2,5-diisopropyl-4'-carboxybenzophenone, see Figure 1.18 [1.58]. Koshima and co-workers reported that the reaction proceeded in the chiral orthorhombic space group $P2_12_12_1$ to reach 100% conversion in 1 hour at 15°C. Upon irradiation, the cell

volume decreased by approximately 3% from 2562.6 $Å^3$ to 2486.2 $Å^3$, and small changes in the cell parameters were observed.

v) External reagents

Considering that crystals are 3-dimensional arrays of closely packed atoms, perhaps the most unexpected type of transformation they can sustain concerns the involvement of external reagents, typically gases [1.76]. Ohashi *et al* reported the first reaction of this kind in the late 1990s, after observing that initially stable dark green crystals of distibene became colourless over the course of several hours on exposure to air while maintaining their crystallinity [1.76]. Subsequent structure determination showed the product to be 1,3,2,4-dioxadistibetane, in which oxygen has inserted across the antimony-antimony double bond of distibene, see Figure 1.19. Although, this reaction occurs rapidly in solution it was an unexpected result in the solid state. Thus, the authors proposed that molecular oxygen was able to overcome packing forces and diffuse through the lattice as a result of the space created by the presence of the bulky tertiary butyl groups.

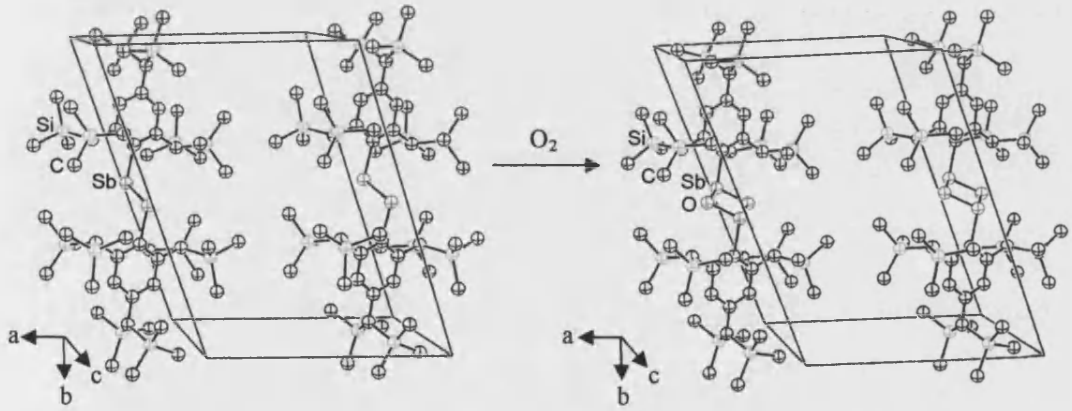

Figure 1.19 - *Comparison of the crystal structures from the single crystal to single crystal transformation of distibene (left) with external oxygen molecules to form 1,3,2,4-dioxadistibetane (right) [1.76].*

One might expect that only a limited number of small molecules would be suitable external reagents for diffusion into a crystal lattice. However, when such single crystal to single crystal transformations are possible they may well be preferable to similar reactions carried out in zeolites, as they avoid the difficulties associated with separating the products from the solid support. Despite this some purification may be required if the conversion does not reach 100% completion.

1.5.2 Solid State Reaction Criteria

Considering that molecular movement in the solid state is restricted it is unsurprising to find that it is not possible to carry out solid state reactions in all crystals. Moreover, given that many transformations involve significant amounts of movement, thereby disrupting the crystal lattice, it seems reasonable to find that many solid state reactions do not reach completion while maintaining the integrity of a single crystal. Nonetheless, efforts to gain an understanding of the factors that control such reactions is an active area of research due to the potential application of such compounds in photosensitive devices [1.77]. To this end, solid state reactions, in particular [2+2] cycloaddition reactions, have been the subject of some detailed studies.

1.5.2.1 Proposed Requirements for Solid State Reactions to Occur

In the 1960s, Schmidt and co-workers began investigating solid state reactions working on the theory that topochemical factors (*i.e.* the geometry of the reactant lattice) would govern the reaction pathway. However, it was recognised that this would not always be the case, for example, where reactions involve long distance electron migration. Their postulation, that, *'a reaction in the solid state occurs with a minimum amount of atomic or molecular movement' [1.67]*, led to several conclusions:

1. Solid state reactions would be highly dependent upon the separation and orientation of potentially reacting molecules.

2. There would be a maximum separation distance beyond which a solid state reaction could not occur.

3. Reactions involving two molecules would occur between nearest neighbours only.

4. The molecular structure of the product would be related to the initial orientation of the molecules in the reactant.

5. Certain types of reaction, such as *cis-trans* isomerisation, would not occur in the solid state as they require large amounts of atomic motion.

In order to test the hypothesis, Schmidt and co-workers combined crystallographic and spectroscopic techniques to carry out extensive investigations into solid state reactions, including the photochemically induced [2+2] cycloaddition reactions of cinnamic acids [1.78][1.79]. These studies led Schmidt to conclude that in order for a solid state [2+2]

cycloaddition reaction to occur upon photochemical irradiation, the potentially reacting double bonds needed to be parallel to each other and separated by no more than 4.2 Å.

In the subsequent years, Schmidt's premise that *'a reaction in the solid state occurs with a minimum amount of atomic or molecular movement,'* has been found to be generally applicable to a wide range of transformations [1.60][1.63]. However, the hypothesis and associated conclusions in relation to photochemical [2+2] cycloaddition reactions do not hold in all cases, and it is worth reviewing some of the exceptions, to criteria 1-3 above.

i) Maximum Separation Distance for the Alkenes in [2+2] Cycloaddition Reactions

A variety of instances have been reported where solid state dimerisation occurs, despite the separation of the reactive carbons being greater than Schmidt's proposed maximum of 4.2 Å. These include 7-chlorocoumarin and methyl *p*-iodocinnamate in which the alkene double bonds are separated by 4.45 Å and 4.30 Å, respectively [1.60]. One proposal is that such 'longer range' reactions are facilitated when the molecular packing is not constrained by strong forces but controlled by the simple packing forces (*i.e.* van der Waals forces) present in all solids, thus allowing greater movement of the molecules. This proposal seems reasonable when considering the *β*-form of *p*-formylcinnamic acid which undergoes a cycloaddition reaction despite a large alkene separation distance of 4.83 Å along the *b*-axis, see Figure 1.20 [1.60][1.80]. Although intermolecular hydrogen bonding is present, it is limited to a pairwise interaction between carboxylic acid groups on adjacent molecules and will not be disrupted by photodimerisation.

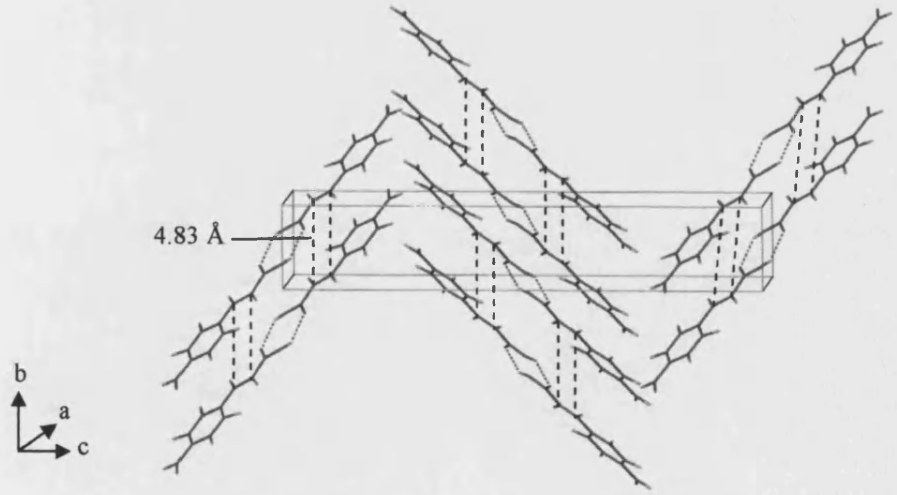

Figure 1.20 - *Illustration of the β-form of p-formylcinnamic acid which undergoes a [2+2] cycloaddition reaction despite the distances between carbons being 4.83 Å [1.60][1.80].*

It is also noteworthy that crystals containing alkenes separated by less than 4.2 Å do not necessarily dimerise upon irradiation. For example, crystals of methyl 4-hydroxy-3-nitro-*trans*-cinnamate [1.81] are photostable despite the closest carbon-carbon distances between double bonds being 3.87 Å. In this case it is believed that the extensive intermolecular hydrogen bonding accounts for reactant stability thereby preventing easy movement of the atoms within the crystal [1.60].

ii) Orientation of Alkene Double Bonds in [2+2] Cycloaddition Reactions

Given the examples discussed above in Section 1.5.2.1(i), it seems reasonable to suggest that a photodimerisation reaction may be possible in crystals of methyl *m*-bromocinnamate, where the separation between the carbon atoms are 3.53 Å and 4.33 Å [1.60][1.82]. Although, there are no strong intermolecular interactions in the solid state the compound is photostable. One proposed explanation for this stability is the twist angle of 31° between the potentially reactive double bonds. However, this theory is not supported by the hydrogen bonded co-crystals of phthalic acid and cinnamamide (1:2), where the reactive carbons are twisted by 97° with respect to each other and separated by 4.86 Å (C_{10}-C_{19}) and 3.82 Å (C_{11}-C_{20}), see Figure 1.21 [1.64]. Despite this, irradiation still produces a yield of 13% of the photodimer, breaking both Schmidt's distance and orientation criteria for the double bonds and suggesting that [2+2] cycloaddition reactions are not controlled solely by topochemical factors.

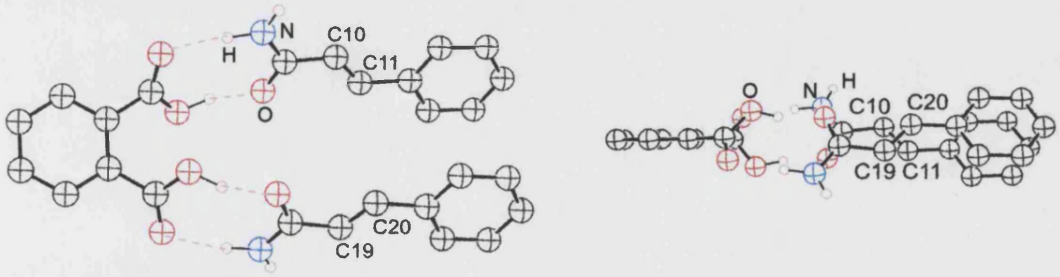

Figure 1.21 - *(left) Hydrogen bonding in co-crystals of trans-cinnamide and phthalic acid. (right) Illustration of twist between the reactive alkene double bonds [1.64].*

iii) Atomic Motion during Single Crystal to Single Crystal Transformations

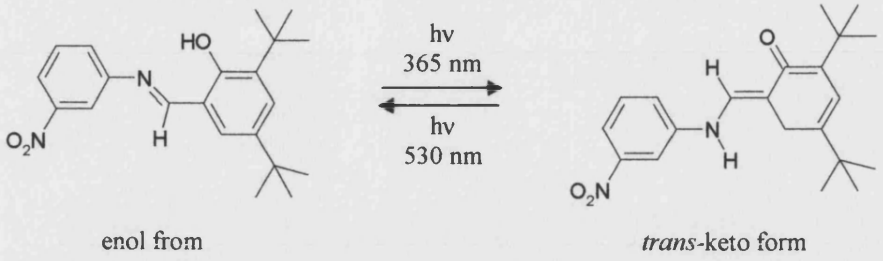

enol from *trans*-keto form

Figure 1.22 – *Illustration of the enol-keto transformation that occurs in crystals of salicylideneaniline upon irradiation [1.83].*

Schmidt's proposal that a single crystal to single crystal transformation should occur with '*a minimum amount of atomic or molecular movement*', certainly seems logical if the integrity of a single crystal is to be maintained. It is, therefore, interesting to find that a variety of seemingly impossible solid state reactions, each requiring large amounts of atomic motion, have been reported across a range of transformations. These conversions include the fully reversible enol-keto transformation that occurs in photochromic salicylideneaniline crystals upon irradiation at 365 nm. The pale yellow crystals containing the enol form undergo a colour change to dark red when irradiation has generated around 10% of the keto form, see Figure 1.22 [1.83]. Other cases worthy of note include: the photoaddition of guest acetophenone and *p*-fluoroacetophenone to host deoxycholic acid where a 180° rotation of the acetophenone acetyl group has to occur prior to bond formation [1.84], and the intramolecular cyclisation of *N*-methyl-*N*-{(*E*)-methylmethacryloyl}anilide in clathrate inclusion crystals which also requires a 180° rotation around the C_8-C_9 bond, see Figure 1.23 [1.85].

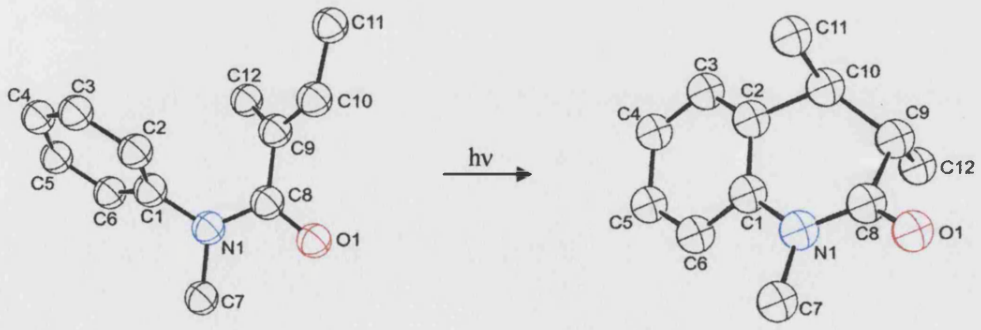

Figure 1.23 - *Photocyclisation reaction of N-methyl-N-{(E)-methylmethacryloyl}anilide in clathrate inclusion crystals produces a 26% yield upon irradiation [1.85].*

Several theories have been suggested to explain the occurrence of these improbable solid state reactions including the possibility that they occur at defect sites in the crystals [1.64]. However, in the case of the enol-keto transformation of salicylideneaniline (Figure 1.22), the authors proposed that the required movement is relatively easy if the pair of benzene rings move in a manner analogous to the pedals on a bike [1.83]. Alternatively, it is possible that any of the discussed conversions occurred because there is significant 'free' space around the reactant molecules and since the irradiations were carried out at room temperature the atoms had enough energy to overcome the packing forces [1.85]. Given the amount of atomic motion that occurs in each of these transformations it is unsurprising that the conversion rates remain low when the single crystal integrity is lost. The initial preservation of the crystal integrity during transformations is likely to be due to the unreactive component maintaining the crystal lattice. Examination of space filling diagrams from the reactant crystal structures of salicylideneaniline and *N*-methyl-*N*-{(*E*)-methylmethacryloyl}anilide in clathrate inclusion crystals indicates a reasonable amount of void space in the lattices possibly favouring the argument for free space, see Figure 1.24.

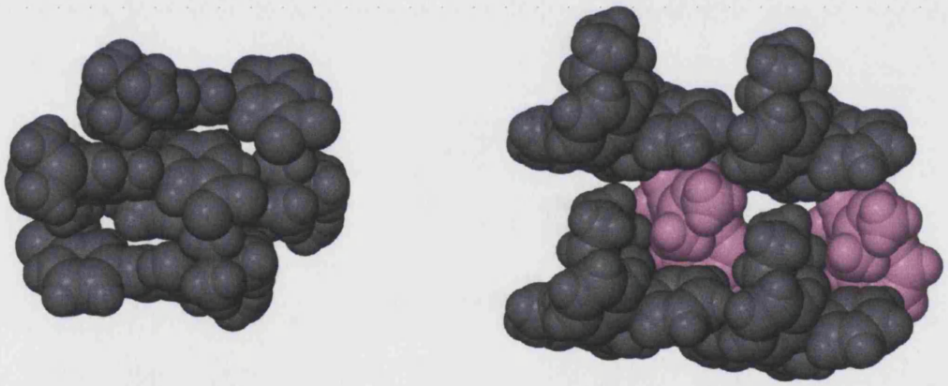

Figure 1.24 – *Space filling diagrams for (left) salicylideneaniline at 90 K (right) N-methyl-N-{(E)-methylmethacryloyl}anilide (pink) in inclusion crystals at room temperature.*

1.5.2.2 Heterogeneous versus Homogeneous Single Crystal to Single Crystal Transformations [1.63][1.86][1.87]

When a compound undergoes a solid state reaction, the main obstacle to a photochemical single crystal to single crystal transformation reaching completion is degradation of the crystal throughout the experiment. During the irradiation process the product lattice forms within the reactant lattice, generally in a topochemical fashion thereby maintaining the crystallographic symmetry of the reactant lattice. However, the formation of the product distorts the initial lattice. To overcome this problem, the aim is to achieve a

homogeneous transformation rather than a heterogeneous transformation, the reasons for which are discussed below:

1. *Heterogeneous transformations* – During irradiation the molecules closest to the surface react initially, while molecules embedded further in the crystal do not. The reaction progresses at the interface between the two crystal lattices, and ultimately the concentration of product molecules becomes too high for the reactant lattice to support and the crystal disintegrates. This type of transformation is common when the radiation used is close to the absorption maximum of the compound, as the intensity of such radiation drops off rapidly throughout the crystal.

2. *Homogeneous transformations* – During the transformation, molecules dispersed throughout the crystal react enabling the reactant lattice to support the newly forming product lattice. It is possible to achieve this type of conversion by using 2 photon excitation, where a molecule undergoes a concerted absorption of two photons [1.83], but it is more common to irradiate the sample in its long wavelength absorption tail.

Enkelmann, Novak and co-workers demonstrated the effect of the radiation wavelength in the [2+2] cycloaddition reaction of *trans*-cinnamic acid [1.63]. They found that broad band irradiation destroyed the crystal, whereas irradiation into the long wavelength absorption tail resulted in a 100% conversion to the photodimer, truxillic acid, see Figure 1.25. Despite this success, it is very commonly difficult to achieve 100% conversions since crystals often degrade throughout the reaction, even when irradiated in their long wavelength absorption tail [1.87].

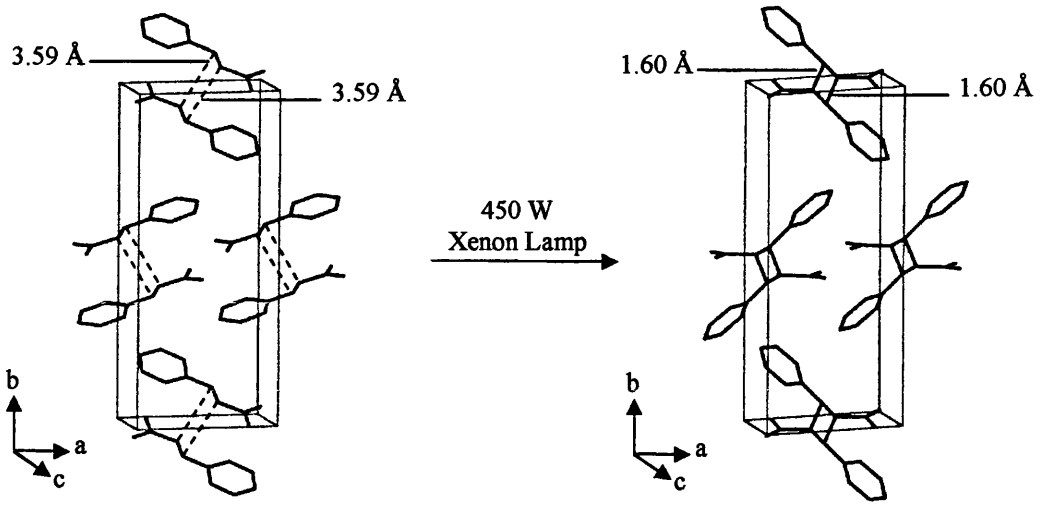

Figure 1.25 - *Photodimerisation of trans-cinnamic acid to form truxillic acid (100%) through tail absorption irradiation [1.63].*

1.5.2.3 The Study of Solid State [2+2] Cycloaddition Reactions using X-Ray Diffraction

While a variety of techniques can be employed to study solid state reactions including UV, IR, NMR and X-ray diffraction, the focus of the discussion here is on the use of the latter. Although single crystal experiments can provide more instructive structural information, they rely on the integrity of a crystal being maintained for a significant period of time. On the other hand, powder diffraction only requires the compound to remain crystalline during the transformation, but the compression of data makes it more difficult to extract structural information (Section 1.3). As a result, powder diffraction is normally only used to monitor the course of a solid state reaction by following the appearance of peaks unique to the product and the disappearance of those relating to the reactant in either a qualitative or quantitative manner [1.57].

One of the reasons for studying solid state reactions is that they provide a potential route towards obtaining information about the reaction pathway of a certain conversion type. To this end, single crystal to single crystal transformations are particularly useful. Despite the fact that the likelihood of gaining crystal structures all the way along a reaction pathway is low, it may be possible to make deductions about the reaction pathway when reactant and product structures are obtained from the same crystal, as in the case of the intramolecular cyclisation of thioamide to form β-thiolactam [1.68]. It may also be possible to acquire the structures of reasonably long lived metastable intermediates or monitor a change in lattice parameters, as obtained during the slow photoaddition reaction of guest acetophenone and *p*-fluoroacetophenone to host deoxycholic acid [1.88], all of which can indicate the molecular reaction pathway.

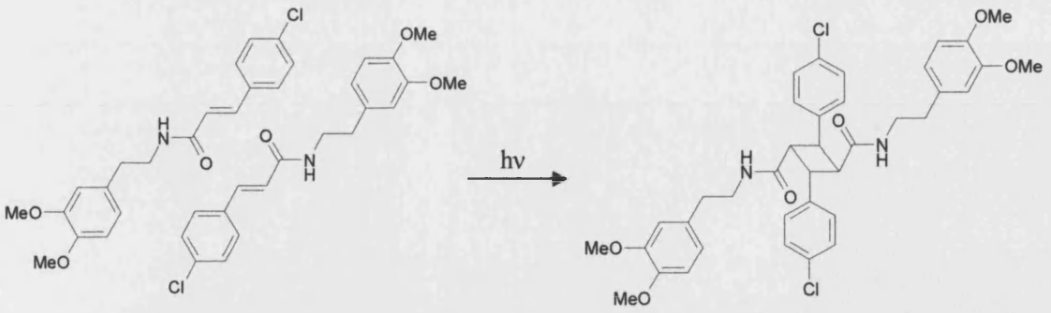

Figure 1.26 - *The photodimerisation reaction of 4-chlorocinnamoyl-O,O'-dimethyldopamine [1.87].*

Figure 1.26 schematically illustrates the photodimerisation of 4-chlorocinnamoyl-*O,O'*-dimethyldopamine where the parallel double bonds are initially separated by 4 Å [1.87]. While this reaction reaches completion without degradation of the crystal many single crystal to single crystal transformations do not and it is therefore important to determine the product yield. One of the lowest photodimer populations to be reported is 4.5% for the [2+2] cycloaddition reaction of *trans*-cinnamamide, which decomposed even when it was irradiated in its long wavelength absorption tail. The atomic positions corresponding to the dimer were located using difference synthesis after the monomer had been refined anisotropically [1.66].

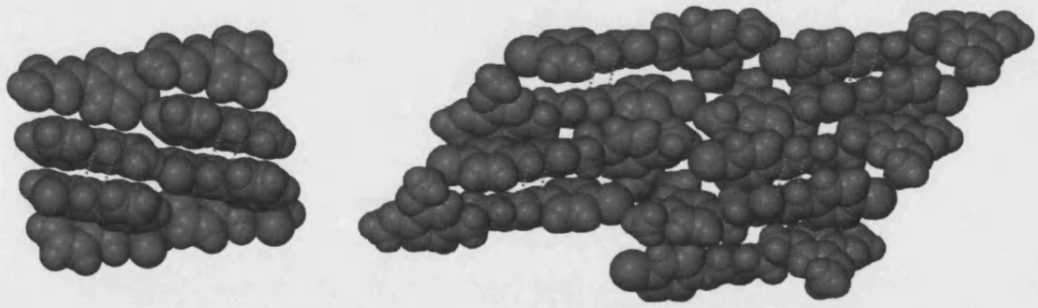

Figure 1.27 – *Space filling diagrams (left) trans-cinnamamide [1.66] (right) 4-chlorocinnamoyl-O,O'-dimethyldopamine [1.87]. The dashed red lines indicate one example of a potential dimerisation site both double bonds are parallel and separated by just over 4 Å.*

Both sets of double bonds are parallel and separated by just over 4 Å in *trans*-cinnamamide and 4-chlorocinnamoyl-*O,O'*-dimethyldopamine, and the different conversions could perhaps be explained if there was less free space in the lattice of the former preventing easy movement of the molecules. However, both lattices appear to have similar amounts of free space, as illustrated in Figure 1.27. As a result, the most likely explanation for the degradation of *trans*-cinnamamide crystals is the presence of

intermolecular hydrogen bonding that is disrupted upon dimerisation, resulting in an energy loss such that the crystal lattice can no longer be maintained. Although, 4-chlorocinnamoyl-*O,O'*-dimethyldopamine also contains intermolecular hydrogen bonding this is maintained in the product, where two adjacent hydrogen bonded chains become joined as a result of the dimerisation, see Figure 1.28.

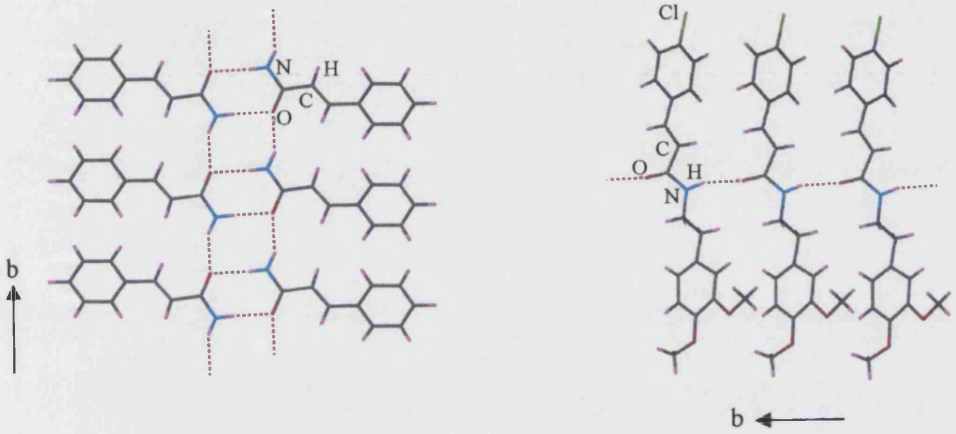

Figure 1.28 - *Illustration of hydrogen bonding (left) trans-cinnamamide [1.66](right) 4-chlorocinnamoyl-O,O'-dimethyldopamine (right) [1.87] along b-axis.*

1.5.3 Summary

A wide variety of interesting single crystal to single crystal transformations have been discussed. The fact that they occur in the solid state minimises the possible movement of the atoms, meaning that the structure of the product can often be predicted on the basis of the initial orientation of the molecules. In addition, the chemist normally has greater control over the reaction product than might be achieved in solution, rendering solid state transformations particularly useful as routes for asymmetric synthesis. However, the behaviour of a compound in the solid state is not necessarily the same as in solution, with the irradiation of compounds such as *trans*-cinnamic acid resulting in isomerisation in solution and dimerisation in the solid state [1.60][1.63][1.67].

Schmidt's pioneering studies in the 1960s, working on the hypothesis that *'a reaction in the solid state occurs with a minimum amount of atomic or molecular movement'* [1.67], assumed that topochemical factors governed solid state reactions. The conclusions drawn from his studies on the necessary requirements for the potential occurrence of solid state photochemical [2+2] cycloaddition reactions, provide a good guideline during compound selection, *i.e.* they should have potentially reactive double bonds aligned parallel to each other and separated by less than 4.2 Å. However, there are a number of examples in which these conditions are broken, and it appears that other factors such as intermolecular

forces need to be taken into account along with topochemical factors when identifying compounds likely to react [1.60][1.67][1.78][1.79].

Alterations in the manner of irradiation, to being in the long wavelength absorption tail or using 2 photon excitation, can certainly promote a homogeneous as opposed to heterogeneous transformation, but these changes cannot guarantee that high conversions will be achieved before the loss of single crystal integrity. Nonetheless, despite problems with crystal quality, combining single crystal and powder X-ray diffraction techniques can provide valuable information on reactions in the solid state.

1.6 References

[1.1] Woolfson M.M. (1997) *An Introduction to X-Ray Crystallography,* 2nd Edition. Cambridge University Press.

[1.2] Trueblood K.N., Pickworth Glusker J. (1985) *Crystal Structure Analysis A Primer,* 2nd Edition. Oxford University Press.

[1.3] Clegg, W. (1998) *Crystal Structure Determination,* Oxford University Press.

[1.4] Mahon, M.F. (1998/1999) *CHEY0005 lecture notes,* University of Bath; Mahon, M.F. (1999/2000) *CHEY0013 lecture notes,* University of Bath; Mahon, M.F. (2001/2002) *CHEY0069 lecture notes,* University of Bath.

[1.5] Giacovazzo, C., Monaco, H.L., Artioli, G., Viterbo, D., Ferraris, G., Gilli, G., Zanotti, G., Catti, M. (2002) *Fundamentals of Crystallography,* 2nd Edition, Oxford University Press.

[1.6] Daintith, J. (2000) *Oxford Dictionary of Chemistry,* 4th Edition, Oxford University Press.

[1.7] Stout, G.H., Jensen, L.H. (1989) *X-ray Structure Determination: A Practical Guide,* 2nd Edition, Wiley Interscience.

[1.8] BCA-CCG Intensive Course in X-ray Structural Analysis Notes.

[1.9] Edited by Hahn, T. (2005) *International Tables for X-ray Crystallography, Volume A,* International Union of Crystallography.

[1.10] Andreev, Y.G., Bruce, P.G. (1998) *J. Chem. Soc., Dalton Trans.,* 4071-4080.

[1.11] Otwinowski, Z., Minor, W. (1997) *Macromolecular Crystallography, part A,* C.W. Carter, Jr. & R. M. Sweet, Eds., Academic Press.

[1.12] Duisenberg, A.J.M.(1992) *J. Appl. Cryst.,* **25,** 92-96.

[1.13] Farrugia, L.J. (1999) *J. Appl. Cryst.* **32,** 837-838.

[1.14] SHELXTL Version 6.14 (2000) Bruker AXS.

[1.15] Beurskens, P. T., Beurskens, G., Bosman, W. P., de Gelder, R., Garcia-Granda, S., Gould, R. O., Israel, R., Smits, J. M. M. (1996) Crystallography Laboratory, University of Nijmegen, The Netherlands.

[1.16] Sheldrick, G.M. (1998) Institüt für Anorganische Chemie der Universität, Tammanstrasse 4, D-3400 Göttingen, Germany.

[1.17] Altomare A., Burla M.C., Camalli M., Cascarano G.L., Giacovazzo C., Guagliardi A., Moliterni A.G.G., Polidori G.,Spagna R. (1999) *J. Appl. Cryst.* **32,** 115-119.

[1.18] Sheldrick, G.M. (1993) Institüt für Anorganische Chemie der Universität, Tammanstrasse 4, D-3400 Göttingen, Germany.

[1.19] WINGX Manual; Farrugia, L.J. (1999) *J. Appl. Cryst.* **32,** 837-838.

[1.20] Trueblood K.N., Pickworth Glusker J. (1985) *Crystal Structure Analysis A Primer,* 2nd Edition. Oxford University Press.

[1.21] Kariuki, B.M., Zin, D.M.S., Tremayne, M., Harris, K.D.M. (1996) *Chem. Mater.,* **8,** 565-569.

[1.22] Andreev, Y.G., MacGlashan, G.S., Bruce, P.G. (1997) *Phys. Rev. B,* **55(18),** 12011-12017.

[1.23] Boultif, A., Louër, D. (1991) *J. Appl. Cryst.,* **24,** 987-993.

[1.24] Visser, J.W. (1969) *J. Appl. Cryst.,* **2,** 89-95.

[1.25] Werner, P.E., Eriksson, L., Westdahl, M. (1985) *J. Appl. Cryst.,* **18,** 367-370.

[1.26] Shirley, R. (2000) *Acta Cryst.,* **A56,** s350.

[1.27] Shirley, R., Louër, D. (1978) *Acta Cryst.,* **A34,** s382.

[1.28] Kohlbeck, F., Hörl, E.M. (1978) *J. Appl. Cryst.,* **11,** 60-61.

[1.29] Taupin, D. (1973) *J. Appl. Cryst.,* **6,** 380-385.

[1.30] FJZNv6.22a, Shirley, R. (1999).

[1.31] Harris, K.D.M., Tremayne, M. (1996) *Chem. Mater.,* **8,** 2554-2570.

[1.32] Markvardsen, A.J., David, W.I.F., Johnson, J.C., Shankland, K. (2001) *Acta Cryst.,* **A57,** 47-54.

[1.33] Pawley, G. S. (1981) *J. Appl. Cryst.,* **14,** 357-361.

[1.34] DASH instruction manual. (2004) Cambridge Crystallographic Data Centre, 12 Union Road, Cambridge. CB2 1EZ. UK.

[1.35] Patterson, A.L. (1934) *Phys. Rev.,* **46,** 372-376.

[1.36] Alberti, G., Vivani, R., Murcia Mascarós, S. (1998) *J. Molecular Structure,* **470,** 81-92.

[1.37] Bataille, T., Auffrédic, J-P., Louër, D. (1999) *Chem. Mater.,* **11,** 1559-1567.

[1.38] Boudaren, A., Auffrédic, J-P., Louër, M., Louër, D. (2000) *Chem. Mater.,* **12,** 2324-2333.

[1.39] Langford, J.I., Louër, D. (1996) *Rep. Prog. Phys.,* **59,** 131-234.

[1.40] Tremayne, M., Kariuki, B.M., Harris, K.D.M. (1997) *Angew. Chem. Int. Ed. Engl.,* **36,** 770-772.

[1.41] Harris, K.D.M., Tremayne, M, Lightfoot, P., Bruce, P.G. (1994) *J. Am. Chem. Soc.* **116**, 3543-3547.

[1.42] Kirkpatrick, S., Gelatt, C.D., Vecchi, M.P. (1983) *Science,* **220,** 671-680.

[1.43] Metropolis, N., Rosenbluth, A.W., Rosenbluth, M.N., Teller, A.H., Teller, E. (1953) *J. Chem. Phys.,* **21(6),** 1087-1092.

[1.44] Parker, S. (2001/2002) *CHEY0039 lecture notes,* University of Bath.

[1.45] Andreev, Y.G., Lightfoot, P., Bruce, P.G. (1996) *Chem. Commun.,* 2169-2170.

[1.46] Harris, K.D.M., Tremayne, M, Kariuki, B.M. (2001) *Angew. Chem. Int. Ed.*, **40,** 1626-1651.

[1.47] Press, W.H., Flannery, B.P., Teukolsky, S.A., Vetterling, W.T. (1986) *Numerical Recipes* Cambridge University Press, Cambridge (ISBN 0521308119).

[1.48] David, W.I.F., Shankland, K., Shankland, N. (1998) *Chem. Commun.,* 931-932.

[1.49] DASH David, W.I.F., Shankland, K., available from Cambridge Crystallographic Data Centre, 12 Union Road, Cambridge. CB2 1EZ. UK.

[1.50] Rietveld, H.M. (1969) *J. Appl. Cryst.,* **2,** 65-71.

[1.51] Allen, F.H. (2002) *Acta Cryst.,* **B58,** 380-388.

[1.52] ICSD, Gmelin, Germany.

[1.53] PDB, Brookhaven National Laboratory, Upton, New York, USA.

[1.54] MDF, National Research Council of Canada, Montreal Road, Ottawa, Ontario, Canada.

[1.55] Allen, F.H., Baalham, C.A., Lommerse, J.P.M, Raithby, P.R. (1998) *Acta Cryst.,* **B54,** 320-329.

[1.56] Auf de Heyde, T.P.E., Bürgi, H. (1989) *Inorg. Chem.,* **28,** 3960-3969.

[1.57] Suzuki, T., Fukushima, T., Yamashita, Y., Miyashi, T. (1994) *J. Am. Chem. Soc.,* **116,** 2793-2803.

[1.58] Koshima, H., Matsushige, D., Miyauchi, M. (2001) *Cryst. Eng. Comm.,* **33,** 1-3.

[1.59] Tashiro, K., Zadorin, A.N., Saragai, S., Kamae, T., Matsumoto, A., Yokoi, K., Aoki, S. (1999) *Macromolecules,* **32,** 7946-7950.

[1.60] Ramamurthy, V., Venkatesan, K. (1987) *Chem. Rev.,* **87,** 433-481.

[1.61] Irngartinger, H., Skipinski, M. (2000) *Tetrahedron,* **56,** 6781-6794.

[1.62] Matsumoto, A., Yokoi, K., Aoki, S., Tashiro, K., Kamae, T., Kobayashi, M. (1998) *Macromolecules,* **31,** 2129-2136.

[1.63] Enkelmann, V., Wegner, G., Novak, K., Wagener, G. (1993) *J. Am. Chem. Soc.,* **115,** 10390-10391.

[1.64] Ohba, S., Hosomi, H., Ito, Y. (2001) *J. Am. Chem. Soc.,* **123,** 6349-6352.

[1.65] Varshney, D.B., Papaefstathiou, G.S., MacGillivray, L.R. (2002) *Chem. Commun.,* 1964-1965.

[1.66] Hosomi, H., Ito, Y., Ohba, S. (2000) *Acta Cryst.*, **B56,** 682-689.

[1.67] Cohen, M.D., Schmidt, G.M.J. (1964) *J. Chem. Soc.*, 1996-2000.

[1.68] Sakamoto, M. Takahashi, M., Kamiya, K., Yamaguchi, K., Fujita, T., Watanabe, S. (1996) *J. Am. Chem. Soc.*, **118,** 10664-10665.

[1.69] Hosomi, H., Ito, Y., Ohba, S. (1998) *Acta Cryst.*, **B54,** 907-911.

[1.70] Dzakpasu, A.A., Phillips, S.E.V, Scheffer, J.R., Trotter, J. (1976) *J. Am. Chem. Soc.*, **98,** 6049-6051.

[1.71] Cheung, E., Rademacher, K., Scheffer, J.R., Trotter, J. (2000) *Tetrahedron,* **56,** 6739-6751.

[1.72] Leibovitach, M., Olovsson, G., Scheffer, J.R., Trotter, J. (1998) *J. Am. Chem. Soc.*, **120,** 12755-12769.

[1.73] Addadi, L., van Mil, J., Lahav. M. (1982) *J. Am. Chem. Soc.*, **104,** 3422-3429.

[1.74] Elgavi, A., Green, B.S., Schmidt, G.M.J. (1973) *J. Am. Chem. Soc.*, **100,** 2058-2059.

[1.75] Sarkar, N., Nayek, A., Ghosh, S. (2004) *Org. Lett.*, **6,** 1903-1905.

[1.76] Tokitoh, N., Arai, Y., Sasamori, T., Okazaki, R., Nagase, S., Uekusa, H., Ohashi, Y. (1998) *J. Am. Chem. Soc.*, **120,** 433-434.

[1.77] Ramos, A.S.F, Techert, S. (2003) *Phys. Chem. Chem. Phys.*, **5,** 5176-5181.

[1.78] Cohen, M.D., Schmidt, G.M.J. (1964) *J. Chem. Soc.*, 2000-2013.

[1.79] Cohen, M.D., Schmidt, G.M.J. (1964) *J. Chem. Soc.*, 2014-2021.

[1.80] Nakanishi, H., Hasegawa, M., Mori, T. (1985) *Acta Cryst.*, **C41,** 70-71.

[1.81] Hanson, A.W. (1975) *Acta Cryst.*, **B31,** 1963-1965.

[1.82] Leiserowitz, L., Schmidt, G.M.J. (1965) *Acta Cryst.*, **18,** 1058-1067.

[1.83] Harada, J., Uekusa, H., Ohashi, Y. (1999) *J. Am. Chem. Soc.*, **121,** 5809-5810.

[1.84] Chang, H.C., Popovitz-Biro, R., Lahav, M., Leiserowitz, L. (1982) *J. Am. Chem. Soc.*, **104,** 614-616.

[1.85] Hosomi, H., Ohba, S., Tanaka, K., Toda, F. (2000) *J. Am. Chem. Soc.*, **122,** 1818-1819.

[1.86] Kim, J.H., Jaung, J.Y., Jeong, S.H. (2002) *Optical Materials,* **21,** 395-400.

[1.87] Ohba, S., Ito, Y. (2003) *Acta Cryst.*, **B59,** 149-155.

[1.88] Chang, H.C., Popovitz-Biro, R., Lahav, M., Leiserowitz, L. (1987) *J. Am. Chem. Soc.*, **109,** 3883-3893.

Chapter 2

Solid State [2+2] Cycloaddition Reactions – A Database Study

2.1 Introduction

As stated previously (Section 1.5.2.1), a pioneering study in the 1960s by Schmidt and co-workers [2.1][2.2][2.3] postulated that *'a reaction in the solid state occurs with a minimum amount of atomic or molecular movement'*. It was further concluded that a solid state [2+2] cycloaddition reaction is only likely to occur if the distance between the reacting carbons is less than 4.2 Å and the double bonds are arranged in a parallel fashion.

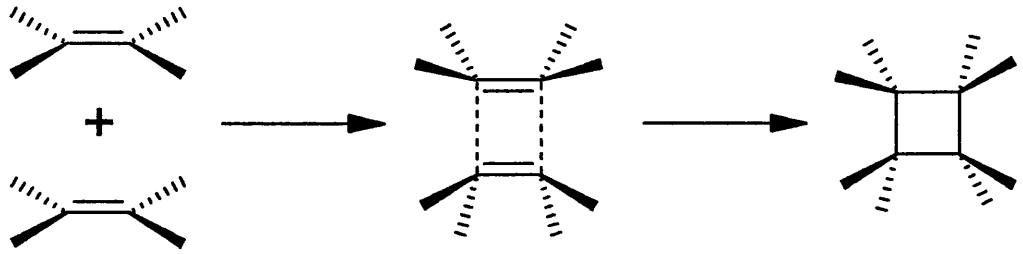

Figure 2.1 – *Illustration of the manner in which a solid state [2+2] cycloaddition reaction may occur.*

The chapter details a Cambridge Structural Database (CSD) study aimed at gaining a mechanistic understanding of solid state [2+2] cycloaddition reactions (Figure 2.1), wherein the reactant and product fragments are two alkene double bonds and a cyclobutane ring respectively.

2.1.1 Structure-Structure Correlation Hypothesis [2.4]

One method of utilizing the information contained within the CSD to obtain information on a reaction pathway of a solid state [2+2] cycloaddition is to employ the Bürgi-Dunitz structure-structure correlation hypothesis which states that:

'Although direct observation of a molecule along the reaction pathway does not seem feasible, its visualization at least does. According to the structure correlation hypothesis, the gradual distortion or static deformation that a molecular fragment of interest manifest collectively over a large variety of crystalline frameworks may be assumed to mirror the distortion which that fragment would undergo along a given reaction coordinate. The various crystals or molecular structures are considered to constitute a series of 'frozen-

in' points, or snapshots, taken along the reaction pathway, which, when viewed in the correct order, yield a cinematic film of the reaction.' [2.4]

The methodology suggests that the database can be used to construct structural datasets with common chemical substructures corresponding to either the reactant or product fragment for the reaction of interest. The data relating to the geometrical parameters of the substructures provide information on the chemical environment and energetics of the species, which can be analysed and plotted in order to identify significant distortions which may correspond to a reaction coordinate. Clearly this is only feasible if there are a significant number of data points, thus allowing extraction of meaningful conclusions from the deformations within the datasets.

The basis of the structure-structure correlation hypothesis can perhaps be more clearly visualised by considering the schematic representation of a reaction coordinate depicted in Figure 2.2(a), which represents all of the changes in geometrical parameters that occur throughout the course of a reaction. It is accepted that the majority of the substructures identified from the CSD would occupy a position in their respective energy minima i.e. either reactant or product. However, a small percentage may lie at higher energies further along the reaction coordinate, and it is these structures that can potentially be used to indicate a reaction pathway between the two minima, Figure 2.2(b).

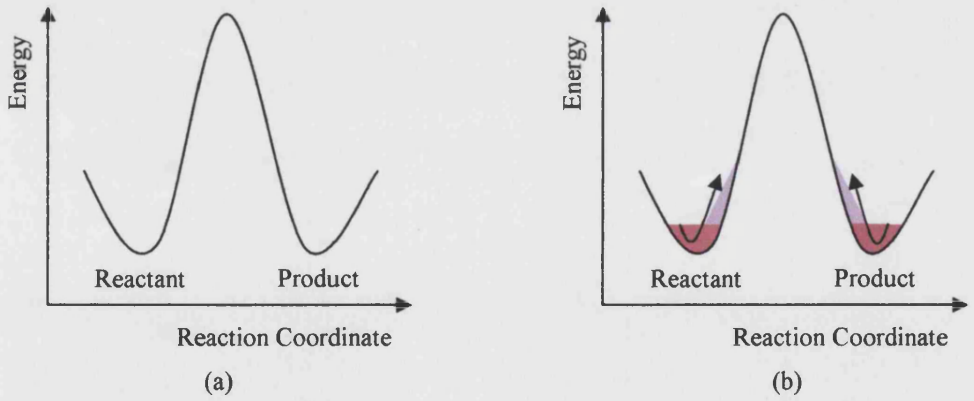

Figure 2.2 - *(a) Schematic representation of a reaction coordinate taken to represent all changes in interatomic geometrical parameters (i.e. distances and angles) during the reaction. (b) Illustration of where structures in the CSD may appear on the reaction coordinate in pink, those indicated in light pink are the ones at higher energy that may indicate the reaction pathway.*

A number of studies [2.5][2.6][2.7] have been carried out based on this hypothesis, one such example is the investigation into the S_N2 ligand exchange reactions in tetrahedrally coordinated metal species where:

$$X\text{–}M\text{---}Y \rightarrow X\text{---}M\text{–}Y$$

The results of the research indicated a lengthening of the X-M bond to a Van der Waals distance and a corresponding reduction in the M-Y distance to a bonding distance. In addition it was noted that the angle between X and one of the other ligands attached to the metal decreases from a value above 90° to one below 90° as the X-M bond breaks and the new M-Y bond forms [2.8].

A solid state [2+2] cycloaddition reaction involves four main atoms that eventually form a cyclobutane ring in the product species, clearly individual atoms cannot be viewed in isolation as the reaction could not occur without the presence of the other three. Each atom whether contained in a reactant or product fragment has several geometrical parameters associated with it namely, angles, torsions and bonding or interaction distances. Thus, once more, it would be inappropriate to consider each set of atomic parameters in isolation. Consequently, it is necessary to employ a method of data analysis capable of combining information that relates parameters of the same type for all four atoms. In this study principal component analysis was used to determine the significant distortions within the dataset, which were subsequently visualized using plots of symmetry deformation coordinates (SDCs).

2.1.2 Principal Component Analysis [2.9][2.10]

Principal component analysis is a multivariate statistical analysis technique which aims to reduce the dimensionality of a dataset and identify meaningful underlying trends. The results are expressed as principal components that describe the deformations within the dataset, each has an associated Eigenvalue that provides an indication of the distortions significance with respect to the other coordinates, *i.e.* the deformation with the largest Eigenvalue is the most important. The sum of the Eigenvalues for a particular set of symmetry deformation coordinates is equal to the number of coordinates in the set, and the values may be more clearly understood in terms of the percentage of the total variance for which the associated component accounts. The application of the method relies on two main factors:

1. Generally, the data being studied need to relate to parameters of the same type e.g. angles, torsion angles or bonds. Combinations of different sorts of variable can only be accommodated if the data have been appropriately scaled so that the significance of any variations are comparable, as otherwise the variance would be dominated by the parameter with the largest range.

2. The dataset must be symmetry-expanded in accordance with the highest topological symmetry of the search fragment, to account for all of the possible permutational isomers, as this determines which of the original parameters can be linearly correlated.

The principal components themselves describe deformations within the dataset in terms of irreducible representations that are closely related to symmetry deformation coordinates. If more than one irreducible representation has the same symmetry then the principal components associated with them will be a mixture of the representations, whereas, if only one symmetry coordinate is associated with a distortion it will be directly correlated to the respective principal component.

2.1.3 Symmetry Deformation Coordinates (SDCs) [2.11][2.12]

Symmetry deformation coordinates provide a means of describing how each deformation occurs with respect to the geometry of the reference fragment. It is important to note that SDCs cannot always be viewed as being unique, and may only be possible in combination with another deformation. SDCs for the reference geometry can be readily calculated using group theory.

2.2 Database Search Methodology

Two initial sets of searches were carried out in the CSD: the first forming the 'reactant' dataset consisted of crystal structures where the two alkene groups were separated by no more than the sum of the Van der Waals radii of carbon plus 20%, while the second constituting the 'product' dataset identified compounds containing a cyclobutane ring. Along with an overall dataset for each category, containing all of the structures that matched the search criteria separate organic and metal-organic datasets were created, to determine whether the presence of a metal affected the reaction pathway. The search fragments for each of the searches are illustrated in Figure 2.3.

Figure 2.3 - *Search fragments (i) alkene (ii) cyclobutane.*

Employment of principal component analysis to identify trends in the datasets rendered it necessary to identify the highest symmetry possible for each of the search

fragments before the symmetry deformation coordinates could be derived in terms of the parameters defined in the reactant and product searches. In the case of the reactant where the intra- and inter-molecular C---C distances are different this is D_{2h}, while for the product in which the carbon-carbon distances around the cyclobutane ring are the same it is D_{4h}.

The search methodologies are described below and were carefully constructed to ensure that the results were not biased by structures unlikely to undergo a solid state [2+2] cycloaddition reaction.

2.2.1 General Search Criteria

In both the reactant and product searches criteria were applied to eliminate structures having:

- A crystallographic *R*-factor > 10%.
- Residual errors after CSD validation checks.
- Crystallographic disorder.
- Polymeric bonds.

2.2.2 D_{2h} Reference Geometry Search Criteria

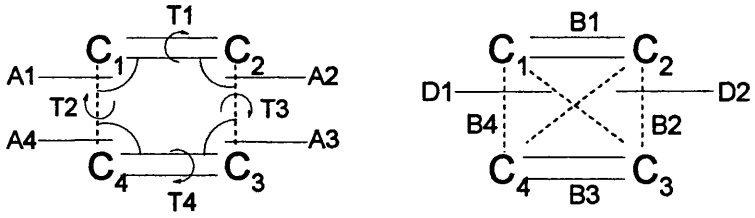

Figure 2.4 – *Definition of search parameters for the 'non-bonded' reactant datasets.*

The search fragment and geometrical parameters defined in the reactant searches are illustrated in Figure 2.4. In order to satisfy Schmidt's hypothesis [2.1][2.2][2.3] that a solid state [2+2] cycloaddition reaction can only occur if the reacting carbons are separated by less than 4.2 Å, the C---C distances B2 and B4 were constrained to be less than the sum of the Van der Waals radii of carbon plus 20% *i.e.* 4.078 Å. Distances B2 and B4 were allowed to be either intermolecular or intramolecular provided that potentially reacting carbons in the same molecule were separated by a minimum of 4 atoms. Since large amounts of molecular motion are extremely unlikely to occur in the solid state, the sum of the cross distances D1 and D2 was set to be greater than the sum of the distances B2 and B4. Fullerenes and fragments that contained one of the alkene carbons attached by a double bond to another

atom were rejected as these are unlikely to undergo a solid state [2+2] cycloaddition reaction.

The PERMUTE function within QUEST is not compatible with non-bonded searches, so the initial dataset as output was permuted externally [2.13] to account for the D_{2h} reference geometry using the atomic and geometrical permutations listed in Figure 2.5.

Carbon atom permutations			
1	2	3	4
3	4	1	2
2	1	4	3
4	3	2	1

Angle permutations				Torsion angles permutations				Distance permutations			
1	2	3	4	1	2	3	4	1	2	3	4
3	4	1	2	4	3	2	1	3	4	1	2
2	1	4	3	1	3	2	4	1	4	3	2
4	3	2	1	4	2	3	1	3	2	1	4

Figure 2.5 - *(Above) Atom permutations for D_{2h} reference geometry. (Below) Permutational operators for D_{2h} reference geometry in terms of angles, torsion angles and distances.*

Two additional datasets were created from the non-bonded D_{2h} dataset to identify structures that would undergo either (i) an intermolecular or (ii) an intramolecular [2+2] cycloaddition reaction. The purpose of this approach was to establish whether the two reaction pathways might show differences, as potentially reacting alkenes contained in the same molecule may have less freedom to move with respect to each other in certain directions, as compared to alkene fragments in separate molecules.

2.2.3 D_{4h} Reference Geometry Search Criteria

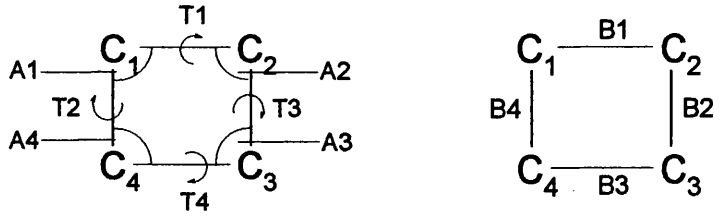

Figure 2.6 - *Illustration of search criteria for the 'bonded' product searches.*

To facilitate easy comparison of results, the search fragment and geometrical parameters used in the 'product' searches were defined in the same manner as those employed in the 'reactant' searches, see Figure 2.6. In addition to the general search parameters discussed earlier (Section 2.2.1), structures containing a C-C bond between C_1 and C_3 or C_2 and C_4 were rejected along with the two fragments illustrated in Figure 2.7,

since they were deemed unlikely to have been formed from a solid state [2+2] cycloaddition reaction and consequently inclusion of their more defined structures would bias the results.

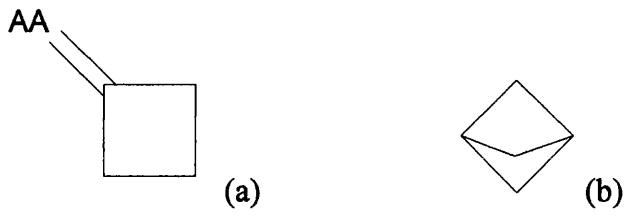

Figure 2.7 – *Search fragments eliminated from dataset. (a) AA is any atom.*

In order to account for the topological D_{4h} symmetry of the fragment the PERMUTE function within QUEST was used, thus producing 8 fragments from each hit in accordance with the atomic and geometrical permutations listed in Figure 2.8.

Carbon atom permutations

1	2	3	4
1	4	3	2
2	1	4	3
2	3	4	1
4	1	2	3
4	3	2	1
3	2	1	4
3	4	1	2

Angle permutations				Torsion angles permutations				Distance permutations			
1	2	3	4	1	2	3	4	1	2	3	4
1	4	3	2	2	1	4	3	4	3	2	1
2	1	4	3	1	3	2	4	1	4	3	2
2	3	4	1	3	1	4	2	2	3	4	1
4	1	2	3	2	4	1	3	4	1	2	3
4	3	2	1	4	2	3	1	3	2	1	4
3	2	1	4	3	4	1	2	2	1	4	3
3	4	1	2	4	3	2	1	3	4	1	2

Figure 2.8 - *(Above) Atom permutations for D_{4h} reference geometry. (Below) Permutational operators for angles, torsion angles and distances for D_{4h} reference geometry.*

2.2.4 Software

The CSD searches were carried out using QUEST3D version 5 [2.14] working on the CSD version 5.25 (November 2003, 298,097 structures) [2.14]. LARGEVISTA [2.15], a modification of the VISTA program extended to handle up to 199,999 fragments, was used to carry out data analysis and construct scatter plots.

2.3 Derivation of Symmetry Deformation Coordinates

2.3.1 D_{2h} Reference Geometry

2.3.1.1 Angles for D_{2h} Reference Geometry

The complete derivation of the symmetry deformation coordinates in terms of the angles defined in the D_{2h} searches is set out below. Since the method is the same for each set of search parameters (angles, distances and torsion angles) it is only explained in detail once during this chapter. The total number of symmetry deformation coordinates obtained in each case is equal to the number of parameters of the same type being compared, i.e. four for all of the examples provided within.

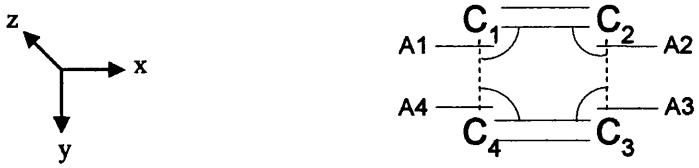

Figure 2.9 - *Illustration of angles for D_{2h} reference geometry.*

Each of the symmetry operations under the D_{2h} point group were applied to the angles defined in Figure 2.9, and the number of parameters that remained unchanged using each operation recorded to give the following reducible representation:

D_{2h}	E	$C_2(z)$	$C_2(y)$	$C_2(x)$	i	σ^{xy}	σ^{xz}	σ^{yz}
	4	0	0	0	0	4	0	0

The next stage involved determining the symmetry of the angular deformations being studied by using the formula in Box 2.1 to determine the contribution of the irreducible representations to the reducible representation. Clearly it is only necessary to consider the symmetry operations that have non-zero entries in the reducible representation, E and σ^{xy} in this case, as the contribution of the irreducible representation to the reducible representation in terms of the other symmetry operations will be zero. The results of the analysis are set out in Table 2.1.

Box 2.1 – *Contribution of IR to RR.*

Contribution of IR to RR = $1/g \Sigma n_R \chi_R \chi_{IR}$

Where g – total number of symmetry operations for point group

n_R – number of symmetry operations in a class

χ_R – character in reducible representation (RR) for symmetry operation

χ_{IR} – character in irreducible representation (IR) for symmetry operation

Table 2.1 - *Contribution of irreducible representation to reducible representation for the angles defined in the D_{2h} reactant searches.*

D_{2h}		
A_g	= 1/8 x ((1 x 4 x 1) + (1 x 4 x 1))	= 1
B_{1g}	= 1/8 x ((1 x 4 x 1) + (1 x 4 x 1))	= 1
B_{2g}	= 1/8 x ((1 x 4 x 1) + (1 x 4 x -1))	= 0
B_{3g}	= 1/8 x ((1 x 4 x 1) + (1 x 4 x -1))	= 0
A_u	= 1/8 x ((1 x 4 x 1) + (1 x 4 x -1))	= 0
B_{1u}	= 1/8 x ((1 x 4 x 1) + (1 x 4 x -1))	= 0
B_{2u}	= 1/8 x ((1 x 4 x 1) + (1 x 4 x 1))	= 1
B_{3u}	= 1/8 x ((1 x 4 x 1) + (1 x 4 x 1))	= 1

The final reduction $\mathbf{A_g + B_{1g} + B_{2u} + B_{3u}}$ indicated four angular deformations each with a different symmetry, which must be related to the angles defined in the search, and thus express the symmetry deformation coordinates in terms of A1 to A4. This was achieved as follows:

1.) The effect each symmetry operation from the D_{2h} point group has on one of the angles e.g. A1 was determined by recording the final position of the angle after each operation.

D_{2h}	E	$C_2(z)$	$C_2(y)$	$C_2(x)$	i	σ^{xy}	σ^{xz}	σ^{yz}
A1	A1	A3	A2	A4	A3	A1	A4	A2

2.) Consider A_g the first of the angular deformation established from the irreducible representation, the characters in the D_{2h} point group table corresponding to each of the symmetry operations for this symmetry label are as follows:

D_{2h}	E	$C_2(z)$	$C_2(y)$	$C_2(x)$	i	σ^{xy}	σ^{xz}	σ^{yz}
A_g	1	1	1	1	1	1	1	1

3.) The characters from the point group table are then combined with the angular positions, thus for deformation with A_g symmetry the following relationship to the angles A1 to A4 is obtained.

$$\begin{aligned} A_g &= A1 + A3 + A2 + A4 + A3 + A1 + A4 + A2 \\ &= 2A1 + 2A2 + 2A3 + 2A4 \\ &= 2(A1 + A2 + A3 + A4) \end{aligned}$$

4.) To obtain the symmetry deformation coordinate with A_g symmetry (arbitrarily labelled SA1), in terms of the angles, it is necessary to normalise the result above using a normalisation coefficient n such that $(1/n)^2$ multiplied by the number of coefficients is equal to 1, for the A_g coordinate.

$$\begin{aligned} SA1 &= 1/\sqrt{y} \times 2(A1 + A2 + A3 + A4) \\ &\textit{(Where } y = (2)^2 \times 4 = 16\textit{)} \\ &= 2/\sqrt{16} \times (A1 + A2 + A3 + A4) \\ &= \tfrac{1}{2} \times (A1 + A2 + A3 + A4) \end{aligned}$$

(Thus the normalisation coefficient $n = 2$).

The other three symmetry deformation coordinates relating to B_{1g}, B_{2u} and B_{3u}, were derived in the same manner and arbitrarily labelled SA2, SA3 and SA4 respectively. Table 2.2 below summarises the results.

Table 2.2 – *Symmetry deformation coordinates for D_{2h} reference geometry in terms of angles.*

SDC label	SDC	IR
SA1	½ *(A1 + A2 + A3 + A4)	A_g
SA2	½ *(A1 - A2 + A3 - A4)	B_{1g}
SA3	½ *(A1 + A2 - A3 - A4)	B_{2u}
SA4	½ *(A1 - A2 - A3 + A4)	B_{3u}

The effect that the angle symmetry deformation coordinates (SA1-SA4) have on the product fragment is illustrated in Figure 2.10. It is important to note that the symmetry deformation coordinates cannot necessarily be examined in isolation, and can sometimes only occur in combination with another deformation. For example, SA1 can only be applied to the D_{2h} fragment in combination with a twist.

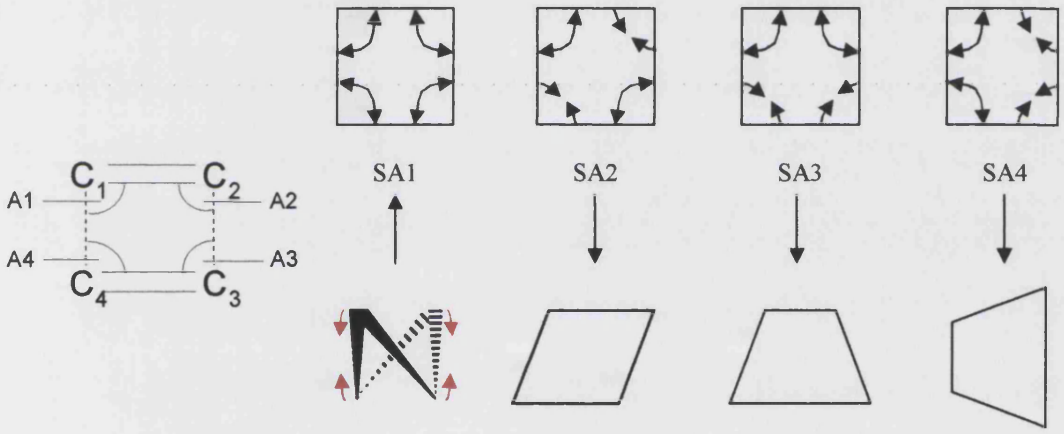

Figure 2.10 – *Illustration of the symmetry deformation coordinates for D_{2h} point group in terms of angles A1-A4.*

2.3.1.2 Torsion Angles for D_{2h} Reference Geometry

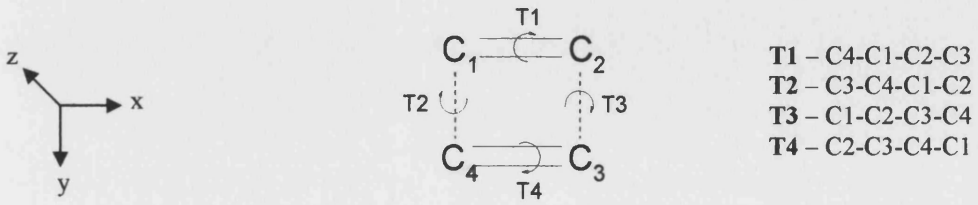

Figure 2.11 - *Torsion angles definitions for D_{2h} geometry.*

The symmetry operations for the D_{2h} point group were applied to the torsion angles (Figure 2.11) in the same way as described for the angles (Section 2.3.1.1), with the exception that unlike angles, torsion angles have an associated direction. This direction can be reversed by a symmetry operation, resulting in the following torsion angle representation that reduced to $\mathbf{2A_u + B_{2g} + B_{3g}}$.

D_{2h}	E	$C_2(z)$	$C_2(y)$	$C_2(x)$	i	σ^{xy}	σ^{xz}	σ^{yz}
	4	0	2	2	0	-4	-2	-2

Table 2.3 below lists the symmetry deformation coordinates derived for the D_{2h} reference geometry in terms of the torsion angles.

Table 2.3 – *Symmetry deformation coordinates for D_{2h} reference geometry in terms of torsion angles.*

SDC label	SDC	IR
ST1	½ *(T1 + T2 + T3 + T4)	A_u (a)
ST2	½ *(T1 – T2 – T3 + T4)	A_u (b)
ST3	1/√2 *(T1 – T4)	B_{2g}
ST4	1/√2 *(T3 – T2)	B_{3g}

It is noteworthy that the puckering angle θ, commonly used to describe the conformation of cyclobutane rings has a linear relationship to ST2, hence plots of ST2 convey equivalent information, see Figure 2.12 [2.16].

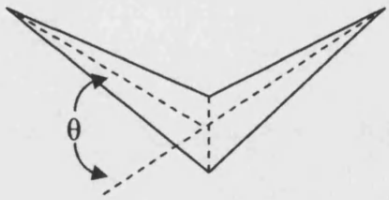

Figure 2.12 - *Puckering angle θ [2.12].*

2.3.1.3 Distances for D_{2h} Reference Geometry

Figure 2.13 - *Illustration of distances for D_{2h} geometry.*

The following representation was produced after applying the symmetry operations of the D_{2h} point group to the distances defined in the non-bonded 'reactant' searches (Figure 2.13).

D_{2h}	E	$C_2(z)$	$C_2(y)$	$C_2(x)$	i	σ^{xy}	σ^{xz}	σ^{yz}
	4	0	2	2	0	4	2	2

This reducible representation for the reactant dataset was reduced to $\mathbf{2A_g + B_{2u} + B_{3u}}$, and gave rise to the following symmetry deformation coordinates for the distances B1 to B4 (see Table 2.4).

Table 2.4 – *Symmetry deformation coordinated for D_{2h} reference geometry in terms of distances.*

SDC label	SDC	IR
SB1	½ *(B1 + B2 + B3 + B4)	A_g (a)
SB2	½ *(B1 - B2 + B3 – B4)	A_g (b)
SB3	1/√2 *(B1 – B3)	B_{2u}
SB4	1/√2 *(B2 – B4)	B_{3u}

The effect of each of the symmetry deformation coordinates on the distances B1 to B4 for the D_{2h} product fragment are illustrated in Figure 2.14.

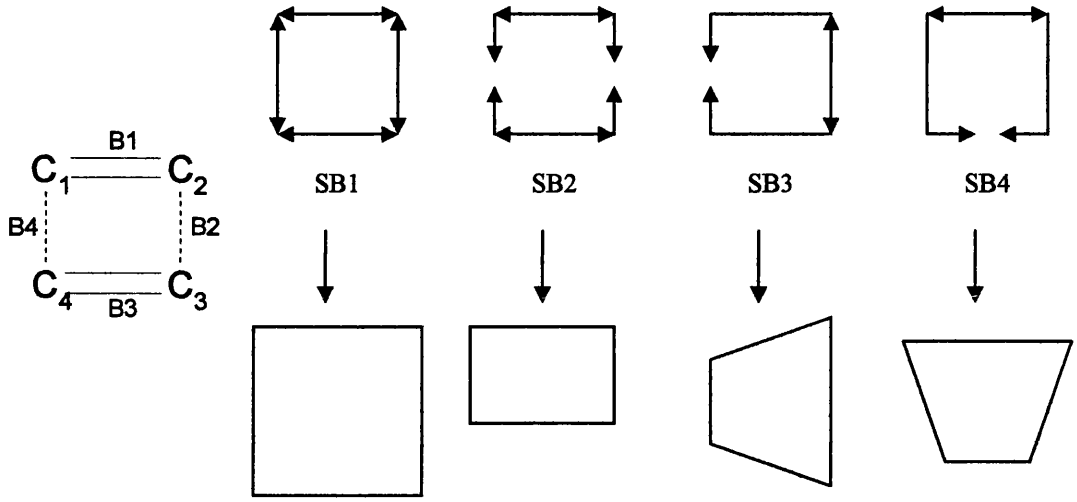

Figure 2.14 – *Illustration of symmetry deformation coordinates for D_{2h} point group in terms of B1-B4.*

2.3.2 D_{4h} Reference Geometry

2.3.2.1 Angles for D_{4h} Reference Geometry

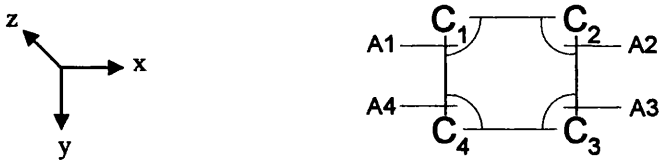

Figure 2.15 - *Definition of angles for D_{4h} geometry.*

The derivation of symmetry deformation coordinates for the D_{4h} 'product' dataset followed the same principles as described for the 'reactant' D_{2h} species described in Section 2.3.1.1. The following reducible representation was produced after applying the symmetry operations for the D_{4h} point group to the angles defined in Figure 2.15.

D_{4h}	E	$2C_4$	C_4^2	$2C_2$	$2C_2'$	i	$2S_4$	σ_h	$2\sigma_v$	$2\sigma_d$
	4	0	0	0	2	0	0	4	0	2

This reduced to $\mathbf{A_{1g} + B_{2g} + E_u}$, i.e. four terms with the first two being singularly degenerate and the final E_u term being doubly degenerate. Table 2.5 below lists the resultant symmetry deformation coordinates for the D_{4h} reference geometry in terms of the angles depicted in Figure 2.15.

Table 2.5 – *Symmetry deformation coordinates for D_{4h} reference geometry in terms of angles.*

SDC label	SDC	IR
SA1	½ *(A1 + A2 + A3 + A4)	A_{1g}
SA2	½ *(A1 - A2 + A3 - A4)	B_{2g}
SA3	1/√2 *(A1 - A3)	E_u (a)
SA4	1/√2 *(A4 - A2)	E_u (b)

An illustration of the effect that the angle symmetry deformation coordinates (SA1-SA4) have on the D_{4h} product fragment is provided in Figure 2.16. Again it is not possible to view all of these coordinates in isolation, SA1 can only occur in combination with a twist, while SA3 and SA4 can only occur in combination with a twist and changes in two of the bond lengths.

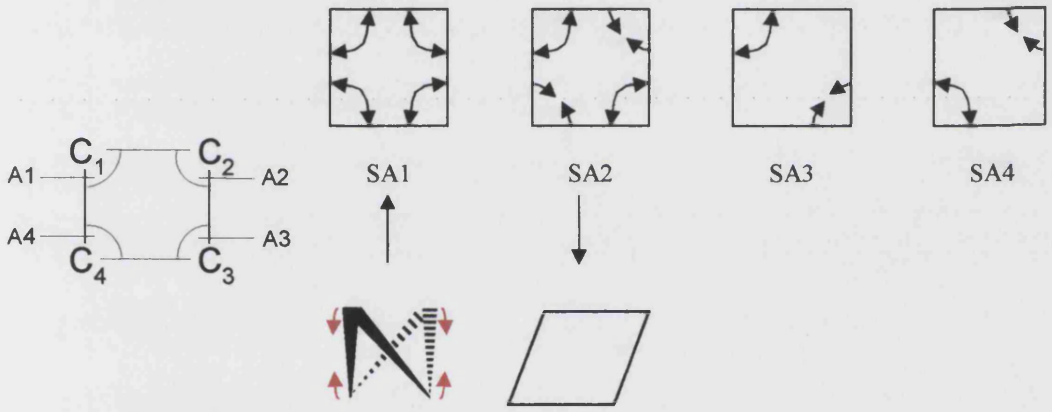

Figure 2.16 – *Illustration of the symmetry deformation coordinates for D_{4h} point group in terms of angles A1-A4.*

2.3.2.2 Torsion Angles for D_{4h} Reference Geometry

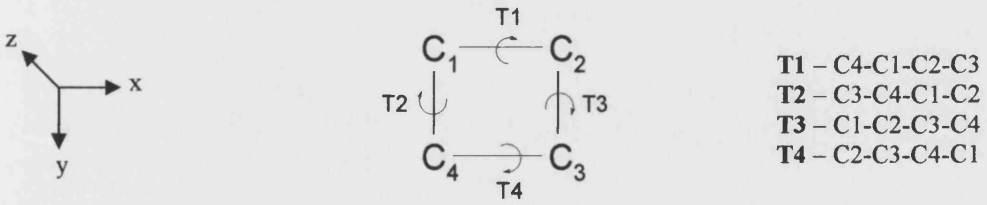

Figure 2.17 - *Torsion angle definitions for D_{4h} geometry.*

The symmetry operations for the D_{4h} point group were applied to the torsion angles (Figure 2.17) giving the following representation, which reduced to $\mathbf{A_{1u} + B_{1u} + E_g}$.

D_{4h}	E	$2C_4$	C_4^2	$2C_2$	$2C_2'$	i	$2S_4$	σ_h	$2\sigma_v$	$2\sigma_d$
	4	0	0	2	0	0	0	-4	-2	0

The symmetry deformation coordinates for the D_{4h} point group in terms of the torsion angles are listed in Table 2.6 below.

Table 2.6 – *Symmetry deformation coordinated for D_{4h} reference geometry in terms of torsion angles.*

SDC label	SDC	IR
ST1	½ *(T1 + T2 + T3 + T4)	A_{1u}
ST2	½ *(T1 – T2 – T3 + T4)	B_{1u}
ST3	1/√2 *(T3 – T2)	E_g (a)
ST4	1/√2 *(T1 – T4)	E_g (b)

2.3.2.3 Distances for D_{4h} Reference Geometry

Figure 2.18 - *Distance definitions for D_{4h} reference geometry.*

Application of the symmetry operations for the D_{4h} point group to the distances (B1 to B4) defined in Figure 2.18 gave the following results:

D_{4h}	E	$2C_4$	C_4^2	$2C_2$	$2C_2'$	i	$2S_4$	σ_h	$2\sigma_v$	$2\sigma_d$
	4	0	0	2	0	0	0	4	2	0

Reduction of this representation gave an irreducible contribution of $\mathbf{A_{1g} + B_{1g} + E_u}$, which produced the symmetry deformation coordinates listed in Table 2.7.

Table 2.7 – *Symmetry deformation coordinated for D_{4h} reference geometry in terms of distances.*

SDC label	SDC	IR
SB1	½ *(B1 + B2 + B3 + B4)	A_{1g}
SB2	½ *(B1 - B2 + B3 – B4)	B_{1g}
SB3	1/√2 *(B2 – B4)	E_u (a)
SB4	1/√2 *(B1 - B3)	E_u (b)

Figure 2.19 illustrates the effect of each symmetry deformation coordinate on the distances B1 to B4 for the D_{4h} product fragment.

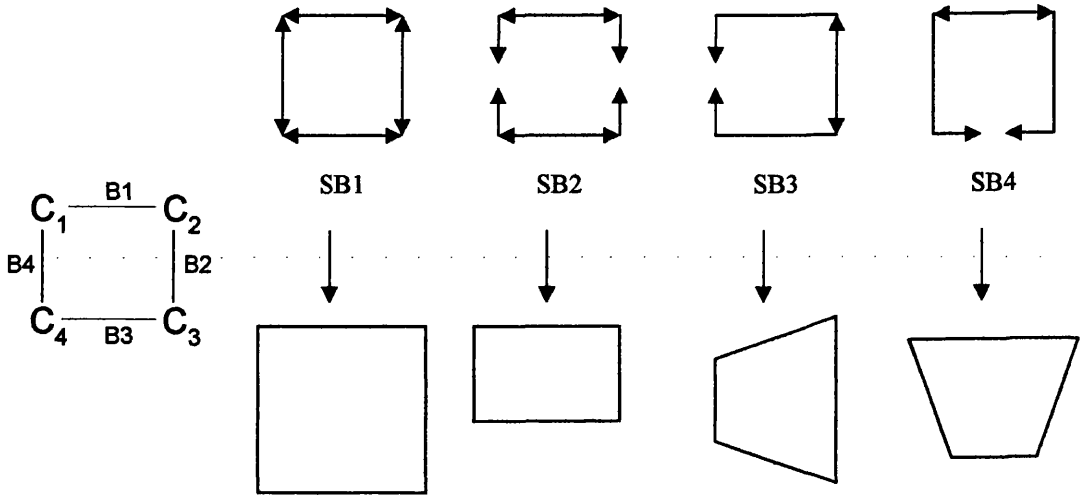

Figure 2.19 – *Illustration of symmetry deformation coordinates for D_{4h} point group in terms of B1-B4.*

2.4 D_{2h} Reference Geometry Searches - Results

2.4.1 Principal Component Analysis

10,808 refcodes matched the search criteria giving 90,232 fragments for analysis after symmetry expansion. The results of the principal component analysis in terms of the angles, torsion angles and distances are given in Table 2.8.

Table 2.8 – *Results of principal component analysis for D_{2h} reactant dataset.*

PC	SDC	Eigenvalue	Variance	Symmetry Operator	SDC Label
1	**½ *(A1 - A2 + A3 - A4)**	**3.773**	**94.330**	**B_{1g}**	**SA2**
2	½ *(A1 - A2 - A3 + A4)	0.150	3.747	B_{3u}	SA4
3	½ *(A1 + A2 + A3 + A4)	0.075	1.886	A_g	SA1
4	½ *(A1 + A2 - A3 - A4)	0.001	0.037	B_{2u}	SA3
1	**½ *(T1 – T2 – T3 + T4)**	**3.977**	**99.415**	**A_u (b)**	**ST2**
2	½ *(T1 + T2 + T3 + T4)	0.016	0.401	A_u (a)	ST1
3	1/√2 *(T1 – T4)	0.002	0.057	B_{2g}	ST3
4	1/√2 *(T3 – T2)	0.005	0.127	B_{3g}	-ST4
1	**½ *(B1 - B2 + B3 – B4)**	**1.872**	**46.807**	**A_g (b)**	**SB2**
2	**½ *(B1 + B2 + B3 + B4)**	**1.475**	**36.876**	**A_g (a)**	**SB1**
3	1/√2 *(B1 – B3)	0.354	8.839	B_{2u}	SB3
4	1/√2 *(B2 – B4)	0.299	7.479	B_{3u}	-SB4

The main symmetry deformation coordinates accounting for more than 15% of the variance, are highlighted in bold in Table 2.8 and throughout the results section, as the Burgi-Dunitz structure-structure correlation hypothesis suggests that it is these that should later be used to try to identify potential reaction coordinates, since they indicate the significant distortions within the dataset.

As discussed in the search methodology, the overall D_{2h} dataset was split firstly to identify organic and metal organic species (see Tables 2.9 and 2.10) and secondly to separate potentially reacting alkene fragments that would follow either an inter- or intra-molecular reaction pathway (see Tables 2.9 and 2.11).

Table 2.9 - *Comparison of the number of refcodes and fragments being analysed in the subsets of the main D_{2h} dataset.*

	Alkene	Intermolecular Alkene	Intramolecular Alkene	Organic Alkene	Metal Organic Alkene
Number of Refcodes	10840	10271	831	6621	4219
Number of Fragments	90312	84232	6080	54560	35752

Table 2.10 - *Comparison of the principal component analysis results for the organic and metal organic datasets with the overall D_{2h} dataset.*

SDC Label	SDC	Alkene		Organic Alkene		Metal Organic Alkene	
		Eigen value	Variance	Eigen value	Variance	Eigen value	Variance
SA1	½ *(A1 + A2 + A3 + A4)	0.075	1.885	0.065	1.618	0.093	2.328
SA2	**½ *(A1 - A2 + A3 - A4)**	**3.773**	**94.324**	**3.799**	**94.971**	**3.729**	**93.228**
SA3	½ *(A1 + A2 - A3 - A4)	0.001	0.037	0.001	0.032	0.002	0.044
SA4	½ *(A1 - A2 - A3 + A4)	0.150	3.755	0.135	3.379	0.176	4.399
ST1	½ *(T1 + T2 + T3 + T4)	0.016	0.402	0.016	0.392	0.016	0.409
ST2	**½ *(T1 – T2 – T3 + T4)**	**3.977**	**99.414**	**3.976**	**99.400**	**3.977**	**99.435**
ST3	1/√2 *(T1 – T4)	0.005	0.127	0.006	0.148	0.004	0.102
ST4	1/√2 *(T3 – T2)	0.002	0.057	0.002 (-ST4)	0.060 (-ST4)	0.002	0.055
SB1	**½ *(B1 + B2 + B3 + B4)**	**1.479**	**36.977**	**1.461**	**36.514**	**1.505**	**37.629**
SB2	**½ *(B1 - B2 + B3 – B4)**	**1.871**	**46.786**	**1.934**	**48.339**	**1.772**	**44.309**
SB3	1/√2 *(B1 – B3)	0.350	8.761	0.322	8.060	0.398	9.953
SB4	1/√2 *(B2 – B4)	0.299 (-SB4)	7.477 (-SB4)	0.284 (-SB4)	7.088 (-SB4)	0.324 (-SB4)	8.109 (-SB4)

Table 2.11 - *Comparison of the principal component analysis results for the inter- and intra-molecular datasets with the overall D_{2h} dataset.*

SDC Label	SDC	Alkene		Intermolecular Alkene		Intramolecular Alkene	
		Eigen value	Variance	Eigen value	Variance	Eigen value	Variance
SA1	½ *(A1 + A2 + A3 + A4)	0.075	1.885	0.073	1.815	0.091	2.275
SA2	**½ *(A1 - A2 + A3 - A4)**	**3.773**	**94.324**	**3.794**	**94.844**	**3.566**	**89.140**
SA3	½ *(A1 + A2 - A3 - A4)	0.001	0.037	0.001	0.029	0.005	0.116
SA4	½ *(A1 - A2 - A3 + A4)	0.150	3.755	0.132	3.312	0.339	8.469
ST1	½ *(T1 + T2 + T3 + T4)	0.016	0.402	0.016	0.395	0.017	0.425
ST2	**½ *(T1 – T2 – T3 + T4)**	**3.977**	**99.414**	**3.979**	**99.471**	**3.963**	**99.073**
ST3	1/√2 *(T1 – T4)	0.005	0.127	0.003	0.082	0.016	0.409
ST4	1/√2 *(T3 – T2)	0.002	0.057	0.002	0.052	0.004	0.092
SB1	**½ *(B1 + B2 + B3 + B4)**	**1.479**	**36.977**	**1.421**	**35.516**	**1.840**	**46.007**
SB2	**½ *(B1 - B2 + B3 – B4)**	**1.871**	**46.786**	**1.953**	**48.831**	**1.275**	**31.883**
SB3	1/√2 *(B1 – B3)	0.350	8.761	0.338	8.453	0.454	11.342
SB4	1/√2 *(B2 – B4)	0.299 (-SB4)	7.477 (-SB4)	0.288 (-SB4)	7.200 (-SB4)	0.431 (-SB4)	10.768 (-SB4)

Tables 2.10 and 2.11 both illustrate that there were no significant variations between the principal component analysis results for any of the subsets of the main dataset, apart from the ordering of SB1 and SB2 for the intramolecular dataset highlighted in red on Table 2.11. This change was not considered to be important as these deformation coordinates account for the majority of the variation in all of the D_{2h} datasets and principal component analysis simply tells you where the significant deformations lie, as opposed to indicating which deformation(s) represent a reaction pathway. In addition, the analysis was based on a much smaller number of fragments than used for the other datasets.

2.4.2 Discussion

In order to look for potential reaction coordinates scatter plots were constructed from the complete dataset using the main symmetry deformation coordinates. Figures 2.20 to 2.25 below show the significant plots for the overall D_{2h} reference geometry search.

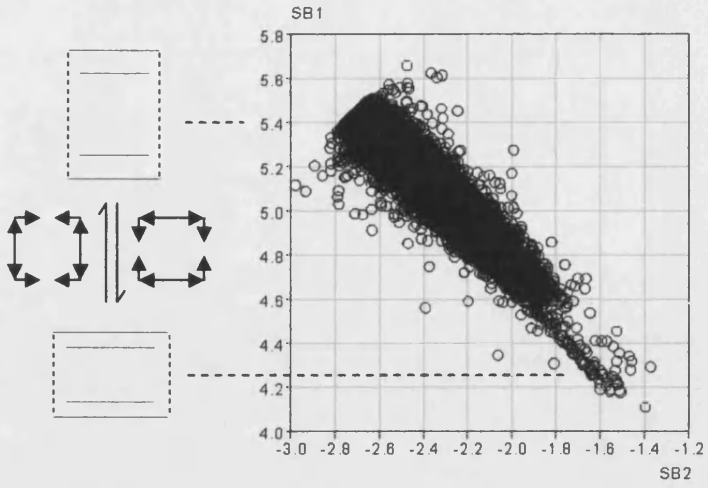

Figure 2.20 – *SB1 (Å) vs. SB2 (Å), with an illustration of the effect of SB1 and SB2 on the D_{2h} geometry.*

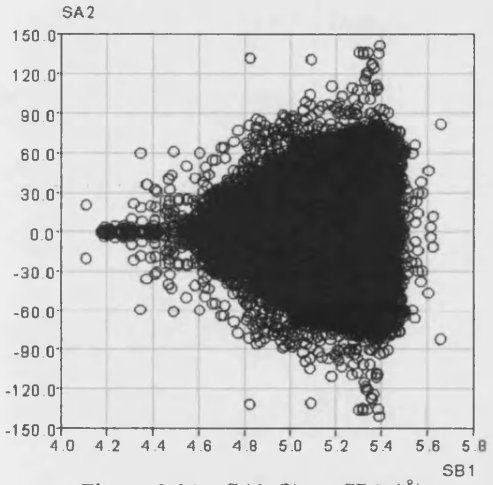

Figure 2.21 - *SA2 (°) vs. SB1 (Å).*

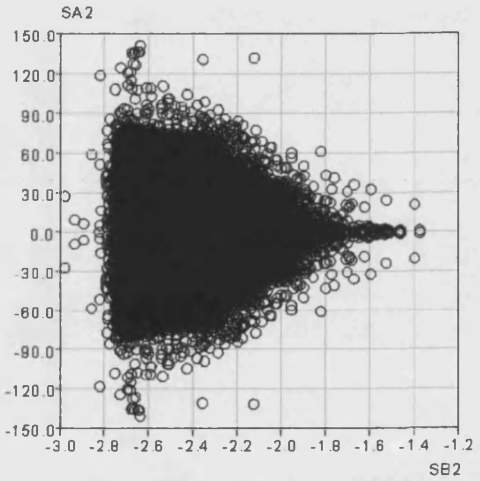

Figure 2.22 – *SA2 (°) vs. SB2 (Å).*

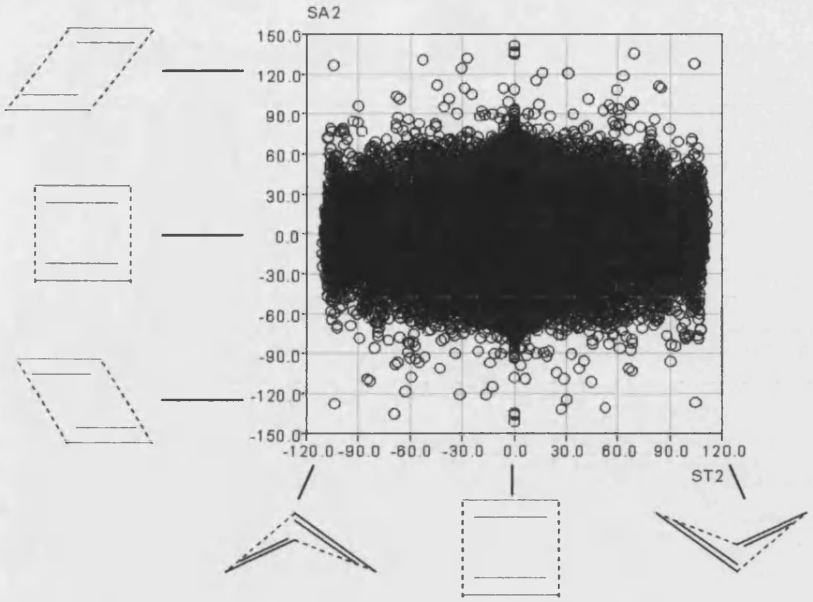

Figure 2.23 - *SA2 (°) vs. ST2 (°), with an illustration of the effect of SA2 and ST2 on the D_{2h} geometry.*

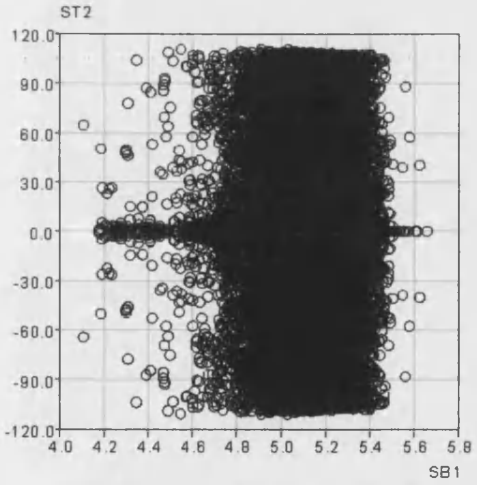

Figure 2.24 - *ST2 (°) vs. SB1 (Å).*

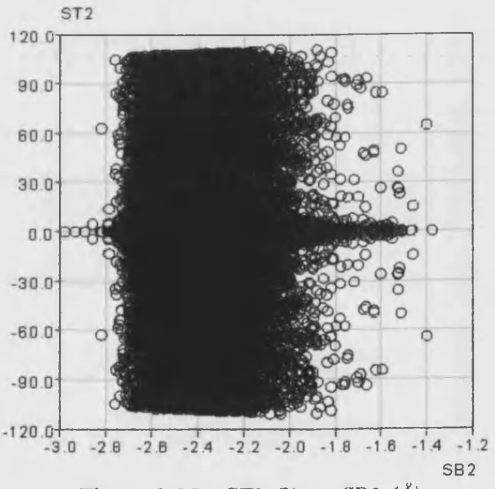

Figure 2.25 - *ST2 (°) vs. SB2 (Å).*

The first plot, Figure 2.20 (SB1 vs. SB2) indicates that as the sum of the distances (SB1) decreases so does the difference between the sum of the bonded (B1 + B3) and non bonded (B2 + B4) distances. In other words as SB1 decreases the distance between the two alkene bonds is getting shorter.

Figures 2.21 and 2.22 (SA2 vs. SB1 and SA2 vs. SB2) both illustrate that, as the alkene groups get closer together, the difference between the sum of the pairs of angles diagonal to each other i.e. (A1 + A3) and (A2 + A4) decrease. An alternative way to view this is to say that the angles are all tending towards similar values as the distance between the double bonds reduces. However, they are not necessarily heading towards 90° as shown by

Figure 2.23 (SA2 vs. ST2) which shows a wide variation in the value of ST2 for all values of SA2.

The final two plots Figures 2.24 and 2.25 (ST2 vs. SB1 and ST2 vs. SB2) show that although there is a concentration of scatter points around 0° for ST2 as the separation between the double bonds reduces a significant proportion of the points have non zero values. This suggests that as the distance between the alkenes decreases there is no requirement for them to be parallel to each other.

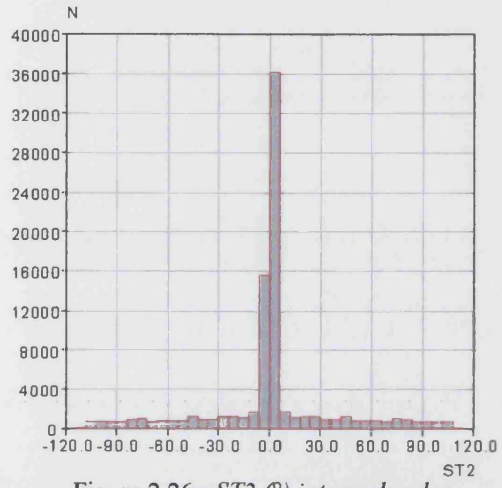

Figure 2.26 - *ST2 (°) intermolecular.*

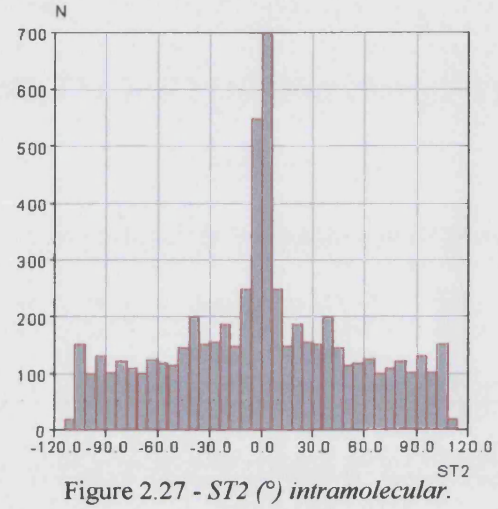

Figure 2.27 - *ST2 (°) intramolecular.*

The complete set of scatter plots from all of the D_{2h} datasets (organic, metal organic, inter- and intra-molecular) are not included here, but provided in Appendix 2.1 on CD. The only significant feature of note from the individual searches is that the range of ST2 values for fragments that might undergo an intermolecular reaction was smaller than that for those substructures contained in intramolecular dataset. This is not surprising as the orientation of the alkene fragments in the latter would likely be more constrained (Figures 2.26 and 2.27). However, the search results from all of the subsets of the overall data showed the same general trends as those discussed above, including those relating to SB1 and SB2 of the intramolecular dataset. This further highlights the fact that principal component analysis can only be used as a tool to identify significant deformations that may indicate a reaction pathway.

2.5 D_{4h} Reference Geometry Searches - Results

2.5.1 Principal Component Analysis

The search produced 1717 refcodes resulting in a D_{4h} expanded dataset of 24592 fragments. Table 2.12 summarises the results of the principal component analysis in terms of the angles, torsion angles and distances.

Table 2.12 – *Results of the principal component analysis for the D_{4h} product dataset.*

PC	SDC	Eigenvalue	Variance	Symmetry Operator	SDC Label
1	**½ *(A1 + A2 + A3 + A4)**	**2.119**	**52.982**	**A_{1g}**	**SA1**
2	**½ *(A1 - A2 + A3 - A4)**	**1.183**	**29.575**	**B_{2g}**	**SA2**
3	1/√2 *(A1 - A3)	0.349	8.722	E_u (a)	SA3
4	1/√2 *(A4 - A2)	0.349	8.722	E_u (b)	SA4
1	**½ *(T1 – T2 – T3 + T4)**	**3.999**	**99.980**	**B_{1u}**	**ST2**
2	½ *(T1 + T2 + T3 + T4)	0.000	0.007	A_{1u}	ST1
3	1/√2 *(T1 – T4)	0.000	0.006	E_g (a)	ST3
4	1/√2 *(T3 – T2)	0.000	0.006	E_g (b)	ST4
1	**½ *(B1 + B2 + B3 + B4)**	**1.298**	**32.438**	**A_{1g}**	**SB1**
2	**½ *(B1 - B2 + B3 – B4)**	**0.931**	**23.272**	**B_{1g}**	**SB2**
3	**1/√2 *(B1 – B3)**	**0.886**	**22.145**	**E_u (a)**	**SB3**
4	**1/√2 *(B2 – B4)**	**0.886**	**22.145**	**E_u (b)**	**-SB4**

The majority of the variance within the dataset is accounted for by the symmetry deformation coordinates highlighted in bold in Table 2.12. It is important to note that the distance symmetry deformation coordinates all appear equally significant, due to the fact that all the bond lengths around a cyclobutane ring are similar and very little variation is possible due to the well defined ring structure.

As with the D_{2h} searches the D_{4h} dataset was separated into organic and metal organic species to check for any significant differences in the trends identified by principal component analysis (see Tables 2.13 and 2.14).

Table 2.13 - *Comparison of the number of refcodes and fragments being analysed in the subsets of the main D_{4h} dataset.*

	Cyclobutane	Organic Cyclobutane	Organometallic Cyclobutane
Number of Refcodes	1730	1536	194
Number of Fragments	24744	21760	2984

Table 2.14 - *Comparison of the principal component analysis results for the organic and metal organic datasets with the overall D_{4h} dataset.*

SDC Label	SDC	Cyclobutane		Organic Cyclobutane		Organometallic Cyclobutane	
		Eigen value	Variance	Eigen value	Variance	Eigen value	Variance
SA1	**½ *(A1 + A2 + A3 + A4)**	**2.119**	**52.982**	**2.091**	**52.283**	**1.641**	**41.019**
SA2	**½ *(A1 - A2 + A3 - A4)**	**1.179**	**29.487**	**1.244**	**31.095**	**1.242**	**31.049**
SA3	1/√2 *(A1 - A3)	0.351	8.763	0.332	8.311	0.559	13.966
SA4	1/√2 *(A4 - A2)	0.351	8.763	0.332	8.311	0.559	13.966
ST1	½ *(T1 + T2 + T3 + T4)	0.000	0.007	*1	*1	0.001	0.013
ST2	**½ *(T1 – T2 – T3 + T4)**	**3.999**	**99.981**	**3.999**	**99.984**	**3.999**	**99.968**
ST3	1/√2 *(T1 – T4)	0.000	0.006	*1	*1	0.000	0.009
ST4	1/√2 *(T3 – T2)	0.000	0.006	*1	*1	0.000	0.009
SB1	**½ *(B1 + B2 + B3 + B4)**	**1.297**	**32.432**	**1.388**	**34.699**	**0.989**	**24.725**
SB2	**½ *(B1 - B2 + B3 – B4)**	**0.929**	**23.229**	**0.876**	**21.896**	**1.107**	**27.667**
SB3	**1/√2 *(B1 – B3)**	**0.887**	**22.170**	**0.868**	**21.703**	**0.952**	**23.804**
SB4	**1/√2 *(B2 – B4)**	**0.887 (-SB4)**	**22.170 (-SB4)**	**0.868 (-SB4)**	**21.703 (-SB4)**	**0.952**	**23.804**

*1 The values for these principal components were inconsistent with the symmetry deformation coordinates as defined here. This was not considered significant as 99.98% of the variance was accounted for by ST2, and the remaining deformations coordinates are therefore essentially insignificant with respect to this analysis.

Comparing the results of the principal component analysis for the overall dataset with the organic and metal organic subsets did not indicate any significant differences. The

order of the first two distance principal components (SB1 and SB2 highlighted in red in Table 2.14) had switched for the metal organic species, however, as with the D_{2h} searches this was put down to the fact that the analysis can only indicate deformations that may be significant and was again based on a small subset of results.

2.5.2 Discussion

A selection of the 21 scatter plots constructed from the main symmetry deformation coordinates identified in the D_{4h} searches are provided in Figures 2.28 to 2.33, with the complete set of plots provided in Appendix 2.2 on CD. It is worth noting that many of the variations are much smaller than see for the 'reactant' dataset due to the definition of the cyclobutane ring.

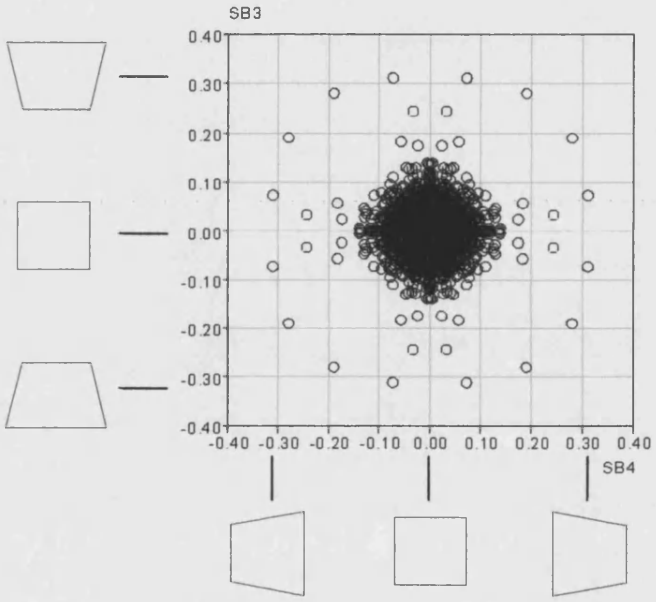

Figure 2.28 - *SB3 (Å) vs. SB4 (Å), with an illustration of the effect of SB3 and SB4 on the D_{4h} geometry.*

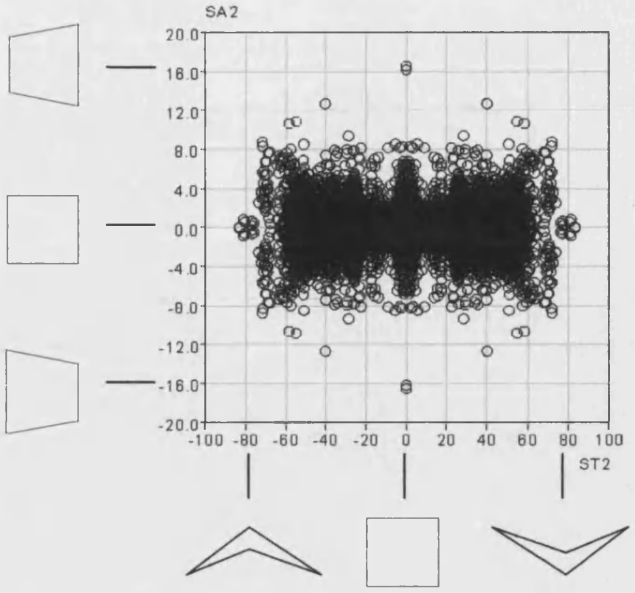

Figure 2.29 - *SA2 (°) vs. ST2 (°), with an illustration of the effect of SA2 and ST2 on the D_{4h} geometry.*

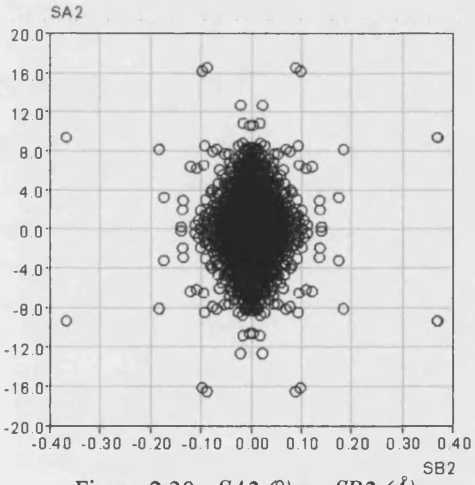

Figure 2.30 - *SA2 (°) vs. SB2 (Å).*

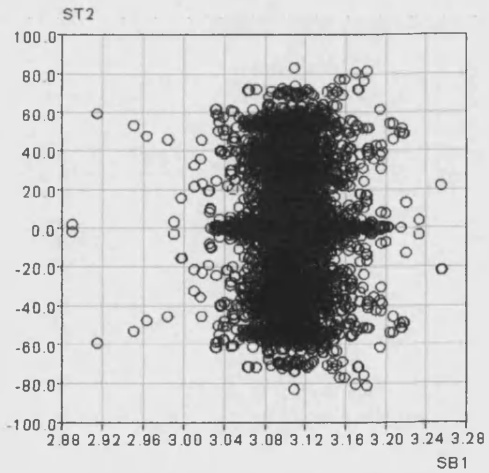

Figure 2.31 - *ST2 (°) vs. SB1 (Å).*

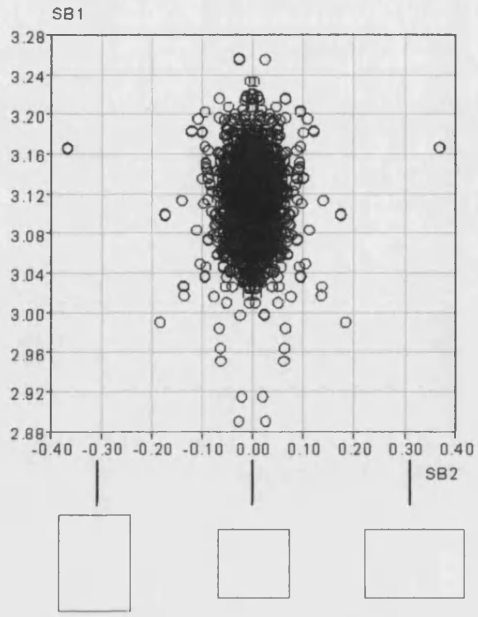

Figure 2.32 - *SB1 (Å) vs. SB2 (Å), with an illustration of the effect of SB1 and SB2 on the D_{4h} geometry.*

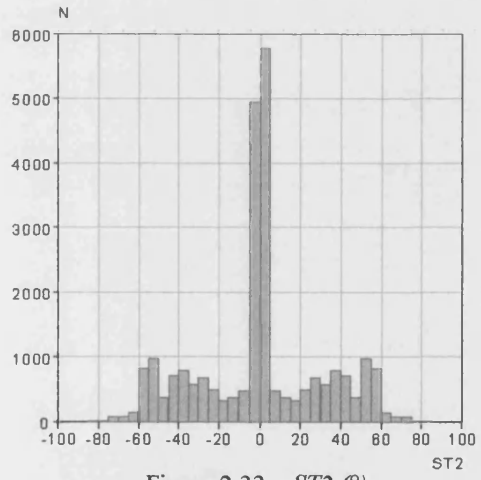

Figure 2.33 – *ST2 (°).*

The first plot, Figure 2.28 (SB3 vs. SB4) illustrates that there are only small variations in (B1 – B3) and (B4 – B2), in other words all of the bond lengths are approximately the same around the ring. It is noteworthy that SB3 and SB4 are identical due to the use of the PERMUTE function during the searches to account for the D_{4h} symmetry of the search fragment.

Figure 2.29 (SA2 vs. ST2) shows that while there is only a small difference between the sum of the angles on a diagonal to each other i.e. (A1 + A3) and (A2 + A4) a wide range is observed for ST2. In combination with Figure 2.30 (SA2 vs. SB2), which indicates that the sum of opposite distances tend to be equal, it can be concluded that both the angles and bonded distances around the cyclobutane ring are similar even when the ring is not planar.

Figures 2.31 and 2.32 (SB1 vs. SB2 and ST2 vs. SB1) suggest that as the sum of the distances around the ring decreases the difference between individual distances remains small and the cyclobutane ring can be either planar or puckered.

The structures with ST2 values above +60° or below -60° on the histogram (Figure 2.33) could only have been formed by an intramolecular [2+2] cycloaddition reaction. Hence these product structures were somewhat predefined by the geometry of the reactant.

The complete set of scatter plots from all of the D_{4h} datasets (organic and metal organic) showed the same general trends as discussed herein and hence are not included at this point, but are provided in Appendix 2.2 on CD. No significant differences were seen for the plots relating to the metal organic SB1 and SB2 plots, which (as with the intermolecular D_{2h} dataset) indicates that principal component analysis is simply a tool to identify significant deformations within a dataset as opposed to directly identifying the ones that may indicate a reaction pathway.

2.6 Conclusions

Figures 2.34 and 2.35 illustrate two of the scatterplots from the reactant and product searches re-plotted on the same axes. They suggest that structures from the two sets of searches lie on the same reaction pathway, with the 'empty' areas between the clusters of points corresponding to regions of high potential energy.

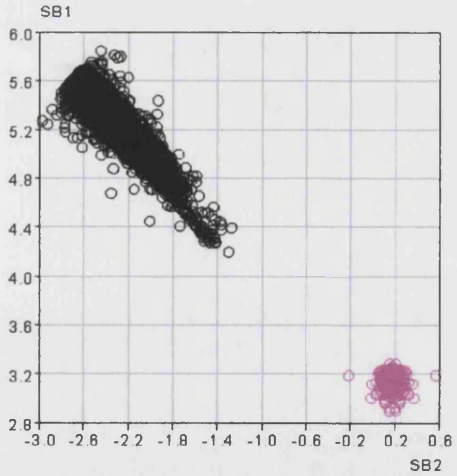

Figure 2.34 – *SB1 (Å) vs. SB2 (Å) (black – reactant, purple - product).*

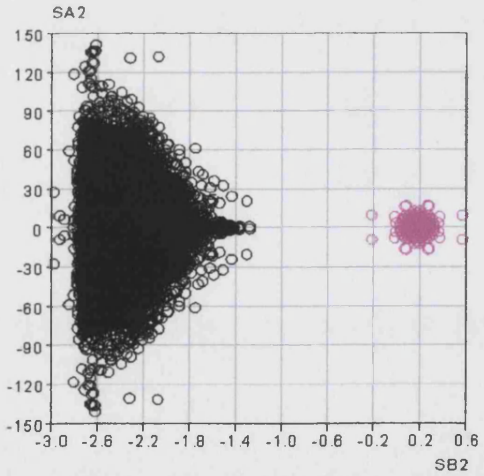

Figure 2.35 – *SA2 (°) vs. SB2 (Å) (black – reactant, purple – product).*

Moreover, the results also suggest that the formation of the cyclobutane ring occurs through a decrease in the intermolecular separation of the alkenes (represented by the parameters B2 and B4) which is accompanied by an increase in the bonded distances (B1 and B3). Associated with this trend is a decrease in the variation of the angles around the

potentially forming cyclobutane ring. Interestingly, in contradiction to Schmidt's hypothesis, there is no evidence that the double bonds need to be parallel, and a large degree of twist can be accommodated provided that similar angles are maintained around the ring. This indicates that the cyclobutane can develop directly as either a planar or puckered ring [2.17], with similar distances and angles around the ring. This observation is supported by experimental evidence from fourteen compounds in the CSD which are reported to have formed via solid state [2+2] cycloaddition reactions and exhibiting both planar and puckered structures, see Figure 2.36.

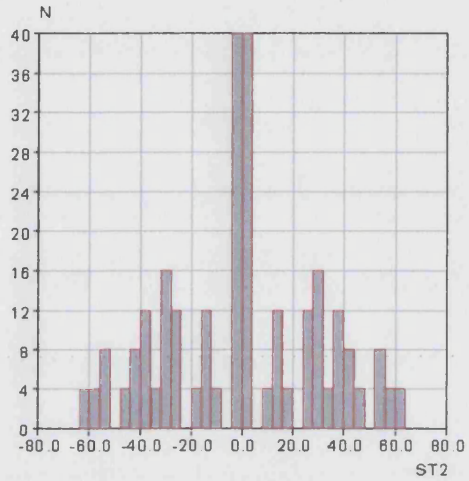

Figure 2.36 – *ST2 (°) plot for cyclobutane fragments reported to have formed from a solid state [2+2] cycloaddition reaction.*

It has been observed that the reaction pathways for organic, metal organic, inter- or intra-molecular reactant species do not exhibit any significant differences, despite the fact that fragments which may potentially follow an intra-molecular reaction pathway showed the expected evidence of a more predefined geometry. Once formed, the cyclobutane rings have similar geometrical parameters whether they are part of organic or metal organic species.

2.7 References

[2.1] Cohen, M.D., Schmidt, G.M.J. (1964) *J. Chem. Soc.*, 1996-2000.

[2.2] Cohen, M.D., Schmidt, G.M.J. (1964) *J. Chem. Soc.*, 2000-2013.

[2.3] Cohen, M.D., Schmidt, G.M.J. (1964) *J. Chem. Soc.*, 2014-2021.

[2.4] Auf de Heyde, T.P.E., Bürgi, H. (1989) *Inorg. Chem.*, **28,** 3960-3969.

[2.5] Bürgi, H., Dunitz, J.D. (1983) *Acc. Chem. Res.*, **16,** 153-161.

[2.6] Alvarez, S., Pinsky, M., Avnir, D. (2001) *Eur. J. Inorg. Chem.*, 1499-1503.

[2.7] Raithby, P.R., Shields, G.P., Allen, F.H., Motherwell, W.D.S. (2000) *Acta Cryst.*, **B56,** 444-454.

[2.8] Bürgi, H., Dunitz, J.D. (1983) *Acc. Chem. Res.*, **16,** 153-161.

[2.9] Shields, G.P. (1997) *Systematic Studies in Structural Chemistry,* Ph.D. thesis University of Cambridge.

[2.10] Clegg, W., *et. al.* (2003) *The 9th BCA/CCG Intensive Teaching School X-ray Structural Analysis.*

[2.11] Murray-Rust, P., Bürgi, H.-B., Dunitz, J.D. (1978) *Acta Cryst.*, **B34,** 1787-1793.

[2.12] Murray-Rust, P., Bürgi, H.-B., Dunitz, J.D. (1979) *Acta Cryst.*, **A35,** 703-713.

[2.13] Shields, G.P. (2003) *D_{2h} Permute Program,* Cambridge Crystallographic Data Centre, 12 Union Road, Cambridge. CB2 1EZ. UK.

[2.14] Allen, F.H. (2002) *Acta Cryst.*, **B58,** 380-388.

[2.15] Shields, G.P. (2003) *Largevista,* Cambridge Crystallographic Data Centre, 12 Union Road, Cambridge. CB2 1EZ. UK.

[2.16] Dunitz, J.D. (1979) *X-ray Analysis and the Structure of Organic Molecules,* Cornell University Press, Ithaca, USA, 423-424.

[2.17] Allen, F.H. (1984) *Acta Cryst.*, **B40,** 64-72.

Chapter 3

Solid State [2+2] Cycloaddition Reactions - An Experimental Investigation

3.1 Introduction

As discussed in Section 1.5.2.1, a number of compounds have emerged that do not fulfil Schmidt's topochemical criteria for a [2+2] cycloaddition reaction, but nonetheless undergo a solid state transformation. Conversely, many examples exist of compounds that do not react despite appearing highly suited to a cycloaddition on the basis of these same criteria. Solid state reactions afford the opportunity to control and predict a reaction product on the basis of the reactant structure. However, confident design of materials that will produce a targeted product using this solid state methodology is by no means routine, and a complete understanding of the factors that affect such reactions is required.

Thus, it is worth examining the molecular orbitals involved in [2+2] cycloaddition reactions in order to understand why the Woodward-Hoffmann rules specify that photochemical irradiation is required to induce such transformations [3.1]. Figure 3.1 shows the molecular orbital diagram corresponding to the carbon double bond of an alkene, from which it can be seen that the highest occupied molecular orbital (HOMO) is a bonding π orbital, while the lowest unoccupied molecular orbital (LUMO) is the antibonding π^*.

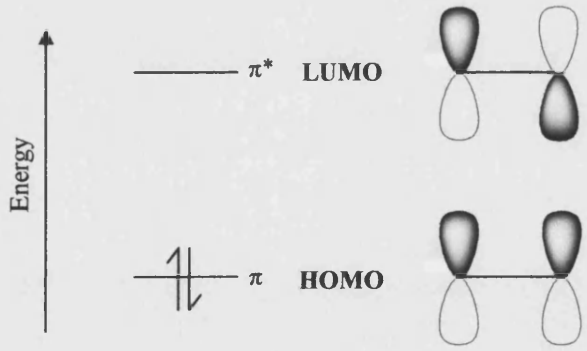

Figure 3.1 - *Illustration of the HOMO and LUMO for an alkene.*

In order to form a cyclobutane ring from two alkenes the orbital symmetry of the HOMO and LUMO must be the same. However, in the ground state this is not the case and only one bonding interaction is possible, see Figure 3.2(a). Photochemical excitation promotes an electron from the ground state HOMO into the ground state LUMO, producing

a photochemical HOMO with the same symmetry as the ground state LUMO. Thus two bonding interactions are possible leading to a cyclobutane ring, see Figure 3.2(b).

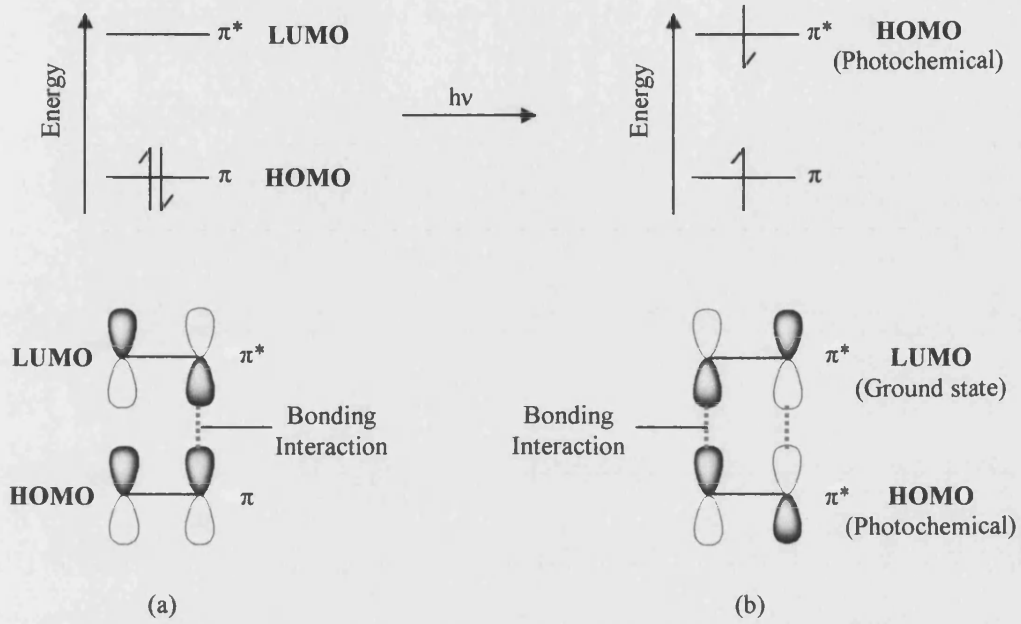

Figure 3.2 - *(top) Effect of UV irradiation on the electron distribution in the frontier molecular orbitals of two alkenes. (bottom) Illustration of the interactions between the HOMO and LUMO for two potentially reacting alkenes to form a cyclobutane ring, (a) ground state, (b) photochemically initiated.*

3.2 Experimental

3.2.1 Experimental Aims

The practical investigations detailed within this chapter constitute experimental studies examining [2+2] cycloaddition reactions. These investigations aim to provide further insight into the factors affecting such conversions, from both a theoretical (Chapter 2) and experimental perspective. Thus, analysis of the experimental work attempts to extend Schmidt's studies from the 1960s to try and obtain a greater appreciation of the factors affecting solid state [2+2] cycloaddition reactions. The investigative approach can be split into three stages:

1. *Irradiation of compounds to determine whether they undergo any structural change* - A series of compounds potentially suitable for undergoing solid state [2+2] cycloaddition reactions are identified from the Cambridge Structural Database (CSD) [3.2], and irradiated with a 150 W mercury lamp. Powder X-ray diffraction and infrared spectroscopy are used to detect any structural changes that occur.

2. *Obtaining a structure solution of irradiation products* - A combination of single crystal and powder X-ray diffraction techniques are employed in an effort to obtain a crystal structure from irradiated samples of any compound showing structural changes in Stage 1 above, with a view to determining whether a [2+2] cycloaddition reaction has occurred.

3. *Examination of transformation mechanisms* - Powder diffraction is employed to determine whether conversions identified in the second stage occur heterogeneously or homogeneously within crystalline samples. In theory, if a reaction occurs homogeneously the whole sample should be in the same structural state, whereas in a heterogeneous transformation there should be evidence of more than one of the following species at any one time: reactant, product or intermediate.

3.2.2 Selection of Compounds

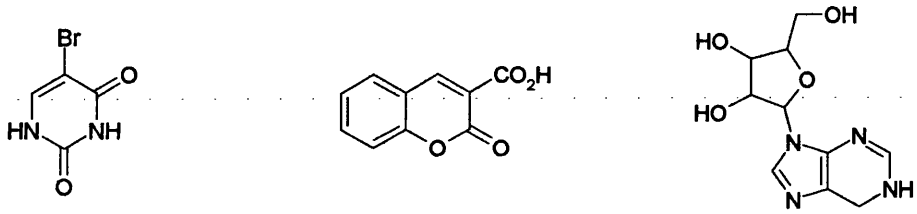

5-Bromouracil | Coumarin-3-carboxylic acid | Inosine

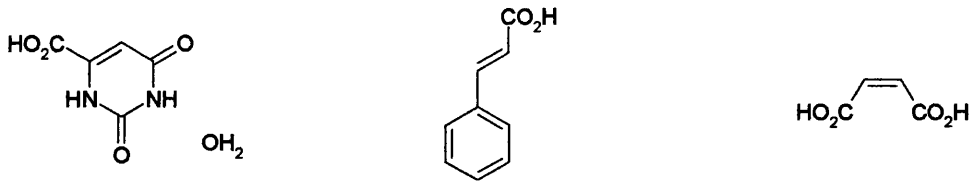

Orotic acid monohydrate | *Trans*-cinnamic acid | Maleic acid

Figure 3.3 - *The structures of the six compounds being studied [3.3][3.4][3.5][3.6][3.7][3.8].*

The CSD was used to identify five compounds for which solid state [2+2] cycloaddition reactions have not been reported, but that contain potentially reactive double bonds separated by less than 4.2 Å (Schmidt's proposed maximum for such conversions), see Figure 3.3. These were coumarin-3-carboxylic acid, inosine, 5-bromouracil, maleic acid and orotic acid monohydrate. In addition *trans*-cinnamic acid was selected to act as a reference since its single crystal to single crystal transformation to truxillic acid has previously been

reported [3.9]. The separation distances between the relevant carbon double bonds in the potential reactants are provided in Table 3.1.

Table 3.1 - *Separation distances for the potentially reacting carbon double bonds in the selected compounds.*

Compound	C---C separation distances for the nearest carbons in potentially reacting double bonds (Å).
Coumarin-3-carboxylic acid [3.3]	3.690, 3.690
Inosine [3.4]	3.585, 3.619
5-Bromouracil [3.5]	3.947, 3.947
Maleic acid [3.6]	3.808, 3.808
Orotic acid monohydrate [3.7]	3.792, 3.792
Trans-cinnamic acid [3.8]	3.590, 3.590

3.2.3 Source of Compounds for Irradiation

Coumarin-3-carboxylic acid, *trans*-cinnamic acid, inosine, 5-bromouracil, maleic acid and orotic acid monohydrate were all purchased from Aldrich. The powder X-ray diffraction patterns, from ground samples of each compound as supplied, were the same as the corresponding traces simulated from the single crystal structures with no evidence of impurities. Hence, the samples were used without further purification.

Single crystals of coumarin-3-carboxylic acid were obtained by recrystallisation from Dichloromethane (DCM).

3.2.4 Irradiation of Compounds

For the powder diffraction experiments each compound was well ground using a pestle and mortar. The inside surface of a glass container was then thinly covered with the ground material and irradiated with a 150 W mercury lamp. Samples were taken at certain time intervals during the irradiation and used to fill capillaries from which measurements were made.

For the single crystal experiment, a data collection was effected from an unirradiated crystal of coumarin-3-carboxylic acid and the same crystal was then irradiated with a 150 W mercury lamp for 3 weeks while held under a cryostream set at 150 K before a second data collection was carried out. The heating effect of the mercury lamp was approximately 12 °C at 10 cm, so the temperature at the crystal may have been slightly above 150 K.

3.2.5 Powder X-ray Diffraction

3.2.5.1 Experimental set-up

Powder diffraction data were acquired on a Bruker AXS D8 ADVANCE powder diffractometer fitted with Göebel mirrors in transmission geometry, with the generator set at 40 kV, 40 mA using copper radiation. All samples were ground using a pestle and mortar and loaded into capillaries with a diameter of either 0.5 mm or 0.7 mm. Two types of data collection were made:

- *Short runs to determine whether irradiation causes a change in the sample.* Data were collected in a single run using a locked coupled scan mode over the 2-theta range 4-50°, with a step size of 0.02° per second. An exit slit of 2 mm was employed at the Göebel mirrors, along with a detector slit of 0.2 mm and an antiscatter slit of 1°.

- *Long runs suitable for Rietveld refinement.* Data were collected in a locked coupled scan mode with a step size of 0.01° and a step time of 4 seconds. Four runs were collected with 2-theta ranges of 4-70°, 20-70°, 40-70° and 60-70°. The purpose of this approach was to reduce the uncertainty in the weaker high angle information by merging the data using Powder4 [3.10]. At the Göebel mirrors a 2 mm exit slit was used, with a 0.2 mm detector slit and a 1° antiscatter slit.

3.2.5.2 Software

Indexation was carried out using CRYSFIRE [3.11] (Section 1.3.2.4). Structure solution was carried out in DASH [3.12] with subsequent Rietveld refinement carried out in GSAS [3.13]. The errors output by GSAS are grossly underestimated due to the refinement process being more basic than that used for single crystal refinements, which employ a full correlation covariance matrix. In view of this, errors are not quoted on bond lengths or angles as they are not meaningful.

3.2.6 Single Crystal X-ray Diffraction

3.2.6.1 Data Collection

Single crystal X-ray diffraction data were collected at 150 K on a Nonius Kappa CCD four-circle diffractometer fitted with an area detector and cryostream. A summary of the experimental details for each of the structures discussed in this chapter are included in Table 3.8 at the end of this chapter, with bond lengths and angles listed in Appendix 3.1.

3.2.6.2 Software

Structure solutions were carried out using SHELXS-86 [3.14], with subsequent refinements in SHELXL-97 [3.15]. Diagrams were created using ORTEP3 for Windows [3.16], POV-RAY [3.17] or MERCURY [3.18] and WINGX publication routines [3.19] were employed to produce the tables from the crystallographic CIF files.

3.2.7 Infrared (IR) Spectroscopy

Infrared data were collected on a Nicolet Nexus FT-IR spectrometer, using 32 scans at 2 cm^{-1} resolution over the range 4000-500 cm^{-1}. The spectra were collected as Nujol mulls and all major peaks were consistent with the reported structures for coumarin-3-carboxylic acid, inosine, 5-bromouracil, maleic acid and orotic acid monohydrate. A comparison of the spectra for coumarin-3-carboxylic acid and its irradiation product showed them to be similar although not identical. The signal at 3056 cm^{-1} assigned to the O-H stretching frequency of the carboxylate group in coumarin-3-carboxylic acid, disappeared upon irradiation and a new peak at 3175 cm^{-1} appeared that could be assigned to the carboxylate group in the photoproduct.

3.2.8 Nuclear Magnetic Resonance (NMR) Spectroscopy

NMR data was collected on a Bruker AV300 spectrometer. The spectrum obtained from coumarin-3-carboxylic acid in $CDCl_3$ was consistent with the reported structure with no evidence of impurities. It was not possible to obtain an NMR spectrum for the irradiation product of coumarin-3-carboxylic acid which was insoluble, however, the spectrum obtained after irradiation showed no evidence of remaining reactant or soluble amorphous side products.

3.3 Results for Compounds Identified as Potential Candidates for Solid State [2+2] Cycloaddition Reactions

All six compounds, 5-bromouracil, coumarin-3-carboxylic acid, inosine, orotic acid monohydrate, *trans*-cinnamic acid and maleic acid, illustrated in Figure 3.3, were irradiated for 3 days in the manner described in Section 3.2.4. Under these conditions *trans*-cinnamic acid is known to begin transforming to truxillic acid although the complete conversion takes 15 days [3.20]. As previously stated, this compound was included as a reference to confirm that the irradiation was appropriate for inducing the desired reaction. Of the remaining five compounds only coumarin-3-carboxylic acid showed any change in its powder diffraction patterns or IR spectra after a 3 day period, see Figure 3.4.

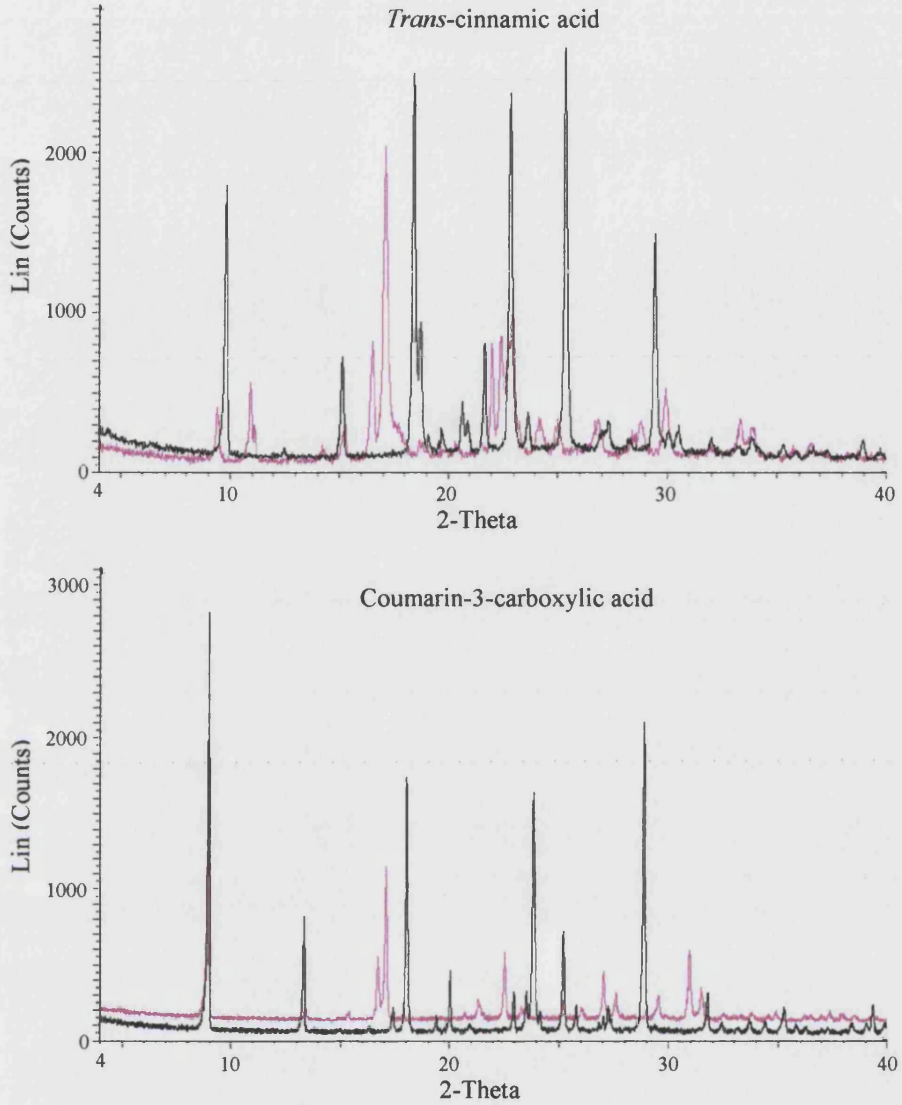

Figure 3.4 – *Comparison of the powder patterns obtained (black) before and (purple) after 3 days irradiation with a mercury lamp, (top) trans-cinnamic acid, (bottom) coumarin-3-carboxylic acid.*

Comparison of the powder diffraction patterns obtained from a sample of *trans*-cinnamic acid before and after irradiation confirmed that the method of irradiation was suitable to induce a transformation.

Examination of the powder diffraction pattern obtained from an irradiated sample of coumarin-3-carboxylic acid, reveals that the product appears to be crystalline and gives clear sharp peaks. Consequently, a combined single crystal and powder X-ray diffraction experiment was undertaken to determine the structure of the irradiation product of coumarin-3-carboxlic acid, for which, single crystals could not be obtained by recrystallisation as the irradiation product was found to be insoluble in the solvents that were tried.

3.4 Coumarin-3-carboxylic acid ($C_{10}H_6O_4$)

3.4.1 Single Crystal Structure of Coumarin-3-Carboxylic Acid (k03has1)

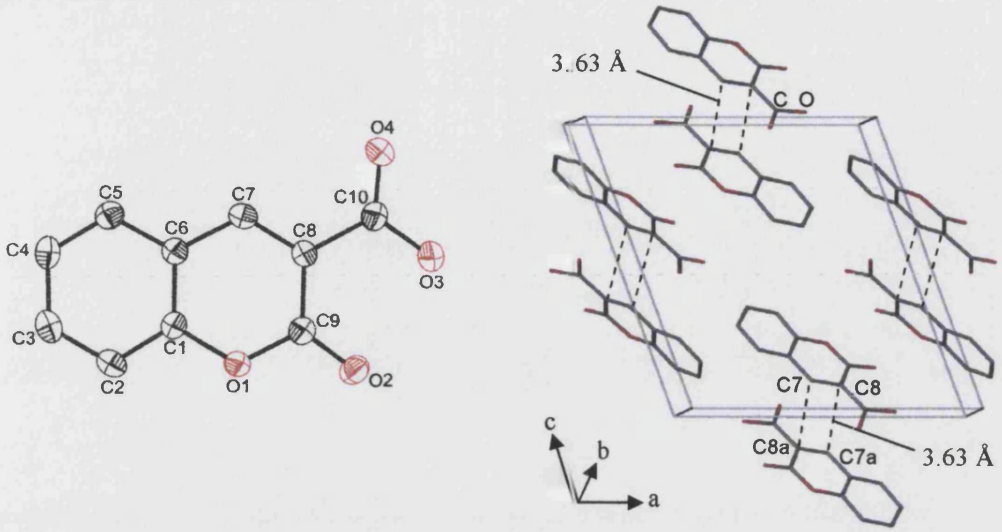

Figure 3.5 - *(left) Coumarin-3-carboxylic acid, ellipsoids plotted at 50% level, (right) Packing diagram for coumarin-3-carboxylic acid with the closest C_7---C_{8a} and C_8---C_{7a} distances highlighted (where the subscript 'a' indicates a symmetry related molecule).*

Figure 3.5 shows the crystal structure of coumarin-3-carboxylic acid ($C_{10}H_6O_4$), which crystallizes in the monoclinic space group $P2_1/n$ with one molecule in the asymmetric unit. The structure solution obtained here was consistent with that previously reported for the compound [3.3].

Each molecule of coumarin-3-carboxylic acid is approximately planar, with the atoms C_1 to C_9 and O_1 to O_2 deviating by less than +/-0.10(1) Å from the least-squares plane of the aromatic ring (C_1 to C_6), and torsion angles involving the carboxylic acid functionality and the rest of the molecule of +4.3(3)° (C_7-C_8-C_{10}-O_4) and +3.3(3)° (C_9-C_8-C_{10}-O_3). The C_7-C_8 distance of 1.348(3) Å corresponds to a C=C bond, which is 3.632(3) Å (C_7---C_{8a} and C_8---C_{7a}) from the closest equivalent double bond in another molecule. Given the evidence of structural change in the powder diffraction experiment and that this separation is below the 4.2 Å limit, it was thought probable that this compound might undergo the photochemically induced solid state [2+2] cycloaddition reaction illustrated in Figure 3.6. The subscript '*a*' will be used throughout to represent atoms related to those in the asymmetric unit by the symmetry operator (1-x, -y, -z).

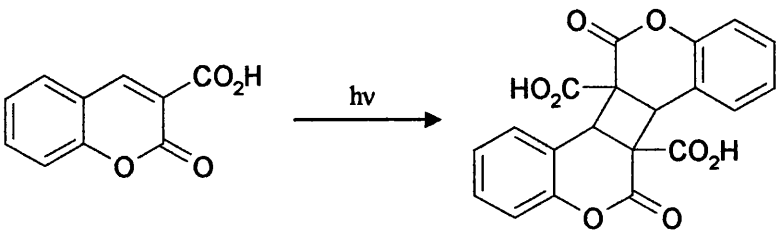

Figure 3.6 - *Proposed [2+2] cycloaddition reaction for coumarin-3-carboxylic acid under a mercury lamp.*

3.4.2 Powder Diffraction Studies on the Irradiation Product of Coumarin-3-Carboxylic Acid

A structure solution was attempted using a powder diffraction pattern obtained from an irradiated sample of coumarin-3-carboxylic acid. It is far more complicated to obtain a crystal structure from powder as opposed to single crystal data, since the former experiment provides 1-dimensional data while the latter affords 3-dimensional data. Hence, each stage of the solution is described below with further details in Sections 1.3.2.4 to 1.3.2.8.2:

3.4.2.1 Indexation for the Irradiation Product of Coumarin-3-Carboxylic Acid

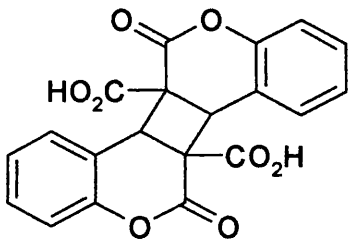

Figure 3.7 - *Expected product from the irradiation of coumarin-3-carboxylic acid in the solid state.*

The position of the first 20 peaks were identified in DASH and input into CRYSFIRE, a suite of 7 indexation programs for powder diffraction data. As discussed in Section 1.3.2.4, the peak overlap often makes it difficult to index low symmetry molecules, and, as a result it is usual to place limits on the cell parameters to give the software additional information on where a solution might be expected. The proposed product molecule ($C_{20}H_{12}O_8$) is illustrated in Figure 3.7, and contains 28 non hydrogen atoms. Working on the assumption that the volume of a non hydrogen atom is 18 $Å^3$, and that the unit cell contains a maximum of four asymmetric units consisting of no more than one product molecule each, it seems reasonable to expect the unit cell volume to be less than 2016 $Å^3$. Consequently, coupled with the compact nature of the expected product, long cell

axes would be unlikely. The information and limits used to index the pattern are provided in Table 3.2.

Table 3.2 - *Limits used to try and obtain an indexation from the powder pattern obtained from an irradiated sample of coumarin-3-carboxylic acid.*

Parameter	Limit
Wavelength	Cu 1.5406 Å
Volume	0-2000 Å
Maximum cell axes lengths (a,b,c)	15 Å
Range for $\beta°$	90-125°
Peak position error	0.03
Systems searched	All except Triclinic

The top rated 9 indexations were essentially in agreement with each other, giving the unit cell parameters provided in Table 3.3, with figures of merit ranging from 30.6 to 32.79. It has been frequently noted that a good indication of having found the correct unit cell is concurrent with many of the highest ranked solutions being the same, although this is not absolute in itself.

Table 3.3 - *Indexation obtained for the powder diffraction pattern from an irradiated sample of coumarin-3-carboxylic acid.*

Parameter	Value	Parameter	Value
a	12.501(3) Å	α	90.00°
b	5.976(3) Å	β	112.88(3)°
c	11.397(3) Å	γ	90.00°
Volume	784.4 Å^3		

3.4.2.2 Space Group Determination and Pawley Refinement for the Irradiation Product of Coumarin-3-Carboxylic Acid

EXTINCTION SYMBOL [3.21], is a computer program that compares the observed and predicted peak positions for each space group in order to identify candidates with the best fit to the data. In this case the software indicated that the most probable space group was $P2_1/n$, the same as found for coumarin-3-carboxylic acid. This seems reasonable as

many reported single crystal to single crystal transformations occur topochemically with the space group symmetry of the reactant lattice being maintained.

Eight peaks that appeared to be single were selected from the diffraction pattern and subjected to a Pawley refinement (Section 1.3.2.6), giving a profile χ^2 of 1.28.

3.4.2.3 Model Construction for the Irradiation Product of Coumarin-3-Carboxylic Acid

Structure solution within *Dash* is based on simulated annealing, a direct space approach (Section 1.3.2.7.2). Thus rather than determining the position of the atoms with respect to each other, it requires the user to input a model of the expected product which it tries to locate within the unit cell. In order to increase the chances of a successful structure solution, it is necessary to create as accurate a model as possible by combining information about the anticipated product with geometric parameters for similar fragments.

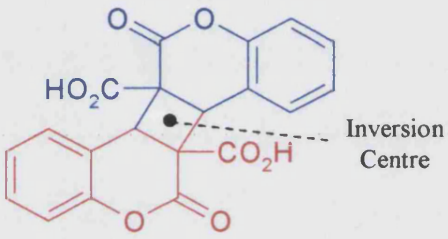

Figure 3.8 - *Illustration of the inversion symmetry relationship between two asymmetric units in the predicted product from the irradiation of coumarin-3-carboxylic acid. One asymmetric unit is red, while the other is blue.*

Examination of the cell volume (784.40 Å^3) suggests that the unit cell is most likely to contain two product molecules. Given that the monoclinic space group ($P2_1/n$) has four equivalent positions the asymmetric unit will consist of half a product molecule (*i.e.* $C_{10}H_6O_4$), which would, by necessity be located proximate to a crystallographic inversion centre that serves to generate the remainder of the molecule, see Figure 3.8.

Two alternative approaches were used to try and construct a suitable model of the asymmetric unit using an MM2 energy minimization within CHEMDRAW3D [3.22], the validity of each in terms of their geometric parameters was confirmed by comparison with similar fragments in the CSD:

1. Firstly, a model of the complete product was generated in CHEMDRAW3D. It was noted that the cyclobutane ring was puckered, and, as such it would be unlikely to have formed during a solid state [2+2] cycloaddition reaction of coumarin-3-carboxylic acid, where the potentially reacting double bonds are in the same plane. In order to obtain the contents of the asymmetric unit without altering any of the bond lengths or angles the symmetry related section of the product molecule was deleted in ACD CHEMSKETCH [3.23]. Structure solution attempts using this model were unsuccessful, probably as a result of the molecular geometry imposed by the presence of a puckered cyclobutane ring in the complete product molecule.

2. Secondly, in order to try to overcome the problems of imposed molecular geometry detailed for the first model above, a model of coumarin-3-carboxylic acid was generated and the alkene bond (as highlighted in Figure 3.9) deleted in ACD CHEMSKETCH. The purpose of this approach was to allow the distance between the carbon atoms, formally of the double bond, to vary freely which would hopefully leave the remainder of the molecule free to adopt its preferred configuration.

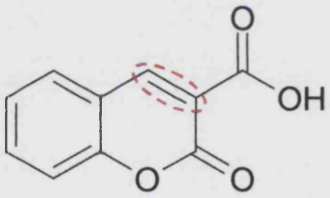

Figure 3.9 - *Diagram indicating the alkene bond that was removed from a model of coumarin-3-carboxylic acid during structure solution of its irradiation product.*

3.4.2.4 Structure Solution for the Irradiation Product of Coumarin-3-Carboxylic Acid

Structure solution attempts relate solely to trials with the second model detailed above. The initial temperature and rate of cooling were not specified, and no restraints were placed upon the four torsion angles (Figure 3.10) determined as 'variable' by DASH. Ten simulated annealing runs of 1×10^7 moves were carried out with 5500 moves at each temperature. The target profile chi-squared multiplier was set to 1.0, *i.e.* the aim of the structure solution was to achieve a final profile χ^2 value that matched the Pawley χ^2 of 1.28 (Section 3.4.2.2).

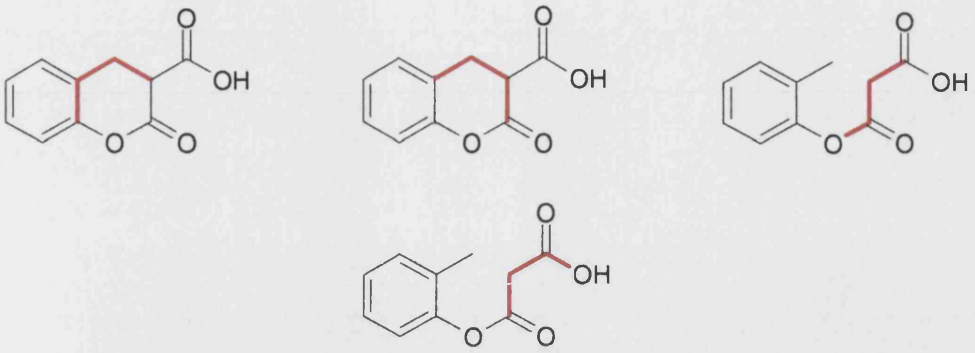

Figure 3.10 - *Illustration of the four torsion angles (highlighted in red) that were free to vary during the simulated annealing runs.*

The solutions obtained from the 10 runs were very similar as reflected in the final profile χ^2 values which ranged from 2.27 to 2.32. Despite the unconstrained nature of the model, only insignificant differences were observed in the final atomic positions when the structure solutions were overlaid, see Figure 3.11. All of these solutions indicated that the irradiation of coumarin-3-carboxylic acid had formed the predicted [2+2] cycloaddition product.

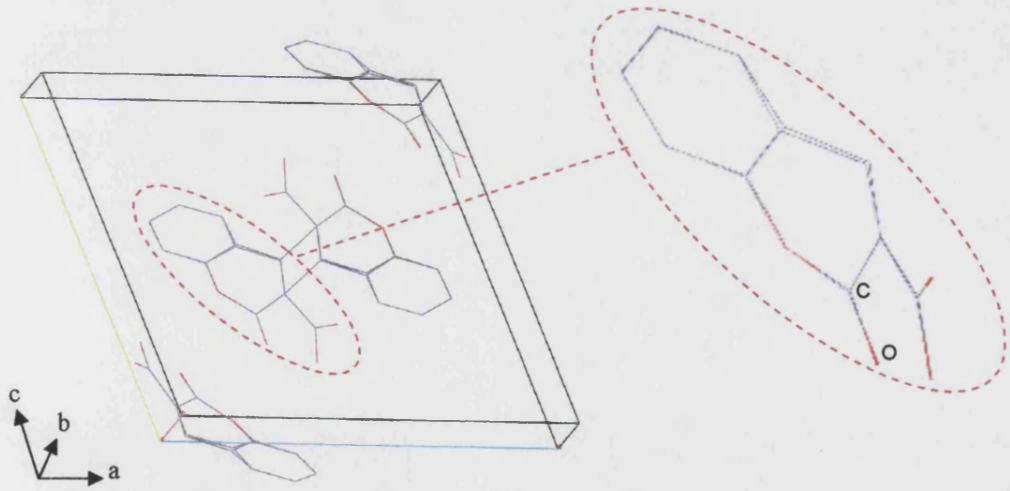

Figure 3.11 - *Overlay of unit cell contents for the 10 solution runs for the structure of the irradiation product arising from coumarin-3-carboxylic acid, (insert) asymmetric unit.*

3.4.2.5 Rietveld Refinement for the Irradiation Product of Coumarin-3-Carboxylic Acid

The final stage in structure determination from powder data is employment of Rietveld refinement to optimize the atomic positions and unit cell parameters. This was completed using *GSAS*. The peak shape parameters and all of the atomic positions were refined with the geometric parameters restrained to their mean values, as identified from

similar fragments in the CSD, +/- 0.02 Å (bond lengths) or +/-3° (angles). The individual temperature factors for the non hydrogen atoms were not refined as the data were not considered to be of sufficient quality due to a fall off in diffraction intensity at high angle. The Rietveld refinement fit was good, although the final R_{wp} and R_{exp} values were 9.00% and 7.91% respectively. These values are slightly higher than would ideally be desired, and this was attributed to the fall off in diffraction intensity, see Figure 3.12.

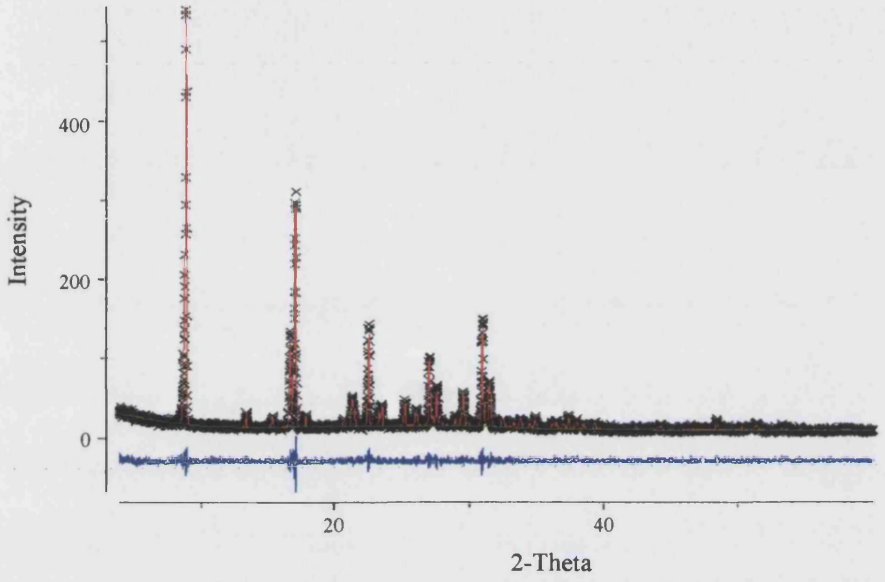

Figure 3.12 - *Rietveld refinement plot for the structural model of the irradiation product from coumarin-3-carboxylic acid. R_{wp} 9.00%, R_{exp} 7.91%. (black) observed, (red) calculated, (green) background, (blue) difference between observed and calculated.*

3.4.2.6 Refined Powder Diffraction Structure of the Irradiation Product of Coumarin-3-Carboxylic Acid

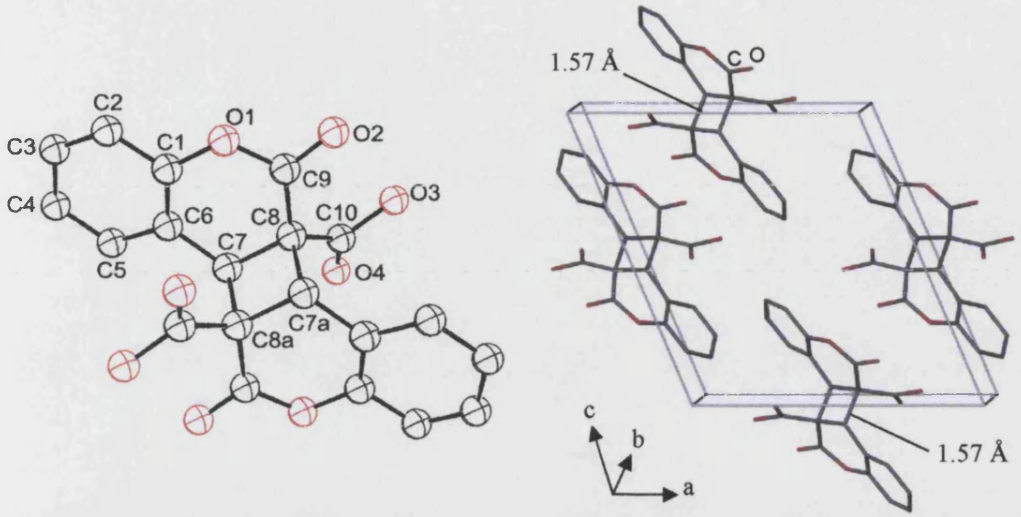

Figure 3.13 - *Structure solution of the irradiation product of coumarin-3-carboxylic acid from powder X-ray diffraction data, (left) irradiation product, (right) packing diagram for irradiation product.*

The structure solution obtained from powder X-ray diffraction data of an irradiated sample of coumarin-3-carboxylic acid is illustrated in Figure 3.13, where the *a* and *c* axis have been transformed along with the symmetry operators and fractional coordinates to ensure consistency of the axes throughout this chapter. It shows that the compound has undergone a solid state [2+2] cycloaddition reaction forming the product proposed in Figure 3.6. The monoclinic $P2_1/n$ symmetry of the reactant lattice is maintained in the product lattice, with the asymmetric unit corresponding to half of the product molecule.

While the aromatic ring (C_1 to C_6) is still planar, the remainder of the molecule is not. The carboxylic acid group has bent away from the additional $C_{10}H_6O_4$ unit with a C_7-C_8-C_{10}-O_4 torsion angle of +15.5°, and a C_9-C_8-C_{10}-O_3 torsion angle of -32.1°. The C_7-C_8 bond length is 1.540 Å, indicating that the bond is single, while the C_7-C_{8a} and C_8-C_{7a} distances of 1.567 Å also correspond to C-C single bonds.

3.5 Single Crystal Structure of the Irradiation Product from Coumarin-3-Carboxylic Acid

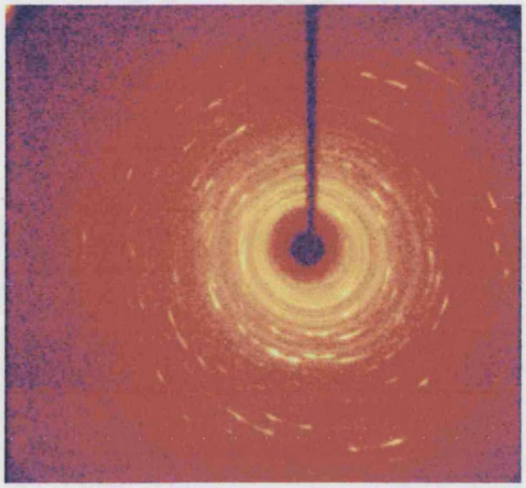

Figure 3.14 - *One frame of data from the 'single' crystal irradiation product of coumarin-3-carboxylic acid (h03has1).*

As stated previously, in Section 3.2.4, having obtained a single crystal structure of coumarin-3-carboxylic acid, the same crystal was irradiated for 3 weeks while maintaining the temperature at 150 K using a cryostream. The integrity of the single crystal had decreased significantly during the irradiation, and the fact that a structure solution was obtained from the poor quality X-ray diffraction data (see Figure 3.14) is a testament to the capabilities of modern diffractometers. It also indicates why the use of powder diffraction to study such transformation is advantageous, since the crystalline quality of the material can be much lower than that desirable for a single crystal data collection.

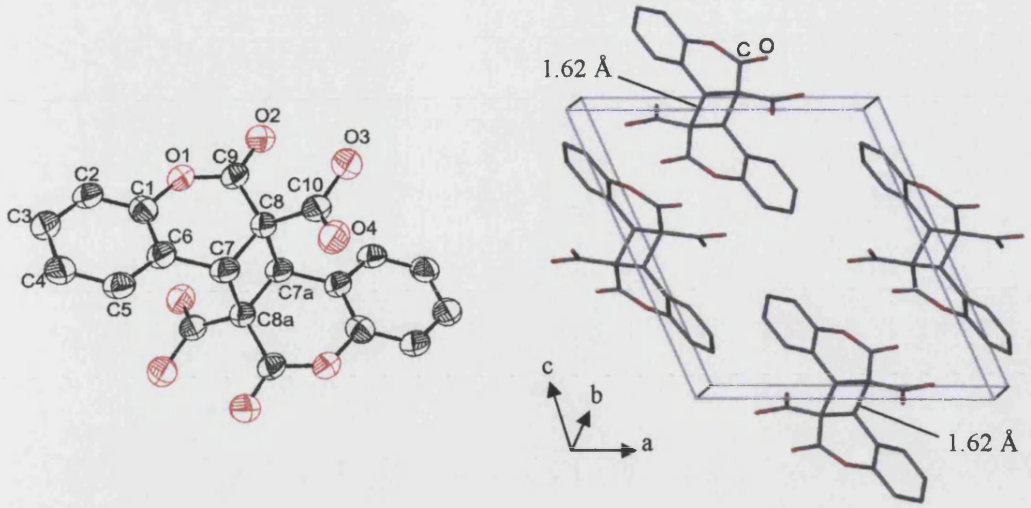

Figure 3.15 – *(left) Coumarin-3-carboxylic acid product after irradiation, ellipsoids plotted at 50% level. (right) Packing diagram for product with C_7-C_{8a} and C_8-C_{7a} distance highlighted.*

The single crystal structure, for the irradiation product of coumarin-3-carboxylic acid, solved in the monoclinic space group $P2_1/n$, with half a dimer molecule in the asymmetric unit, see Figure 3.15.

It is clear that the molecule is no longer approximately planar, with the atoms (C_7-C_9, O_1-O_2) deviating by up to 0.77(1) Å from a least squares plane calculated through the aromatic ring (C_1 to C_6), and torsion angles involving the carboxylic acid functionality and the rest of the molecule of +14.3(6)° (C_7-C_8-C_{10}-O_4) and -32.8(6)° (C_9-C_8-C_{10}-O_3). The distances around the newly formed cyclobutane ring of 1.543(7) Å (C_7-C_8 and C_{7a}-C_{8a}) and 1.617(7) Å (C_7-C_{8a} and C_8-C_{7a}) correspond to carbon single bonds. The bond lengths and angles throughout the structure were consistent with similar fragments in the CSD.

3.6 Comparison of Powder and Single Crystal Solutions for the Irradiation Product of Coumarin-3-Carboxylic Acid

The loss of information that results from the compression of a 3-dimensional single crystal dataset into a 2-dimensional powder diffraction pattern, generally means that structure solutions obtained from powders are less accurate than those from single crystals. However, in this case the integrity of the single crystal had reduced upon irradiation, hence, the validity of the structure solutions from the two techniques was established by comparison.

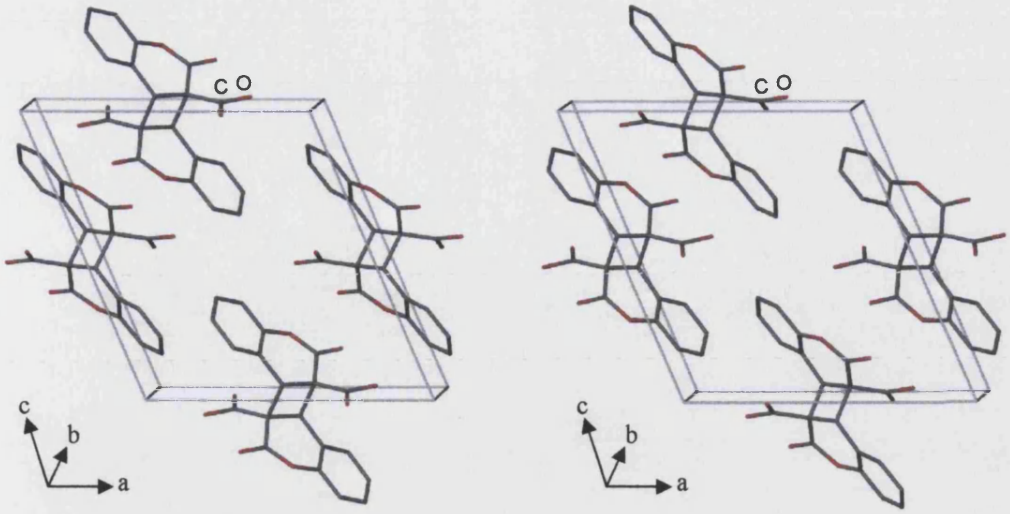

Figure 3.16 - *Comparison of packing diagrams for the irradiation product of coumarin-3-carboxylic acid, (left) single crystal, (right) powder.*

Table 3.4 - *Comparison of unit cell data for single crystal and powder structure solutions for the irradiation product of coumarin-3-carboxylic acid.*

Solution	*a* (Å)	*b* (Å)	*c* (Å)	α (°)	β (°)	γ (°)	V (Å^3)
Single Crystal (150 K)	11.348 (5)	5.881 (5)	12.376 (5)	90.00	113.236 (5)	90.00	758.9 (8)
Powder (298 K)	11.395 (1)	5.970 (1)	12.493 (1)	90.00	112.859 (2)	90.00	783.1 (1)

An initial examination of the two structures showed that they appeared very similar from a global perspective both in terms of their packing (Figure 3.16) and their unit cell parameters, see Table 3.4. The close agreement was further confirmed by a comparison of the atomic positions, illustrated in Figure 3.17 and selected geometric parameters in the vicinity of the newly formed cyclobutane ring, provided in Table 3.5. Although, the match is not perfect it is very good and certainly within experimental error.

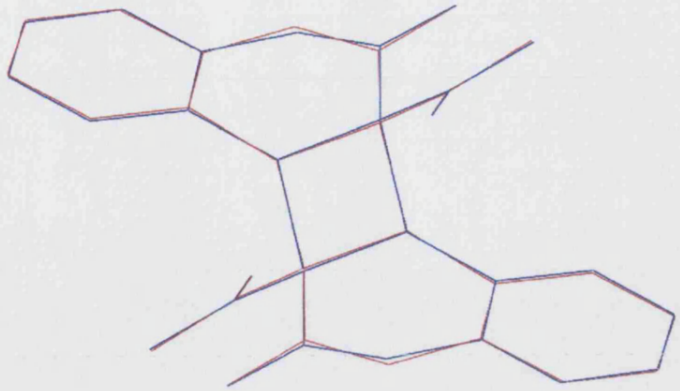

Figure 3.17 - *Overlay of the structure solutions for the irradiation product of coumarin-3-carboxylic acid, (red) powder, (blue) single crystal.*

Table 3.5 - *Comparison of selected parameters for the irradiation product of coumarin-3-carboxylic acid.*

Parameter	Single Crystal	Powder Diffraction
C_7-C_8 and C_{7a}-C_{8a}	1.543(7) Å	1.540 Å
C_7-C_{8a} and C_8-C_{7a}	1.617(7) Å	1.567 Å
C_7-C_8-C_{10}-O_4	+14.3(6)°	+15.5°
C_9-C_8-C_{10}-O_3	-32.8(6)°	-32.1°

While obtaining a single crystal by recrystallising a sample of the irradiation product would clearly have been favourable, it was not possible due to insolubility. However, this study has clearly demonstrated that powder diffraction is a valuable and viable alternative to single crystal X-ray diffraction in such cases.

3.7 Comparison of the Unirradiated and Irradiated Structures of Coumrain-3-Carboxylic Acid

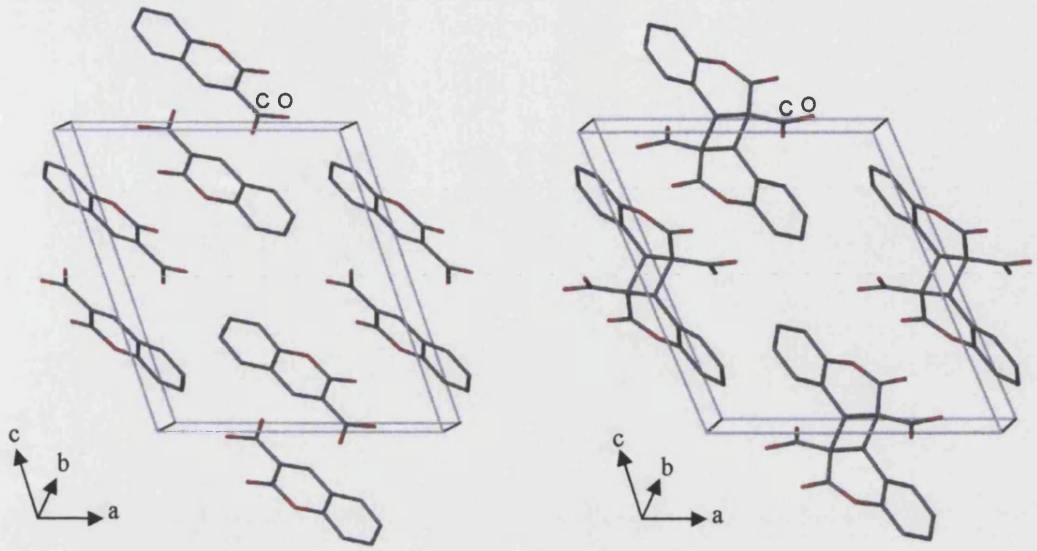

Figure 3.18 - *Comparison of structures (left) unirradiated sample of coumarin-3-carboxylic acid, (right) irradiated sample of coumarin-3-carboxylic acid.*

Upon irradiation in the solid state coumarin-3-carboxylic acid undergoes a dimerisation, as illustrated in Figure 3.18. While the monoclinic $P2_1/n$ symmetry of the reactant lattice is maintained in the product, the unit cell parameters do alter to accommodate the atomic positions in the new dimer molecule. As one might expect from the initial orientation of the coumarin-3-carboxylic acid molecule, this change is most apparent in the *b*- and *c*-axes lengths which decrease as the dimerisation occurs with a concomitant alteration of the β angle, see Table 3.6.

Table 3.6 - *Comparison of unit cell data for single crystal structure solutions of unirradiated and irradiated samples of coumarin-3-carboxylic acid.*

Solution	*a* (Å)	*b* (Å)	*c* (Å)	α (°)	β (°)	γ (°)	V (Å^3)
Unirradiated (150K)	11.2410 (7)	5.4821 (4)	13.7463 (12)	90.00	107.11 (1)	90.00	809.6 (1)
Irradiated (150K)	11.348 (5)	5.881 (5)	12.376 (5)	90.00	113.236 (5)	90.00	758.9 (8)

The most noticeable structural change that occurs in coumarin-3-carboxylic acid upon irradiation is in the position of the carboxylic acid group which shifts away from the second $C_{10}H_6O_4$ fragment. The C_7-C_8 and C_{7a}-C_{8a} bonds increase from double bond lengths

to those of C-C single bonds, and the separation of the two closest double bonds (C_7-C_{8a} and C_8-C_{7a}) decrease from non-bonding distances to those of a carbon single bond, see Table 3.7.

Table 3.7 - *Comparison of selected parameters from single crystal structure solutions of unirradiated and irradiated samples of coumarin-3-carboxylic acid.*

Parameter	Unirradiated	Irradiated
C_7-C_8 and C_{7a}-C_{8a}	1.348(3) Å	1.543(7) Å
C_7-C_{8a} and C_8-C_{7a}	3.632(3) Å	1.617(7) Å
C_7-C_8-C_{10}-O_4	+4.3(3)°	+14.3(6)°
C_9-C_8-C_{10}-O_3	+3.3(3)°	-32.8(6)°

3.8 Discussion on the Solid State Reactivity of the Six [2+2] Cycloaddition Candidate Compounds Studied

All of the potentially reactive double bonds in the six compounds are separated by less than the 4.2 Å deemed significant by Schmidt [3.24], who also identified as important that potentially reacting alkene bonds should be parallel to each other. This is not the case for inosine, but a study of relevant structures in the CSD reported to have formed as a result of solid state photochemical [2+2] cycloadditions illustrates that this does not always have to be true, see Section 2.6. However, examination of the six [2+2] cycloaddition candidate structures suggests that hydrogen bonding may be responsible for the inertness observed in 5-bromouracil, inosine, orotic acid monohydrate and maleic acid, see Figure 3.19.

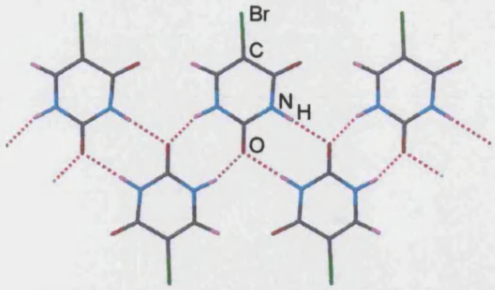

5-Bromouracil

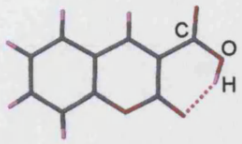

Coumarin-3-carboxylic acid

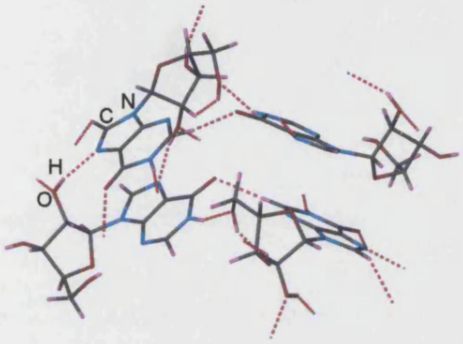

Inosine

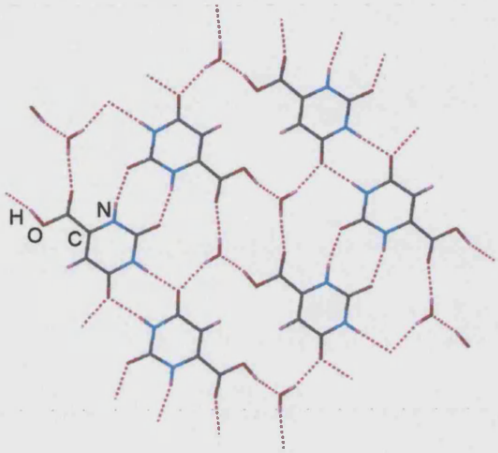

Orotic acid monohydrate

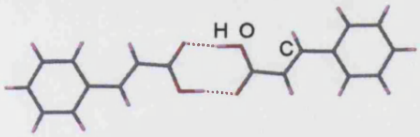

Trans-cinnamic acid

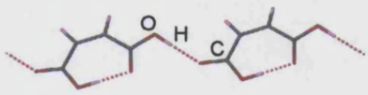

Maleic acid

Figure 3.19 - *Illustration of hydrogen bonding (shown by dashed lines) in the six compounds studied. [3.3][3.4][3.5][3.6][3.7][3.8].*

Two of the compounds, 5-bromouracil and maleic acid, form hydrogen bonded chains, while orotic acid monohydrate forms a hydrogen bonded sheet and inosine forms a 3-dimensional hydrogen bonded network. In order for these species to react these interactions would have to be broken, which is energetically unfavourable. In *trans*-cinnamic acid there is intermolecular hydrogen bonding between two adjacent molecules, while coumarin-3-carboxylic acid only exhibits one intramolecular hydrogen bond and both of these interactions are maintained in the respective irradiation products, see Figure 3.20. In fact truxillic acid, the irradiation product of *trans*-cinnamic acid, contains hydrogen bonded chains as a result of dimerisation of the reactant molecules.

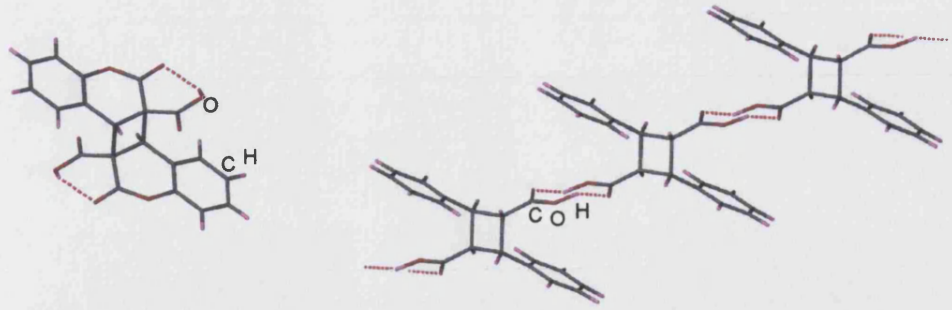

Figure 3.20 - *Illustration of the hydrogen bonding in the irradiation products of: (left) coumarin-3-carboxylic acid, (right) trans-cinnamic acid [3.9].*

Use of the CSD to examine the reactant structures of a series of compounds reported to have arisen from solid state [2+2] cycloaddition reactions (Section 2.6) supported the theory that the presence of strong hydrogen bonding can affect whether or not a reaction occurs. It was found that 11 out of 14 examples showed little or no hydrogen bonding in either the reactant or product structures, hence paralleling with coumarin-3-carboxylic acid and *trans*-cinnamic acid. Moreover, it was noted that in the 3 examples where extensive hydrogen bonding was present in the reactant crystal structure it was maintained in the irradiation product. Consequently, the existence of hydrogen bonding in the reactant lattice cannot be ignored when selecting candidates for solid state [2+2] cycloaddition reactions.

3.9 Monitoring [2+2] Cycloaddition Reactions using Powder X-ray Diffraction

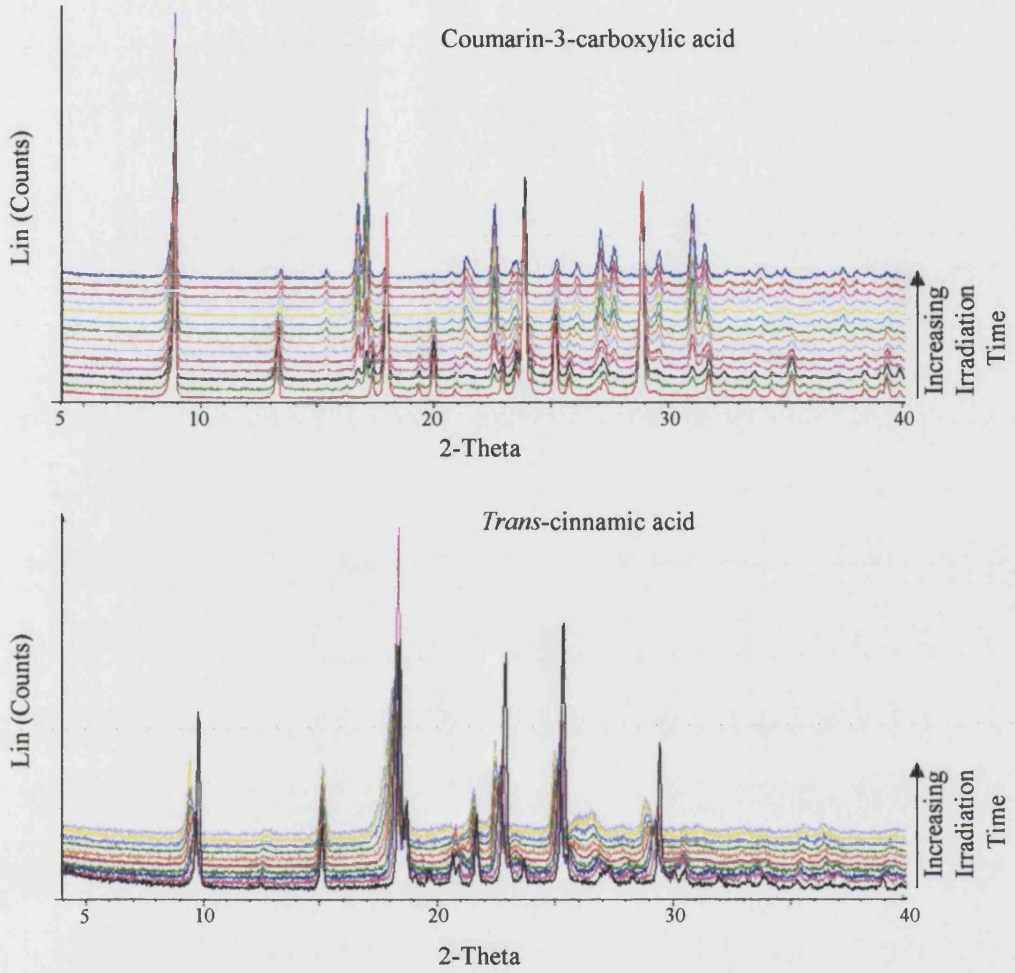

Figure 3.21 - *Powder diffraction patterns taken after samples had been irradiated for increasing lengths of time, (top) coumarin-3-carboxylic acid, (bottom) trans cinnamic acid.*

Figure 3.21 shows that the powder diffraction patterns recorded from samples of coumarin-3-carboxylic acid and *trans*-cinnamic acid alter as the irradiation time increases over the course of a day. The purpose of these investigations was to establish whether the conversions occurred in a homogeneous or heterogeneous fashion. In this context, it is necessary to examine in more detail a small section of each pattern to determine how the change occurs, see Figure 3.22.

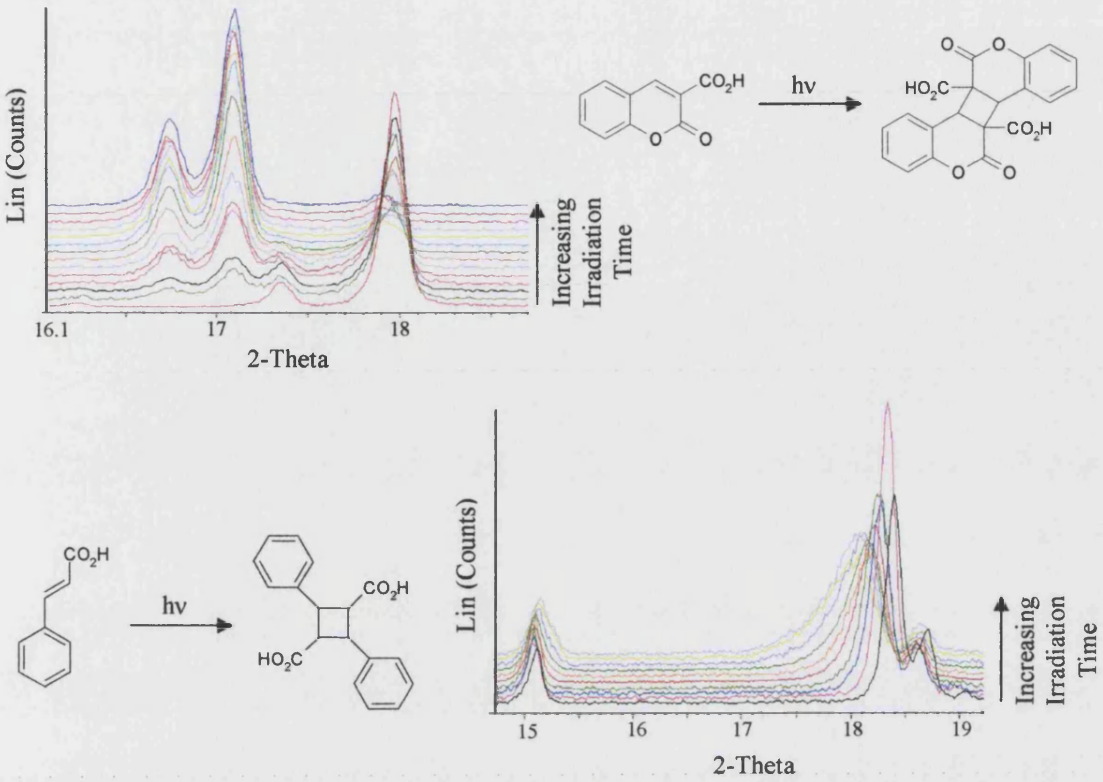

Figure 3.22 - *Small section of powder diffraction patterns taken every 2 hours from samples being irradiated with the relevant transformation indicated at the side (top) coumarin-3-carboxylic acid, (bottom) trans cinnamic acid.*

In between the patterns obtained at the beginning and end of the transformation of coumarin-3-carboxylic acid, the powder diffraction traces contained peaks corresponding to both the reactant and product, but nothing else. This suggests that the transformation occurs heterogeneously with the compound either having converted or remaining unreacted at any given point during the reaction. In the case of *trans*-cinnamic acid, all of the patterns obtained after an initiation period show no evidence for the presence of the reactant, and nor do they indicate that the product is present before the end of the reaction. This implies that the conversion occurs homogeneously with the whole sample in the same state. The apparent difference in mechanism may explain why *trans*-cinnamic acid readily undergoes a single crystal to single crystal transformation to form truxillic acid, while the integrity of the single crystals in the coumarin-3-carboxylic acid case diminish as the irradiation time increases. However, it is important to note that studying the reactions in this manner only indicates the presence of crystalline species and will not, for instance, show if amorphous intermediates occur during the reaction process.

3.10 Summary and Conclusions

Crystalline solids have highly ordered close packed structures, as a consequence, reactions in the solid state cannot be expected to occur with the same freedom as those in the liquid or gas phase, and indeed they do not. This is summarized by Schmidt's postulation that: *'a reaction in the solid state occurs with a minimum amount of atomic or molecular movement'* [3.24]. Based on his studies with cinnamic acids, Schmidt was able to propose limits on the conditions acceptable for a photochemical [2+2] cycloaddition reaction, *i.e.* the potentially reacting double bonds should be parallel to each other and separated by less than 4.2 Å. However, the database study demonstrated that there was no apparent requirement for the double bonds to be planar and a puckered cyclobutane ring can form directly, provided that the distances between the reacting carbons tend towards similar values along with the angles around the potentially forming ring.

Despite selecting the compounds for study within this chapter on the basis of their crystal structures containing alkene double bonds separated by less than 4.2 Å, only one new solid-state [2+2] cycloaddition reaction was identified, that of coumarin-3-carboxylic acid. The most likely explanation for the inertness of the remaining four compounds, 5-bromouracil, orotic acid monohydrate, maleic acid and inosine appears to be the presence of extensive intermolecular hydrogen bonding. As a result it is probably energetically unfavourable for them to react, as these interactions would have to be overcome and may be lost in the product. On the other hand there is only limited hydrogen bonding in both coumarin-3-carboxylic acid and *trans*-cinnamic acid, which is maintained in the irradiation product. This theory was supported by a brief CSD study which found little or no hydrogen bonding in the reactant and product structures of a variety of compounds reported to undergo solid state [2+2] cycloaddition reactions.

The structure solutions obtained for the irradiation product of coumarin-3-carboxylic acid established that a topochemical solid state [2+2] cycloaddition reaction had occurred, giving the expected product. Although, the single crystal structure was of poor quality, a result of crystal integrity diminishing upon irradiation, it confirmed the powder structure solution.

Examination of the series of powder diffraction patterns collected after various irradiation times, for coumarin-3-carboxylic acid and *trans*-cinnamic acid, indicated that the transformation was heterogeneous for the former and homogeneous for the latter. This perhaps, goes some way towards explaining why the conversion of *trans*-cinnamic acid to truxillic acid readily occurs in a single crystal to single crystal fashion, while the integrity of single crystals of coumarin-3-carboxylic acid decrease upon irradiation. Although, it is not possible to predict whether a transformation will occur within a single crystal, it is pertinent to note that the structure of truxillic acid consists of hydrogen bonded chains not present in

trans-cinnamic acid which may serve to strengthen the crystal lattice as it forms thus preventing the degradation of the crystal.

A variety of factors appear to influence whether or not a solid state [2+2] cycloaddition reaction is likely to occur from separation distance to hydrogen bonding. Although, it is not yet possible to accurately predict compounds that will undergo such conversions, studies to try to obtain further insights are very important, as solid state reactions offer greater control over the product than is achievable in the liquid or gas phase. However, in order to take advantage of this, it is necessary to be able to design materials capable of producing the desired product. Towards this end, powder diffraction is an invaluable technique for studying solid state [2+2] cycloadditon reactions, with the potential to obtain structure from irradiated samples where the integrity of a single crystal cannot be maintained and the insolubility of the product prevents recrystallisation. In addition, it has been demonstrated that the technique can provide mechanistic information on whether a conversion occurs homogeneously or heterogeneously.

3.11 References

[3.1] McMurry, J.(1995) *Organic Chemistry,* Brooks/Cole Publishing Company.

[3.2] Allen, F.H. (2002) *Acta Cryst.*, **B58**, 380-388.

[3.3] TICHUI, Dobson, A. J., Gerkin, R. E. (1996) *Acta. Cryst.*, **C52,** 3081-3083.

[3.4] INOSIN11, Subramanian, E. (1979) *Cryst. Struct. Commun.*, **8**, 777-785.

[3.5] BRURAC10, Sternglanz, H., Bugg, C.E. (1975) *Biochim. Biophys. Acta,* **378**, 1-11.

[3.6] MALIAC, Shahat, M. (1952) *Acta Cryst.*, **5**, 763-768.

[3.7] OROTAC, Takusagawa, F., Shimada, A. (1973) *Bull. Chem. Soc. Jpn.*, **46**, 2011-2019.

[3.8] CINMAC03, Wierda, D.A., Feng, T.L., Barron, A.R. (1989) *Acta. Cryst., Sect C, Cryst. Struct. Commum.*, **45**, 338-339.

[3.9] Enkelmann, V., Wegner, G., Novak, K., Wagener, G. (1993) *J. Am. Chem. Soc.*, **115,** 10390-10391.

[3.10] Dragoe, N. (2004) *Powder4 for Windows.*

[3.11] Shirley, R. (2000) *Acta Cryst.*, **A56,** S350.

[3.12] DASH David, W.I.F., Shankland, K., available from Cambridge Crystallographic Data Centre, 12 Union Road, Cambridge. CB2 1EZ. UK.

[3.13] Larson, A.C., Von Dreele, R.B. (2000) *"General Structure Analysis System (GSAS)", Los Alamos National Laboratory Report LAUR* 86-748.

[3.14] Sheldrick, G.M. (1998) Institüt für Anorganische Chemie der Universität, Tammanstrasse 4, D-3400 Göttingen, Germany.

[3.15] Sheldrick, G.M. (1993) Institüt für Anorganische Chemie der Universität, Tammanstrasse 4, D-3400 Göttingen, Germany.

[3.16] Farrugia, L. J. J. (1997) *Appl. Cryst.*, **30,** 565.

[3.17] Cason, C. (2000) *POVRAY, Persistence of Vision.*

[3.18] Bruno, I.J., Cole, J.C., Edgington, P.R., Kessler, M.K., Macrae, C.F., McCabe, P., Pearson, J., Taylor, R. (2002) *Acta Cryst.*, **B58**, 389-397.

[3.19] Farrugia, L.J. (1999) WinGX publication routines.

[3.20] Ramamurthy, V., Venkatesan, K. (1987) *Chem. Rev.*, **87,** 433-481.

[3.21] Markvardsen, A.J., David, W.I.F., Johnson, J.C., Shankland, K. (2001) *Acta Cryst.*, **A57**, 47-54.

[3.22] CS ChemDRAW3D (1999) CambridgeSoft Corporation, 100 Cambridge Park Dr. Cambridge, MA, 02140-2317.

[3.23] ACD Chemsketch (1994) Advanced Chemistry Development Inc. 90 Adelaide Street West, Toronto, Ontario, M5H 3V9, Canada.

[3.24] Cohen, M.D., Schmidt, G.M.J. (1964) *J. Chem. Soc.*, 1996-2000.

3.12 Summary of Crystallographic Data

Table 3.8 - *Summary of experimental data for single crystal structures of coumarin-3-carboxylic acid (k03has1) and its irradiation product (h03has1).*

Compound	k03has1	h03has1
Empirical formula	$C_{10}H_6O_4$	$C_{20}H_{12}O_8$
M	190.16	380.31
Crystal system	Monoclinic	Monoclinic
Space group	$P2_1/n$	$P2_1/n$
Wavelength (Å)	0.71073	0.71073
a (Å)	11.2410(7)	11.348(5)
b (Å)	5.4821(4)	5.881(5)
c (Å)	13.7463(12)	12.376(5)
α (°)	90	90
β (°)	107.11(1)	113.236(5)
γ (°)	90	90
V (Å^3)	809.62(11)	758.9(8)
Z	4	2
Absorption coefficient (mm^{-1})	0.123	0.131
Reflections collected	4016	2945
Independent reflections	1617	1409
R_{int}	0.0531	0.1044
R_1, w$R2$	0.0495, 0.1093	0.0841, 0.1770
R indices (all data)	0.0967, 0.1281	0.1906, 0.2227

Chapter 4

Carbonyl-Carbonyl Interactions in First-row Transition Metal Complexes

4.1 Introduction

The impact of intermolecular interactions on material properties can be significant [4.1]. This chapter presents research on investigations into solid state carbonyl-carbonyl interactions in transition metal compounds, with a view to establishing (a) if they exist, and (b) if they follow the same pattern and significance as those observed in organic carbonyl compounds [4.2]. In this context, one must consider the types of interaction that can occur and why solid state interactions are of interest.

4.1.1 Intermolecular Interactions [4.3]

In many areas of chemistry there is a drive to control and understand reactions, which ranges from accurately predicting a product or its solid state structure to designing materials with specific properties [4.4][4.5]. An appreciation of intermolecular interactions plays an important part in trying to achieve these goals, since these interactions affect both the chemical and physical properties of materials from melting and boiling points to chemical reactivity and stability. The effect of one type of intermolecular interaction, hydrogen bonding, is demonstrated by considering the boiling points of the hydrogen halides, which in the absence of additional interactions would be predicted to rise linearly due to stronger Van der Waals (or London dispersion) forces proportional to the size of the diatomic. In fact the boiling point for HF is much greater than would be expected since the small size and high electronegativity of fluorine allows the formation of strong hydrogen bonds absent in the other hydrogen halides, see Figure 4.1 [4.6].

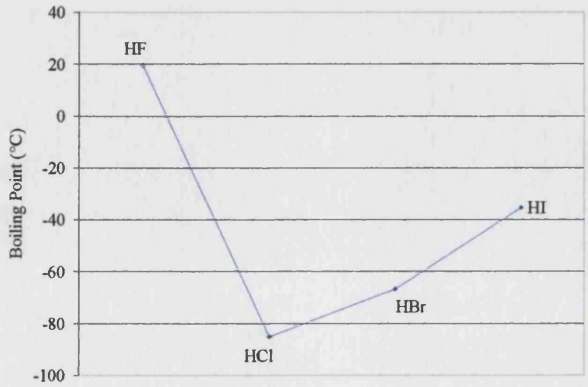

Figure 4.1 - *Boiling points for the hydrogen halides.*

Clearly, the influence of intermolecular interactions cannot be ignored and consequently an understanding of the interaction types possible between atoms or molecules and their relative strengths is very important. In the solid state, compounds usually prefer to form the most energetically stable structure by maximising the strength of interactions between molecules and minimising the free space around themselves. Figure 4.2 illustrates examples of the different sorts of intermolecular interactions from the main general categories described below [4.3]:

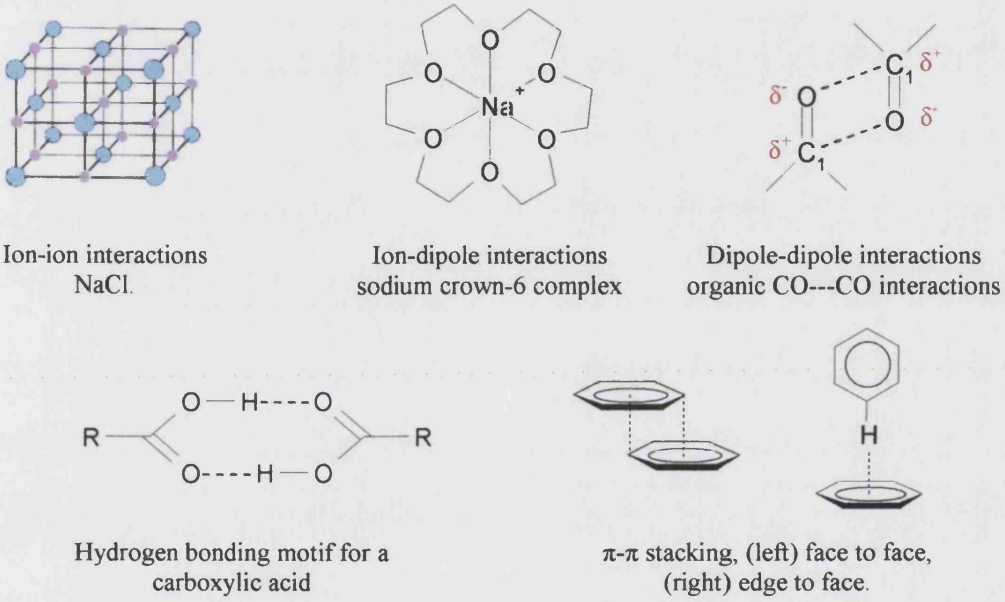

Figure 4.2 - *Examples of different types of solid state interaction.*

- **Ion-ion interactions** - *(100-350 kJ mol^{-1}); these are ionic bonds and are of comparable strength to covalent bonds, a common example is a NaCl lattice in which each positively charged sodium ion is surrounded by six negatively charged chlorides and vice-versa [4.3].*

- **Ion-dipole interactions** - *(50-200 kJ mol^{-1}); these include ions bonding with polar molecules and coordinative bonds, e.g. a positively charged sodium ion interacting with the oxygen lone pairs in a crown ether complex.*

- **Dipole-dipole interactions** - *(5-50 kJ mol^{-1}); the interaction of two oppositely charged dipoles with each other, e.g. carbonyl-carbonyl interactions which can occur because the CO bond is polarised.*

- **Hydrogen bonding** - *(4-120 kJ mol^{-1}); this is an electrostatic interaction that is essentially a type of dipole-dipole interaction and can be very strong. They are commonly observed in compounds where a hydrogen atom, bound to an electronegative atom such as oxygen, interacts with another electronegative atom e.g. in carboxylic acids. In general hydrogen bonds are assumed where the separation between the donor (D) and acceptor (A) atoms does not exceed 3.0 Å, and the D-H---A angle lies between 120° and 180°, although hydrogen bonding can be accepted beyond these limits, and with donor and acceptor atoms that are not as electronegative as oxygen and nitrogen.*

- **π-π stacking** - *(0-50 kJ mol^{-1}); a weak electrostatic interaction between the electron rich and electron poor sections of aromatic rings. They can occur in one of two ways, face-to-face or edge-to-face in both cases the maximum separation should not exceed 3.7 Å and in the former the two rings need to be offset by around 1 Å.*

- **Van der Waals forces** - *(<5 kJ mol^{-1}) very weak electrostatic interactions that occur in all atoms and molecules due to polarization of an electron cloud by a nearby nucleus.*

4.1.2 Carbonyl Interactions in Organic Compounds

The presence of solid state intermolecular interactions in carbonyl containing organic compounds becomes apparent when studying related compounds such as ethene (CH_2=CH_2) and formaldehyde (CH_2=O) in terms of their melting points which are -169°C and -117°C, respectively. The Van der Waals forces will be similar in both compounds as they are approximately the same size and shape (see Figure 4.3) however, the presence of a C-O dipole in formaldehyde results in the molecule being more polar than ethene. Thus, the intermolecular interactions in formaldehyde are greater than those found in ethene, and they also account for the relative melting point differences. A similar trend is seen for other related compounds, such as 2-methyl propene and acetone.

(a) (b)

Figure 4.3 - *(a) formaldehyde, (b) ethene.*

4.1.3 Carbonyl-Carbonyl Interactions in Organic Compounds

The occurrence of carbonyl-carbonyl interactions in organic compounds has been widely recognised for many years [4.7][4.8]. In the 1960s Bolton [4.8] realised that the crystal structure of alloxan was not dictated by N-H---O hydrogen bonds as might be expected but carbonyl-carbonyl interactions. A total of three such interaction motifs have subsequently been identified by Taylor *et. al.* [4.9] and Gavezzotti [4.10] from solid state studies on proteins and carbonyl containing structures respectively, as illustrated in Figure 4.4.

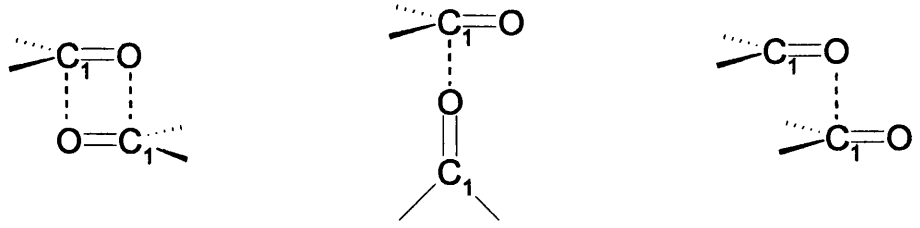

Motif (A) Motif (B) Motif (C)

Figure 4.4 - *Illustration of the three main organic carbonyl-carbonyl interaction motifs that have been identified [4.9][4.10].*

In 1998, a comprehensive solid state study using the crystallographic data available in the Cambridge Structural Database (CSD) was carried out to determine the prevalence of the three organic interaction motifs identified in Figure 4.4 [4.2]. Findings indicated the presence of 7.2% (A), 1.3% (B) and 1.4% (C), with a total of 14.7% of organic carbonyls found to form close contacts in which at least one intermolecular C---O distance was less than 3.6 Å, although no other interaction motifs were identified. In conjunction with the database study, the interaction energies for motifs (A) and (B) were calculated and found to be attractive at -22.3 kJ mol^{-1} and -7.6 kJ mol^{-1}, respectively, based on an intermolecular separation of 3.02 Å for the carbonyl functionalities in propanone molecules. Moreover,

although propanone carbonyls can get closer to each other relative to larger more sterically bulky molecules, interaction energies were still found to be significant at longer distances.

4.1.4 Bonding in Transition Metal Carbonyl Compounds

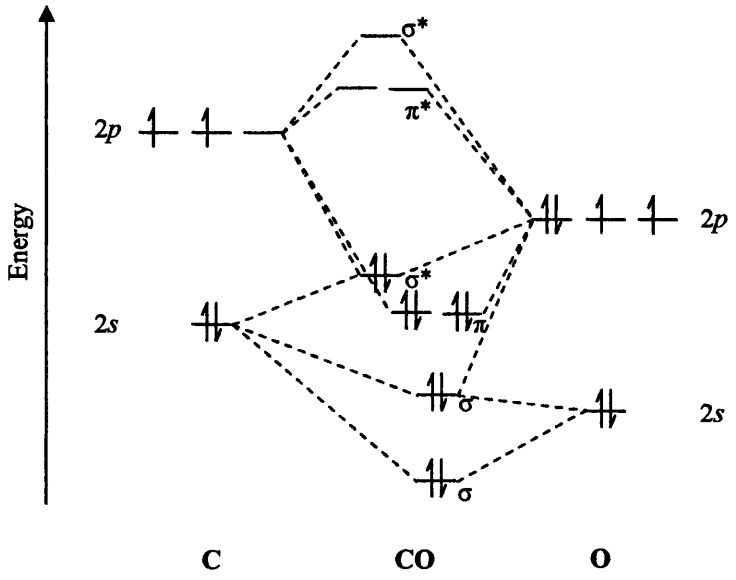

Figure 4.5 - *MO diagram for CO [4.11].*

The MO diagram (Figure 4.5) for the carbonyl moiety shows that the highest occupied molecular orbital (HOMO) is the antibonding σ^*, while the lowest unoccupied molecular orbital (LUMO) corresponds to two degenerate antibonding π^* orbitals. Both of these molecular orbitals have more carbon than oxygen character because they are respectively closer in energy to the carbon 2*s*- and 2*p*- orbitals than those on oxygen. In transition metal complexes, the carbonyl utilises both the HOMO and LUMO to bond to the transition metal through the carbon in two ways (Figure 4.6):

1. A σ-bond interaction is formed with the carbonyl donating electron density from the filled σ^* orbital into a vacant metal *p*- or *d*-orbital, since this removes electron density from the antibonding HOMO it serves to strengthen the carbonyl bond while creating an M-C bond.

2. A back-bonding interaction also forms with the metal donating electron density from a filled *d*-orbital into the unoccupied LUMO on the carbonyl, the π^* orbitals, while this helps to strengthen the M-C bond it weakens the carbonyl bond.

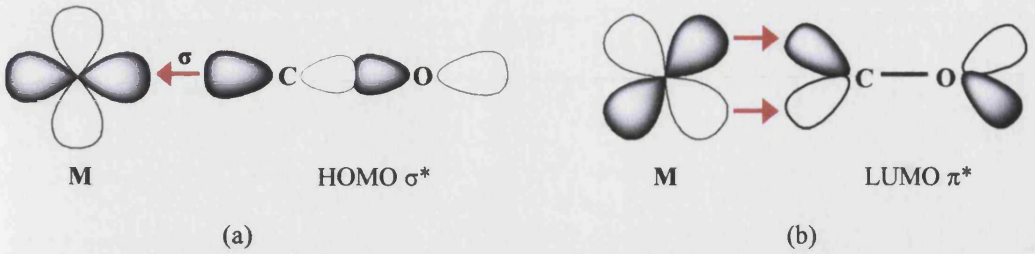

(a) (b)

Figure 4.6 - *Bonding modes in transition metal carbonyl complexes: (a) sigma bond electron donation from filled HOMO on CO into empty d-orbitals on metal (b) back-bonding from filled metal d-orbitals to the empty LUMO on CO.*

The strength of sigma donation in transition metal carbonyls is fairly constant irrespective of the metal involved, however back-bonding increases when there is more electron density available in the metal *d*-orbitals. As back-bonding weakens the carbonyl bond it is generally possible to gain an insight into the strength of the interaction by examining the CO stretching frequency in the IR spectrum, which decreases as the carbonyl bond is weakened, see Figure 4.7.

	ν_{CO} (cm^{-1})
Free CO	2143
$Ni(CO)_4$	2060
$Co(CO)_4^-$	1890
$Fe(CO)_4^{2-}$	1790

↓ Back-bonding increases
Electron density increases

Figure 4.7 - *Illustration of the effect of back-bonding on the carbonyl stretching frequency.*

4.1.5 Solid State Carbonyl Interactions in Carbonyl Containing Transition Metal Complexes

As with all crystal structures, the packing in carbonyl containing transition metal compounds arises from a balance between steric and electronic factors. In addition, isomerisation can be observed when the molecules are structurally flexible due to the potential energy surface being smooth. As a result a similar energy is found for more than one molecular conformation. The interactions that govern the formation of solid state structures for carbonyl containing transition metal compounds have only recently begun to be systematically examined [4.12][4.13][4.14]. However, the area of solid state hydrogen bonding interactions involving carbonyls contained in transition metal complexes have been the subject of detailed studies by Braga and co-workers. Their investigations indicated that when carbonyl ligands attached to transition metals are in strong hydrogen bonding environments, *i.e.* surrounded by groups such as carboxylic acids or hydroxyl groups, C-O---H-O interactions are present if other strong donor-strong acceptor interactions are not

possible. Interestingly, the hydrogen bonding interaction patterns in the transition metal complexes were found to be similar to those observed in organic compounds, see Figure 4.8 [4.15][4.16].

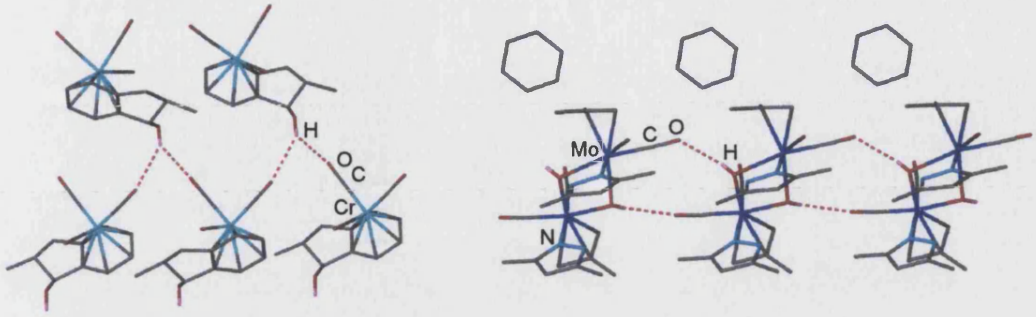

Figure 4.8 - *Illustration of hydrogen bonding in carbonyl containing transition metal complexes, (left) {($C_6H_4(C_5H_4MeOH)$}$Cr(CO)_3$ [4.17], (right) [$(\mu\text{-}H)_2${(η^3-2-MeC_3H_4)$(CO)_2$-3,5-Me_2-pyrazole)}$_2Mo_2$] [4.18].*

In addition to forming hydrogen bonding interactions with strong donors, a number of weak hydrogen bonds of the type C-H---O-C were also identified in carbonyl containing transition metal complexes. Examining the O---H distance in these compounds led Braga to conclude that the interaction was at its strongest when the CO ligand formed a μ_3-bridge, due to the basicity being greater than for μ_2-bridging or terminal carbonyl ligands. The weak hydrogen bonding interactions in transition metal complexes were found to be comparable to those seen in organic compounds with similar distances (O---H, 2.44 Å - 2.62 Å) and a directional nature (C-O---H angle of around 140°) [4.15].

4.2 Database Search Methodology

4.2.1 Focus of the Searches

Only two of the carbonyl-carbonyl interaction motifs identified in organic compounds (Figure 4.4), are potentially possible in carbonyl containing transition metal compounds, namely motifs (A) or (B). The steric bulk from the other ligands around the metal centre would render the motif (C) interaction geometry unachievable in transition metal species. The searches detailed here, are constructed to allow a comparison to be made between potential solid state carbonyl-carbonyl interactions in organic and transition metal compounds.

4.2.2 General Search Criteria

Structures were eliminated from the final datasets in all of the searches described below if they had:

- An *R*-factor > 5%.
- Residual errors after CSD validation checks.
- Crystallographic disorder.
- Polymeric bonds.

4.2.3 Software

The software was detailed in Section 2.2.4.

4.2.4 Transition Metal Carbonyl Species

Three searches were carried out for the first row transition metal carbonyl species: the first two identified compounds containing the possible interaction motifs illustrated in Figure 4.9, while the third was used to estimate the total number of first row transition metal carbonyl fragments in the database.

Figure 4.9 - *Potential interaction motifs, where Tr is any first row transition metal.*

In addition to carrying out searches where *Tr* was defined as any first row transition metal, four additional datasets were created for each search in which *Tr* was specified as either Cr, Mn, Fe or Co. The objective in varying *Tr* was to analyse whether or not any significant variations could be identified in the interaction geometry that might arise from differences in the magnitude of the C=O dipole as a result of changes in the back-bonding capabilities of different metals.

4.2.4.1 Transition Metal Motif (A) Search Criteria

The distances, angles and torsion angles for motif (A) were defined as illustrated in Figure 4.10.

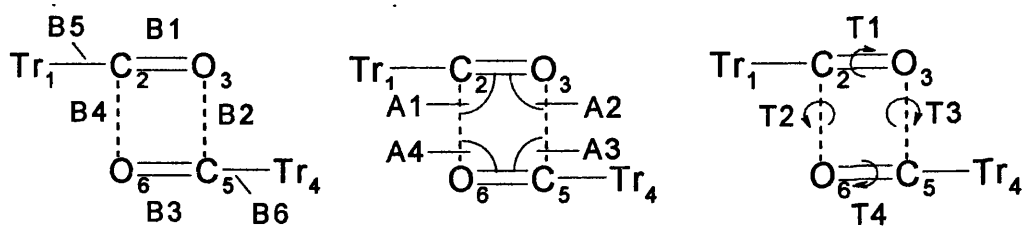

Figure 4.10 - *Illustration of search parameters for motif (A) where Tr is any first row transition metal.*

In addition to the general search criteria described above, the sum of the cross distances C_2---C_5 and O_3---O_6 was set to be greater than the sum of the intermolecular distances B2 and B4. This precludes a twist of more than 90° which is unlikely to correspond to an interaction geometry as the more positive carbons would be closer to each other than to the more negatively charged oxygen atoms and vice-versa. It was also stipulated that the distances B2 and B4 should not exceed the sum of the Van der Waals radii of carbon and oxygen plus 12% *i.e.* 3.6 Å.

The highest symmetry of motif (A) is C_{2h}. Thus C_2 is equivalent to C_5 while O_3 is equivalent to O_6 by symmetry. In view of the fact that the atoms cannot be given a unique identification label within QUEST, the data had to be permuted after completion of the search to account for this in accordance with the permutational operators given in Figure 4.11 using an external program [4.19].

Atom Permutations					
1	2	3	4	5	6
4	5	6	1	2	3

Distance Permutations						Torsion angle Permutations				Angle Permutations			
1	2	3	4	5	6	1	2	3	4	1	2	3	4
3	4	1	2	6	5	4	3	2	1	3	4	1	2

Figure 4.11 - *Atom permutations for C_{2h} reference geometry (top). Permutational operators for C_{2h} reference geometry in terms of distances, torsion angles and angles (bottom).*

4.2.4.2 Transition Metal Motif (B) Search Criteria

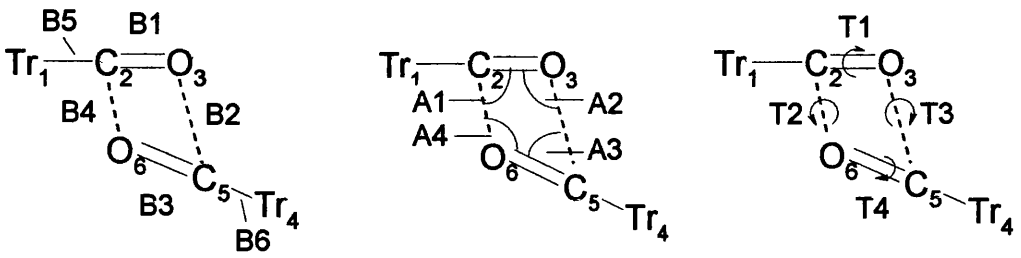

Figure 4.12 - *Illustration of search parameters for motif (B) where Tr is any first row transition metal.*

In the searches to identify structures containing motif (B) the geometrical parameters were defined as set out in Figure 4.12. The potential interaction distance B4 was defined as less than 3.6 Å, while B2 was set to exceed this distance, in order to prevent hits corresponding to motif (A) appearing in this dataset. To ensure a perpendicular motif, limits were placed on two of the angles such that A2 was less than 120° while A4 had to lie between 140° and 180°.

In the case of motif (B) (point group C_s) the search fragment does not possess a higher topological symmetry, hence there is no requirement to permute the data as each atom is uniquely defined in the search.

4.2.4.3 Carbonyl Containing Transition Metal Species Search Criteria

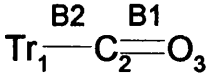

Figure 4.13 - *Search parameters, Tr is any first row transition metal.*

This search was invoked to determine the total number of first row transition metal carbonyl fragments within the database so that the fraction that might exhibit possible interactions can be estimated. The search parameters are illustrated in Figure 4.13.

4.2.4.4 Cr, Mn, Fe and Co Searches - Search Criteria

Only four of the first row transition metals, Cr, Mn, Fe and Co, were found to have enough fragments for separate analysis. Three searches were carried out for each of these metal in the same manner as described for *Tr* above *i.e.* motif (A), (B) and an overall dataset to determine the total number of each metal carbonyl fragment in the dataset.

4.2.5 Organic Carbonyl Species

To allow easy comparison of the results, the organic carbonyl searches were constructed in a similar manner to those for the transition metal species. The interaction motifs for the first two searches are shown in Figure 4.14, while the third search was constructed to gain an estimation of the total number of organic carbonyl fragments in the database. This study forms an extension to work previously reported by Baalham *et al.* [4.2], however, the focus here is only on the two organic carbonyl-carbonyl interaction motifs that can also occur in transition metal carbonyl complexes.

Figure 4.14 - *Potential interaction motifs.*

4.2.5.1 Organic Motif (A) Search Criteria

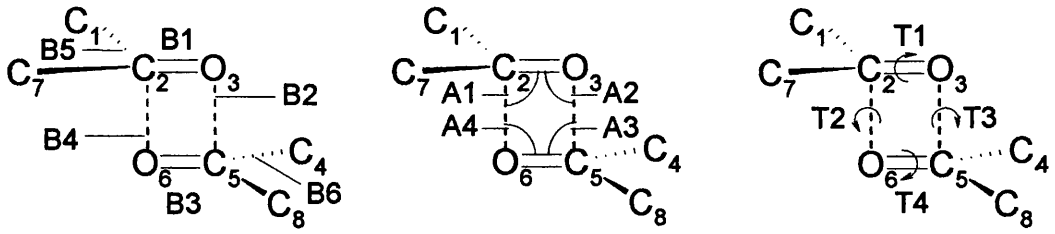

Figure 4.15 - *Illustration of search parameters for motif (A).*

Figure 4.15 illustrates the geometrical parameters as defined for the organic motif (A) fragment. The additional search criteria were identical to those for the corresponding first row transition metal carbonyl search, *i.e.* the distances B2 and B4 could not exceed 3.6 Å and the sum of the cross distances C_2---C_5 and O_3---O_6 had to be greater than the sum of the intermolecular distances (B2 + B4)

Motif (A) in the organic case also has C_{2h} symmetry and thus the data had to be permuted in accordance with the permutational operators given in Figure 4.16.

Atom Permutations							
1	2	3	4	5	6	7	8
4	5	6	1	2	3	8	7

Distance Permutations						Torsion angle Permutations				Angle Permutations			
1	2	3	4	5	6	1	2	3	4	1	2	3	4
3	4	1	2	6	5	4	3	2	1	3	4	1	2

Figure 4.16 - *Atom permutations for C_{2h} reference geometry (Top). Permutational operators for C_{2h} reference geometry in terms of distances, torsion angles and angles (Bottom).*

4.2.5.2 Organic Motif (B) Search Criteria

The distances, angles and torsion angles for motif (B) are shown in Figure 4.17.

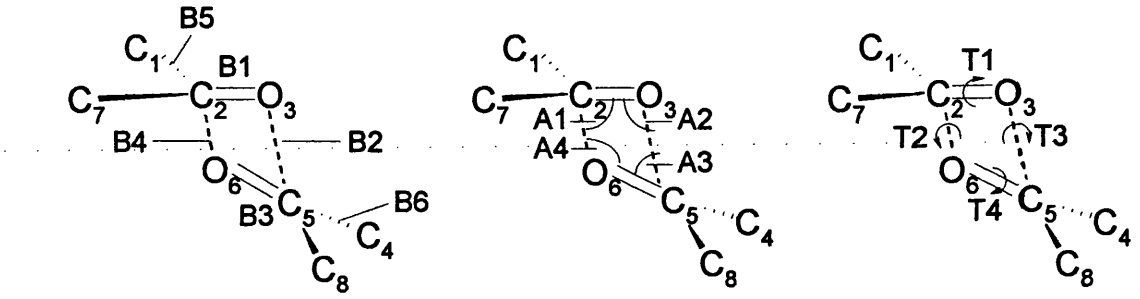

Figure 4.17 - *Illustration of search parameters for motif (B).*

The additional limits applied to the search parameters for motif (B) were:

- B4 ≤ 3.6 Å.
- B2 > 3.6 Å.
- A2 ≤ 120°.
- 140° ≤ A4 ≤ 180°.

These restrictions were also used in the equivalent transition metal carbonyl searches. Once again there was no requirement to permute the data since the search fragment does not possess a higher topological symmetry.

4.2.5.3 Carbonyl Containing Organic Compounds

The final search in this set was used to gain an estimation of the total number of carbonyl fragments in organic compounds contained within the database, the search parameters are shown in Figure 4.18.

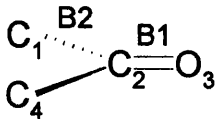

Figure 4.18 - *Search parameters for the overall organic dataset.*

4.3 Transition Metal Carbonyl Species – Results and Discussion

4.3.1 Transition Metal Motif (A) Searches

The search produced 2430 refcodes that matched the search criteria which after symmetry expansion gave 8786 fragments for analysis.

Table 4.1 shows the mean values obtained for the distances and angles defined in the search. Since the search data were permuted in accordance with the C_{2h} symmetry of the search fragment, parameters that are symmetry related such as B1 and B3 have the same values. A selection of histograms and scatterplots constructed from this dataset to try to determine the most likely geometry for a potential interaction motif are provided in Figures 4.19 to 4.26, while the remainder are included in Appendix 4.1 on CD.

Table 4.1 - *Mean values for the search parameters for motif (A) in overall Tr dataset.*

Parameter	Mean		Parameter	Mean
B1/B3	1.140 Å		A1/A3	73.4°
B2/B4	3.404 Å		A2/A4	104.0°
B5/B6	1.812 Å			

N.B. The dataset contains species with various coordination numbers and oxidation states.

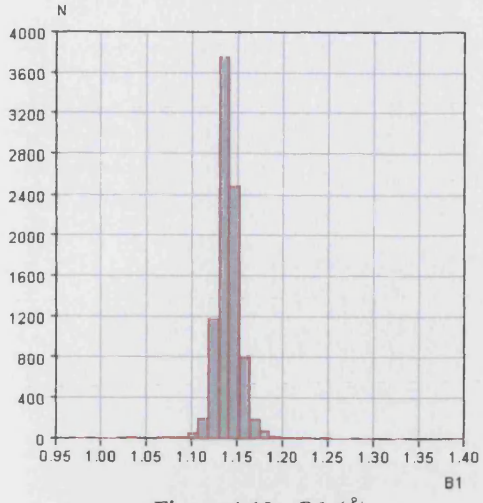

Figure 4.19 - *B1 (Å).*

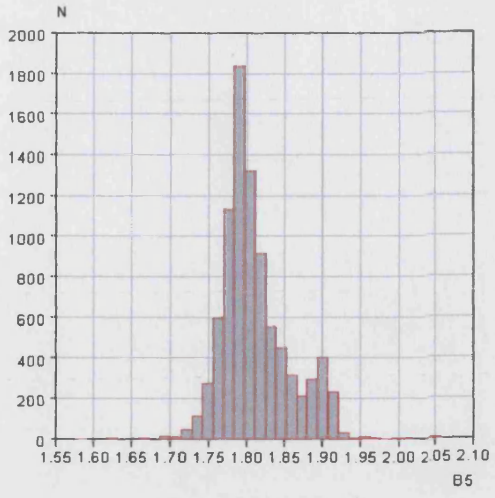

Figure 4.20 - *B5 (Å).*

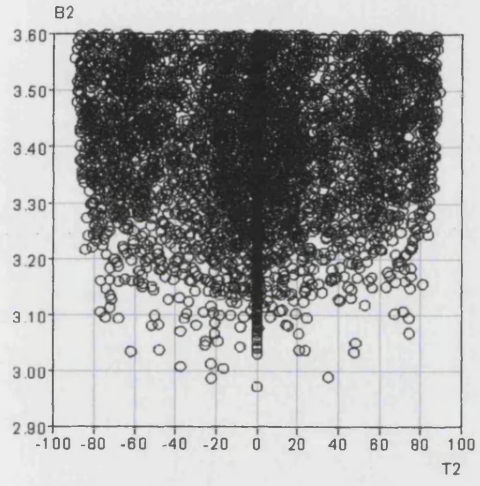

Figure 4.21 - *B2(Å) vs. T2 (°)*

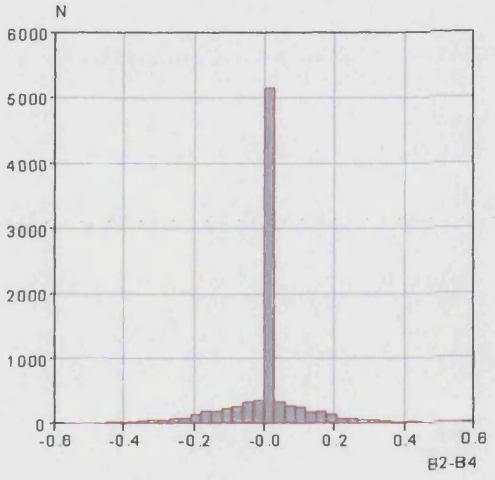

Figure 4.22 - *(B2-B4) (Å).*

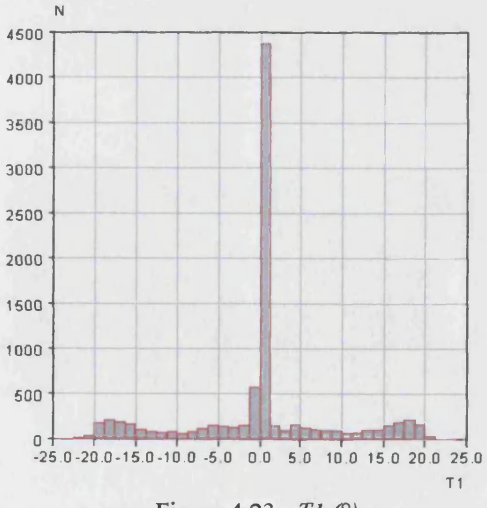

Figure 4.23 - *T1 (°).*

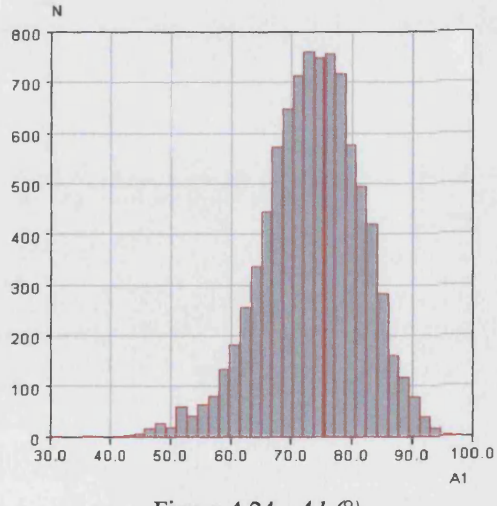

Figure 4.24 - *A1 (°).*

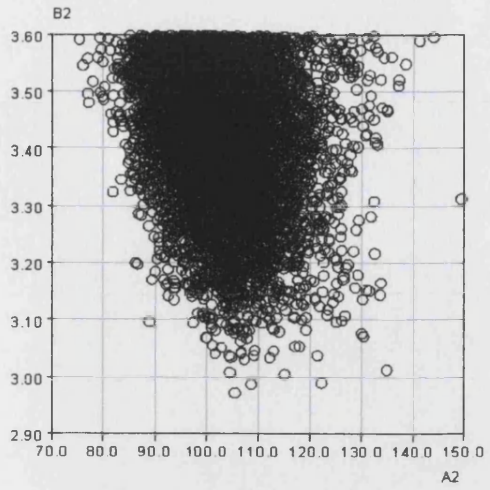

Figure 4.25 - *B2 (Å) vs. A2 (°).*

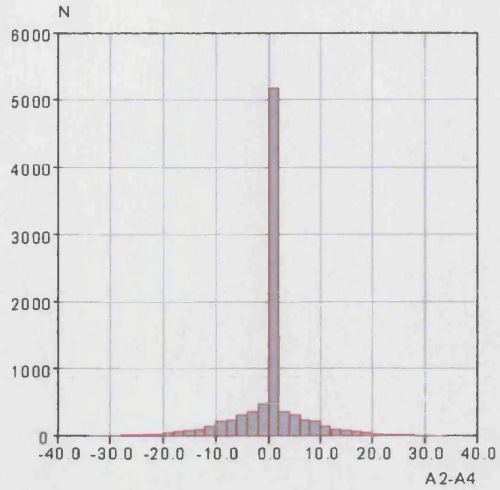

Figure 4.26 - *A2-A4 (°).*

Figure 4.19 exhibits a tight range as it relates to the bonding distance B1 (C=O). The spread of points observed for the Tr-C bond (B5) (Figure 4.20) is reasonable since the radii of the different metal ions contained within the dataset are not the same, while the range of intermolecular distances (B2) is as expected much greater, see Figure 4.21 (B2 vs. T2). Even at the shorter intermolecular separations (B2) a range of values for the torsion angle (T2) are observed suggesting that carbonyls may not have to be in the same plane to interact. Despite the large breadth of points for B2, the values of B2 and B4 are approximately the same as shown by Figure 4.22 (B2-B4).

The large number of occurrences relating to fragments with torsion angles of 0° (2576 out of 8786) in Figures 4.21 and 4.23 corresponds to structures in which the carbonyls are related by an inversion centre. However a significant number (6210 out of 8786) of the fragments in this dataset show non-zero values for T1 or T2 again indicating that planarity may not be essential.

The distribution of values in Figure 4.24 (A1) is relatively large covering a range of over 40°, comparable to the range seen for A2 in Figure 4.25 (B2 vs. A2). Generally, A1 and A3 are less than 90°, while A2 and A4 are almost exclusively greater than 90°, in situations where this is not the case the reverse is true. In the main the opposite angles are similar, although they do not have to be as illustrated in Figure 4.26 (A2-A4), an equivalent plot was observed for (A1-A3).

It is interesting to note in Figure 4.25 (B2 vs. A2) that as the intermolecular separation (B2) decreases the spread of points observed for A2 gets smaller. Thus, at the shortest B2 distances of around 3.0 Å, A2 tends towards its mean of 104°, perhaps suggesting that this geometry is the most favourable to achieve the strongest interaction.

4.3.2 Transition Metal Motif (B) Searches

A total of 2264 refcodes matched the search criteria for motif (B) producing 5426 fragments for analysis. Table 4.2 summarises the mean values for the distance and angular parameters. As with motif (A) a series of histograms and scatterplots were constructed to assist with the identification of the characteristics pertaining to the potential interaction motif (B). A selection of these plots are shown in Figures 4.27 to 4.32, with the remainder provided in Appendix 4.2 on CD.

Table 4.2 - *Mean values for the search parameters for motif (B) in overall Tr dataset.*

Parameter	Mean		Parameter	Mean
B1	1.137 Å		A1	75.0°
B2	4.276 Å		A2	88.6°
B3	1.138 Å		A3	21.9°
B4	3.372 Å		A4	151.1°
B5	1.813 Å			
B6	1.809 Å			

N.B. The dataset contains species with various coordination numbers and oxidation states.

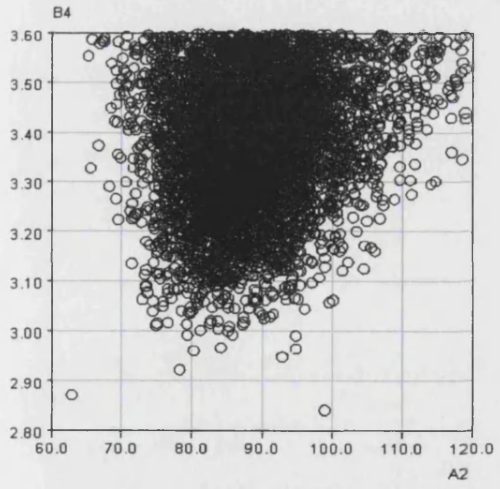

Figure 4.27 - *B4 (Å) vs. A2 (°).*

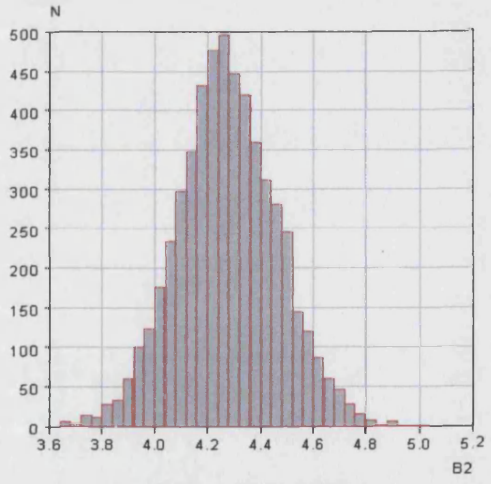

Figure 4.28 - *B2 (Å).*

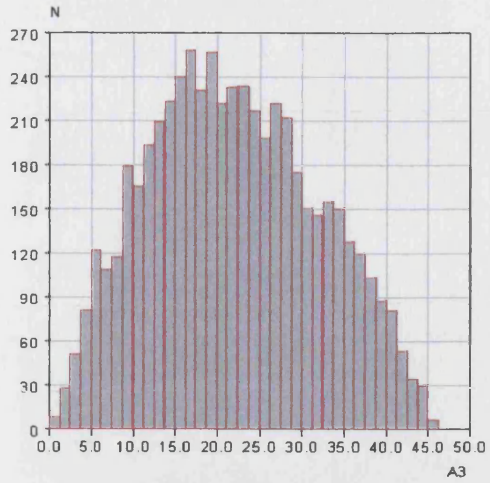

Figure 4.29 - *A3 (°).*

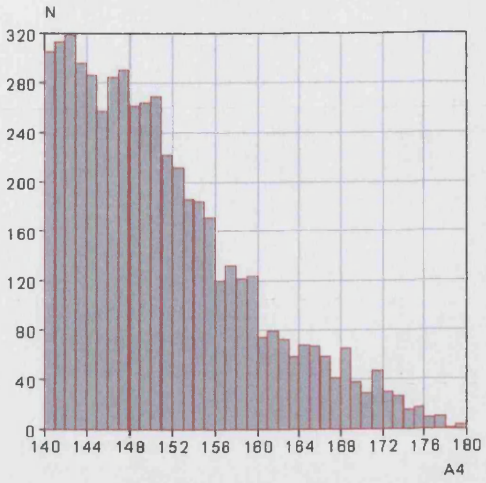

Figure 4.30 - *A4 (°).*

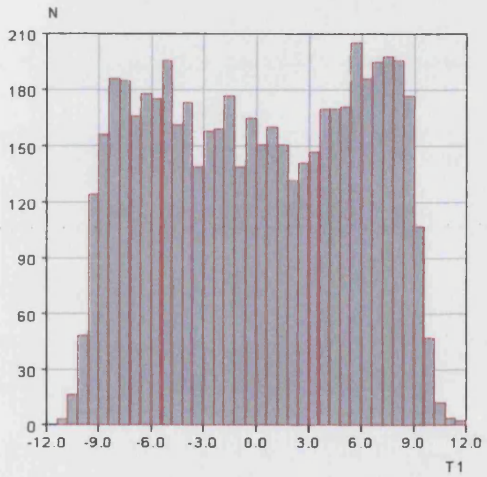

Figure 4.31 - *T1 (°).*

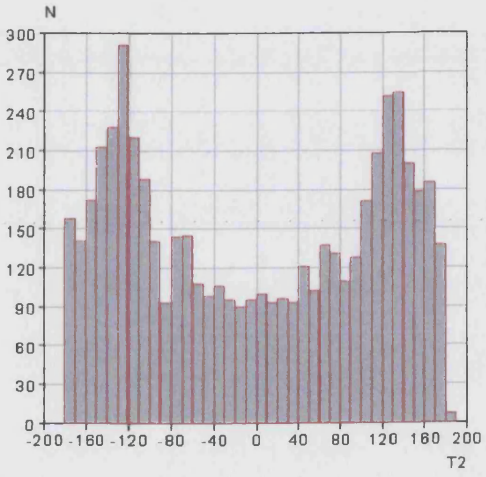

Figure 4.32 - *T2 (°).*

The histograms for the bonding distances B1, B3, B5 and B6 were essentially the same as those relating to the corresponding distances for motif (A) and hence are not replotted here. However, the same observations can be made, firstly, the range of values corresponding to the C=O bond lengths (B1 and B3) is small and secondly, the spread of values for the Tr-C bond lengths (B5 and B6) is due to the radii of the different metal ions contained within the dataset not being the same.

Figure 4.27 (B4 vs. A2) shows the same trends as seen for motif (A) with the range of angular values for A2 decreasing as the potential interaction distance B4 gets smaller. At the shortest intermolecular separation distances (approximately 3.0 Å), A2 tends towards values which span 80° to 90°, perhaps indicating that this geometry is necessary to achieve the strongest interaction. Although, it is also possible that the geometry at the smallest separations may arise from a balance between the interaction and packing energies. The other non-bonded parameter, B2, extends over a reasonable range centred around 4.276 Å.

The value of B2 will get larger as the orientation of the two carbonyls with respect to each other becomes more perpendicular, see Figure 4.28.

The spread of values for each of the angular parameters is approximately 40°, as illustrated by Figures 4.27, 4.29 and 4.30. The plot relating to A4 (Figure 4.30) appears truncated as the search was constructed to ensure that the fragments in the dataset were reasonably perpendicular, and therefore corresponded to motif (B).

A range of values were observed for all of the torsion angles indicating that the potentially interacting carbonyls do not necessarily have to be in the same plane, as illustrated by Figures 4.31 and 4.32 (T1 and T3). Unlike the case of motif (A), there is no concentration of points around 0° in this instance as the interacting carbonyls cannot be related to each other by a crystallographic inversion centre in motif (B).

4.3.3 Carbonyl Containing Transition Metal Species

The number of species in the database containing a first row transition metal bonded to a carbonyl is 6076, with 29703 individual fragments. The parameters defined in this search were bonding distances with mean values of 1.143 Å and 1.804 Å for B1 (C=O) and B2 (Tr-C) respectively. They both have similar ranges to those observed for the corresponding bonding distances in the two potential interaction motifs, and the spread of points for B2 is likely to relate to the fact that the radii of the different metal ions within the dataset will not be the same, see Figures 4.33 and 4.34.

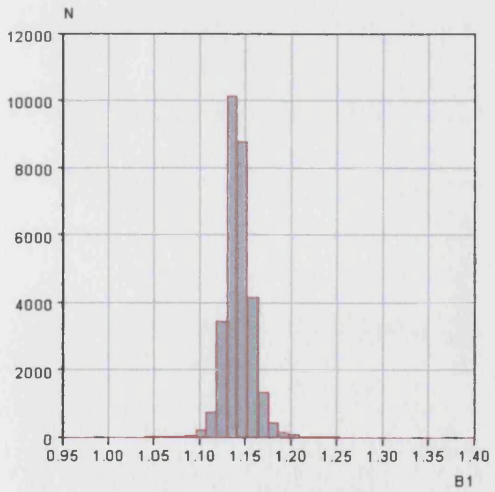

Figure 4.33 - *B1 (Å).*

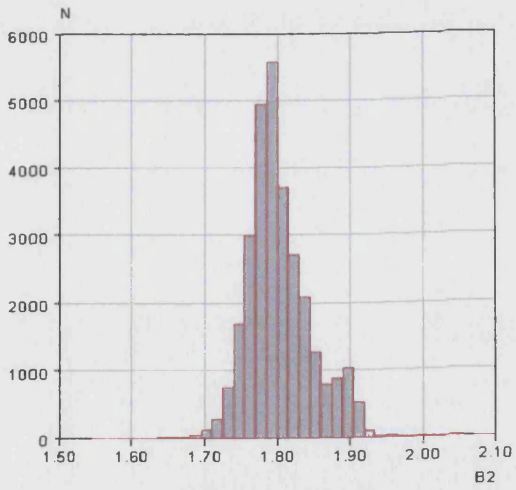

Figure 4.34 - *B2 (Å).*

4.3.4 Comparison of the Transition Metal Datasets

Tables 4.3 and 4.4 below, show a comparison of the mean values for the distance and angular parameters from the three datasets where appropriate. The C=O bond length is represented by the parameter B1 in the overall searches (M-C=O), and both B1 and B3 in the

searches to identify motifs (A) and (B), hence B1 for the overall dataset is compared to both B1 and B3 for motifs (A) and (B). Likewise the comparison between the Tr-C bond length across the three datasets requires B2 in the overall searches to be compared to B5 and B6 in the searches for motifs (A) and (B).

Table 4.3 - *Comparison of the mean values for the distances B1 to B6 for the overall Tr datasets.*

Search	Parameter					
	B1 (Å)	B2 (Å)	B3 (Å)	B4 (Å)	B5 (Å)	B6 (Å)
Motif (A)	1.140	3.404	1.140	3.404	1.812	1.812
Motif (B)	1.137	4.276	1.138	3.372	1.813	1.809
M-C=O	1.143	-	1.143 (B1)	-	1.804 (B2)	1.804 (B2)

Table 4.4 - *Comparison of the mean values for the angles A1 to A4 for the overall Tr datasets.*

Search	Parameter			
	A1 (°)	A2 (°)	A3 (°)	A4 (°)
Motif (A)	73.4	104.0	73.4	104.0
Motif (B)	75.0	88.6	21.9	151.1

No significant differences were observed in the bonding distances, B1, B3, B5 or B6 across the three searches, suggesting that any potential interaction does not disrupt either the Tr-C or C=O bond. The mean values for the potential interaction distances are very similar for both motifs at 3.404 Å and 3.372 Å respectively for (A) and (B).

As expected the mean angular geometries for the two motifs are significantly different, as the first motif (A) incorporates two close C---O contacts in a parallelogram, while the second motif (B) forms only one close C---O distance in a perpendicular like manner.

The two datasets for motifs (A) and (B) account for 9819 carbonyl fragments, since the total number of fragments is 29703 this suggests that approximately 33% of first row transition metal carbonyls may exhibit intermolecular carbonyl-carbonyl interactions. It is reasonable to assume that for structures containing more than one carbonyl, it will not be possible for all C=O moieties to interact favourably with neighbouring molecules, while allowing the molecules to pack efficiently. Consequently, it is noteworthy that the percentage of structures containing metal carbonyls which involve at least one of the interaction motifs (A) or (B) discussed previously is approximately 51%. This suggests that

intermolecular carbonyl-carbonyl interactions in transition metal compounds may well be significant.

4.4 Cr, Mn, Fe and Co Searches – Results and Discussion

Table 4.5 lists the total number of refcodes and fragments recorded for each of the searches in which the transition metal was specified separately as chromium, manganese, iron or cobalt. The information relating to the overall transition metal dataset is included throughout this section for comparison.

Table 4.5 - *Number of refcodes and fragments recorded for each metal in the different searches.*

Metal	Search	Number of Refcodes	Number of Fragments (after symmetry expansion for Motif (A)).
Tr	Motif (A)	2430	8786
	Motif (B)	2264	5426
	M-C=O	6076	29703
Cr	Motif (A)	457	1592
	Motif (B)	325	660
	M-C=O	1264	5722
Mn	Motif (A)	370	1288
	Motif (B)	358	808
	M-C=O	967	4418
Fe	Motif (A)	1130	3898
	Motif (B)	1083	2331
	M-C=O	2924	13516
Co	Motif (A)	442	1668
	Motif (B)	450	1312
	M-C=O	1044	5625

The histograms and scatterplots for each of the new searches showed the same trends as seen for the corresponding overall datasets Sections 4.3.1, 4.3.2 and 4.3.3, hence they are only contained in Appendix 4.3 on CD and not re-plotted here. Tables 4.6 to 4.8 below provide a comparison of the mean distances and angles relating to the three searches for each metal.

Table 4.6 - *Comparison of mean values for the distance and angle parameters for motif (A).*

Parameter	Tr	Cr	Mn	Fe	Co
B1/B3 (Å)	1.140	1.144	1.142	1.140	1.135
B2/B4 (Å)	3.404	3.397	3.393	3.403	3.418
B5/B6 (Å)	1.812	1.879	1.820	1.788	1.795
A1/A3 (°)	73.4	72.4	72.7	73.2	75.6
A2/A4 (°)	104.0	104.9	105.5	104.1	101.9

NB. The datasets contain species with various coordination numbers and oxidation states.

Table 4.7 - *Comparison of mean values for the distance and angle parameters for motif (B).*

Parameter	Tr	Cr	Mn	Fe	Co
B1 (Å)	1.137	1.141	1.138	1.138	1.133
B2 (Å)	4.276	4.283	4.256	4.269	4.301
B3 (Å)	1.138	1.142	1.139	1.139	1.134
B4 (Å)	3.372	3.378	3.369	3.371	3.377
B5 (Å)	1.813	1.887	1.830	1.793	1.801
B6 (Å)	1.809	1.887	1.825	1.789	1.796
A1 (°)	75.0	74.6	74.1	74.3	76.7
A2 (°)	88.6	88.5	89.6	89.0	87.0
A3 (°)	21.9	21.3	21.7	21.3	22.8
A4 (°)	151.1	150.7	151.6	151.4	150.3

N.B. The datasets contain species with various coordination numbers and oxidation states.

Table 4.8 - *Comparison of mean distance parameters for M-C=O searches.*

Parameter	Tr	Cr	Mn	Fe	Co
B1 (Å)	1.143	1.148	1.144	1.143	1.137
B2 (Å)	1.804	1.864	1.811	1.782	1.788
Ionic Radii (pm)	-	73	67	61	65

N.B. The datasets contain species with various coordination numbers and oxidation states.

The data presented in these tables do not indicate that any significant differences in interaction geometry arise as a result of changing the metal, although it is noteworthy that the variation in B2 across the four metals reflects the fact that as the ionic radii for the metal

decreases the bond length gets shorter. The mean interaction distances for motifs (A) and (B) are around 3.404 Å and 3.372 Å respectively in all of the searches, while the average angular geometries are illustrated in Figure 4.35 using the values from the overall dataset since these were comparable to the results from the Cr, Mn, Fe and Co searches.

Figure 4.35 - *The average angular geometry for motifs (A) and (B).*

The torsion angle plots again indicated a concentration of points around 0° for motif (A) due to some of the carbonyl fragments being related by a crystallographic inversion centre. However, both motifs showed a range of torsion angles in all of the metal searches suggesting that potentially interacting carbonyls may not have to be in the same plane.

Table 4.9 - *Comparison of the percentage of metal carbonyls potentially involved in an interaction for the different metals.*

Metal	Number of fragments potentially involved in an interaction	Total number of M-C=O fragments	Percentage of M-C=O involved in potential interactions
Tr	9819	29703	33%
Cr	1456	5722	25%
Mn	1452	4418	33%
Fe	4280	13516	32%
Co	2146	5625	38%

Using the same caveats as for the *Tr* datasets, Table 4.9 provides an estimate of the percentage of transition metal carbonyl fragments involved in possible intermolecular interactions for each of the individual metals. As can be seen, differences are observed, as values range from 25% for Cr to 38% for Co. However, no explanation is obvious for this variation, and it is most likely to be an artifact of the fact that the separate metal searches only involve around 1000 refcodes or structures each, so a small number of additional potentially interacting fragments has a significant effect on the overall percentage.

4.5 Organic Carbonyl – Results and Discussion

The organic searches formed an extension to the previously reported work discussed in Section 4.1.3. In view of the fact that the results obtained here were consistent with the initial study an in depth discussion was felt unnecessary, however, a summary of the key points is included below to allow comparison with the transition metal carbonyl dataset. The complete set of histograms and scatterplots constructed from these searches are contained in Appendix 4.4 on CD.

The total number of refcodes and fragments obtained for each of the three organic searches are recorded in Table 4.10. While Tables 4.11 and 4.12 present a comparison of the mean distance and angular parameters from these datasets where appropriate. As with the transition metal searches, a comparison of the C=O bond length requires B1 in the overall searches (C=O) to be compared to both B1 and B3 in the searches to identify motifs (A) and (B), while a comparison of the C-C bond length involves B2 in the overall searches and B5 and B6 in the searches for motifs (A) and (B).

Table 4.10 - *Number of refcodes and fragments obtained in the three organic searches.*

Search	Number of Refcodes	Number of Fragments
Motif (A)	511	1160 (after symmetry expansion)
Motif (B)	174	201
Organic C=O Fragments	7035	9770

Table 4.11 - *Comparison of Distance Parameters for Organic Carbonyl Compounds.*

Search	Parameter					
	B1 (Å)	B2 (Å)	B3 (Å)	B4 (Å)	B5 (Å)	B6 (Å)
Motif (A)	1.219	3.337	1.219	3.337	1.498	1.498
Motif (B)	1.213	4.662	1.212	3.274	1.501	1.505
Organic Carbonyl	1.220	-	1.220 (B1)	-	1.496 (B2)	1.496 (B2)

Table 4.12 - *Comparison of Angle Parameters for Organic Carbonyl Compounds.*

Search	Parameter			
	A1 (°)	A2 (°)	A3 (°)	A4 (°)
Motif (A)	82.5	96.8	82.5	96.8
Motif (B)	96.3	69.0	22.7	153.5

It can be seen from Table 4.11 that the presence of a carbonyl-carbonyl interaction does not appear to disrupt intramolecular bonding, with C=O and C-C distances maintained in the regions of 1.220 Å and 1.496 Å, respectively. The mean interaction distances are similar for the two motifs at 3.337 Å for (A) and 3.272 Å for (B). The average angular geometry for motif (A) suggests a sheared antiparallel motif (Figure 4.36) that can be distorted, since the torsion angles indicate that the carbonyl fragments do not have to lie in the same plane, see Figure 4.37 and Figure 4.38. The concentration of points at T = 0° arises because many of the carbonyls are related by a crystallographic centre of inversion. The torsion angle plots for motif (B) also indicated that the interacting fragments could be twisted with respect to one another, see Figure 4.39 and Figure 4.40, while the mean values obtained for the angles (Table 4.12) are consistent with an approximately perpendicular interaction motif.

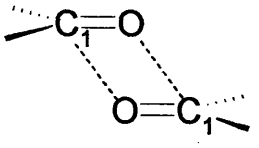

Figure 4.36 - *Illustration of the sheared antiparallel motif adopted by motif (A).*

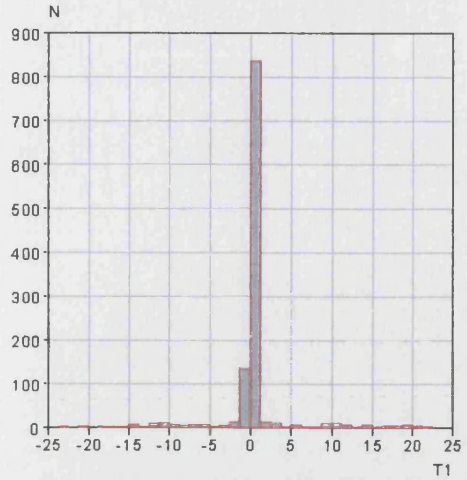

Figure 4.37 - *T1 (°) histogram for motif (A).*

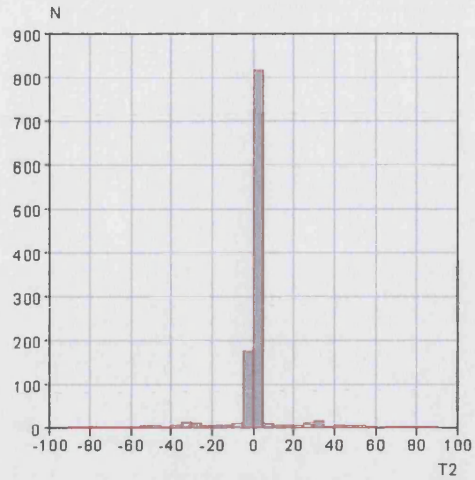

Figure 4.38 - *T2(°) histogram for motif (A).*

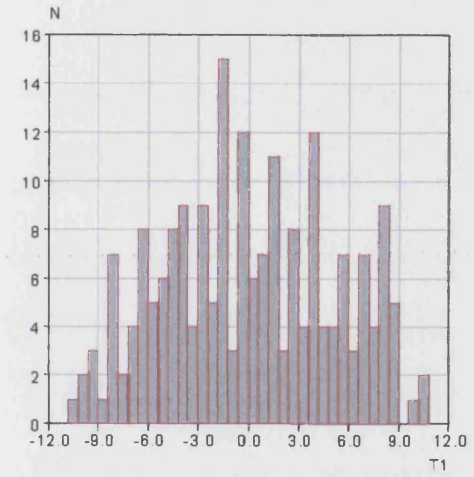

Figure 4.39 - *T1 (°) histogram for motif (B).*

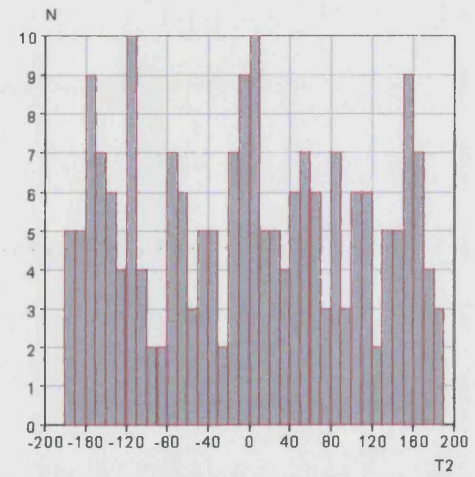

Figure 4.40 - *T2(°) histogram for motif (B).*

Using the same provisos as for the first row transition metal carbonyl compounds, one may concludes that approximately 781 out of a total 9770 organic carbonyl fragments or 8% of the organic carbonyls possibly interact in a manner consistent with either of the two motifs illustrated here.

4.5.1 Comparison of the Transition Metal and Organic Datasets

A comparison of the average distance parameters identified in the transition metal and organic carbonyl searches is provided in Table 4.13. As discussed in Sections 4.3.4 and 4.5, a comparison of the C=O bond lengths requires B1 of the overall dataset to be compared to both B1 and B3 in the searches for motifs (A) and (B), while a comparison of the Tr-C or C-C bond lengths involves B2 of the overall datasets with B5 and B6 from the searches for motifs (A) and (B).

Table 4.13 - *Comparison of bond lengths in carbonyl containing transition metal and organic compounds.*

Species	Search	Parameter					
		B1 (Å)	B2 (Å)	B3 (Å)	B4 (Å)	B5 (Å)	B6 (Å)
Tr	Motif (A)	1.140	3.404	1.140	3.404	1.812	1.812
	Motif (B)	1.137	4.276	1.138	3.372	1.813	1.809
	M-C=O	1.143	-	1.143 (B1)	-	1.804 (B2)	1.804 (B2)
Organic	Motif (A)	1.219	3.337	1.219	3.337	1.498	1.498
	Motif (B)	1.213	4.662	1.212	3.274	1.501	1.505
	M-C=O	1.220	-	1.220 (B1)	-	1.496 (B2)	1.496 (B2)

The C=O bond lengths and the potential interaction distances are very similar for both the transition metal and organic species with differences being insignificant at about 0.1 Å. Interestingly in motif (B) the non interacting intermolecular distance B2 is much shorter in the transition metal case at 4.276 Å than the equivalent 'organic' value of 4.662 Å and the reasons for this become apparent when examining the mean angular geometries for the two motifs provided in Figure 4.41. In the organic motif the carbonyls have slipped past each other with A1 being above 90°. However, in the transition metal dataset this has not occurred and A1 is less than 90° probably due to the steric bulk around the metal center, resulting in O_3 and C_5 (Figure 4.41) being closer to each other than in the organic case. The steric effect of the ligands is also evident in the mean angular geometry for motif (A) which appears to be less rectangular in shape for the transition metal carbonyl moiety as opposed to the organic carbonyl species.

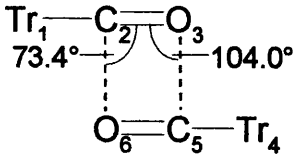

Motif (A)

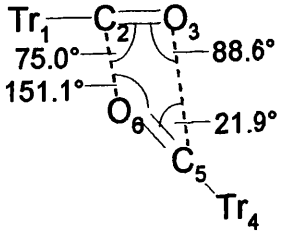

Motif (B)

Figure 4.41 - *Comparison of angular geometries for the two different interaction motifs in both the transition metal and organic cases.*

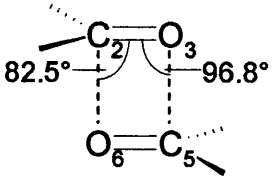

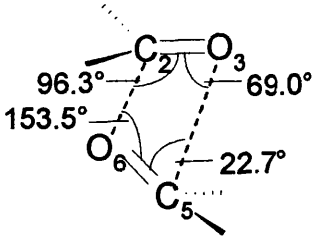

The final Table 4.14, provides a comparison of the occurrence of carbonyl-carbonyl interactions in motifs (A) and (B) in the transition metal and organic datasets.

Table 4.14 - *Comparison of occurrence of interaction motifs for transition metal carbonyls and organic carbonyl species.*

Search	Motif	Number of potentially interacting fragments	Total number of M-C=O fragments	Percentage of M-C=O involved in specified potential interaction type
Tr	A	4393	29703	15%
	B	5426		18%
	A + B	9819		33%
Organic	A	580	9770	6%
	B	201		2%
	A + B	781		8%

It appears that carbonyl-carbonyl interactions in transition metal compounds are far more common than in the organic case with 33% of the available fragments interacting compared to the organic 8% (14% when all short C---O distances are included). Moreover, initial calculations have suggested that the carbonyl-carbonyl interaction energy in transition metal compounds for motif (A) is attractive at around -20 kJ mol^{-1} at a separation of

approximately 3.0 Å [4.20][4.21], similar to the organic case of -22 kJ mol^{-1} at the same distance. However, it is important to register two points before over deducing the significance of this disparity. Firstly, many transition metal complexes contain multiple carbonyl fragments and therefore they have to be close to each other when packed. Secondly, organic compounds often have the opportunity to form other interactions, such as hydrogen bonds, which are likely to form in preference to a carbonyl-carbonyl interaction as their energy is more favourable.

4.6 Conclusions

The results obtained from the overall transition metal carbonyl datasets suggested that a potential interaction does not affect either the Tr-C or the C=O bond distances. The mean interaction distances for the two motifs were very similar at 3.404 Å (A) and 3.372 Å (B), and there appeared to be no requirement for the carbonyls to be in the same plane in either case as a range of torsion angles was observed. The concentration of points around T = 0° for motif (A) arises from the fact that some of the carbonyls are related by a crystallographic centre of inversion. The datasets for the four metals, chromium, manganese, iron and cobalt did not show any significant variations from each other in terms of the interaction geometry or distance.

It was interesting to note that the possible carbonyl-carbonyl interaction motifs in transition metal compounds were not the same as the corresponding organic cases. These differences are likely arise as a result of the steric bulk from the other ligands on the transition metal complexes preventing the carbonyls from achieving the same angular geometries as seen for the organic fragments.

The results here have indicated that carbonyl-carbonyl interactions may be more significant in transition metal complexes than organic compounds with around 33% of the available carbonyl fragments potentially interacting as compared to 14%. However, initial calculations have shown the interaction energy for the transition metal motif (A) to be very similar to the organic case at similar separations. Nonetheless, these investigations do suggest that carbonyl-carbonyl interactions may have an influence on the crystal structures adopted by carbonyl containing transition metal compounds, along with the hydrogen bonding interactions identified by Braga.

It is important to note that this study is by no means conclusive as transition metal carbonyl complexes often contain multiple carbonyl fragments and, therefore, they are likely to end up near each other in the crystal structures whether or not they are involved in an interaction. Even assuming that an attractive interaction occurs, the energetic gain from this may be lost through repulsive interactions between two similarly polarized carbon or oxygen atoms in other carbonyl fragments. In other words the close contact of carbonyls in

transition metal complexes may simply occur because it is the most efficient way for the molecules to pack. Hence, the current investigation suggests the need for additional computational studies in order to calculate the energetics in a variety of transition metal carbonyl containing complexes with a view to making a definitive conclusion with respect to intermolecular carbonyl-carbonyl interactions in transition metal complexes.

4.7 References

[4.1] Shriver, D.F., Atkins, P.W., Langford, C.H. (1994) *Inorganic Chemistry,* Oxford University Press.

[4.2] Allen, F.H., Baalham, C.A., Lommerse, J.P.M, Raithby, P.R. (1998) *Acta Cryst.,* **B54,** 320-329.

[4.3] Steed, J.W. *et al.* (2000) *Supramolecular Chemistry,* Wiley.

[4.4] Price, S.S.L. (2004) *Cryst. Eng. Comm.,* **6,** 344-353.

[4.5] Matsumoto, A., Tanaka, T., Tsubouchi, T., Tahiro, K., Saragai, S., Nakamoto, S. (2002) *J. Am. Chem. Soc.,* **124,** 8891-8902.

[4.6] Boiling points for the hydrogen halides http://www.airliquide.com/en/business/products/gases/gasdata/

[4.7] Bolton, W. (1965) *Acta. Cryst.,* **18,** 5-10.

[4.8] Bolton, W. (1964) *Acta. Cryst.,* **17,** 147-152.

[4.9] Taylor, R., Mullaley, A., Mullier, G.W. (1990) *Pest. Sci.,* **29,** 197-213.

[4.10] Gavezzotti, A. (1990) *J. Phys. Chem.,* **94,** 4319-4325.

[4.11] Shriver, D.F., Atkins, P.W., Langford, C.H. (1994) *Inorganic Chemistry, Second Edition,* Oxford University Press.

[4.12] Braga, D., Grepioni, F. (1994) *Acc. Chem. Res.,* **27,** 51-56.

[4.13] Braga, D., Grepioni, F., Wadepohl, H., Gebert, S., Calhorda, M.J., Veiros, L.F. (1995) *Organometallics,* **14,** 5350-5361.

[4.14] Braga, D., Grepioni, F. (1996) *Chem. Comm.,* 571-578.

[4.15] Braga, D., Grepioni, F. (1997) *Acc. Chem. Res.,* **30,** 81-87.

[4.16] Braga, D., Grepioni, F., Sabatino, P., Desiraju, G.R. (1994) *Organometallics,* **13,** 3532-3543.

[4.17] Gentric, E., Le Borgne, G., Grandjean, D. (1978) *J. Organomet. Chem.,* **155,** 207-220.

[4.18] Rettig, S.J., Storr, A., Trotter, J. (1988) *Can. J. Chem.,* **66,** 97-100.

[4.19] Shields, G. *Permute program.,* Cambridge Crystallographic Data Centre, 12 Union Road, Cambridge. CB2 1EZ. UK.

[4.20] Chisholm, J. *Personal Communication.*

[4.21] Clot, E. *Personal Communication.*

Chapter 5
Photo-Crystallography

5.1 Introduction

Photo-crystallography is used to determine the structures of molecules in metastable or excited states which have been generated by illumination of the crystal. The technique is still in its infancy having become practicable by advances in both the instrumentation and software available for X-ray diffraction experiments, which have allowed ever smaller samples to be studied in shorter time frames and at lower temperatures. There are essentially three methodologies that can be employed in such experiments, depending on the lifetime (τ) of the species of interest. These strategies are [5.1]:

1. *Steady state* – ($\tau >$ minutes); In such cases the lifetime of the excited state species is greater than the duration of the experiment, *i.e.* metastable. Hence once induced, typically by pumping with a broad band light source or laser, this excited state remains stable throughout the data collection. As well as looking at species with long lifetimes this approach can also be applied to compounds showing irreversible structural change as a result of excitation.

2. *Pseudo steady state* – (ms $\leq \tau \leq$ minutes); Species suitable for study in this manner have lifetimes shorter than the duration of the experiment. However, excited state populations can be maintained if they are continuously irradiated using an optical source with a repetition rate greater than τ.

3. *Pump-probe* – (ns $\leq \tau \leq$ ms); The experimental design, for species with lifetimes in the μs to ms range, typically includes a mechanical chopper which is carefully timed to ensure that the sample is being excited (pumped) and measured (probed) at the same time. The speed at which this process reoccurs is designed to match the repetition rate of the laser, and the length of the X-ray pulse is carefully controlled to match the lifetime of the excited state. This methodology is suitable for species with very short lifetimes, but it is far more complicated to carry out than the first two approaches. For species with excited state lifetimes in the ns to μs range the inherent time structure of the synchrotron can be used instead of a mechanical chopper to control the timing of the X-ray probe during the experiment.

In general, photo-crystallographic experiments require the use of fairly small crystals, since the penetration depth of the light is typically only of the order of a few microns. However, the sample still needs to be large enough to produce a strong diffraction pattern in order that the excited state can be clearly identified. As a result, synchrotron radiation is often employed in preference to conventional laboratory sources, since it is much more intense and allows smaller samples to be studied.

The term 'photo-crystallography' covers a wide variety of phenomena that can be induced in the solid state including spin crossover [5.2], bond length contractions/expansions [5.3] and linkage isomerism [5.4]. However, the work within this chapter focuses on metastable photo-induced linkage isomerism, and hence it is the only process for which further discussion is included.

5.1.1 Photochemical Linkage Isomerism

Light induced isomerism in metal complexes has been recognised since the late 1970s [5.5], however, the first crystallographic study was not conducted until the early 1990s when Woike *et al* [5.6] used neutron diffraction to study the photo induced structural changes that occur is sodium nitroprusside, $Na_2[Fe(CN)_5(NO)]\cdot 2H_2O$. The same compound was subsequently used by Coppens *et al* [5.4][5.7] to carry out the first X-ray diffraction experiment into such phenomena. From the residual electron density map, clear evidence was found for a change in the coordination mode of the NO group, from η^1 (N) in the ground state to η^2 (N and O) in the MS2 metastable state, see Figure 5.1.

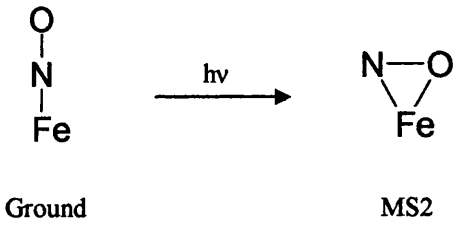

Figure 5.1 - *Illustration of the manner in which the photochemically induced linkage isomerism occurs in the MS2 metastable state of $Na_2[Fe(CN)_5(NO)]\cdot 2H_2O$ [5.4].*

Like the nitrosyl ligand, sulphur dioxide can also exhibit changes in coordination mode upon excitation. Potentially it can bind to the metal centre in a variety of ways, see Figure 5.2, although currently only half of the illustrated binding modes, namely (a), (b), (c) and (e), have been observed [5.8].

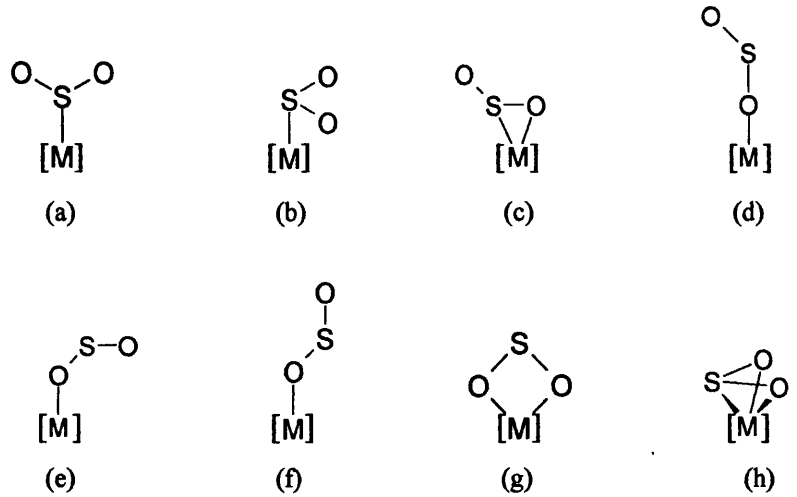

Figure 5.2 - *Potential binding modes for SO_2 [5.8].*

In the late 1970s, Dew and Johnson provided the earliest reported evidence of metastable sulphur dioxide linkage isomerism from a low temperature infrared study on the ruthenium complex, $[Ru(NH_3)_4Cl(SO_2)]Cl$ [5.5]. They observed changes in the stretching frequencies relating to the SO_2 group which occurred both in KBr disks and Nujol mulls ruling out Br^- substitution in the former. On the basis of their measurements they identified two metastable states, MS1 and MS2, as well as a short lived intermediate species for which they postulated the reaction scheme shown in Figure 5.3.

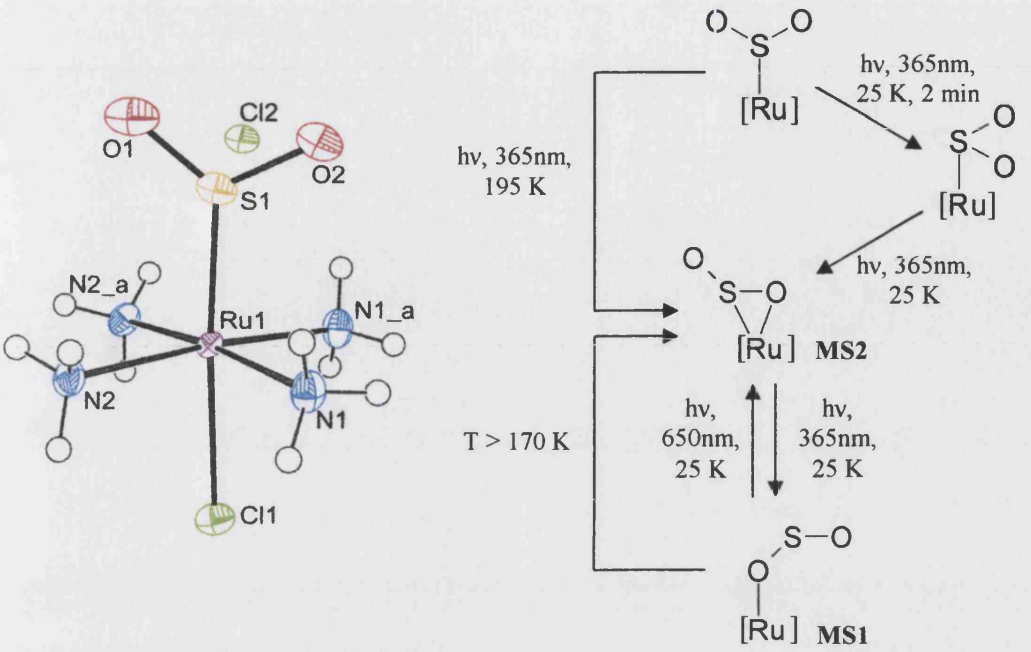

Figure 5.3 - *(left) Crystal structure of $[Ru(NH_3)_4Cl(SO_2)]Cl$, ellipsoids are represented at the 50% probability level, and '_a' signifies atoms related to the asymmetric unit by (x, 3/2-y, z) (right) Postulated reaction scheme for the linkage isomerism of SO_2 in $[Ru(NH_3)_4Cl(SO_2)]Cl$ from IR measurements [5.5].*

The first photocrystallographic experiments examining the linkage isomerism of SO_2 were conducted by Coppens *et al* on two similar ruthenium sulphur dioxide complexes, $[Ru(NH_3)_4Cl(SO_2)]Cl$ and $[Ru(NH_3)_4(H_2O)(SO_2)](C_6H_5SO_3)_2$. Single crystals of each compound were irradiated with a 488 nm Ar^+ CW laser at 90 K producing MS2 metastable state populations of 10% and 11% respectively [5.8]. In conjunction with X-ray crystallographic analysis, a series of DFT calculations were carried out, from which the conformation of MS1 was proposed, see Figure 5.4 [5.8]. The experimental (MS2) and theoretical (MS1) structures obtained for the two linkage isomers were consistent with the reaction scheme postulated in Figure 5.3.

Figure 5.4 - *Illustration of the calculated conformation of MS1 for (a) $[Ru(NH_3)_4Cl(SO_2)]Cl$, (b) $[Ru(NH_3)_4(H_2O)(SO_2)](C_6H_5SO_3)_2$ [5.8].*

5.1.2 Experimental Strategy

The investigations discussed within this chapter constitute a study on the light induced linkage isomerism of the sulphur dioxide fragment in $[Ru(NH_3)_4(H_2O)(SO_2)](C_6H_5SO_3)_2$. The two main objectives were to:

1. *Extend the studies carried out by Coppens et al [5.9] on the MS2 state of* $[Ru(NH_3)_4(H_2O)(SO_2)](CH_3C_6H_4SO_3)_2$. The effect of irradiation time on the percentage conversion is examined in conjunction with the influence of different light sources on the maximum levels of excitation that can be achieved. In addition, a *pseudo* steady state measurement is attempted using this compound, since the excitation is known to be observable crystallographically, to confirm whether the experimental strategy employed is suitable for such studies.

2. *Attempt to obtain crystallographic evidence for other linkage isomers of* $[Ru(NH_3)_4(H_2O)(SO_2)](CH_3C_6H_4SO_3)_2$. The reaction scheme postulated by Dew and Johnson [5.5] for the linkage isomerism of SO_2 in $[Ru(NH_3)_4Cl(SO_2)]Cl$ indicated the presence of another metastable state, MS1, in addition to MS2 and another transient species. Crystallographic studies are invoked to obtain evidence for at least one of these other isomers.

5.2 Synthesis

5.2.1 Infrared (IR) Spectroscopy

Infrared data was collected on a Nicolet Nexus FT-IR spectrometer, using 32 scans at 2 cm^{-1} resolution over the range 4000-500 cm^{-1}. The spectra were collected as Nujol mulls.

5.2.2 $[Ru(III)(NH_3)_5Cl]Cl_2$ [5.10]

$$[Ru(III)(NH_3)_6]Cl_3 \xrightarrow[\text{ii) conc. HCl, reflux}]{\text{i) } H_2O\text{, heat}} [Ru(III)(NH_3)_5Cl]Cl_2$$

2.456g (0.0079 mole) of $[Ru(III)(NH_3)_6]Cl_3$ was dissolved in 27 ml of water by warming, and to this solution was added 27 ml of concentrated HCl. The solution was refluxed for 3.5 hours during which a yellow precipitate formed. The precipitate was

filtered, washed first with 1:1 water:HCl and then methanol before being dried under vacuum at room temperature.

A yield of 2.050g, 0.007 mole (88%) of $[Ru(III)(NH_3)_5Cl]Cl_2$ was obtained. The major peaks in the infrared spectrum were assigned. The peaks at 3210 cm^{-1} (NH, symmetric stretch, strong), 1621 cm^{-1} (NH, asymmetric deformation, medium) and 791 cm^{-1} (NH, rock, medium) were consistent with the literature values [5.10].

5.2.3 $[Ru(II)(NH_3)_4(HSO_3)_2]$ [5.10]

$$[Ru(III)(NH_3)_5Cl]Cl_2 \xrightarrow[\text{ii) } NaHSO_3,\ SO_2(g)\ 75°]{\text{i) } H_2O,\ 75\text{-}85°} [Ru(II)(NH_3)_4(HSO_3)_2]$$

2.050g (0.007 mole) of $[Ru(III)(NH_3)_5Cl]Cl_2$ was dissolved in 82 ml of H_2O at 85°C. An excess 2.900g (0.028 mole) of solid $NaHSO_3$ was added at 75°C, and sulphur dioxide gas was bubbled slowly through the solution for 1 hour. The solution was subsequently allowed to cool slowly to room temperature with continued saturation of sulphur dioxide. Yellow crystals formed during the reaction and these were filtered off and washed first with water and then methanol before being dried under vacuum at room temperature.

A yield of 1.879g, 0.0057 mole (81%) of $[Ru(II)(NH_3)_4(HSO_3)_2]$ was obtained. The major infrared peaks were assigned with those at 3260 cm^{-1} (NH, symmetric stretch, strong), 1641 cm^{-1} (NH, asymmetric deformation, medium) and 796 cm^{-1} (NH, rock, medium) being consistent with the literature values [5.10].

5.2.4 $[Ru(II)(NH_3)_4(SO_2)Cl]Cl$ [5.10]

$$[Ru(II)(NH_3)_4(HSO_3)_2] \xrightarrow{\text{i) 1:1 HCl, heat}} [Ru(II)(NH_3)_4(SO_2)Cl]Cl$$

1.897g (0.0057 mole) of $[Ru(II)(NH_3)_4(HSO_3)_2]$ was dissolved in 220 ml of 1:1 water:HCl by heating at the boiling point (130°C) for around 15 minutes. The solution which had turned a deep red colour was filtered hot and the filtrate reheated to redissolve any crystals that had formed, before leaving to cool slowly in an oil bath overnight. Orange red needle shaped crystals of $[Ru(II)(NH_3)_4(SO_2)Cl]Cl$ were filtered and washed with 1:1 water:HCl then methanol before being dried under vacuum at room temperature.

A yield of 1.403g, 0.0046 mole (81%) of $[Ru(II)(NH_3)_4(SO_2)Cl]Cl$ was obtained. The major peaks in the infrared spectrum were assigned, with those at 3230 cm^{-1} (NH, symmetric stretch, strong), 1631 cm^{-1} (NH, asymmetric deformation, medium), 788 cm^{-1} (NH, rock, medium), 1309 cm^{-1} and 1285 cm^{-1} (SO, asymmetric stretch, strong) being consistent with the literature values [5.10].

5.2.5 $[Ru(II)(NH_3)_4(H_2O)(SO_2)](CH_3C_6H_4SO_3)_2$ [5.9]

$$[Ru(II)(NH_3)_4(SO_2)Cl]Cl_2 \xrightarrow{\text{i) } CH_3C_6H_4SO_3H{\cdot}H_2O,\ 90^\circ} [Ru(II)(NH_3)_4(H_2O)(SO_2)](C_6H_5SO_3)_2$$

Toluene sulphonic acid monohydrate 0.419g (0.0022 mole) was dissolved in 16 ml of water. 0.094g (0.0003 mole) of $[Ru(II)(NH_3)_4(SO_2)Cl]Cl$ was added and the mixture heated to 90°C with vigorous stirring, the solid dissolved in several minutes. The resulting solution was left to cool slowly in an oil bath overnight. Yellow-orange plate like crystals of $[Ru(II)(NH_3)_4(H_2O)(SO_2)](C_6H_5SO_3)_2$ were then filtered and washed with diethyl-ether before being air dried.

The published method [5.9] used 0.2g of toluene sulphonic acid in 10 ml of water with 50mg of $[Ru(II)(NH_3)_4(SO_2)Cl]Cl$. However, initial attempts were unsuccessful with these ratios and the solution merely turned pink after several days. Hence we decided to employ toluene sulphonic acid monohydrate and lower volumes of water in the synthesis; the method reported here gave the best crystals.

A yield of 0.151g, 0.00025 mole (85%) of $[Ru(NH_3)_4(H_2O)(SO_2)](CH_3C_6H_4SO_3)_2$ was obtained. These crystals were used in subsequent photo-crystallography experiments.

5.3 Photo-Crystallography

5.3.1 Experimental

5.3.1.1 Data Collection

Single crystal X-ray diffraction data were collected on Station 9.8 at Daresbury synchrotron, using a D8 diffractometer fitted with either a Bruker Smart or Bruker Apex 2 CCD detector. Cooling of the sample was achieved through the use of a cryostream or helijet.

The single crystal work detailed in this chapter was collected over several Daresbury allocation periods giving a total of around 20 days of experimentation, during which time approximately 130 datasets were collected and analysed. The structures were sequentially numbered under either tosylateXX or rutXX, where XX represents the structure number,

depending on the experimental session in which they were collected. A summary of the experimental details for each of the structures discussed in this chapter are included in Table 5.3 at the end of this chapter, with bond lengths and angles listed in Appendix 5.1.

5.3.1.2 Experimental Set-up

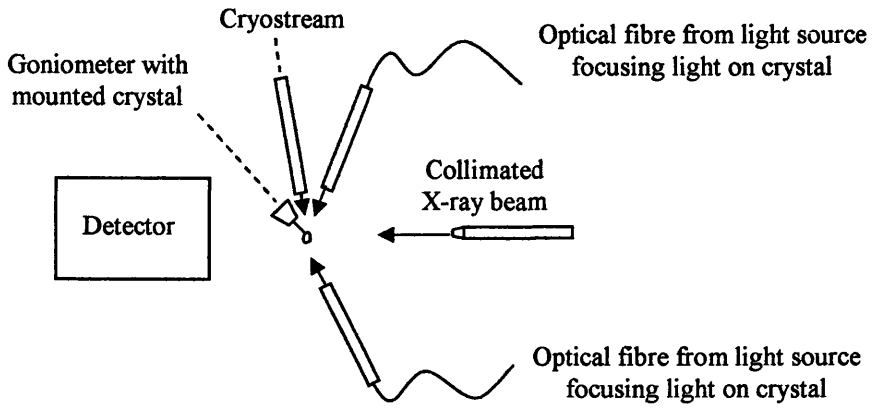

Figure 5.5 - *Schematic of experimental set-up.*

The experimental set-up is illustrated in Figures 5.5 and 5.6. The diffractometer was surrounded by sheets of black pond liner to remove exterior light, which previous experiments had shown would be sufficient to induce slight excitation in the tosylate crystals. The light source was located outside the black pond liner and optical fibres were used to focus the light onto the sample. A shutter was fitted to the cryostream allowing the crystal to be flash warmed and cooled in the dark. Both the light source and the cryostream shutter were attached to electronic timers and could be operated from outside the hutch without disturbing the experimental area.

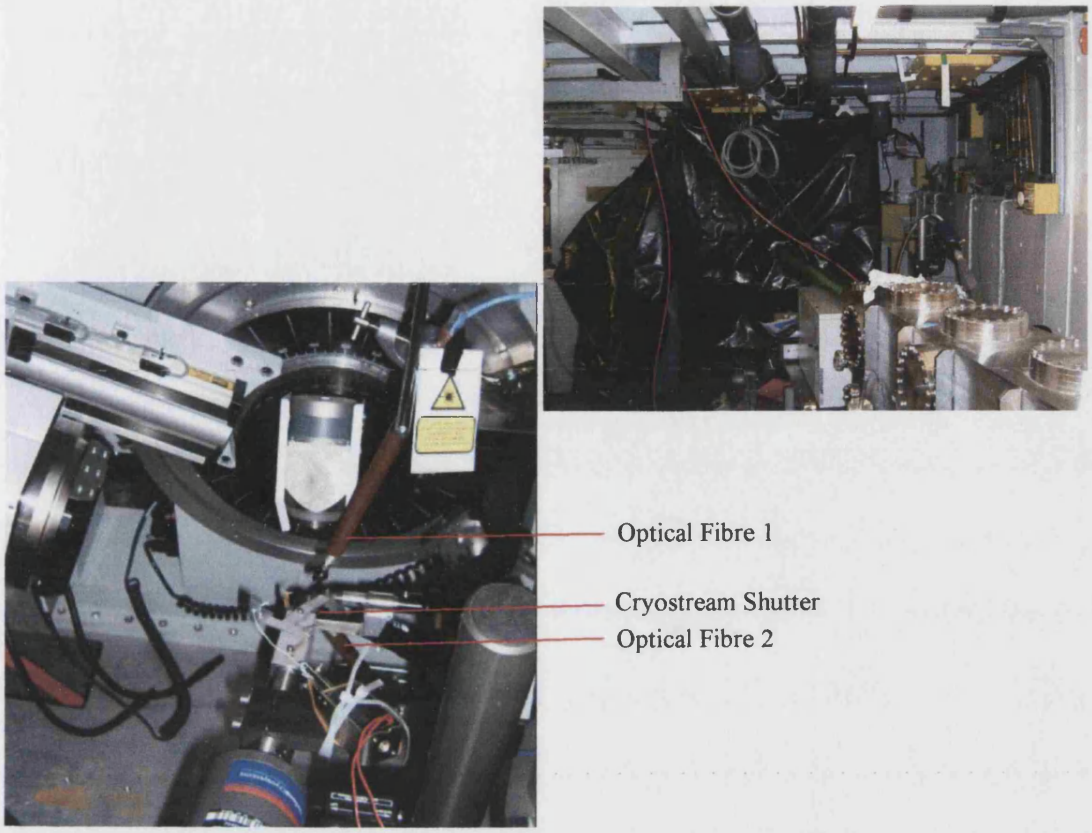

Figure 5.6 - *Photographs of experimental set-up, (left) around crystal, (right) around goniometer.*

5.3.1.3 Irradiation Procedure to Obtain MS2 for $[Ru(NH_3)_4(H_2O)(SO_2)](CH_3C_6H_4SO_3)_2$

A variety of light sources were employed to generate the metastable state: a 5mW green laser pointer (532 nm), a 100mW 532 nm diode laser and broad band 'white' microscope lights. All of these had been shown to generate MS2, however, experiments carried out in Cambridge had indicated that the 100mW 532 nm diode laser should induce the maximum excitation [5.11].

The investigation procedure for studying MS2 required the following considerations:

1. *Ensuring that the metastable state could be fully dissipated between measurements without damaging the integrity of the single crystal.* This was achievable by raising the sample to room temperature, where the lifetimes of the metastable states are of the order of seconds. Subsequently, the crystal could be returned to the experimental temperature (100 K) for further data collections.

2. *Testing all of the light sources to determine the percentage of MS2 as a function of irradiation time.* The effects of prolonged irradiation on the sample are unknown; it is possible that the maximum excitation is rapidly achieved or that it rises as the length of exposure increases. In order to conduct these experiments, the light sources were controlled by an electronic timer and the excitation levels monitored as a function of exposure time at 100 K. Ground state structures were collected at appropriate intervals to ensure that MS2 was not present prior to irradiation and that the quality of the single crystal was not deteriorating.

3. *Attempting a pseudo steady state measurement.* The data collections were carried out at temperatures where MS2 would be decaying, since its lifetime was less than the duration of the experiment. The sample was continuously irradiated throughout the measurements at 250 K, 260 K, 270 K and 280 K, and the percentage excitation determined in each case.

5.3.1.4 Irradiation Procedure to Observe MS1 for $[Ru(NH_3)_4(H_2O)(SO_2)](CH_3C_6H_4SO_3)_2$.

The structure of MS2 had been previously identified in a photo-crystallographic study, however, MS1 had not been observed, although its conformation had been predicted from DFT calculations [5.8]. In theory, MS1 should be stable at low temperatures as IR experiments had identified it (Section 5.1.1), and in an attempt to try and observe it experimentally a single crystal of $[Ru(NH_3)_4(H_2O)(SO_2)](CH_3C_6H_4SO_3)_2$ was irradiated at 12.5 K using a deuterium light source.

5.3.1.5 Software

The software employed throughout the chapter was discussed in Section 3.2.6.2.

5.3.1.6 Caveats for the Results

Before analysing the experimental results two points should be noted; firstly the percentage excitation was determined crystallographically, and not confirmed by any other experimental method. This means that while the metastable state populations are relatively comparable to each other between experiments, they may not be absolute as there is a high correlation between occupancies of the atoms and their displacement parameters. Secondly, throughout this chapter an accurate comparison of bond lengths and angles for the sulphur dioxide fragment is not possible either due to low levels of excitation or large amounts of disorder within the SO_2 fragments.

5.4 Results

5.4.1 Ground State Structure of $[Ru(NH_3)_4(H_2O)(SO_2)](CH_3C_6H_4SO_3)_2$

5.4.1.1 Obtaining a Ground State Structure for $[Ru(NH_3)_4(H_2O)(SO_2)](CH_3C_6H_4SO_3)_2$.

In order to obtain a clean unpolluted ground state, the crystal had to be maintained at room temperature, in the dark. This allowed the excitation to dissipate, as the metastable states are only stable for any significant period of time at low temperatures. Upon gradual warming and cooling the crystalline quality of the sample diminished. However, employment of a cryostream shutter allowed the temperature to be rapidly altered while maintaining the integrity of the crystal. The excitation was found to be fully reversible, and ground state structures obtained at various points during the experiment were comparable to the initial refinement.

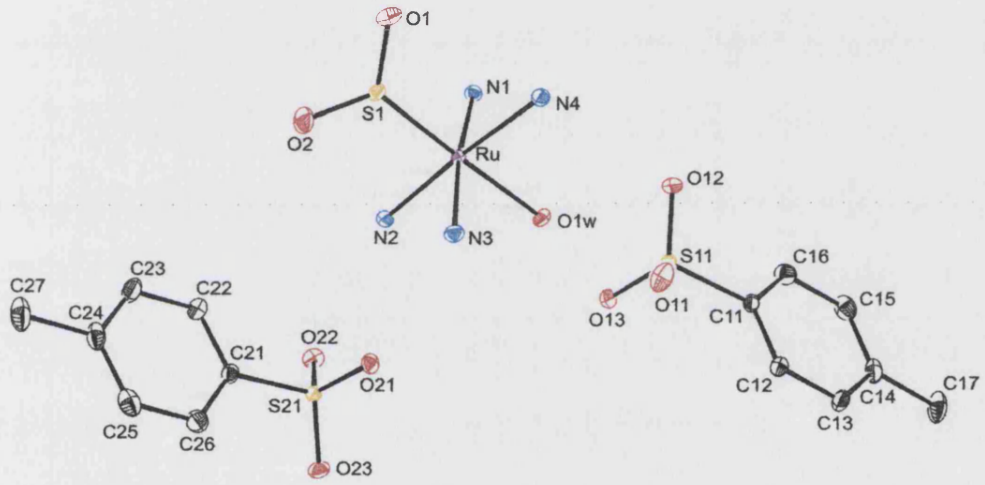

Figure 5.7 - *$[Ru(NH_3)_4(H_2O)(SO_2)](CH_3C_6H_4SO_3)_2$ ground state structure at 100 K (tosylate2). Ellipsoids are represented at the 50% probability level.*

Figure 5.7 shows the asymmetric unit for the ground state of the ruthenium tosylate complex, $[Ru(NH_3)_4(H_2O)(SO_2)](CH_3C_6H_4SO_3)_2$, which crystallised in the triclinic space group *P*-1. The coordination geometry around the ruthenium atom is octahedral, with an S_1-Ru-O_{1w} angle of 178.18(3)° and *trans* nitrogen angles of 171.68(4)° (N_1-Ru-N_3) and 176.12(4)° (N_2-Ru-N_4). The sulphur dioxide has an O_1-S_1-O_2 angle of 115.95(7)°, and is η^1 coordinated to the metal centre through the sulphur atom. The bond lengths and angles throughout the structure were unremarkable and consistent with those found for similar fragments in the Cambridge Structural Database (CSD).

The supramolecular array for tosylate2 showed that the structure consisted of alternate organic and organometallic layers, with weak offset π-π stacking between pairs of symmetry related phenyl rings in adjacent tosylate groups at separations of 3.77(1) Å (C_{11}-

C_{16}) and 3.67(1) Å (C_{21}-C_{26}). Four types of hydrogen bonding were observed throughout the structure with the following donor to acceptor distance ranges; 2.939(2) Å - 3.334(2) Å (moderate, N-H...O), 3.644(1) Å - 3.922(1) Å (weak, N-H...S), 2.663(1) Å - 2.690(2) Å (moderate, O-H...O) and 3.580(1) Å - 3.586(1) Å (weak, O-H...S), see Figure 5.8.

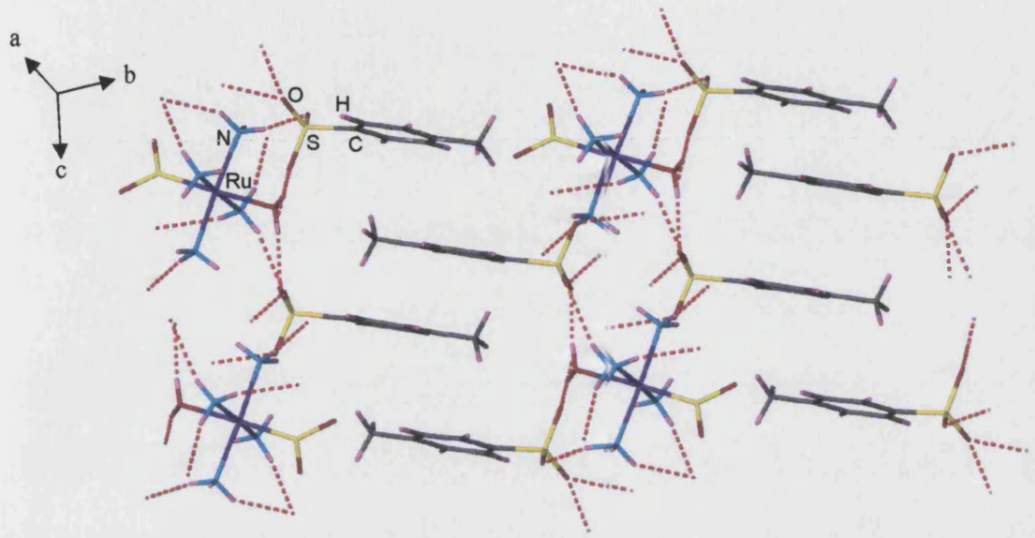

Figure 5.8 - *Hydrogen bonding shown by dashed lines in ground state crystal structure of* $[Ru(NH_3)_4(H_2O)(SO_2)](CH_3C_6H_4SO_3)_2$ *at 100 K (tosylate2).*

5.4.2 MS2 Metastable State of $[Ru(NH_3)_4(H_2O)(SO_2))](CH_3C_6H_4SO_3)_2$

5.4.2.1 Modelling the MS2 Metastable State in $[Ru(NH_3)_4(H_2O)(SO_2)](CH_3C_6H_4SO_3)_2$

Several alternative methods were evaluated in the data analysis in order to find the most accurate way of modelling the MS2 metastable state fragment:

1) *Normalising the 'ground state' fragment of the metastable state to have the same geometry as the true ground state.* In this case the FRAG command was used to fix the geometry of the 'ground state' portion in the metastable state crystal, to that of the pure ground state. The metastable state SO_{22} fragment was then identified from a difference electron density map. This compares with the approach adopted by Coppens [5.9], however, the results were not fully satisfactory in this instance with large peaks and holes evident proximate to atoms in the residual electron density map, suggesting that the geometry of our fragment had altered slightly from that observed in the pure ground state.

2) *Modelling the MS2 metastable state fragment as disorder.* The experiments to be carried out on MS2 (Section 5.3.1.3), examining the effect of irradiation time on the excitation and attempting to obtain a *pseudo*-steady state measurement at higher temperature, require the same treatment of the metastable state fragment(s) in order to obtain meaningful results. The occupancies of the sulphur dioxide fragments were associated with free variables, the sum of which were set to equal 1 using SUMP. No restraints were placed upon the bond lengths in the SO_2 group of the MS2 fragment although the anisotropic temperature factors were constrained to be similar with SIMU. While the second disordered MS2 fragment is probably real, the levels were too small to model accurately and hence they were excluded, resulting in small residual electron density peaks (less than 1.5 $eÅ^{-3}$) around the SO_2 groups in many of the excited structures. This was the method that was employed, although the structures with the highest levels of excitation showed some evidence of a second component of MS2; this was very small.

5.4.2.2 Structure of MS2 in $[Ru(NH_3)_4(H_2O)(SO_2)](CH_3C_6H_4SO_3)_2$

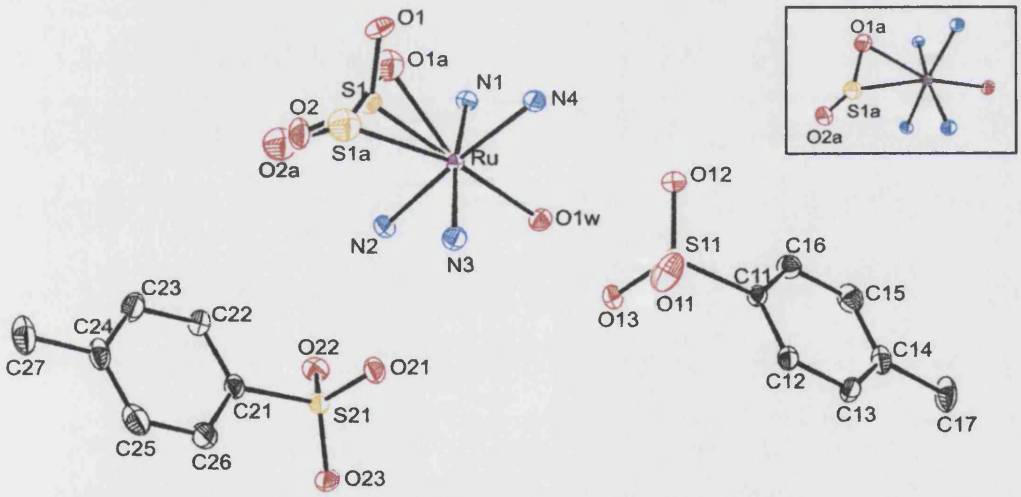

Figure 5.9 - *Asymmetric unit for $[Ru(NH_3)_4(H_2O)(SO_2)](CH_3C_6H_4SO_3)_2$ containing the MS2 metastable state (tosylate14). (Insert) MS2 fragment.*

The crystal structure obtained after 9.2 hours of irradiation with the microscope lights at 100 K, (tosylate14), is illustrated in Figure 5.9. It contained approximately 15% of MS2, and maintained the triclinic *P*-1 symmetry of the ground state with small changes in the unit cell parameters that could not have been due to heating effects from the microscope lights as these were switched off during the data collection, see Table 5.1.

Table 5.1 - *Comparison of unit cell data obtained from structures of the ground state and MS2 (15%).*

	a (Å)	*b* (Å)	*c* (Å)	*α* (°)	*β* (°)	*γ* (°)	V (Å^3)
Ground (tosylate2)	6.6945 (3)	13.1054 (5)	13.6251 (6)	94.457 (2)	92.854 (2)	103.579 (2)	1155.6 (8)
MS2 (15%) (tosylate14)	6.6729 (3)	13.1003 (6)	13.7073 (6)	94.579 (1)	92.651 (1)	103.392 (1)	1159.4 (9)

While the ground state fragment (S_1, O_1, O_2) exhibited octahedral coordination at the ruthenium atom, MS2 (S_{1A}, O_{1A}, O_{2A}) revealed seven atoms attached to the metal centre. This was as a result of a change in the coordination mode of the SO_2 group from η^1 (S_1) to η^2 (S_{1a} and O_{1a}), with O-S-O angles of 115.82(1)° and 121.2(11)°, respectively. The *trans* nitrogen angles were comparable to those observed in the clean ground state (tosylate2) at 171.56(6)° (N_1-Ru-N_3) and 176.00(6)° (N_2-Ru-N_4), as was the S_1-Ru-O_{1w} angle of 178.65(4)°. The hydrogen bonding and π-π stacking in tosylate14, and all of the structures collected during this study that analysis showed to contain both the ground and MS2 states, were comparable to that observed in tosylate2 with similar distances and angles.

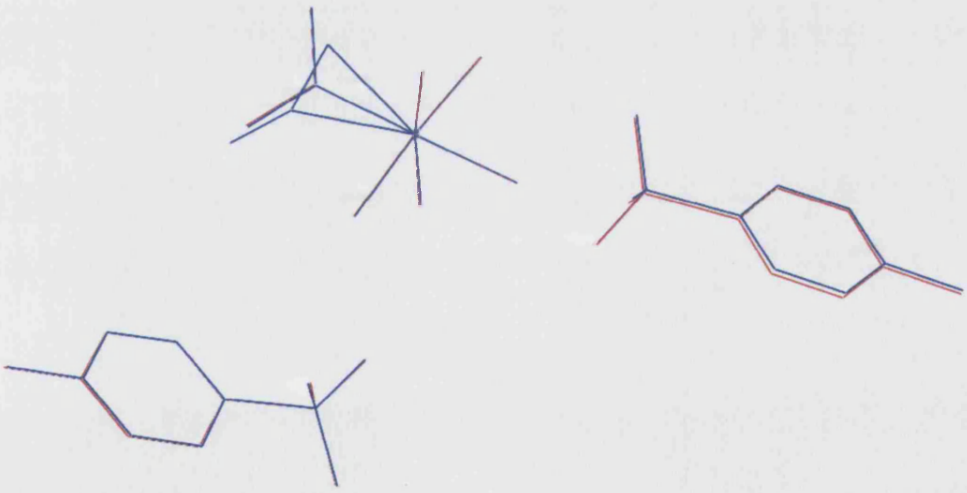

Figure 5.10 - *Overlay of asymmetric units for tosylate2 (red) and tosylate14 (blue).*

The change in coordination mode of the sulphur dioxide appeared to have had very little effect on the overall crystal structure, with the two asymmetric units mapping almost exactly onto each other, see Figure 5.10. This may possibly be due to the small amount (15%) of MS2 present in the structure. However, there is some free space around the sulphur dioxide fragment in the ground state, which may be sufficient to accommodate the

change in binding mode without significant distortion to the rest of the structure, see Figure 5.11.

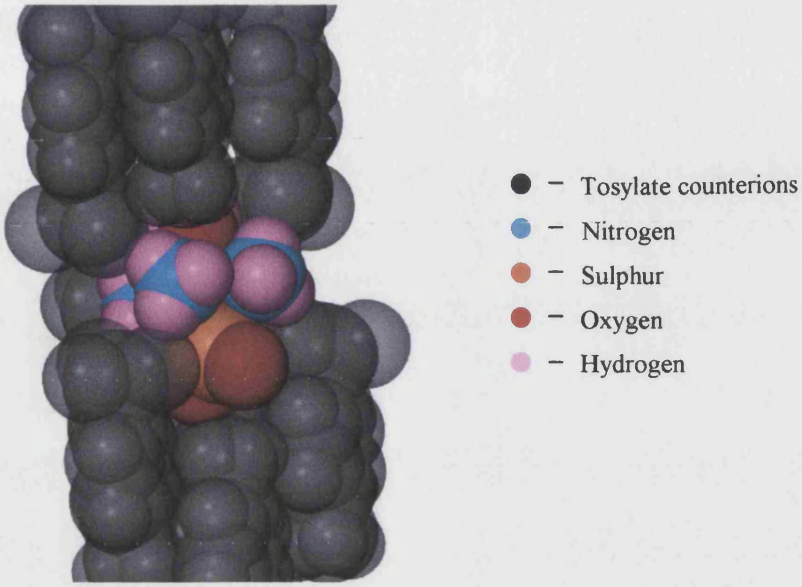

Figure 5.11 - *Space filling diagram for the ground state structure tosylate2, (central fragment, solid fill) [Ru(NH$_3$)$_4$(H$_2$O)(SO$_2$)] with SO$_2$ group pointing down, (grey, transparent) tosylate groups.*

5.4.3 Effect of Irradiation Time on Excitation Levels of MS2 in [Ru(NH$_3$)$_4$(H$_2$O)(SO$_2$)](CH$_3$C$_6$H$_4$SO$_3$)$_2$

In order to establish the maximum excitation possible and how quickly it is achieved for the different light sources, multiple datasets were collected on the same crystal after increasing periods of irradiation at 100 K. The irradiation was carried out in a cumulative manner, by exposing a crystal, that had been shown to be in the ground state, to light for a certain time after which the lights were turned off and a data collection made. The crystal was subsequently irradiated again and another data collection made without dissipating the metastable state. The results are illustrated graphically in Figure 5.12.

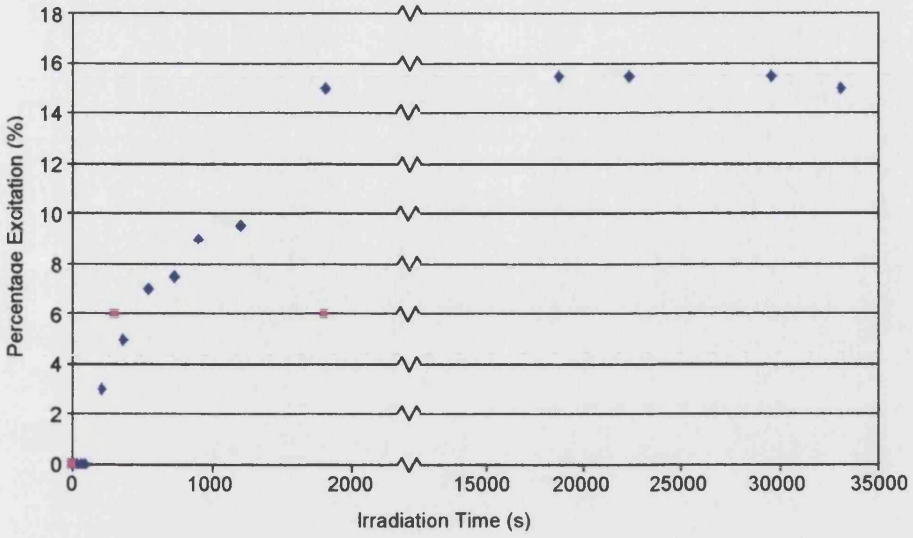

Figure 5.12 - *Graph showing the excitation levels as a function of irradiation time. (blue) microscope lights, (pink) 100mW 532 nm green laser.*

The levels of MS2 observed in the sample following irradiation with the microscope lights were initially dependent on the exposure time of the sample, up until approximately 15% excitation at around 30 minutes. Beyond this point no further increase was achieved despite irradiating the crystal for an additional 8.7 hours. The same time dependence was not found in the case of the 100mW green laser and the maximum excitation of 6% was first recorded after just 5 minutes. Despite the fact that no measurements were made below this time point to determine exactly how long the excitation took, or if lower levels of MS2 were present at shorter irradiation times, it is apparent that the laser excitation is more rapid than that obtained with microscope lights.

Although, preliminary measurements on small amounts of sample held in a KBr matrix, had indicated that the 100mW 532 nm laser was the most favourable method of illumination [5.11], it only produced a total of around 6% of MS2, compared to the 15% achieved using the microscope lights. As detailed in the experimental set-up (Section 5.3.1.2), the light was directed onto the crystal using optical fibres, but since laser light does not tend to travel very efficiently along these fibres, a higher excitation might have been achieved by using mirrors to focus the laser output. However, it was subsequently calculated that the penetration depth for the 532 nm laser was only of the order of a few microns and less than that for the broad band light source [5.12]. Consequently, the higher excitation with the microscope lights becomes less surprising as the crystals used in X-ray diffraction experiments are much larger than the powdered grains of sample that were present in the KBr matrix of the initial studies. The 5mW green laser pointer did not appear to induce any

excitation in the crystal, but it may simply not have been intense enough to penetrate into the crystal.

5.4.4 Effect of Temperature on Excitation Levels of MS2 in $[Ru(NH_3)_4(H_2O)(SO_2)](CH_3C_6H_4SO_3)_2$

The lifetime of the MS2 metastable state is temperature dependent and although at 100 K the decay during the experiment is not significant, at higher temperatures this is not the case. In an initial attempt to analyse a *pseudo* steady state, a series of datasets were collected at temperatures above 250 K, which initial spectroscopic measurements had indicated was the temperature that MS2 ceases to be metastable. Hence, the excited state species would be decaying during the experiment. The excitation levels were determined at 250 K, 260 K, 270 K and 280 K, with the microscope lights on throughout the data collection, see Figure 5.13.

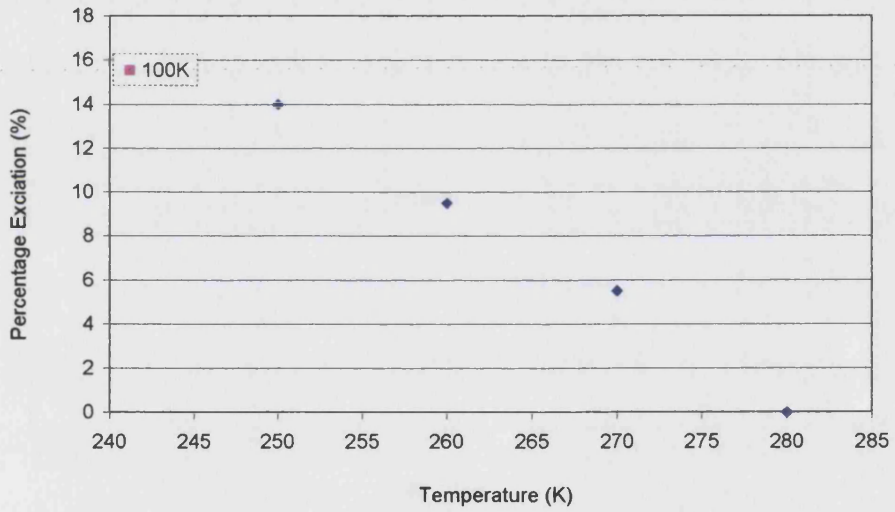

Figure 5.13 - *Graph showing temperature effects on excitation levels, all data was collected with the microscope lights on turbo throughout the experiment.*

The plot reveals a linear relationship between the percentage excitation and the temperature at which the measurement was made. Since an equibrilation period was facilitated before each dataset was collected, it seemed reasonable to suggest that the graph is showing the *pseudo* steady state populations that can be sustained by the microscope lights at each of the temperatures. This was further confirmed by a data collection made at 250 K in the dark, which showed an excitation of 8% compared to the 14% seen with the lights on.

The microscope lights were the only light source used to irradiate the sample in this series of measurements as they had given the maximum excitation levels in the earlier

experiments (Section 5.4.3). However, a future study using the laser may show that it is a more suitable source at the higher temperatures, since it achieves a more rapid excitation and might be able to maintain a larger MS2 population.

5.4.5 MS1 Metastable State of $[Ru(NH_3)_4(H_2O)(SO_2)](CH_3C_6H_4SO_3)_2$

5.4.5.1 Modelling the MS1 Metastable State in $[Ru(NH_3)_4(H_2O)(SO_2)](CH_3C_6H_4SO_3)_2$

A crystal of $[Ru(NH_3)_4(H_2O)(SO_2)](CH_3C_6H_4SO_3)_2$ was irradiated at 12.5 K using a deuterium light source in order to generate MS1. The amounts of each of the metastable states present in rut72 were modelled by associating the site occupation factors for each of the sulphur atoms with different free variables, the sum of which were set to equal 1, using SUMP. The conversion to MS1 was 'unclean' with the crystal also containing MS2, hence there were five modelled positions for the sulphur dioxide group (the ground state and two orientations for both MS1 and MS2), as a result equivalent bond lengths were restrained to be similar using SADI. All anisotropic temperature factors for the sulphur dioxide group were refined together subject to a SIMU instruction, although prior to this, the isotropic temperature factor for all of the sulphur atoms and most of the oxygen atoms were reasonable ranging from 0.01 $Å^2$ to 0.03 $Å^2$.

5.4.5.2 Structure of MS1 in $[Ru(NH_3)_4(H_2O)(SO_2)](CH_3C_6H_4SO_3)_2$

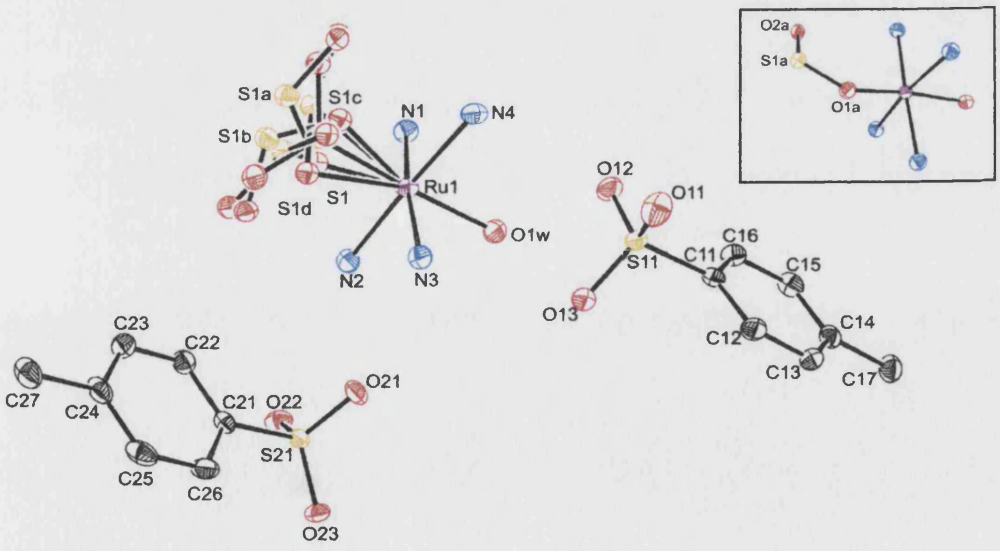

Figure 5.14 - *Asymmetric unit for polluted MS1 (rut72), (insert) MS1 (S_{1A}, O_{1A}, O_{2A}) fragment. Ellipsoids are represented at the 50% probability level.*

Figure 5.14 shows the structure obtained after 75 minutes irradiation with a deuterium light source (rut72). The triclinic *P*-1 symmetry of the ground state (tosylate2)

was maintained, and while the volume of the unit cell was unaltered, significant differences were observed in the unit cell angles as highlighted in bold on Table 5.2.

Table 5.2 - *Comparison of unit cell data obtained from structures of the ground state and MS1 (rut72).*

	a (Å)	*b* (Å)	*c* (Å)	α (°)	ß (°)	γ (°)	V (Å^3)
Ground (tosylate2)	6.6945 (3)	13.1054 (5)	13.6251 (6)	**94.457 (2)**	**92.854 (2)**	103.579 (2)	1155.6 (8)
MS1+MS2 (42.5% overall excitation) (rut72)	6.655 (3)	13.109 (6)	13.715 (6)	**91.663 (4)**	**96.450 (4)**	104.721 (4)	1147.8 (9)

The crystal structure of rut72 contained both MS1 and MS2 in the presence of atoms corresponding to the ground state fragment. Both of the metastable state species were disordered over 2 sites, at populations of 23.7% (S_{1A}) and 12.0% (S_{1B}) for MS1, and 6.1% (S_{1C}) and 2.1% (S_{1D}) for MS2. This disorder is unsurprising when considering that MS1 is obtained from the ground state via MS2. Thus, since the sulphur atom of the ground state (S_1) can shift either to the left or the right of its ground state position to form MS2, MS1 can potentially coordinate through either O_1 or O_2, see Figure 5.15. The scheme confirms that the geometry of MS1 is consistent with that calculated from DFT calculations [5.8].

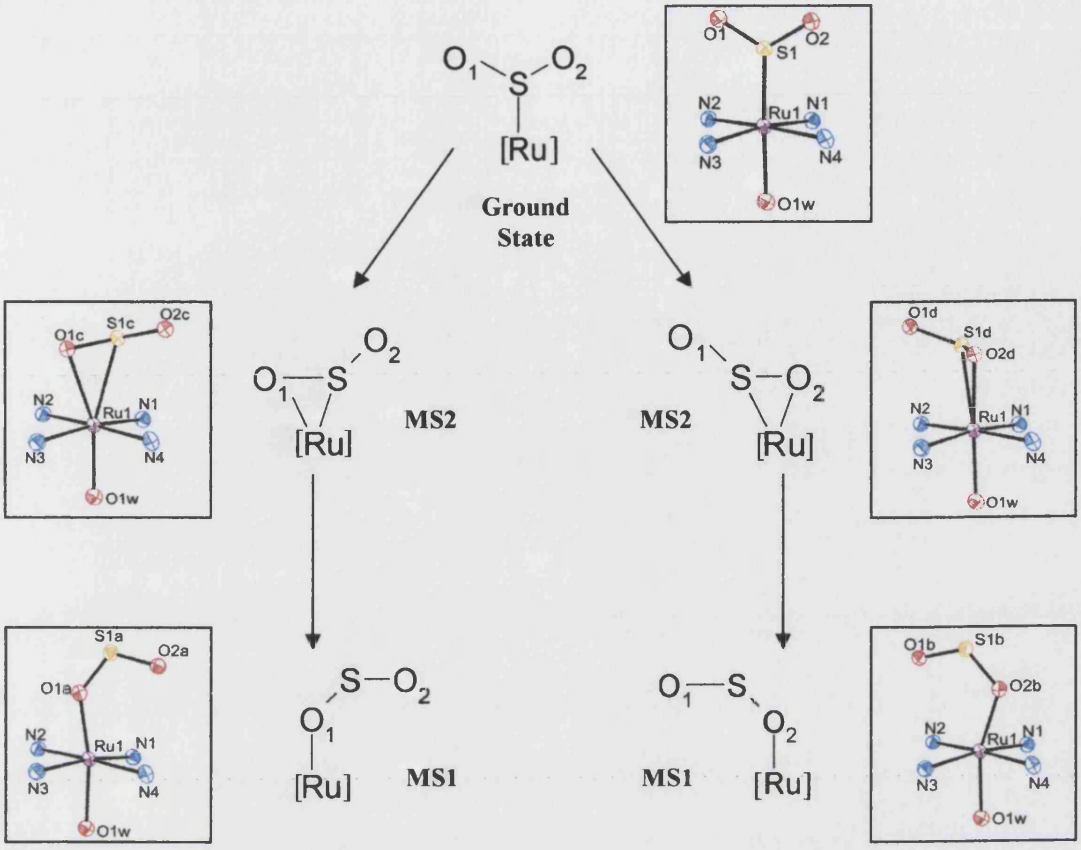

Figure 5.15 - *Illustration of the two pathways by which MS2 and MS1 can form, serving to explain why they are both disordered over two sites. Ellipsoids are represented at the 50% probability level.*

The S_1-Ru_1-O_{1w} angle of 177.32(8)° in rut72 was similar to that observed in the ground state structure (tosylate2), as were the values of 171.7(1)° and 177.2(1)°, for the *trans* N_1-Ru_1-N_3 and N_2-Ru_1-N_4 angles respectively. In the fragments relating to MS1 the *trans*-oxygen angles were 169.3(3)° (O_{1A}-Ru_1-O_{1w}) and 161.7(4)° (O_{2B}-Ru_1-O_{1w}). As previously mentioned (Section 5.1.1), the formation of MS2 from the ground state causes a change in the coordination mode of the sulphur dioxide to the ruthenium from η^1 (S) to η^2 (S and O). In MS1 this has returned to being an η^1 linkage, but this time through one of the oxygen atoms. The high levels of disorder in the SO_2 fragment and the restraints employed in the refinement make it impossible to obtain accurate values for the angles and bond lengths within the MS1 and MS2 coordination modes for this structure. However, these experiments provide unequivocal evidence for the presence of the MS1 state which was previously unreported.

Examination of the packing diagram for rut72 showed it to be similar to the ground state with offset weak π-π stacking between pairs of symmetry related phenyl groups in adjacent tosylate groups at distances of 3.85 (1) Å (C_{11}-C_{16}) and 3.54 (1) Å (C_{21}-C_{26}). The

structure still contains extensive hydrogen bonding, falling into four categories with the following donor to acceptor distance ranges; 2.879(4) Å - 3.368(4) Å (moderate, N-H...O), 3.540(3) Å - 4.195(3) Å (weak, N-H...S), 2.673(3) Å - 2.703(3) Å (moderate, O-H...O) and 3.466(3)Å - 3.535(3)Å (weak, O-H...S). These interactions are illustrated in Figure 5.16.

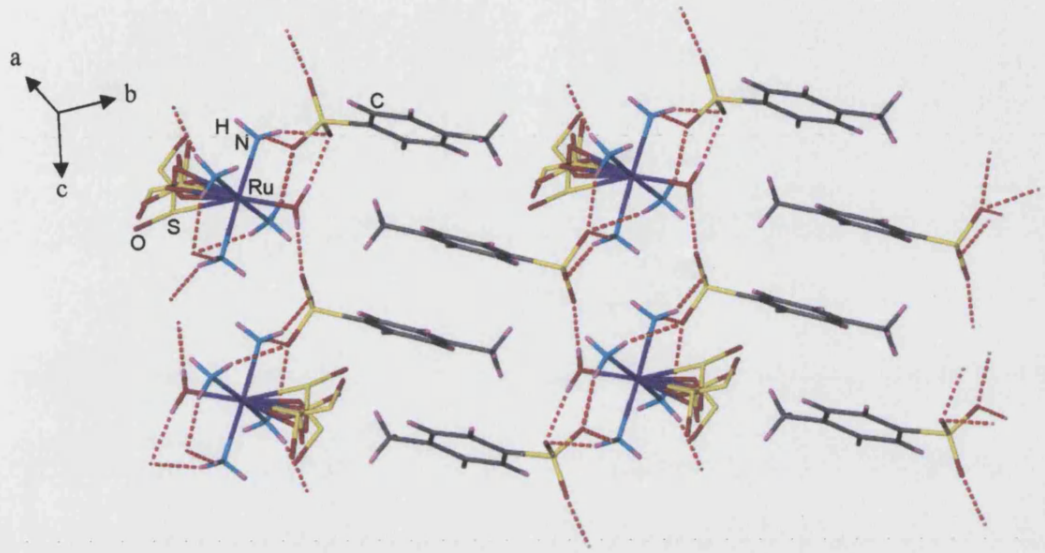

Figure 5.16 - *Hydrogen bonding shown by dashed lines in the metastable state structure, rut72, which contains both MS1and MS2.*

Significant changes in the positions of the tosylate groups with respect to the ruthenium complex were observed in rut72 when compared to the ground state structure (tosylate2), as shown in Figure 5.17. This is not surprising as a large amount of excitation was observed in rut72, and it is reasonable to expect that the tosylate groups would have to alter their positions to accommodate the different coordination mode of the sulphur dioxide. The lack of crystal degradation during the transformation may partially be due to the presence of the hydrogen bonding maintaining the crystal lattice during the excitation (Section 3.10).

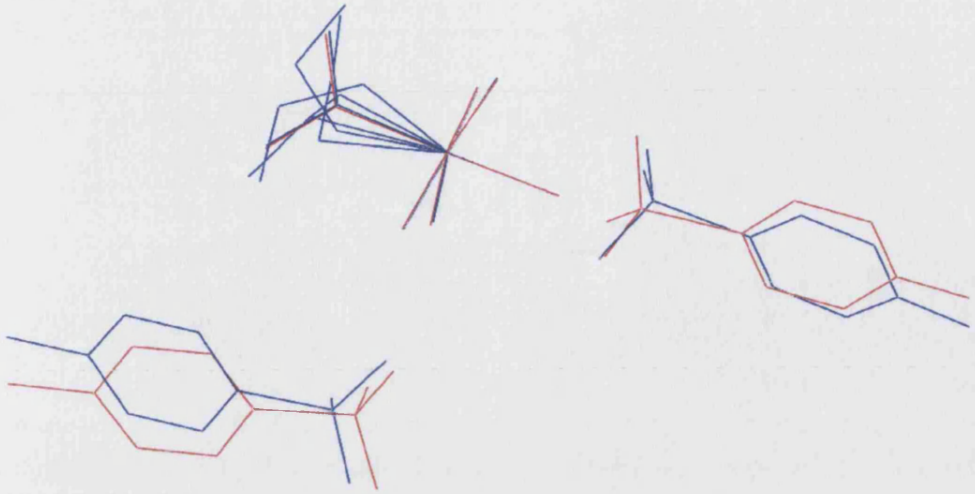

Figure 5.17 - *Overlay of the asymmetric units for tosylate2 (red) and rut72 (blue).*

It is noteworthy that the maximum excitation achievable with a deuterium light source was not obtained instantaneously, but took time to build up as observed when using the microscope lights to induce MS2. A detailed study was not carried out, however a measurement after 30 minutes irradiation revealed the presence of 33.5% of MS1 and 4.5% of MS2, giving an overall excitation of 38% compared to a total of 44% after 75 minutes irradiation.

5.5 Discussion and Conclusions from the Studies on the MS1 and MS2 Metastable States in $[Ru(NH_3)_4(H_2O)(SO_2)](CH_3C_6H_4SO_3)_2$

At present the manner in which light induced excitation occurs within a crystal is a matter for debate, and whether it takes place just on the surface or can occur throughout the sample is unclear. However, it seems reasonable to suggest that light intensity and penetration depth may influence the amount of MS2 that can be generated given that excitation was observed with the 100mW green laser but not with the 5mW green laser, while a higher conversion was achieved using the bright microscope lights as opposed to the 100mW laser. It is also pertinent to recognise that illumination at an absorption maximum as opposed to the side of an absorption peak can affect the rate at which excitation is achieved and whether the integrity of a crystal is maintained as it affects the uniformity of light intensity throughout the crystal (Section 1.5.2.2).

The attempts at maintaining a *pseudo* steady state population of MS2 were successful when using the microscope lights to irradiate the sample. However, a greater level of excitation may be sustained at higher temperatures where the lifetimes are shorter,

by using the single wavelength laser which achieves its maximum excitation in under 5 minutes compared to the 30 minutes taken for the broad band microscope lights.

The first reported crystallographic evidence for the MS1 coordination mode of the sulphur dioxide fragment to the ruthenium centre was achieved by irradiating a ground state crystal at 12.5 K with a deuterium light. Although, the structural model was not clean with evidence of the ground, MS1 and MS2 states, it was of sufficient quality to confirm the geometry of the MS1 metastable state as being similar to that predicted from DFT calculations [5.8]. It was also noted that the excitation levels were dependent on the irradiation time with the broad band light source employed.

To conclude, it is apparent from this series of studies that the method of excitation needs to be designed to suit the sample. Those showing short lifetimes would probably be most suited to single wavelength laser excitation, which appears to be more rapid than that observed with broad band light sources. However, the risk of destroying the sample is increased due to significant heating that arises from the rapid conversions [5.8]. Conversely, species with long lifetimes may be more appropriately irradiated with a broad band source allowing the excitation to be built up gradually and minimising the chance of damaging the crystal integrity.

5.6 References

[5.1] Cole, J.M. (2004) *Chem. Soc. Rev.* **33,** 501-513.

[5.2] Choi, H.J., Sokol, J.J., Long, J.R. (2004) *Inorg. Chem.*, **43,** 1606-1608.

[5.3] Coppens, P., Gerlits, O., Vorontsov, I.I., Kovalevsky, A.Y., Chen, Y-S., Graber, T., Novozhilova, I.V. (2004) *Chem. Comm.* 2144-2145.

[5.4] Carducci, M.D., Pressprich, M.R., Coppens, P. (1997) *J. Am. Chem. Soc.* **119,** 2669-2678.

[5.5] Johnson, D.A., Dew, V.C. (1979) *Inorg. Chem.* **18,** 3273-3274.

[5.6] Rudlinger, M., Schefer, J., Vogt, T., Woike, T., Haussuhl, S., Zollner, H. (1992) *Physica B,* **180,** 293-298.

[5.7] Pressprich, M.R., White, M.A., Vekhter, Y., Coppens, P. (1994) *J. Am. Chem. Soc.* **116,** 5233-5238.

[5.8] Kovalevsky, A.Y., Bagley, K.A., Coppens, P. (2002) *J. Am. Chem. Soc.* **124,** 9241-9248.

[5.9] Kovalevsky, A.Y., Bagley, K.A., Cole, J.M., Coppens, P. (2003) *Inorg. Chem.* **42,** 140-147.

[5.10] Vogt, L.H., Katz, Jr. J.L., Wiberley, S.E. (1965) *Inorg. Chem.* **4,** 1157-1160.

[5.11] Husheer, S. (2004) *Private Communication.*

[5.12] Parker, A.W. *Personal Communication.*

5.7 Summary of Crystallographic Data

Table 5.3 - *Summary of experimental data for single crystal structures.*

Compound	tosylate2	tosylate14	rut72
Empirical formula	$C_{14}H_{28}N_4O_9RuS_3$	$C_{14}H_{28}N_4O_9RuS_3$	$C_{14}H_{28}N_4O_9RuS_3$
M	593.65	593.65	593.65
Crystal system	Triclinic	Triclinic	Triclinic
Space group	*P*-1	*P*-1	*P*-1
Wavelength (Å)	0.69370	0.69370	0.68960
a (Å)	6.6945(3)	6.6729(3)	6.655(3)
b (Å)	13.1054(5)	13.1003(6)	13.109(6)
c (Å)	13.6251(6)	13.7073(6)	13.715(6)
α (°)	94.457(2)	94.579(1)	91.663(4)
β (°)	92.854(2)	92.651(1)	96.450(4)
γ (°)	103.579(2)	103.392(1)	104.721(4)
V (Å^3)	1155.60(8)	1159.35(9)	1147.8(9)
Z	2	2	2
Absorption coefficient (mm^{-1})	1.001	0.998	1.008
Reflections collected	10490	10969	13556
Independent reflections	5928	6150	7121
R_{int}	0.0176	0.0255	0.0436
R_1, w$R2$	0.0231, 0.0626	0.0316, 0.0865	0.0428, 0.0877
R indices (all data)	0.0239, 0.0630	0.0329, 0.0873	0.0695, 0.0976

Chapter 6

Analysis of Twinned Crystal Structures

6.1 Introduction

6.1.1 What is twinning?

A twin can be described as *'a composite crystal built from two or more crystal specimens that are grown together in a specific manner so that there is at least one plane and a direction perpendicular to it that are related in the same manner to the crystallographic axes of both parts of the twin' [6.1].* To describe a twin requires an account of the relative orientation of the different domains and the amount of each domain present.

Twinned datasets used to be routinely discarded due to the inherent problems at the refinement stage, however with the advent of area detectors and rapid advances in software to aid data analysis, successful structure solutions from twinned crystals are becoming more common. Despite this, the importance of investing time ensuring that the best crystal has been selected cannot be stressed enough. Prior to data collection on a twinned crystal, a representative sample of crystals should have been examined to ensure that it is not possible to find a single crystal or remove the additional twin domains which may be apparent. This may be achieved by viewing the sample through a polarising microscope, and attempting to cut the crystal to remove rogue domains.

This chapter aims to provide an introduction to twinning, covering the types of this phenomenon that are observed and how to identify them as well as the methods currently employed to obtain reasonable refinements. Examples of successful refinements for the different types of twin are provided where they have been encountered.

6.1.2 Types of twinning [6.2]

There are four main classes of twin that have been identified. These are:

- Merohedral twins [6.2][6.3][6.4][6.5]

The reciprocal and direct lattices of the twin domains overlap exactly in merohedral twinning, thus the twin operator arises from a symmetry operator of the crystal system but not the point group of the crystal. In the lower symmetry triclinic, monoclinic and orthorhombic crystal systems (*i.e.* with only one associated Laue Group), merohedral twinning can only be exhibited in the form of an inversion twin in non-centrosymmetric space groups, while in the higher symmetry crystal systems an alternate form of merohedral twinning can also occur. One such example is that of a tetragonal structure belonging to the lower symmetry 4/*m* Laue group, nevertheless, all tetragonal unit cells have 4/*mmm*

symmetry and as a result a 2-fold rotation about (1 1 0) exchanging the *a* and *b* axes, commonly results in twinning, see Figure 6.1.

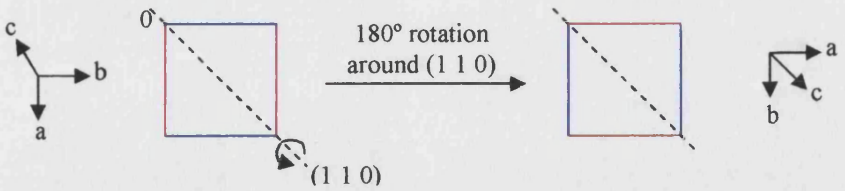

Figure 6.1 - *Illustration of merohedral twinning in a tetragonal crystal belonging to the 4/m Laue group. The twin law relating the two domains is (0 1 0 1 0 0 0 0 -1).*

- Pseudo-merohedral twins [6.2][6.3]

Pseudo-merohedral twinning occurs when the unit cell dimensions mimic those of a higher symmetry crystal system, for example a triclinic crystal with two angles close to 90° appears to be monoclinic, while a monoclinic crystal with a β angle close to 90° imitates the metric symmetry of an orthorhombic crystal. Alternatively, this type of twinning can be observed if a higher symmetry supercell closely related to the correct cell is present, such a case may be observed in a monoclinic crystal if a doubling of one axis produces a centred orthorhombic supercell. As with merohedral twinning all reflections are affected, however in this case the twin operator belongs to the higher symmetry crystal system. Thus, in the case of a monoclinic crystal with a β angle close to 90°, which emulates an orthorhombic crystal, the twin operator is typically a two-fold rotation around either *a* or *c*, both of which are possible in the orthorhombic Laue group *mmm*, but neither are allowed in a monoclinic crystal system.

The proportion of the second domain present determines whether the twinning is apparent from the reciprocal lattice, see Figure 6.2. At approximately a 1:1 ratio of the two domains the diffraction pattern appears to possess orthorhombic symmetry, while at lower ratios the intensity of the diffraction spots is not equal and the twinning may become apparent at an earlier stage.

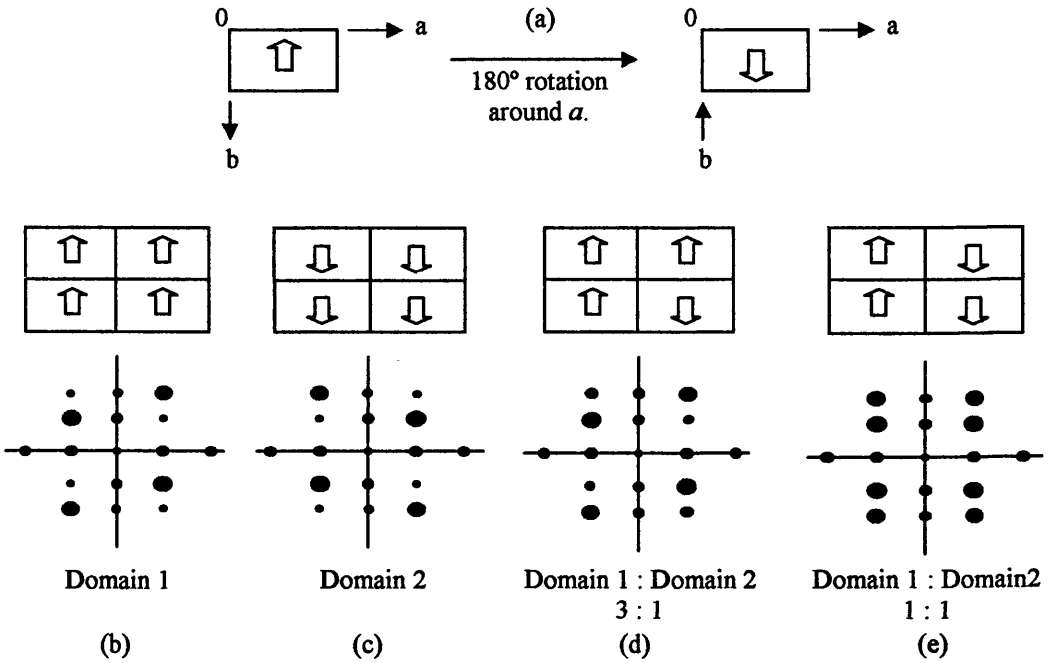

Figure 6.2 - *Illustration of the effect of pseudo-merohedral twinning on the diffraction pattern of a monoclinic crystal with β close to 90°. (a) The twin operator relating the two orientations of the crystal is (1 0 0 0 -1 0 0 0 -1), representing a 180° rotation around a. (b) and (c) show the diffraction pattern from domains 1 and 2 respectively while (d) and (e) demonstrate the effect of different twinning ratios on the resultant diffraction pattern. [6.3]*

- *Non-merohedral twins [6.3][6.4][6.6]*

This type of twinning affects zones of reflections and arises when there is additional symmetry within the supercell. In such cases the diffraction pattern contains 3 types of reflections; those belonging to only one lattice, partially overlapped reflections, and fully overlapped reflections. The twin operator is such cases is arbitrary.

One simple example of non-merohedral twinning is an orthorhombic structure in which $b \approx 2a$, the supercell is thus tetragonal with a resultant pseudo fourfold axis around c, see Figure 6.3.

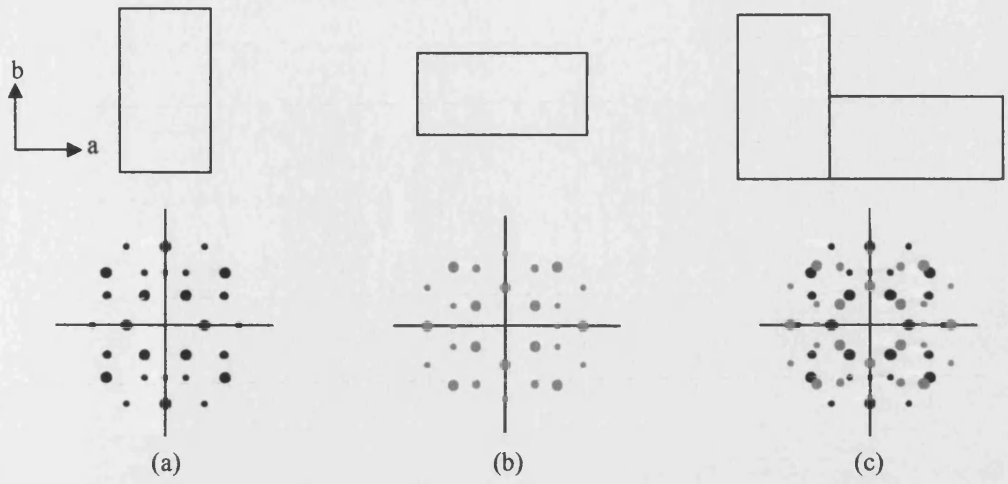

Figure 6.3 - *Illustration of the effect of non-merohedral twinning in an orthorhombic crystal where b≈ 2a, hence producing a tetragonal supercell. (a) and (b) show the diffraction patterns from the two domains individually, they are related by a 90° rotation around the c axis. (c) diffraction pattern from a non-merohedrally twinned crystal in which b≈ 2a. [6.3]*

- Reticular merohedral twins [6.2][6.7]

A special subset of non-merohedral twinning exists whereby, despite the reciprocal lattices overlapping exactly, not all of the reflections are affected. One such example of this type of twinning would be that of obverse/reverse twinning in a rhombohedral structure, where the systematic absences for one domain are present in the diffraction pattern from the other and vice-versa. This can be visualised by considering the hexagonal setting of a rhombohedral crystal which has a two-fold axis parallel to the main three-fold axis, thus creating a pseudo six-fold axis. If the reflection condition for the first domain is $-h + k + l = 3n$ (obverse setting), for the second (reverse setting) it will be $h - k + l = 3n$. To identify the twinning it would be necessary to examine the mean intensities of reflections corresponding to the two domains $-h + k + l = 3n$ and $h - k + l = 3n$, *i.e.* the mean intensities of the obverse and reverse reflections output by most space group identification programs. The ease with which this type of twinning can be recognised depends on the relative proportions of the two domains in a similar manner to that discussed above for pseudo merohedral twinning.

6.1.3 Warning signs for the presence of twinning [6.2][6.5]

There are some commonly accepted warning signs associated with twinning. Clearly not all of the signs are present in every example of twinning, but the presence of several in one structure makes twinning a serious possibility.

1.) The metric symmetry is higher than the Laue symmetry.
2.) The higher symmetry Laue group R_{int} is only slightly higher than that of the lower symmetry Laue group.

$$R_{int} = \frac{\Sigma|F_{obs}^2 - F_{obs(mean)}^2|}{\Sigma[F_{obs}^2]}$$

3.) The space group may appear to be trigonal or hexagonal.
4.) The systematic absences are inconsistent with any known space group.
5.) The structure cannot be solved despite no apparent problems with the data.
6.) The Patterson function is physically impossible, for heavy atom structures.
7.) The $|E^2-1|$ value is lower than expected. Typically the value is around 0.9 for untwined centrosymmetric structures and 0.75 for untwined non-centrosymmetric structures, these values in a twinned structure can be reduced to 0.7 for centrosymmetric and 0.4 for non-centrosymmetric structures.
8.) K = mean (F_{obs}^2)/ mean (F_{calc}^2) is anomalously high for low intensity reflections.
9.) For the most disagreeable reflections F_{obs} is much larger than F_{calc}.
10.) There is one or more unusually long axis.
11.) There are problems with indexation, either the data does not index or many reflections do not fit the cell.
12.) Some reflections are sharp while others are broad or split.

In general, points 1-9 below are associated with pseudo-merohedral and merohedral twinning while 7-12 are typical indications of non-merohedral twinning.

6.1.4 Methods to deal with twinning

Contending with twinned crystals is considerably more complex than dealing with standard single crystal structure solutions, due to the inherent inaccuracies in the measured intensities. However, rapid improvements in available software to manage X-ray diffraction data both at the indexation and refinement stages have meant that structure solution from twinned crystals has become more routine over recent years.

The approaches used to handle twinned data depend on the type of twinning that is present and are outlined below. While each strategy is discussed individually, it is important

to note that a crystal may be twinned in more than one way. Moreover, twinned crystal refinements often require the use of restraints and constraints to maintain chemically sensible bond lengths, geometries and anisotropic displacement parameters, as a consequence of poor data to parameter ratios and poorly measured reflections resulting from diffraction overlaps.

- Merohedral twinning

The diffraction pattern of a merohedrally twinned crystal appears to have a higher Laue symmetry than is correct. As discussed earlier the extent of the second domain present determines whether the twinning is easily detectable from the reciprocal lattice, since all of the reflections are affected. As a result there is no requirement to produce an altered *hkl* data file, as the twin law can be applied to the refinement through use of the TWIN and BASF commands in SHELXL [6.8]. These instructions respectively, give the program the 3 by 3 matrix relating the twin domains, along with a scale factor that specifies the fractional contributions of each domain.

Merohedral twinning is often only identified at the refinement stage, although there may be earlier problems assigning the correct space group. Typically the weighted *R*-factor remains high with F_{obs} greater than F_{calc} for the most disagreeable reflections. An example of this type of twinning is discussed for k05alj09 later in this chapter and further examples can be found in the literature [6.2][6.3].

- Pseudo-merohedral twinning

In structures demonstrating pseudo-merohedral twinning, the diffraction pattern appears to have a higher metric symmetry than the correct crystal system in fact possesses. As with merohedral twinning all of the reflections are affected and the ease with which this type of twinning is identified depends on the relative ratios of the two domains, and both the higher and lower symmetry cells fit all of the reflections (Figure 6.2).

Pseudo-merohedral twinning may become apparent prior to refinement if R_{int} for a higher symmetry Laue group is similar to that of a lower symmetry Laue group other than -1 and if, overall, the reflection conditions do not correspond with any known space group. Identification at the refinement stage as with many examples of twinning, may arise when the weighted *R*-factor (wR_2) remains high with F_{obs} much greater than F_{calc} for the most disagreeable reflections. In order to refine structures demonstrating this type of twinning, it is necessary to determine both the correct cell and its relationship to the higher symmetry cell. The information can then be used to calculate the twin law which is applied to a refinement in SHELXL using the TWIN and BASF commands, without the need to produce an altered reflection file.

This type of twinning is discussed for structures Bath80, k04pjw4 and h05mgd04. The complete derivation of the twin law for Bath80, further examples can be found in the literature [6.2][6.3].

- Non-merohedral twinning

In non-merohedral twins the reciprocal lattices do not overlap exactly and the twinning is identifiable from the diffraction pattern which will contain split reflections or two reflections very close to each but not relating to a long axis. This type of twinning is most easily dealt with at the indexation state, as the correct cell relating to the first domain will not fit all of the reflections. In such cases, indexation programs such as GEMINI [6.9] or DIRAX [6.10] can be employed to identify two (or more) related cells, neither of which can individually account for all of the observed reflections. These programs, can also be used to obtain the twin laws which relate secondary domains to the first domain.

Refinement of such structures in SHELXL requires the production of an HKLF5 file, which is an altered reflection file that has a twin component number associated with each reflection. As discussed earlier the diffraction pattern contains reflections belonging to only one lattice and overlapped reflections. Fully separated reflections are easily dealt with and assigned to their respective domain, while fully overlapped reflections are included if their indicies are found to have integer values, and discarded if not. Partially overlapped reflections are less easily managed, and can either be discarded or scaled, both of these approaches affect the final refinement [6.5]. It is usually a trial and error process to determine the best overlap criteria by which to omit partially overlapped reflections and obtain the optimum refinement [6.11].

This type of twinning is discussed for structure h05gb1, and further examples can be found in the literature [6.11][6.6].

- Reticular merohedral twinning [6.2][6.7]

This type of twinning also requires the generation of an HKLF5 reflection file as not all of the reflections are affected by twinning, however unlike non-merohedral twinning the reciprocal lattices overlap exactly and structures can potentially be solved and refined using the reflections relating to only one domain. Reticular merohedral twinning is not discussed again in this chapter, however examples of this type of refinement can be found in the literature [6.2][6.7].

6.1.5 Data Collection

Single crystal X-ray diffraction data for k05alj09, k04pjw4, h05mgd04 and h05gb1 were collected at 150 K on a Nonius Kappa CCD four-circle diffractometer fitted with an

area detector and cryostream, while Bath80 was collected at 150 K on Station 9.8 at Daresbury synchrotron, using a D8 diffractometer fitted with a Bruker Smart CCD detector and cryostream.

A summary of the experimental details for each of the structures discussed in this chapter are included in Tables 6.10 and 6.11 at the end of this chapter, with bond lengths and angles listed in Appendix 6.1.

6.1.6 Software

The software employed throughout the chapter is the same as discussed in Section 3.2.6.2.

6.2 Merohedral Twinning

6.2.1 k05alj09 – $TiC_{26}H_{30}N_2O_8$

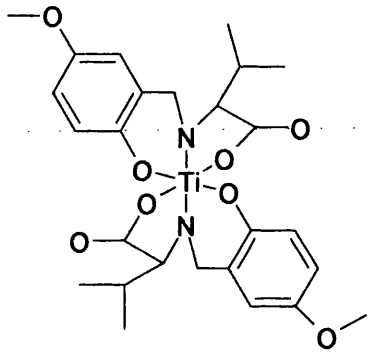

Figure 6.4 - *One molecule of k05alj09 ($TiC_{26}H_{30}N_2O_8$)*

The structure solved easily in the trigonal space group $P3_2$, however, there were problems with the refinement which indicated that the structure might be twinned.

- The difference map had large peaks remaining in chemically unreasonable positions after all of the atoms had been accounted for, which could not be attributed to absorption problems.
- The *R*-factor remained very high (0.2180).
- For the most disagreeable reflections F_{obs}^2 was greater that F_{calc}^2.
- The value of *K* (= mean (F_{obs}^2)/mean (F_{calc}^2)) for the weakest reflections was large (7.531).

It was however noted that the merging *R*-factor for the trigonal system was significantly lower than that for any of the other crystal systems, hence pseudo-merohedral

twinning was precluded. Reticular merohedral twinning was also ruled out on the basis of the reflection statistics, since the mean *I*/sig *I* for all obverse and reverse reflections were the same. All of the reflections fitted the existing cell, although examination of the diffraction pattern indicated the presence of a pseudo 6-fold axis down the *c*-axis, arising from the crystal emulating the higher -3*m* Laue symmetry as opposed to the correct -3 Laue symmetry, see Figure 6.5. All of these factors indicated that merohedral twinning might be present, the most likely case being the interchanging of the *a* and *b* axis, as illustrated in Figure 6.6, where the relevant twin law relating the two domains is also provided.

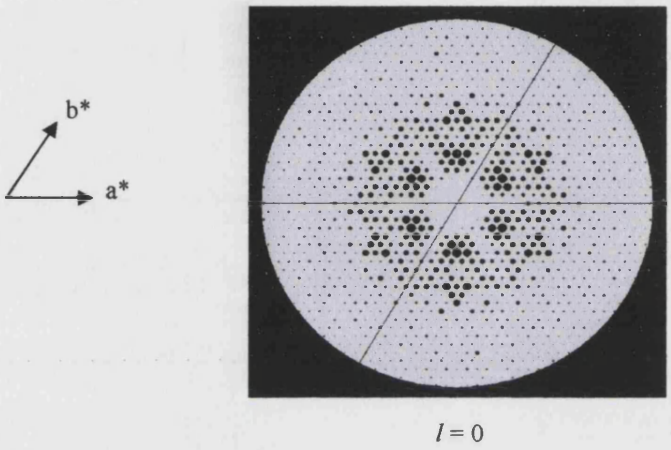

Figure 6.5 - *Illustration of pseudo 6-fold axis down c.*

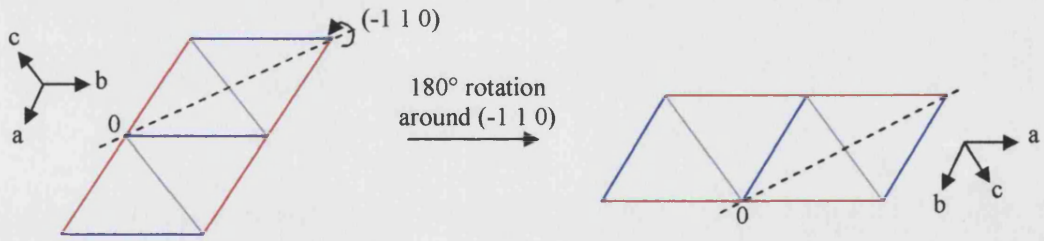

$$\textbf{Twin Law} = \begin{pmatrix} 0 & -1 & 0 \\ -1 & 0 & 0 \\ 0 & 0 & -1 \end{pmatrix}$$

Figure 6.6 - *Illustration of the effect of merohedral twinning in a trigonal crystal system, and the twin law relating the two domains.*

Inclusion of the twin law significantly improved the convergence, which no longer required the use of restraints and all atoms were stable with respect to anisotropic

refinement. Table 6.1 provides a comparison of the refinement results before and after the merohedral twinning was accounted for.

Table 6.1 - *Comparison of final refinements for k05alj09 ($TiC_{26}H_{30}N_2O_8$) with and without the twin law.*

	Trigonal ($P3_2$) no merohedral twinning	Trigonal ($P3_2$) with merohedral twinning
BASF	-	0.41132
R_1	0.2180	0.0457
wR_2	0.5373	0.0625
Largest Difference Peak and Hole (eÅ^{-3})	2.590, -2.762	0.361, -0.430
K weakest reflections	7.531	2.024
s.u. C-C	0.018 - 0.030	0.004 - 0.005
s.u. Ti-N	0.010- 0.013	0.002 - 0.003
s.u. Ti-O	0.010 - 0.013	0.002
s.u. C-O	0.016 - 0.020	0.004 - 0.005
s.u. C-N	0.017 - 0.020	0.004

The titanium atom is 6-coordinate, and adopts a distorted octahedral geometry as required by the ligand bite, with average *trans* O-Ti-O angles of 158.0° and *trans* N-Ti-N angles approximately of 160.3°. Figure 6.7 shows the ORTEP plot for one of the three molecules contained in the asymmetric unit, while Figure 6.8 shows a packing diagram looking down the *c*-axis from which the effect of the 3_2 screw axis can be seen.

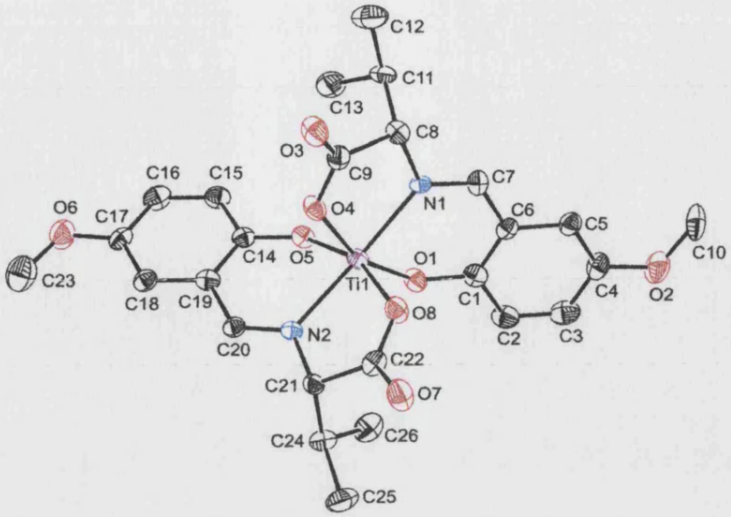

Figure 6.7 - *ORTEP plot for one molecule of k05alj09 ($TiC_{26}H_{30}N_2O_8$). Ellipsoids are represented at the 50% level.*

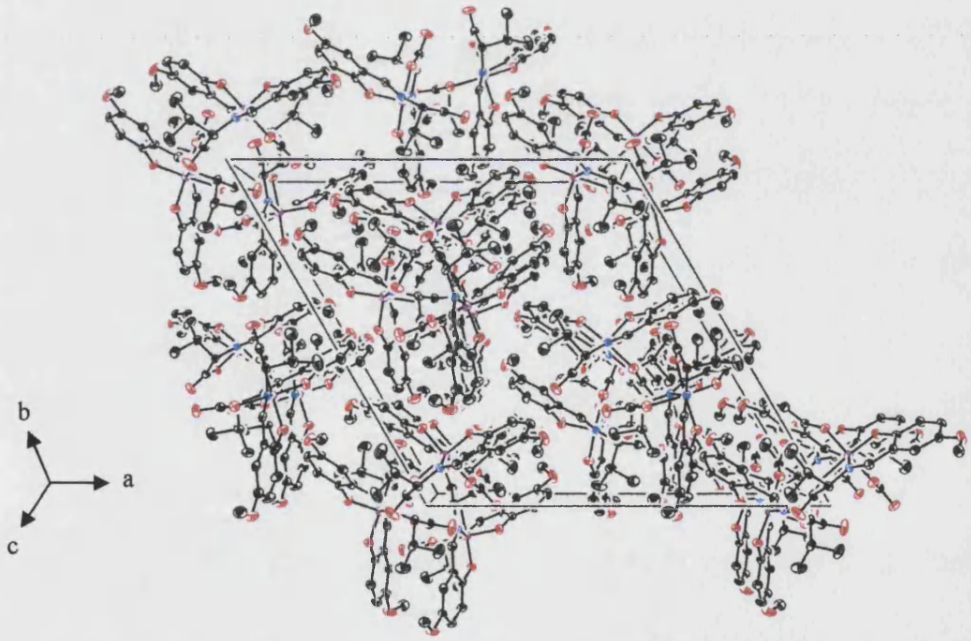

Figure 6.8 - *Packing diagram for k05alj09 ($TiC_{26}H_{30}N_2O_8$) looking down the c-axis, where the effect of the 3_2 screw axis can be seen. Ellipsoids are represented at the 50% level.*

6.3 Pseudo-Merohedral Twinning

6.3.1 Bath80 – $Au_2P_2C_{36}H_{28}Cl_2O{\cdot}DCM$

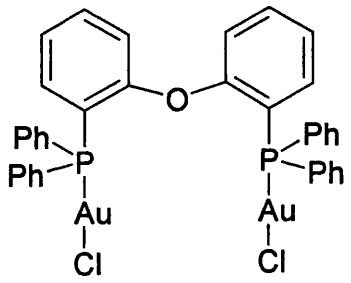

Figure 6.9 - *One molecule of Bath80 ($Au_2P_2C_{36}H_{28}Cl_2O{\cdot}DCM$).*

The structure solved well in the monoclinic space group $P2_1/c$, however there were problems with the refinement, that suggested the structure was twinned.

- The difference map had large peaks remaining in chemically unreasonable positions after all of the atoms had been included.
- For the most disagreeable reflections F_{obs}^2 was greater that F_{calc}^2.
- The value of K (= mean (F_{obs}^2)/mean (F_{calc}^2)) for the weakest reflections was large (23.993).
- There were a large number of systematic absence violations.

6.3.1.1 Derivation of the twin law

Table 6.2 - *Comparison of monoclinic and orthorhombic cells.*

	a (Å)	*b* (Å)	*c* (Å)	*α* (°)	*β* (°)	*γ* (°)	V (Å^3)
Monoclinic (*P*)	8.9229 (16)	20.269 (4)	19.987 (4)	90	102.671 (3)	90	3526.78
Orthorhombic (*C*)	8.9214 (16)	38.991 (7)	20.266 (4)	90	90	90	7049.69

At the cell determination stage it had been noted that there was a closely related orthorhombic cell with twice the volume of the monoclinic cell as a result of the orthorhombic *b*-axis being double the length of the monoclinic *c*-axis, see Table 6.2. Coupled with the problems at the refinement stage this indicated that the structure was likely to exhibit pseudo-merohedral twinning. Since this is the first example of pseudo-merohedral twinning presented within this thesis the complete derivation of the twin law is provided below.

- Determination of a twin law requires three matrices: the first to convert from the lower symmetry cell (monoclinic in this case) to the higher symmetry cell (orthorhombic in this example). The second matrix adds a 2-fold rotation around one axis (*b* in this example) and the final matrix to converts back to the lower symmetry cell. The three matrices are multiplied in the following order.

Orthorhombic ↓ Monoclinic	x	2-fold axis	x	Monoclinic ↓ Orthorhombic
Matrix 3		Matrix 2		Matrix 1

- The first stage is to find the matrix required to convert the monoclinic cell into the orthorhombic cell. This is automatically generated in programs such as LePage if they identify a higher metric symmetry.

$$\begin{pmatrix} -1 & 0 & 0 \\ -1 & 0 & -2 \\ 0 & -1 & 0 \end{pmatrix}$$ Matrix 1

- The matrix of minors (Matrix A) for Matrix 1 is then determined and a matrix of cofactors applied, transposition of this Matrix (B) gives the adjoint of Matrix A (Adj(A)).

$$\begin{pmatrix} -2 & 0 & 1 \\ 0 & 0 & 1 \\ 0 & 2 & 0 \end{pmatrix}$$ Matrix A – *matrix of minors for Matrix 1.*

apply

$$\begin{pmatrix} 1 & -1 & 1 \\ -1 & 1 & -1 \\ 1 & -1 & 1 \end{pmatrix}$$ Matrix of cofactors

$\longrightarrow$

$$\begin{pmatrix} -2 & 0 & 1 \\ 0 & 0 & -1 \\ 0 & -2 & 0 \end{pmatrix}$$ Matrix B

transpose ↓

$$\begin{pmatrix} -2 & 0 & 0 \\ 0 & 0 & -2 \\ 1 & -1 & 0 \end{pmatrix}$$ Adj(A)

- The determinant of Matrix 1 is established.

$$\underset{\text{Adj(A)}}{\begin{pmatrix} -2 & 0 & 0 \\ 0 & 0 & -2 \\ 1 & -1 & 0 \end{pmatrix}} \quad \underset{\text{Matrix 1}}{\begin{pmatrix} -1 & 0 & 0 \\ -1 & 0 & -2 \\ 0 & -1 & 0 \end{pmatrix}} = \begin{pmatrix} 2 & 0 & 0 \\ 0 & 2 & 0 \\ 0 & 0 & 2 \end{pmatrix}$$

Determinant of Matrix 1 = 2

- The inverse of Matrix 1 is then calculated, this is Matrix 3 which converts from the higher symmetry orthorhombic cell back to the monoclinic cell.

$$\text{Inverse (Matrix 1)} = (1/\text{determinant of Matrix 1}) \times \text{Adj(A)}$$

$$= \tfrac{1}{2} \times \begin{pmatrix} -2 & 0 & 0 \\ 0 & 0 & -2 \\ 1 & -1 & 0 \end{pmatrix}$$

$$= \underset{\text{Matrix 3}}{\begin{pmatrix} -1 & 0 & 0 \\ 0 & 0 & -1 \\ 0.5 & -0.5 & 0 \end{pmatrix}}$$

- The final stage involves multiplying matrices 1, 2 and 3 together to give the relevant twin law, where Matrix 2 corresponds to a 2-fold rotation around the *b*-axis.

$$\textbf{Twin Law} = (\text{Matrix 3}) \times (\text{Matrix 2}) \times (\text{Matrix 1})$$

$$= \begin{pmatrix} -1 & 0 & 0 \\ 0 & 0 & -1 \\ 0.5 & -0.5 & 0 \end{pmatrix} \times \begin{pmatrix} -1 & 0 & 0 \\ 0 & 1 & 0 \\ 0 & 0 & -1 \end{pmatrix} \times \begin{pmatrix} -1 & 0 & 0 \\ -1 & 0 & -2 \\ 0 & -1 & 0 \end{pmatrix}$$

$$= \begin{pmatrix} 1 & 0 & 0 \\ 0 & 0 & 1 \\ -0.5 & -0.5 & 0 \end{pmatrix} \times \begin{pmatrix} -1 & 0 & 0 \\ -1 & 0 & -2 \\ 0 & -1 & 0 \end{pmatrix}$$

$$= \begin{pmatrix} \mathbf{-1} & \mathbf{0} & \mathbf{0} \\ \mathbf{0} & \mathbf{-1} & \mathbf{0} \\ \mathbf{1} & \mathbf{0} & \mathbf{1} \end{pmatrix}$$

This twin law is the result of a 180° rotation around the (1 0 2) direct lattice vector, which corresponds to a 180° rotation around the (0 0 1) reciprocal lattice vector. The effect of this in direct space is illustrated in Figure 6.10.

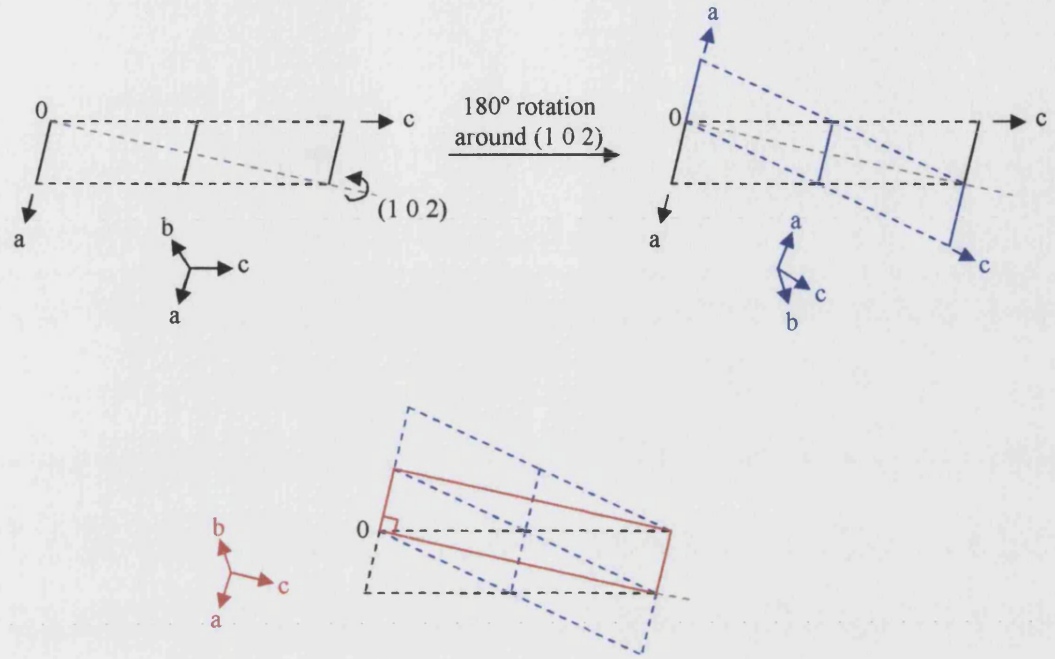

Figure 6.10 - *(Top) Illustration of a 180° rotation around the (1 0 2) direct space vector which corresponds to the twin law (-1 0 0 0 -1 0 1 0 1). The original cell is shown in black while the second domain is illustrated in blue. (Bottom) Illustration of how the orthorhombic supercell (in red) arises from the two monoclinic domains.*

Application of the twin law to the refinement produced a considerable improvement as Table 6.3 shows. The largest residual difference peaks in the electron density map spanned a range of 1.0 – 2.3 eÅ^{-3}, however most of these are located near to the gold or chlorine atoms and are likely to be the result of inaccuracies in the absorption correction. The twinned refinement was stable without the use of restraints on bond lengths, angles or thermal parameters unlike the comparable non twinned refinement.

Table 6.3 - *Comparison of final data for Bath80 ($Au_2P_2C_{36}H_{28}Cl_2O \cdot DCM$) with and without the twin law.*

	Monoclinic ($P2_1/c$) No pseudo merohedral twinning	Monoclinic ($P2_1/c$) with pseudo merohedral twinning
BASF	-	0.23628
R_1	0.1640	0.0465
wR_2	0.3961	0.1121
Largest Difference Peak and Hole (eÅ^{-3})	12.601, -9.813	2.211, -3.156
K weakest reflections	23.993	0.827
s.u. C-C	*	0.011 - 0.017
s.u. Au-Au	0.0018	0.0006
s.u. Au-P	0.008 - 0.009	0.002
s.u. Au-Cl	0.008	0.002
s.u. P-C	0.014 - 0.019	0.008 - 0.010
s.u. O-C	0.020	0.010
s.u. C-Cl	0.040	0.014 - 0.015

* undefined errors.

The final ORTEP plot for Bath80 is shown in Figure 6.11. The structure consists of a di-phosphine ligand bridging two gold atoms, which are separated by 3.004(1) Å suggesting the presence of an aurophilic interaction. The environment around the gold deviates from linearity with P-Au-Cl angles of 170.57(9)° and 174.26(9)° for Au_1 and Au_2 respectively. A torsion angle of +80.9(1)° for Cl_1-Au_1-Au_2-Cl_2 indicates that the two P-Au-Cl fragments are almost perpendicular to each other.

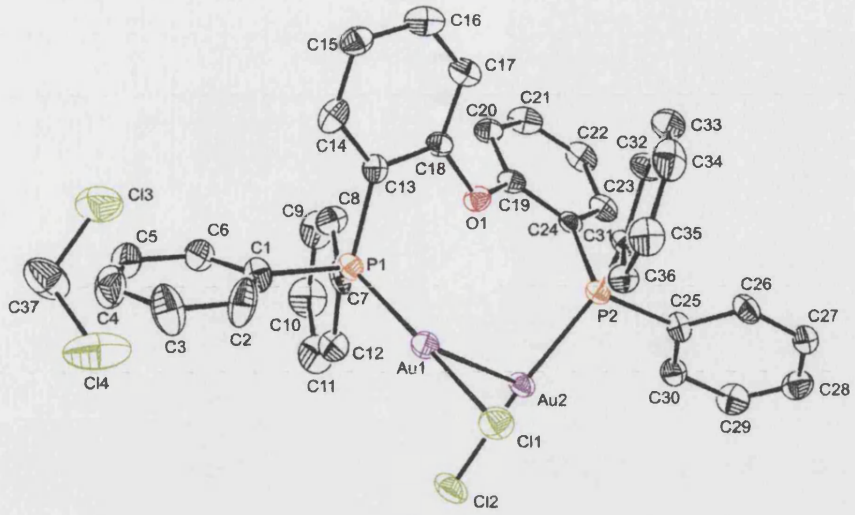

Figure 6.11 - *The asymmetric unit for Bath80 ($Au_2P_2C_{36}H_{28}Cl_2O{\cdot}DCM$). Ellipsoids are represented at the 50% level.*

6.3.2 k04pjw4 – $Pt_2P_4C_{56}H_{82}O_2$

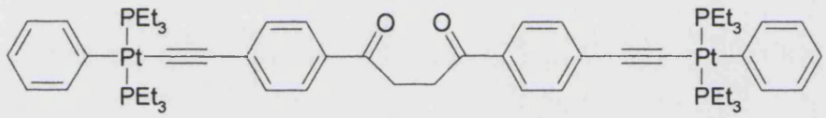

Figure 6.12 - *One molecule of k04pjw4 ($Pt_2P_4C_{56}H_{82}O_2$).*

In contrast to the two structures discussed above, structure solution for this compound was very difficult. However, the problems encountered in the refinement stage were similar to those seen for Bath80:

- The difference map had large peaks remaining in chemically unreasonable positions after all of the atoms had been included in the model.
- For the most disagreeable reflections F_{obs}^2 is greater that F_{calc}^2.
- The value of K (= mean (F_{obs}^2)/mean (F_{calc}^2)) for the weakest reflections was large (57.666).
- There were a large number of systematic absence violations.
- The refinement was unstable and required restraints to maintain the integrity of the structure.

6.3.2.1 Derivation of the twin law

Table 6.4 - *Comparison of Monoclinic and Orthorhombic cells.*

	a (Å)	*b* (Å)	*c* (Å)	*α* (°)	*β* (°)	*γ* (°)	V (Å^3)
Monoclinic (*P*)	9.4610 (1)	19.7770 (3)	30.7490 (4)	90	98.897 (1)	90	5684.11 (13)
Orthorhombic (*I*)	9.4639 (1)	60.7756 (7)	19.7873 (3)	90	90	90	11381.14 (25)

Analysis of the data in LePage [6.12] indicated the presence of a closely related orthorhombic supercell with twice the volume of the monoclinic cell, which resulted from a doubling of the monoclinic *c*-axis to form the orthorhombic *b*-axis, see Table 6.4. The twin law was derived in the same manner as for Bath80 and is provided in Appendix 6.2, below is a summary of the three matrices and the twin law for k04pjw4.

- Matrix 1 – converts the monoclinic cell into the orthorhombic cell.

$$\begin{pmatrix} 1 & 0 & 0 \\ -1 & 0 & -2 \\ 0 & 1 & 0 \end{pmatrix}$$ Matrix 1

- Matrix 2 – adds a 2-fold rotation around the *b*-axis.

$$\begin{pmatrix} -1 & 0 & 0 \\ 0 & 1 & 0 \\ 0 & 0 & -1 \end{pmatrix}$$ Matrix 2

- Matrix 3 – converts back from the orthorhombic cell into the monoclinic cell.

$$\begin{pmatrix} 1 & 0 & 0 \\ 0 & 0 & 1 \\ -0.5 & -0.5 & 0 \end{pmatrix}$$ Matrix 3

The final twin law is then the product of the three matrices

Twin Law = (Matrix 3) x (Matrix 2) x (Matrix 1)

$$= \begin{pmatrix} \mathbf{-1} & \mathbf{0} & \mathbf{0} \\ \mathbf{0} & \mathbf{-1} & \mathbf{0} \\ \mathbf{1} & \mathbf{0} & \mathbf{1} \end{pmatrix}$$

This fortuitously turned out to be the same twin law as observed for Bath80 which can be viewed as a 180° rotation around the (1 0 2) direct lattice vector or the (0 0 1) reciprocal lattice vector. Figure 6.10 earlier illustrated this for Bath80, but the visualisation is equally applicable to this structure.

Inclusion of the twin law greatly improved the refinement as Table 6.5 shows. No restraints were needed to maintain the integrity of the model during refinement with the twin law.

Table 6.5 - *Comparison of refinement data for k04pjw4 ($Pt_2P_4C_{56}H_{82}O_2$) with and without the twin law.*

	Monoclinic ($P2_1/n$) No pseudo merohedral twinning	Monoclinic ($P2_1/n$) with pseudo merohedral twinning
BASF	-	0.41943
R_1	0.2713	0.0578
wR_2	0.6002	0.1076
Largest Difference Peak and Hole (eÅ^{-3})	13.088, -11.492	1.853, -3.158
K weakest reflections	57.666	2.475
s.u. C-C	0.05*	0.015 – 0.020
s.u. Pt-C	0.018 – 0.040	0.011 - 0.014
s.u. Pt-P	0.019 – 0.030	0.003
s.u. P-C	0.013 - 0.040	0.012 - 0.015
s.u. C-O	0.040	0.015

* mostly undefined errors.

The co-ordination geometries of the platinum atoms in the platinum dimer are approximately square planar, with (P-Pt-P) / (C-Pt-C) angles of 174.95(12)° / 178.8(5)° and 174.91(11)° / 176.8(5)° for Pt_1 and Pt_2 respectively. The P-Pt-C angles range from 87.5(4)° to 92.7(3)°. The molecule is twisted relative to the C_{16}-C_{17} bond, with the C_{15}-C_{16}-C_{17}-C_{18} torsion angle being +72(1)°. An ORTEP plot for k04pjw4 ($Pt_2P_4C_{56}H_{82}O_2$) is provided in Figure 6.13.

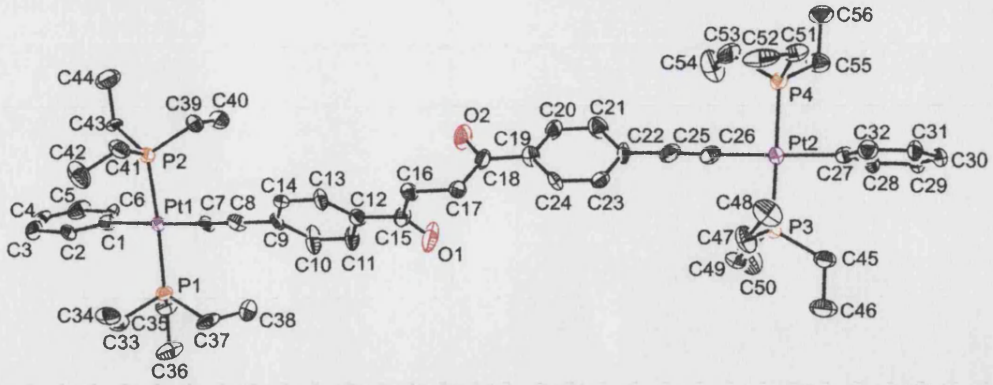

Figure 6.13 - *Structure of k04pjw4 ($Pt_2P_4C_{56}H_{82}O_2$). Ellipsoids are represented at the 50% level.*

6.3.3 h05mgd04 – $C_{34}H_{45}O_2PBr_2$

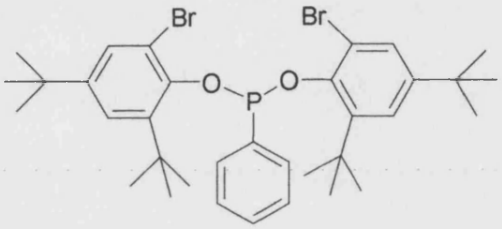

Figure 6.14 - *One molecule of h05mgd04 ($C_{34}H_{45}O_2PBr_2$).*

An orthorhombic structure solution in $Pca2_1$ was achieved, however there were several problems with the refinement consistent with the presence of twinning.

- There were apparent systematic absences that were inconsistent with any orthorhombic space group.
- w$R2$ = 0.2036 upon completion of the structure.
- For most of the disagreeable reflections F_{obs}^2 was greater than F_{calc}^2.
- Structure solution could not be achieved in any other orthorhombic space group.

6.3.3.1 Derivation of the twin law

Table 6.6 - *Comparison of the monoclinic and orthorhombic cells.*

	a (Å)	*b* (Å)	*c* (Å)	*α* (°)	*β* (°)	*γ* (°)	V (Å^3)
Monoclinic (*P*)	9.9601 (1)	28.7318 (4)	23.5196 (4)	90	90.238 (1)	90	6730.58 (16)
Orthorhombic (*P*)	9.9589 (2)	23.5266 (5)	28.7909 (5)	90	90	90	6745.68 (23)

This instance of twinning provides an interesting illustration of another manner in which pseudo merohedral twinning can occur. In this case a monoclinic cell essentially identical to the orthorhombic cell, but with a *β* angle of 90.238(1)° was also identified at the cell determination stage, see Table 6.6. The fact that the *β* angle is so close to 90.0° means that the structure appears to be orthorhombic and twinning can occur by a rotation of 180° around either the *a* or *c*-axis allowable in orthorhombic but not monoclinic cells. Twinning of this type was illustrated in Figure 6.10. A full derivation of the twin law for h05mgd04 is provided in Appendix 6.3, listed below are the three matrices used to determine the twin law

- Matrix 1 - to convert the monoclinic cell into the orthorhombic cell.

$$\begin{pmatrix} -1 & 0 & 0 \\ 0 & 0 & -1 \\ 0 & -1 & 0 \end{pmatrix}$$ Matrix 1

- Matrix 2 - to add a 2-fold rotation around the *b*-axis.

$$\begin{pmatrix} -1 & 0 & 0 \\ 0 & 1 & 0 \\ 0 & 0 & -1 \end{pmatrix}$$ Matrix 2

- Matrix 3 – the inverse of Matrix 1 converts the orthorhombic cell back into the monoclinic cell.

$$\begin{pmatrix} -1 & 0 & 0 \\ 0 & 0 & -1 \\ 0 & -1 & 0 \end{pmatrix}$$ Matrix 3

The product of these three matrices gives the final twin law, which indicates twinning occurring through a 180° rotation around *c*.

Twin Law = (Matrix 3) x (Matrix 2) x (Matrix 1)

$$= \begin{pmatrix} -1 & 0 & 0 \\ 0 & -1 & 0 \\ 0 & 0 & 1 \end{pmatrix}$$

Employing the twin law above and accounting for racemic twinning in the monoclinic space group $P2_1$, greatly improved the final refinement as compared with the orthorhombic $Pca2_1$ option. The diffraction intensity fell off at high angle and restraints were still required to stabilise the carbon atoms particularly those in the disordered tertiary butyl groups. Table 6.7 provides a comparison of the refinements.

Table 6.7 - *Comparison of the initial orthorhombic refinement for h05mgd04 ($C_{34}H_{45}O_2PBr_2$) with subsequent monoclinic refinements with and without taking the twinning into account.*

	Orthorhombic ($Pca2_1$)	Monoclinic ($P2_1$) No pseudo merohedral twinning	Monoclinic ($P2_1$) with pseudo merohedral twinning
BASF	0.37350 (racemic twinning only)	0.37795 (racemic twinning only)	0.14653, 0.20584, 0.26450 (racemic and pseudo merohedral)
R_1	0.0860	0.0933	0.0505
wR_2	0.1931	0.2100	0.0978
Largest Difference Peak and Hole (eÅ^{-3})	0.965, -1.186	1.298, -1.228	0.674, -0.477
K weakest reflections	3.511	4.680	1.090
s.u. O-C	0.012 - 0.014	0.013 - 0.016	0.011 - 0.012
s.u. Br-C	0.009 - 0.011	0.011 - 0.014	0.009 - 0.010
s.u. P-O	0.007 - 0.008	0.008 - 0.009	0.007 - 0.008
s.u. P-C	0.011 - 0.012	0.013 - 0.017	0.010 - 0.011
s.u. C-C	0.008 - 0.020	0.009 - 0.020	0.008 - 0.018

The asymmetric unit in this structure consisted of 4 molecules of a phosphine ligand. Probably as a result of the bulky substituents on the substituted phenyl rings they are almost perpendicular to each other with dihedral angles of 88.96°, 88.72°, 88.36° and 89.39° for

rings C_1-C_6 / C_{21}-C_{26}, C_{35}-C_{40} / C_{55}-C_{60}, C_{69}-C_{74} / C_{89}-C_{94} and C_{103}-C_{108} / C_{123}-C_{128} respectively. The fact that the diffraction pattern of this compound was almost orthorhombic but not quite may indicate that the sample was close to a phase transition, however no variable temperature measurements were made at the time to confirm this. ORTEP plots for h05mgd04 ($C_{34}H_{45}O_2PBr_2$) are illustrated in Figure 6.15 and 6.16.

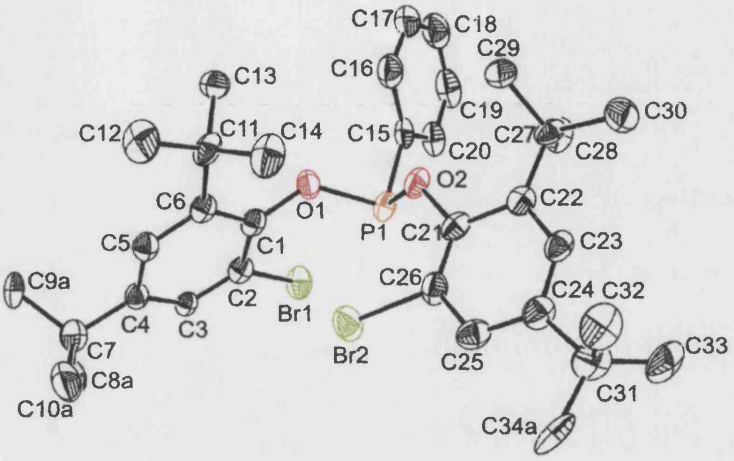

Figure 6.15 - *One molecule of h05mgd04 ($C_{34}H_{45}O_2PBr_2$) with disorder omitted for clarity, the asymmetric unit consists of 4 molecules. Ellipsoids are represented at the 50% level.*

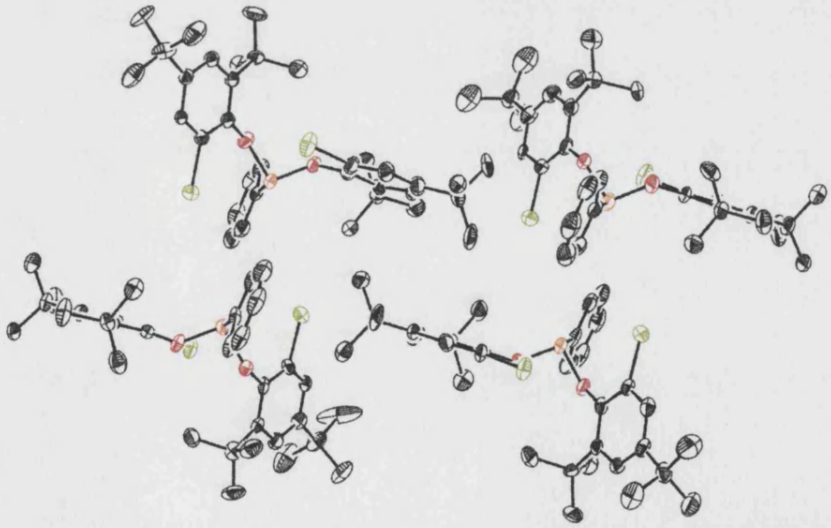

Figure 6.16 - *Asymmetric unit for h05mgd04 ($C_{34}H_{45}O_2PBr_2$), disorder omitted for clarity. Ellipsoids are represented at the 50% level.*

6.4 Non-Merohedral Twinning

6.4.1 h05gb1 – $C_5H_6O_4Br_2$

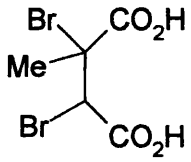

Figure 6.17 - *One molecule of h05gb1 ($C_5H_6O_4Br_2$).*

Despite achieving a structure solution in the triclinic space group *P*-1, there were several problems in the refinement stage that indicated the presence of twinning.

- w*R*2 = 0.4386 upon completion of the structure.
- *K* (= mean (F_{obs}^2)/mean (F_{calc}^2)) for the weakest reflections was large (95.576)
- For most of the disagreeable reflections F_{obs}^2 was greater than F_{calc}^2.
- The difference map had large peaks in chemically unreasonable positions.

6.4.1.1 Determination of the Twin Law

Table 6.8 - *Comparison of the two triclinic cells.*

	a (Å)	*b* (Å)	*c* (Å)	α (°)	ß (°)	γ (°)	V (Å^3)
Triclinic (Cell 1)	6.2120 (2)	11.3140 (3)	23.0150 (7)	96.693 (2)	97.690 (2)	90.056 (1)	1591.86 (8)
Triclinic (Cell 2)	6.2140 (2)	11.3170 (3)	11.5150 (4)	83.286 (1)	82.136 (2)	89.916 (1)	796.58 (4)

In view of the fact that the structure appeared to be twinned, attempts were made to find an alternative cell that was related to the initial cell (Cell 1). Re-indexation identified a second cell (Cell 2) with a *c*-axis half the length of the *c*-axis in the initial cell, see Table 6.8. This resulted in a series of reflections that did not fit the new cell. These were subsequently indexed to give cell parameters matching those of Cell 2 and related to Cell 2 by a 180° rotation around the reciprocal *c**-axis, see Figure 6.18.

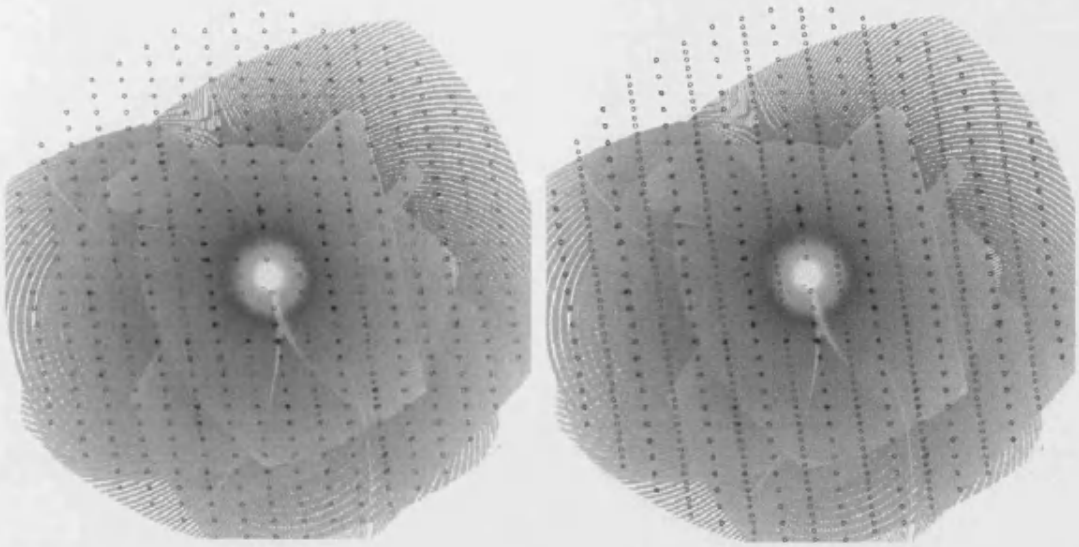

Figure 6.18 - *Precession photograph (h 0 l), (left) red circles indicating the diffraction spots indexed by Cell 2, (right) red circles correspond to the spots indexed by Cell 2 and the green circles correspond to those indexed by a cell related to Cell 2 through a 180° rotation around the reciprocal c*-axis.*

The software to integrate the two cells simultaneously was unavailable, however, an HKLF5 file was created from the integrated reflection file for the main domain (Cell 2) in WINGX using the twin law provided below, which relates the two cells.

$$\textbf{Twin Law} = \begin{pmatrix} -1 & 0 & 0 \\ 0 & -1 & 0 \\ -0.443 & -0.245 & 1 \end{pmatrix}$$

Employing the HKLF5 reflection file during the refinement significantly improved the refinement. One atom, C_6, was unstable when subjected to an anisotropic refinement without restraint, however, the remainder of the atoms were stable. A comparison of the refinement data in both cells is provided in Table 6.9. The proportion of the second domain could not accurately be determined due to the manner in which the twinning was dealt with at the integration stage.

Table 6.9 - *Comparison of refinement data for h05gb1 ($C_5H_6O_4Br_2$) with and without taking account of the non-merohedral twinning.*

	Triclinic (*P*-1) Non-merohedral twinning unaccounted for.	Triclinic (*P*-1) Non-merohedral twinning accounted for
BASF	-	uncalculated
R_1	0.1649	0.0748
wR_2	0.4081	0.1956
Largest Difference Peak and Hole (eÅ^{-3})	5.364, -3.476	2.593, -1.166
K weakest reflections	95.576	3.430
s.u. C-C	0.03 - 0.07	0.009 - 0.010
s.u. C-Br	0.02 - 0.03	0.006 - 0.007
s.u. C-O	0.02 - 0.11	0.009 - 0.010

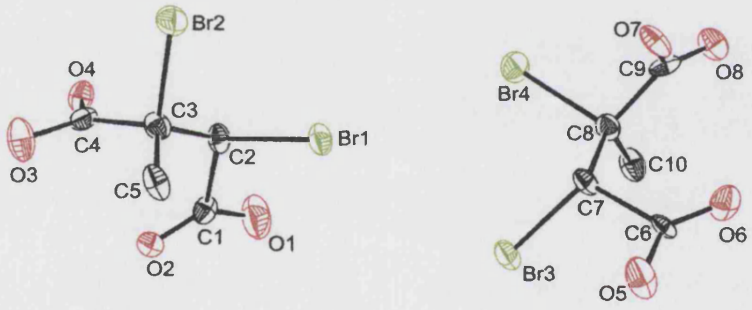

Figure 6.19 - *Asymmetric unit for h05gb1 ($C_5H_6O_4Br_2$). Ellipsoids are represented at the 50% level.*

A final ORTEP plot for h05gb1 ($C_5H_6O_4Br_2$) is provided in Figure 6.19. All of the bond lengths and angles were unremarkable and consistent with similar fragments found in the Cambridge Structural Database. The torsion angles for Br_1-C_2-C_3-Br_2 and Br_3-C_7-C_8-Br_4 were 66.3(5)° and 66.7(5)° respectively.

6.5 References

[6.1] Pickworth Glusker, J., Trueblood, K.N. (1985) *Crystal Structure Analysis A Primer*, 2nd Edition, Oxford University Press.

[6.2] Herbst-Irmer, R., Sheldrick, G., (1998), *Acta Cryst.*, **B54**, 443-449.

[6.3] Parsons, S., (2003), *Acta Cryst.*, **D59**, 1995-2003.

[6.4] Lutz, M. *Twinning Tools in Platon,* powerpoint presentation, Bijvoet Center for Biomolecular Research Dep. Crystal and Structural Chemistry, Utrecht University, Padualaan 8, 3584 CH Utrecht, The Netherlands.

[6.5] Young, V.G.(Jr). *Twinning Workshop,* powerpoint presentation, Department of Chemistry, The University of Minnesota, Minneapolis, MN 55455.

[6.6] Cooper, R.I., Gould, R.O., Parsons, S., Watkin, D.J., (2002), *J. Appl. Cryst.*, **35**, 168-174.

[6.7] Herbst-Irmer, R., Sheldrick, G., (2002), *Acta Cryst.*, **B58**, 477-481.

[6.8] Sheldrick, G.M. (1998) Institüt für Anorganische Chemie der Universität, Tammanstrasse 4, D-3400 Göttingen, Germany.

[6.9] GEMINI (2000) Bruker AXS.

[6.10] Duisenberg, A.J.M.(1992) *J. Appl. Cryst.*, **25,** 92-96.

[6.11] Bolte, M., (2004), *J. Appl. Cryst.*, **37**, 162-165.

[6.12] Spek, A.L. (1988) *J. Appl. Cryst.*, **21,** 578-579.

6.6 Summary of Crystallographic Data

Table 6.10 - *Summary of experimental data for single crystal structures k05alj09, Bath80 and k04pjw4.*

Compound	k05alj09	Bath80	k04pjw4
Empirical formula	$TiC_{26}H_{30}N_2O_8$	$Au_2P_2C_{36}H_{28}Cl_2O\cdot(CH_2Cl_2)$	$Pt_2P_4C_{56}H_{82}O_2$
M	546.41	1088.34	1301.28
Crystal system	Trigonal	Monoclinic	Monoclinic
Space group	$P3_2$	$P2_1/c$	$P2_1/n$
Wavelength (Å)	0.71073	0.6892	0.71073
a (Å)	20.5520(2)	8.9229(16)	9.4610(1)
b (Å)	20.5520(2)	20.269(4)	19.7770(3)
c (Å)	15.9700(1)	19.987(4)	30.7490(4)
α (°)	90	90	90
β (°)	90	102.671(3)	98.897(1)
γ (°)	120	90	90
V (Å^3)	5841.76(9)	3526.8(12)	5684.23(13)
Z	9	4	4
Absorption coefficient (mm^{-1})	0.382	8.021	5.067
Reflections collected	87449	29760	47169
Independent reflections	17344	10004	11698
R_{int}	0.0768	0.0580	0.1103
R_1, w$R2$	0.0457, 0.0625	0.0465, 0.1121	0.0578, 0.1076
R indices (all data)	0.0639, 0.0660	0.0621, 0.1185	0.0894, 0.1288

Table 6.11 - *Summary of experimental data for single crystal structures h05mgd04 and h05gb1.*

Compound	h05mgd04	h05gb1
Empirical formula	$C_{34}H_{45}O_2PBr_2$	$C_5H_6Br_2O_4$
M	676.51	289.92
Crystal system	Monoclinic	Triclinic
Space group	$P2_1$	P-1
Wavelength (Å)	0.71073	0.71073
a (Å)	9.9601(1)	6.2140(2)
b (Å)	28.7318(4)	11.3170(3)
c (Å)	23.5196(4)	11.5150(4)
α (°)	90	83.286(1)
β (°)	90.2377(9)	82.136(2)
γ (°)	90	89.916(1)
V (Å^3)	6730.58(16)	796.58(4)
Z	8	4
Absorption coefficient (mm^{-1})	2.483	10.139
Reflections collected	59706	7176
Independent reflections	26961	7177
R_{int}	0.0659	-
R_1, w$R2$	0.0505, 0.0978	0.0748, 0.1956
R indices (all data)	0.0823, 0.1111	0.0935, 0.2118

Appendix 1.1

Plots of the single crystal structure determinations obtained during the course of this thesis, but not discussed within, are provided in Figures 1.1.1 to 1.1.12, with the ellipsoids represented at the 50% level. The crystallographic tables for these structures are in Appendix 1.2 on the CD.

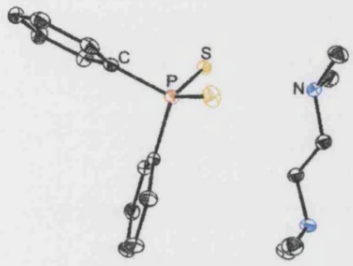

Figure 1.1.1 – *k02prr19 ($[C_{18}H_{27}PS_2N_2]_7$).*

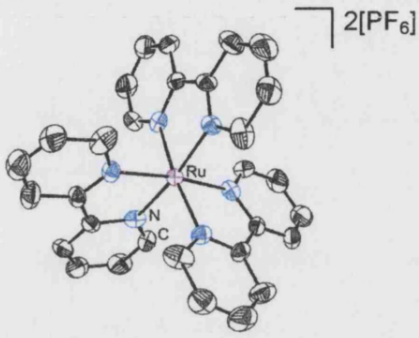

Figure 1.1.2 – *h03prr23 ($[RuN_6C_{30}H_{24}][PF_6]_2$).*

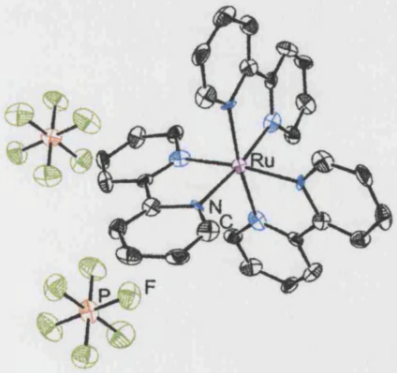

Figure 1.1.3 – *h03prr26 ($[RuN_6C_{30}H_{24}][PF_6]_2$), polymorph of h03prr23.*

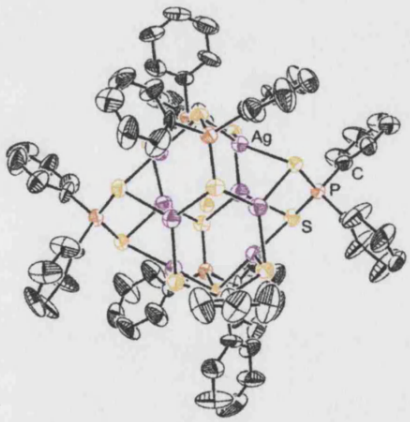

Figure 1.1.4 – *k03prr28 ($[Ag(S_2PPh_2)]_8$).*

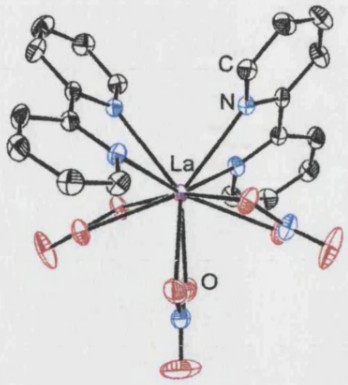

Figure 1.1.5 – *Bath81 ($LaC_{20}H_{16}N_7O_9$).*

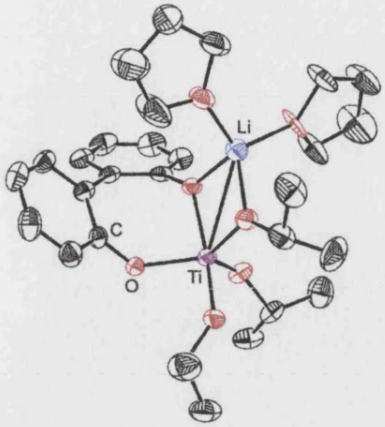

Figure 1.1.6 – *Bath79 ($Ti_2O_{14}C_{58}H_{90}Li_2 \cdot THF$).*

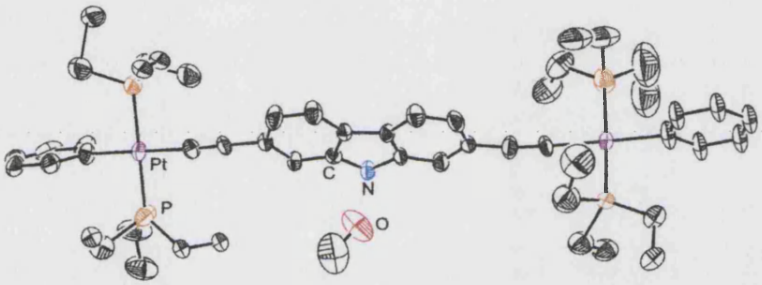

Figure 1.1.7 – *h04prr13 ($Pt_2P_4C_{52}NH_{77} \cdot CH_3OH$).*

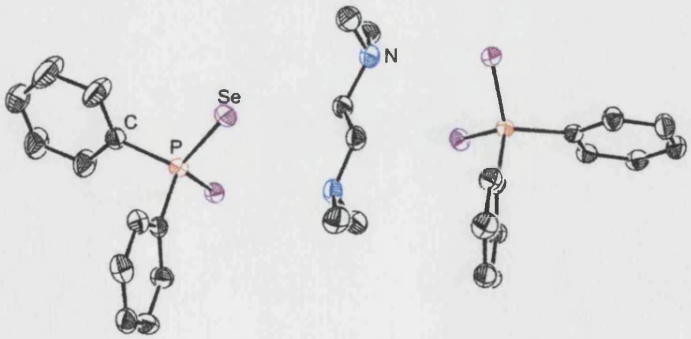

Figure 1.1.8 – *h04prr15 ($C_{30}H_{38}P_2Se_4N_2$).*

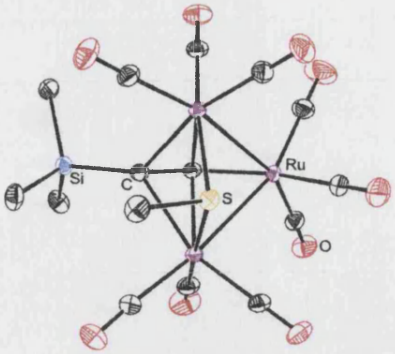

Figure 1.1.9 – *k04prr11 ($Ru_3C_{15}H_{12}O_9SS_i$).*

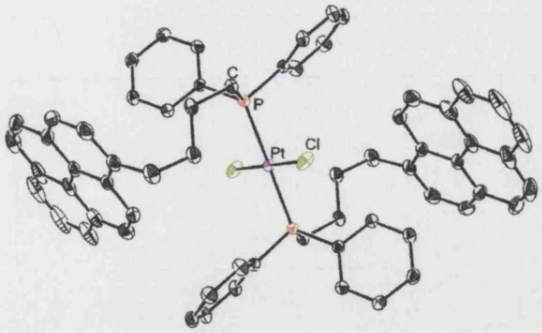

Figure 1.1.10 – *Bath117 ($PtC_{64}H_{54}P_2Cl_2$).*

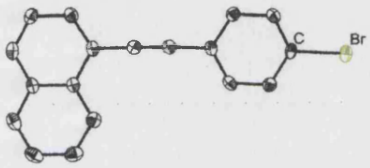

Figure 1.1.11 – *k05prr34 ($C_{18}H_{11}Br$).*

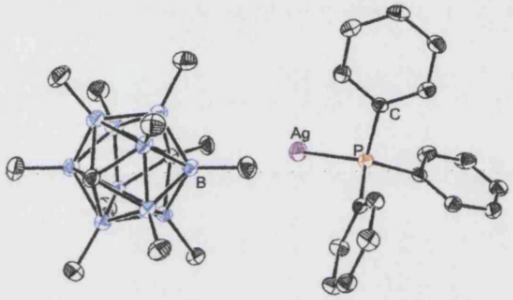

Figure 1.1.12 – *h05prr20 ($AgC_{30}H_{49}B_{11}P$).*

Appendices 1.2, 2.1, 3.1, 4.1, 4.2, 4.3, 4.4, 5.1 and 6.1 can be found on CD at the back of this thesis.

Appendix 6.2 - Derivation of the twin law for k04pjw4

Twin Law = (Orthorhombic ↓ Monoclinic) x (2-fold axis) x (Monoclinic ↓ Orthorhombic)

= (Matrix 3) x (Matrix 2) x (Matrix 1)

The matrix required to convert the monoclinic cell into the orthorhombic cell is

$$\begin{pmatrix} 1 & 0 & 0 \\ -1 & 0 & -2 \\ 0 & 1 & 0 \end{pmatrix}$$

Matrix 1

Determinant of Matrix 1 = 1(2) + 0(0) + 0(-1)

= 2

$$\begin{pmatrix} 2 & 0 & -1 \\ 0 & 0 & 1 \\ 0 & -2 & 0 \end{pmatrix}$$

Matrix A – *matrix of minors for Matrix 1.*

apply

$$\begin{pmatrix} 1 & -1 & 1 \\ -1 & 1 & -1 \\ 1 & -1 & 1 \end{pmatrix}$$

Matrix of cofactors

$$\longrightarrow \quad \begin{pmatrix} 2 & 0 & -1 \\ 0 & 0 & -1 \\ 0 & 2 & 0 \end{pmatrix}$$

Matrix B

transpose ↓

$$\begin{pmatrix} 2 & 0 & 0 \\ 0 & 0 & 2 \\ -1 & -1 & 0 \end{pmatrix}$$

Adj(A)

The matrix required to convert the orthorhombic cell back into the monoclinic cell is the inverse of Matrix 1.

Inverse (Matrix 1) = (1/determinant of Matrix 1) x Adj(A)

$$= \tfrac{1}{2} \times \begin{pmatrix} 2 & 0 & 0 \\ 0 & 0 & 2 \\ -1 & -1 & 0 \end{pmatrix}$$

$$= \begin{pmatrix} 1 & 0 & 0 \\ 0 & 0 & 1 \\ -0.5 & -0.5 & 0 \end{pmatrix}$$

Matrix 3

The twin law for k04pjw4 is then the product of Matrix 1, 2 and 3.

Twin Law = (Matrix 3) x (Matrix 2) x (Matrix 1)

$$= \begin{pmatrix} 1 & 0 & 0 \\ 0 & 0 & 1 \\ -0.5 & -0.5 & 0 \end{pmatrix} \times \begin{pmatrix} -1 & 0 & 0 \\ 0 & 1 & 0 \\ 0 & 0 & -1 \end{pmatrix} \times \begin{pmatrix} 1 & 0 & 0 \\ -1 & 0 & -2 \\ 0 & 1 & 0 \end{pmatrix}$$

$$= \begin{pmatrix} -1 & 0 & 0 \\ 0 & 0 & -1 \\ 0.5 & -0.5 & 0 \end{pmatrix} \times \begin{pmatrix} 1 & 0 & 0 \\ -1 & 0 & -2 \\ 0 & 1 & 0 \end{pmatrix}$$

$$= \begin{pmatrix} \mathbf{-1} & \mathbf{0} & \mathbf{0} \\ \mathbf{0} & \mathbf{-1} & \mathbf{0} \\ \mathbf{1} & \mathbf{0} & \mathbf{1} \end{pmatrix}$$

Appendix 6.3 - Derivation of the twin law for h05mgd04

Twin Law = [Orthorhombic ↓ Monoclinic] x [2-fold axis] x [Monoclinic ↓ Orthorhombic]

= (Matrix 3) x (Matrix 2) x (Matrix 1)

The matrix required to convert the monoclinic cell into the orthorhombic cell is

$$\begin{pmatrix} -1 & 0 & 0 \\ 0 & 0 & -1 \\ 0 & -1 & 0 \end{pmatrix}$$

Matrix 1

Determinant of Matrix 1 = -1(-1) + 0(0) + 0(0)

= 2

$$\begin{pmatrix} -1 & 0 & 0 \\ 0 & 0 & 1 \\ 0 & 1 & 0 \end{pmatrix}$$

Matrix A – *matrix of minors for Matrix 1.*

apply

$$\begin{pmatrix} 1 & -1 & 1 \\ -1 & 1 & -1 \\ 1 & -1 & 1 \end{pmatrix}$$

Matrix of cofactors

$$\longrightarrow \quad \begin{pmatrix} -1 & 0 & 0 \\ 0 & 0 & -1 \\ 0 & -1 & 0 \end{pmatrix}$$

Matrix B

transpose ↓

$$\begin{pmatrix} -1 & 0 & 0 \\ 0 & 0 & -1 \\ 0 & -1 & 0 \end{pmatrix}$$

Adj(A)

The matrix required to convert the orthorhombic cell back into the monoclinic cell is the inverse of Matrix 1.

Inverse (Matrix 1) = (1/determinant of Matrix 1) x Adj(A)

$$= 1 \times \begin{pmatrix} -1 & 0 & 0 \\ 0 & 0 & -1 \\ 0 & -1 & 0 \end{pmatrix}$$

$$= \begin{pmatrix} -1 & 0 & 0 \\ 0 & 0 & -1 \\ 0 & -1 & 0 \end{pmatrix}$$

Matrix 3

The twin law for h05mgd04 is then the product of Matrix 1, 2 and 3.

Twin Law = (Matrix 3) x (Matrix 2) x (Matrix 1)

$$= \begin{pmatrix} -1 & 0 & 0 \\ 0 & 0 & -1 \\ 0 & -1 & 0 \end{pmatrix} \times \begin{pmatrix} -1 & 0 & 0 \\ 0 & 1 & 0 \\ 0 & 0 & -1 \end{pmatrix} \times \begin{pmatrix} -1 & 0 & 0 \\ 0 & 0 & -1 \\ 0 & -1 & 0 \end{pmatrix}$$

$$= \begin{pmatrix} 1 & 0 & 0 \\ 0 & 0 & 1 \\ 0 & -1 & 0 \end{pmatrix} \times \begin{pmatrix} -1 & 0 & 0 \\ 0 & 0 & -1 \\ 0 & -1 & 0 \end{pmatrix}$$

$$= \begin{pmatrix} \mathbf{-1} & \mathbf{0} & \mathbf{0} \\ \mathbf{0} & \mathbf{-1} & \mathbf{0} \\ \mathbf{0} & \mathbf{0} & \mathbf{1} \end{pmatrix}$$